

NASA CR-72487

R-7677

169-28130
NASA CR-72487

SPACE STORABLE PROPELLANT PERFORMANCE STUDY
FINAL REPORT

by

A. Y. Falk
S. D. Clapp
C. K. Nagai

**CASE FILE
COPY**

prepared for

NATIONAL AERONAUTICS AND SPACE ADMINISTRATION

Contract NAS3-11199

ROCKETDYNE

A DIVISION OF NORTH AMERICAN ROCKWELL CORPORATION

NOTICE

This report was prepared as an account of Government sponsored work. Neither the United States, nor the National Aeronautics and Space Administration (NASA), nor any person acting on behalf of NASA:

- A.) Makes any warranty or representation, expressed or implied, with respect to the accuracy, completeness, or usefulness of the information contained in this report, or that the use of any information, apparatus, method, or process disclosed in this report may not infringe privately owned rights; or
- B.) Assumes any liabilities with respect to the use of, or for damages resulting from the use of any information, apparatus, method or process disclosed in this report.

As used above, "person acting on behalf of NASA" includes any employee or contractor of NASA, or employee of such contractor, to the extent that such employee or contractor of NASA, or employee of such contractor prepares, disseminates, or provides access to, any information pursuant to his employment or contract with NASA, or his employment with such contractor.

Requests for copies of this report should be referred to

National Aeronautics and Space Administration
Office of Scientific and Technical Information
Attention: AFSS-A
Washington, D.C. 20546

SPACE STORABLE PROPELLANT PERFORMANCE STUDY
FINAL REPORT

by

A. Y. Falk
S. D. Clapp
C. K. Nagai

prepared for

NATIONAL AERONAUTICS AND SPACE ADMINISTRATION

24 November 1968

Contract NAS3-11199

Technical Management
NASA Lewis Research Center
Cleveland, Ohio

Larry H. Gordon

Rocketdyne
A Division of North American Rockwell Corporation
6633 Canoga Avenue, Canoga Park, California

FOREWORD

This report was prepared for the NASA Lewis Research Center, Cleveland, Ohio, by Rocketdyne, a division of North American Rockwell Corporation. The study was conducted in accordance with Contract NAS3-11199; G.O. 09006.

Mr. L. H. Gordon, NASA Lewis Research Center, served as NASA Technical Project Manager. The Rocketdyne Program Manager was Mr. T. A. Coultas. Technical approach and guidance of the program was directed by Mr. S. D. Clapp, who functioned as Rocketdyne Project Manager.

ABSTRACT

A 13-month applied research program encompassing an analytical, design, and experimental effort to develop high performance injectors for space storable propellants was conducted. The liquid-liquid propellant combination selected for study was FLOX (80% F_2)/55% methane-45% ethane LPG blend. The program was apportioned into three basic technical tasks: Task I--Injector and Thrust Chamber Design, Task II--Injector and Thrust Chamber Fabrication, and Task III--Performance Evaluation Testing. The test matrix covered a range of chamber pressure (50 to 200 psia), mixture ratio (3 to 7), chamber geometry ($15 \text{ inch} \leq L^* \leq 60 \text{ inch}$; at both 2 and 4:1 contraction ratios), and FLOX compositions (70 to 100% F_2). Performance in the reference chamber ($L^* = 30 \text{ inch}$; $\epsilon_c = 2$) at nominal design conditions ($P_c = 100 \text{ psia}$; MR = theoretical optimum c^* value = 5.33) was 97 percent of the shifting equilibrium c^* value. Results of the study provide a sound basis for positive design techniques for application to the general class of "space-storable" propellants.

CONTENTS

Foreword	iii
Abstract	iii
Introduction	1
Summary	5
Parametric Combustion Analysis	9
Propellant Vaporization	9
Mixing Efficiency	17
Experimental Hardware	21
Injectors	21
Thrust Chambers	33
Results	37
Performance	38
Thrust Chamber Heat Transfer	44
Combustion Instability	51
Discussion of Performance Results	57
Effect of Distribution on Performance	57
Effect of Vaporization Performance	61
Performance Prediction	67
Concluding Remarks	71
References	73
<u>Appendix A</u>	
Calculation of Corrected c^* Efficiency	A-1
<u>Appendix B</u>	
Performance Data Measurement Error Analysis	B-1
<u>Appendix C</u>	
Random Walk Measurement Analysis Program	C-1
<u>Appendix D</u>	
Experimental Facilities and Procedures	D-1
<u>Appendix E</u>	
Theoretical Performance, Combustion Gas Properties, and Propellant Densities for FLOX Mistures/LPG Blend	E-1
<u>Appendix F</u>	
Heat Transfer Data Analysis Technique	F-1
<u>Appendix G</u>	
Distribution List	G-1

ILLUSTRATIONS

1. The Effect of Dropsizes on Characteristic Velocity Efficiency (due to vaporization) for Various Chamber Geometries	97
2. Simplified Schematics of Thrust Chamber Geometries Considered for Combustion Model Analysis	98
3. The Effect of Dropsizes on Characteristic Velocity Efficiency (due to vaporization) for Various Chamber Pressures	99
4. Effect of Chamber Pressure on Combustion Gas Property Variation	100
5. Effect of Propellant Dropsizes on c^* Efficiency (due to vaporization) for Various Injector Mixture Ratios	101
6. The Effect of Mixture Ratio on Characteristic Velocity Efficiency (due to vaporization) for Various Initial Propellant Dropsizes	102
7. Effect of Mixture Ratio on c^* Efficiency (due to propellant vaporization) for Initial Equal Propellant Dropsizes of 100 Microns	103
8. Prediction Effect of Nonuniform Distribution on Performance for Several Mixture Ratios	104
9. Schematic Representation of Injector Face Pattern for Typical Like-Doublet Injector	105
10. Geometric Factors Affecting Propellant Distribution for Like- Doublet Injector Elements	106
11. Face View of Like Doublet Injector No. LD-1-M Showing Orifice Pattern	107
12. Typical Element in Model Self-Impinging Doublet Injectors	108
13. Schematic Representation of Face Pattern for Typical Five- Element Model Injector	109
14. Effect of Fan Inclination Angle on Propellant Mixing for the Like-Doublet Injector Pattern	110
15. Effect of Fan Inclination Angle and Intra-Element Spacing on Propellant Mixing for the Like-Doublet Injector Pattern	111
16. Schematic Representation of Typical Face Pattern for Pentad Injectors	112

17. Face View of Pentad Injector No. P-2-M2 Showing Orifice Pattern	113
18. Schematic Representation of Reference ($L^* = 30$ Inches; $\epsilon_c = 2$) Thermally Instrumented Uncooled Motor Used for Injector Optimization Studies	114
19. Schematic Representation of Reference ($L^* = 30$ Inches; $\epsilon_c = 2$) Chamber Assembly Showing Segmented Design and Dimensions	115
20. Schematic Representation of Alternate Contraction Ratio $L^* = 30$ Inches; $\epsilon_c = 4$) Chamber Assembly Showing Segmented Design and Dimensions	116
21. Photograph of 30-Inch L^* Thrust Chamber Assembly Mounted on Thrust Stand	117
22. Comparison of Corrected c^* Efficiencies Based on Measurement of Chamber Pressure and Thrust	118
23. Corrected c^* Efficiency as a Function of Mixture Ratio for Two Pentad and Three Like-Doublet Injectors	119
24. Measured Distribution Efficiency, E_m , and Predicted Effect of Nonuniform Distribution, $\eta_{c^*,dist}$, on Performance as a Function of Mixture Ratio for Two Pentad Injectors	120
25. Measured Distribution Efficiency, E_m , and Predicted Effect of Nonuniform Distribution, $\eta_{c^*,dist}$, on Performance as a Function of Mixture Ratio for Three Like-Doublet Injectors	121
26. Mass and Mixture Ratio Distribution Profiles for Spray From Pentad Injector P-1	122
27. Mass and Mixture Ratio Distribution Profiles for Spray From Pentad Injector P-2	123
28. Mass and Mixture Ratio Distribution Profiles for Spray From Like-Doublet Injector LD-1	124
29. Mass and Mixture Ratio Distribution Profiles for Spray From Like-Doublet Injector LD-2	125
30. Mass and Mixture Ratio Distribution Profiles for Spray From Like-Doublet Injector LD-3	126
31. Characteristic Heat Flux Curves for the 4-on-1 Pentad Injector and Like-Doublet Injector at Common Test Conditions	127

46.	Predicted Effect of Nonuniform Distribution on Performance, η_{c*} , dist', as a Function of Measured Distribution Efficiency, E_m , and Mixture Ratio	142
47.	Measured Mixture Ratio Distribution Efficiency, E_m , as a Function of Fan Inclination Angle and Fan Spacing for Like- Doublet Injectors	143
48.	Measured Distribution Efficiency, E_m , as a Function of Distri- bution Parameter, K, for Two Pentad Injectors	144
49.	Effect of Propellant Dropsizes and Chamber Geometry on Characteristics Velocity Efficiency	145
50.	Comparison of Predicted and Actual Performance for Like- Doublet Injectors	146

TABLES

I.	Summary of Injector Assembly Specifications	77
II.	Model Injector Design Specifications	78
III.	Summary of Model Injector Cold-Flow Data	79
IV.	Chamber Assembly Specifications	80
V.	Summary of Performance Data	81
VI.	Location of Key for Heat Flux Data in Table VII	86
VII.	Summary of Heat Flux Data	87
VIII.	Summary of Cold-Flow Data	93
IX.	Comparison of Combustion Stability of Pentad and Like Doublet Injectors	94
X.	Predicted Fuel Dropsizes Variation as a Function of Injector Design and Operating Conditions	95
XI.	Predicted and Actual Performance at Optimum Mixture Ratio for FLOX/LPG Propellants as a Function of Injector and Thrust Chamber Design and Operating Conditions	96

INTRODUCTION

In recent years, the class of propellants known as "space-storable" has received considerable attention. These propellant combinations, although loosely defined, are characterized by high specific impulse values, high bulk density, hypergolic ignition, overlapping liquid ranges of the fuel and oxidizer, and semi-cryogenic storage temperatures. Typical examples of such propellants are FLOX or OF_2 as oxidizers with the light hydrocarbon (LPG) fuels. These propellants are attractive for missions requiring long-term space storage of propellants and high specific impulse. They may also have application for uprating of existing earth-storable propellant stages wherein higher specific impulse and comparable bulk density are important.

In previous technology programs undertaken with these propellants, the primary objectives were to evaluate their cooling capabilities for space propulsion applications. Generally, high combustion efficiencies were not obtained with the FLOX/LPG propellant combinations. Their low performance has been attributed to a variety of reasons including the fact that peak specific impulse occurs at stoichiometric mixture ratio. This is a difficult operating point at which to obtain high c^* efficiency. Also, the rather high mixture ratio (o/f) values restricts the types of injector element designs that are applicable for a liquid-liquid propellant system.

High performance (delivered c^* efficiency in excess of 95 percent theoretical) has been consistently achieved over a broad range of operating variables with other space-storable propellants. Existing theories and previous experimental results obtained on numerous programs at Rocketdyne strongly suggested that high delivered performance with the light hydrocarbon fuels should not present extraordinary problems. Accordingly, an analytical, design, and experimental program was conducted to establish design criteria for a high-performance injector using the FLOX (80-percent fluorine)/55 percent methane-45 percent ethane LPG blend. A primary goal

of this program was definition of necessary design principles for the development of a FLOX/LPG blend injector capable of delivery of 97 percent of theoretical shifting characteristic exhaust velocity efficiency, at optimum mixture ratio, in a nominal 30-inch L^* chamber. An additional objective of this program was establishment of design criteria which would allow subsequent extrapolation of the program results to other advanced space storable propellant combinations and operating conditions.

A 13-month applied research program was performed to accomplish the program objectives. The program effort was apportioned into three basic technical tasks: Task I--Injector and Thrust Chamber Design, Task II--Injector and Thrust Chamber Fabrication, and Task III--Performance Evaluation Testing.

Task I was directed to the specific objective of injector and thrust chamber design. This task was divided into three subtasks: (1) Task IA--Parametric Combustion Analysis, (2) Task IB--Injector Design, and (3) Task IC--Thrust Chamber Design.

Task IA consisted of an analytical combustion performance study to define injector and thrust chamber design requirements. The basic objective of this study was to determine the effect of propellant atomization and distribution on attainable performance for FLOX/LPG. Theoretical performance calculations were made utilizing a computer program based on a Rocketdyne-developed, one-dimensional, steady-state combustion model for vaporization rate-limited propellant systems. This model has been extensively used at Rocketdyne for several years. Experience has been gained from the application of the model to the calculation of c^* efficiencies which have compared favorable to experimentally measured values. This analytical study permitted computations of c^* efficiency as a function of propellant drop-size (atomization), chamber pressure, mixture ratio, and chamber geometry (L^* and contraction ratio). The analytical study also included computation of the effect of local mixing on performance by employment of a stream tube analysis technique wherein the chamber cross section is divided into discrete

"tubes" of differing mixture ratio and percent mass. Overall performance was defined as a function of departure from ideal distribution by integrating the c^* levels obtained, assuming no mixing between the "stream tubes." These results served as a guide in defining the degree of local mixing which must be produced by the injector.

Task IB was directed toward the design of injectors for the specific FLOX/LPG blend propellant combination. Two injector types (unlike and like impinging stream designs) were designed. These injector designs were based on existing theories, previous experimental results, and the design principles derived from the Task IA effort.

Task IC consisted of design of a thrust chamber assembly to be used during the experimental portion of the program. Currently available design technology was utilized for the design of an uncooled calorimeter chamber and nozzle assembly. The chamber geometry was specified on the basis of the results obtained from the analytical combustion performance study (Task IA).

The Task III performance evaluation test effort included cold-flow and hot-firing experiments using two 4-on-1 and three like-on-like doublet injector designs. The nominal experimental and thrust chamber design conditions were as follows:

1. Chamber Pressure, psia	100
2. Oxidizer	80-20% F_2-O_2
3. Mixture Ratio, o/f	5.33 (maximum theoretical c^*)
4. Thrust Level (sea level), pounds	3000
5. Chamber Contraction Area Ratio	2:1
6. Chamber L^* , inches	30

These nominal conditions were varied over the following ranges:

- | | |
|-----------------------------------|---------------------------|
| 1. Chamber Pressure, psia | 50 to 200 psia |
| 2. Oxidizer | 70 to 100% F ₂ |
| 3. Mixture Ratio | 3 to 7 |
| 4. Thrust Level, pounds | 1500 to 5000 |
| 5. Chamber Contraction Area Ratio | 2 to 4:1 |
| 6. Chamber L*, inches | 15 to 60 |

Experimental results were correlated in terms of mixing and vaporization effects on performance.

SUMMARY

This report presents the results of an analytical and experimental program to develop high-performance injectors for space storable FLOX/LPG propellants. The FLOX (80-percent fluorine)/LPG (55-percent methane/45-percent ethane) propellant system was selected for study. The primary objectives were to define those design principles for application to injectors capable of 97-percent shifting equilibrium c^* performance in a 30-inch L^* chamber (at optimum mixture ratio) for at least two different injector types. An equally important goal of this study was the generalization of these design criteria for subsequent extrapolation to other space storable propellants and operating conditions. The basic premise on which this objective was based was the fundamental argument that only the effects of propellant atomization and distribution would determine the ultimate c^* efficiency of most contemporary space storable propellants. Further, it was postulated that the effects of property differences from propellant to propellant could be resolved strictly on an analytical basis.

The initial phase of this program was directed entirely to analytical modeling studies to determine parametric effects of propellant atomization and distribution. A Rocketdyne-developed combustion model computer program was used to analytically determine the contribution of propellant vaporization to overall delivered c^* efficiency. The effects of propellant droptime and chamber geometry were fully analyzed as were the secondary effects of chamber pressure and mixture ratio. In addition to these variables, only the chemical-physical and equilibrium gas properties of the propellant system were required for this comprehensive analysis. Because basic propellant properties and thermodynamic data are readily available, the combustion model can be universally applied to similar chemical propellant systems. The effects of propellant distribution were also evaluated on an analytical basis using simplified stream tube analysis techniques and the specific equilibrium thermodynamics of the FLOX/LPG bipropellants. The results of this study permitted definition of the required atomization and distribution characteristics of the two candidate injector types which were studied in this program.

A like-doublet injector and a 4-on-1 (pentad) injector were selected for design and evaluation. The size, number, and orientation of the injector elements were based on the preceeding analytical study which defined the required degree of propellant atomization and distribution. Atomization correlations developed by Ingebo at NASA together with previous supporting experiments conducted at Rocketdyne were used to define the specific element geometry for efficient propellant atomization. Propellant distribution criteria of Rupe at JPL together with supporting cold-flow studies were used to define element characteristics and orientation for efficient propellant distribution. Finally, the two basic injector types were geometrically perturbed to provide experimental evaluation and confirmation of propellant atomization and distribution effects originally defined by model analysis.

During the experimental phase, 125 hot-fire experiments and 23 supporting cold-flow tests were conducted to fully characterize the two candidate injectors. The initial test phase was directed at a study of propellant atomization and distribution by making programmed variations in injector element geometry characteristics and by variations in element orientation. In addition, perturbations in chamber pressure and mixture ratio were also undertaken to assess their effect on the spray characteristics and the resultant c^* efficiency. Selected cold-flow tests with inert propellant simulants were conducted to support analysis of propellant distribution effects on injector performance at both design and off-design conditions. The hot-fire experiments to define spray characteristic effects on performance were augmented by supporting heat transfer and stability assessment to aid in selection of the injector type considered best suited for further study with the FLOX/LPG. The results of this first phase hot-fire study indicated that both the like-doublet and 4-on-1 injector could be designed for equal performance capabilities. The supporting heat transfer and stability analysis, however, indicated that the like-doublet injector was inherently much superior to the 4-on-1 injector because of its capability for a controlled lower chamber heat flux load and inherent stability even under off-design conditions.

Although performance capability was essentially identical for both injector types, significant differences in both heat transfer and stability characteristics favored selection of the like-impinging-doublet injector for further experimental study. Performance in the reference chamber ($L^* = 30$ inches; $\epsilon_c = 2$) at nominal design conditions ($P_c = 100$ psia; $MR = 5.33$) was approximately 97 percent of the shifting equilibrium c^* value for both injector types. Subsequent terminal studies were conducted with an optimized like-doublet injector to further assess effects of chamber L^* and contraction ratio. Experimental perturbation of chamber geometry fully confirmed expectations developed from the earlier combustion model studies with respect to chamber geometry, chamber pressure, and mixture ratio effects on resultant performance. Concluding experiments with fluorine concentration changes in the FLOX oxidizer also fully confirmed the preceding analytical studies.

The results of this applied research program clearly indicated that high performing injectors could be developed for FLOX/LPG propellants. Injector design criteria for high performance, compatible heat transfer, and inherent stability for a 100-psia pressure fed propulsion system were developed. More importantly, however, these studies provided a basis for positive design techniques for application to other contemporary space storable propellant systems and to other operating requirements.

PARAMETRIC COMBUSTION ANALYSIS

Rational design of rocket engine components using fundamental engineering principles requires a basic understanding of combustion and its relationship to the physical processes which control it. For most liquid bipropellant systems, of which FLOX/LPG is typical, c^* efficiency is affected by both propellant vaporization and mixing. These two processes can be considered independently (Ref. 1) in their effects on efficiency. A close approximation of overall efficiency can be obtained from

$$\eta_{c^*} = \eta_{c^*, \text{vap}} \times \eta_{c^*, \text{dist}} \quad (1)$$

where

- η_{c^*} = the overall c^* efficiency
- $\eta_{c^*, \text{vap}}$ = the c^* efficiency which would be obtained if propellant mixing were completely uniform, and the only losses were caused by incomplete propellant vaporization
- $\eta_{c^*, \text{dist}}$ = the c^* efficiency which would be obtained if propellant vaporization were entirely complete, and the only losses were caused by nonuniform propellant mixing

Analysis of the parameters which affect c^* efficiency is therefore logically divided into considerations of $\eta_{c^*, \text{vap}}$ and $\eta_{c^*, \text{dist}}$.

PROPELLANT VAPORIZATION

The effects of incomplete propellant vaporization on c^* efficiency can be quantitatively studied by means of an analytical propellant combustion model developed at Rocketdyne several years ago by Lambiris, Combs, and Levine (Ref. 2). This combustion model exists in the form of a Fortran IV Computer Program written for the IBM-360 computer. To determine the degree of propellant vaporization, the combustion model takes into consideration:

1. Compressible combustion gas flow with mass and energy addition

2. Droplet drag in the accelerating combustion gas flow
3. Droplet vaporization with convective heat transfer from the hot combustion gas

These factors result in an analytical description of the "bootstrap" combustion processes typical of rocket engines. The model calculates axial profiles of chamber pressure, combustion gas velocity, vaporization from a range of droplet sizes corresponding to the droplet size distribution produced by the injector, droplet velocities, and the overall percentage of fuel and oxidizer vaporized.

The combustion model takes into account the compressible flow of combustion gases by the normal gas-dynamic equations; taking into account the effects of mass and energy addition from the vaporizing and reacting propellants.

Droplet drag, for the distribution of droplet sizes produced by the injector, is accounted for by the scalar equation shown below:

$$\frac{dV_D}{dt} = \frac{3}{4} \times \frac{C_D \rho_g (V_g - V_D)^2}{\rho_L D} \quad (2)$$

where

V_D = droplet velocity, ft/sec

t = time, seconds

C_D = drag coefficient (a function of droplet Reynolds number)

ρ_g = combustion gas density, lb/ft³

ρ_L = droplet liquid density, lb/ft³

V_g = combustion gas velocity, lb/ft³

D = droplet diameter, feet

Droplet vaporization is accounted for by an equation similar to:

$$\frac{d(D^2)}{dt} = k' = \frac{144 \times 8 \lambda_g}{\rho_L C_{p_v}} \ln \left[1 + \frac{C_{p_v}}{\Delta H_v} (T_g - T_v) \right] \left(1 + 0.6 \text{Pr}^{1/3} \text{Re}^{1/2} \right) \quad (3)$$

where

- k' = droplet vaporization constant, in.²/sec
- D = droplet diameter
- λ_g = combustion gas thermal conductivity
- ρ_L = liquid density
- C_{p_v} = vaporized propellant heat capacity
- ΔH_v = liquid propellant heat of vaporization
- T_g = combustion gas temperature
- T_L = liquid propellant boiling temperature
- Pr = Prandtl Number for the combustion gas
- ρ_g = combustion gas density
- Re = Reynolds Number for combustion gas

For computer solution of Eq. 3, the application is more complex. The simplified expression presented above shows the effects of the various physical parameters on droplet vaporization rate. The last bracketed term on the right-hand side of Eq. 3 represents the effects of forced convection on droplet vaporization, and the remainder of the terms represent the effects of propellant physical properties and combustion gas properties on droplet vaporization rate.

Incomplete propellant vaporization degrades c^* performance in two ways: (1) incomplete vaporization reduces the total amount of combustion gas produced, and (2) if fuel and oxidizer do not vaporize at the same rate,

this can make the burned gas mixture ratio different from the injected liquid mixture ratio, thereby affecting the temperature, molecular weight, etc. of the burned gas. Both of these effects have been included by Priem (Ref. 3) in the following equation which allows the determination of $\eta_{c^*,\text{vap}}$ from parameters calculated by the combustion model computer program:

$$\eta_{c^*,\text{vap}} = \left(\frac{\dot{w}_B}{\dot{w}_I} \right) \left(\frac{c^*_B}{c^*_I} \right) \quad (4)$$

where

- \dot{w}_B = flowrate of burned gas at the geometric throat
- \dot{w}_I = injection flowrate of fuel plus oxidizer
- c^*_B = theoretical c^* corresponding to the composition of the burned gas at the geometric throat
- c^*_I = theoretical c^* corresponding to the injection mixture ratio of liquid fuel and oxidizer

This computerized combustion model, the general nature of which is described in very brief form by Eq. 1 through 4, has been used to parametrically investigate the effects of design and operating variables on $\eta_{c^*,\text{vap}}$ for the FLOX/LPG propellant combination.

The two most important variables affecting $\eta_{c^*,\text{vap}}$ are propellant drop-size and combustion chamber geometry. From Eq. 3, it is seen that the residence time required to completely vaporize a droplet is proportional to the square of the droplet diameter. Equally important, the geometry of the combustion chamber dictates the total residence time during which the droplets must vaporize. If this residence time is too short, the droplets will not be completely vaporized.

The effect of propellant dropsize and chamber geometry on characteristic velocity efficiency due to vaporization, $\eta_{c^*, \text{vap}}$, is shown parametrically in Fig. 1. Curves of $\eta_{c^*, \text{vap}}$ versus dropsize are shown for conventionally shaped thrust chambers (see Fig. 2) having characteristic lengths of 15, 30, and 60 inches. The solid lines ($A_c/A_t = 2$) and dashed lines ($A_c/A_t = 4$) define the effect of contraction ratio at any given L^* value.

Figure 1 will show that when propellant dropsize is small, the effects of chamber geometry are generally attenuated. Conversely, when initial propellant dropsizes are large, chamber geometry effects become pronounced and c^* efficiency becomes much more sensitive to specific geometric features such as chamber length and contraction ratio. For a given initial dropsize and chamber L^* , increase in vaporization efficiency can be effected by reduction of the contraction area ratio (increase of physical length). As an example, with a volume mean dropsize of 70 microns, $\eta_{c^*, \text{vap}}$ of 98 percent can be attained with the 30-inch L^* chamber having the 2-to-1 contraction area ratio. Use of a 4-to-1 contraction area ratio chamber at the same L^* would have resulted in a 1-percent efficiency decrement. With larger initial propellant dropsizes, progressively longer L^* chambers would be required to maintain the same level of efficiency.

Equation 3 is an implicit expression showing that propellant vaporization efficiency is governed by droplet acceleration and heating by the high-temperature combustion gas. For thrust chambers having contraction area ratios greater than about 2, combustion gas flow can be considered incompressible, therefore chamber L^* is a good index of combustion gas residence time. From continuity, combustion gas velocity for the 2-to-1 chamber will always be higher than that for the 4-to-1 chamber. Higher combustion gas velocities will generally be accompanied by an increased velocity lag between combustion gas and propellant droplets. The increased velocity lag between combustion gas and droplet for the smaller

contraction area ratio chambers will tend to result in longer residence time for the droplets. The higher relative velocity between the combustion gas and propellant droplets will also tend to enhance convective heating and resultant droplet vaporization.

The effect of chamber pressure on c^* efficiency due to vaporization is shown in Fig. 3. The curves are for a common mixture ratio ($MR = 5.33$) and chamber characteristic length, L^* , of 30 inches. Curves of $\eta_{c^*,vap}$ versus dropsizes are shown for chamber pressures of 50, 100, and 200 psia. The solid lines ($A_c/A_t = 2$) and dashed lines ($A_c/A_t = 4$) define the effect of contraction ratio at the three chamber pressure values. The effect of chamber pressure on $\eta_{c^*,vap}$ is attenuated when propellant dropsizes are small, while both pressure and geometry effects become more pronounced with larger dropsizes.

As shown in Fig. 4, chamber pressure primarily affects the combustion gas density with only secondary effects on combustion temperature. Increased combustion gas density (Eq. 3) results in an increase in convective heating of the droplets, but also tends to accelerate the droplets because of a corresponding increase in drag force on the droplets. The net effect, however, is toward improved vaporization efficiency, particularly when dropsizes are initially large and lag effects become more pronounced.

The effect of mixture ratio on c^* efficiency (due to vaporization) is shown in Fig. 5 in which $\eta_{c^*,vap}$ is shown as a function of dropsizes for various mixture ratios. The curves are for a chamber pressure of 100 psia and constant thrust chamber geometry ($L^* = 30$ inches, $A_c/A_t = 2$). The effect of mixture ratio is small when initial dropsizes are small, and conversely, becomes more pronounced when initial dropsizes are large. The effect of mixture ratio is not monotonic and a specific optimum mixture ratio less than that corresponding to the theoretical optimum of 5.33 is indicated for maximum vaporization efficiency (shown in supplementary Fig. 6).

A reduced optimum mixture ratio can occur when initial dropsize for fuel and oxidizer are identical. For FLOX/LPG, fuel vaporization is the rate-limiting process and therefore the reactants will combine at a higher than injected mixture ratio in the gas phase.

An explanation of mixture ratio effects can be aided by reference to Fig. 7 in which $\eta_{c^*, \text{vap}}$ is shown as a function of mixture ratio for a nominal dropsize of 100 microns. The contributing product terms defined in the Priem model:

$$\eta_{c^*, \text{vap}} = \left(\frac{\dot{w}_B}{\dot{w}_I} \right) \left(\frac{c^*_B}{c^*_I} \right)$$

are shown as dashed curves. The percent burned is the ratio of total propellant vaporized and reacted to that initially injected. The c^* ratio is a coefficient defining the ratio of the theoretical c^* at the reacted condition to that corresponding to the initial injection mixture ratio.

Other Variables

The effect of other potentially significant variables were examined to assess their effect on vaporization efficiency for FLOX/LPG. Specific areas investigated included the effect of initial droplet injection velocity, initial vaporization conditions, and specific input variables in the combustion model itself.

The initial droplet injection velocity was perturbed by a factor of 3 to determine its effect on the resultant propellant vaporization when all other factors (including dropsize) are held constant. Generally, propellant vaporization is increased at lower initial injection velocities. This results from a longer residence time and in an increased convective heat transfer rate as the drops are gradually accelerated by the combustion gases. Although lower initial droplet velocity generally gives

increased vaporization c^* efficiency, low initial droplet velocity and efficient atomization are contradictory in nature. High propellant injection velocities are required for efficient atomization and this effect will usually far outweigh the potential benefits of reduced initial droplet velocity.

An assumption made in the one-dimensional combustion model program input is the amount of combustion which occurs within the initial injection region. This is required to arrive at a nearly one-dimensional region, and eliminate calculations in the grossly nonuniform injection region (Ref. 4). It is usually assumed that 10 percent of the propellants have vaporized and reacted within 1 inch of the injector face. This initial condition has proven adequate and permits good correlation with observed experimental results. To assess the effect of variations in this assumption, 5, 10, and 20 percent of the propellants consumed were analytically considered and found to have an insignificant influence on performance. Performance variation due to assumption of 5 or 20 percent initial propellants vaporized instead of 10 percent was $< \pm 0.5$ percent in the range of dropsize ($D_{30} \leq 150$) and L^* ($15 \text{ inch} \leq L^* \leq 60 \text{ inch}$) considered. Effects of injection velocity and percent of propellants initially reacted were only significant when the propellant dropsize is large or when geometric restrictions favored lower performance.

Other parameters investigated were the effect of dropsize distribution, physical properties variation with temperature and pressure, inclusion or exclusion of propellant sensible heat capacity and variations of gas and film properties. Again, these variables were of secondary importance and significant only when conditions favored a generally reduced vaporization efficiency (i.e., larger initial dropsize and small chamber L^* geometry). This analysis disclosed that chamber geometry and initial propellant dropsize were of primary importance, and that other variables were of secondary significance.

MIXING EFFICIENCY

The effect of nonuniform mass and mixture ratio distribution is considered to be of importance equal to the vaporization process. Regardless of injector type, uniform mixing is a prerequisite for high combustion efficiency. In the absence of uniform mass and mixture ratio distribution, local striated regions of fuel and oxidizer rich will persist throughout the rocket chamber. Because of the short axial dimensions associated with rocket chambers, turbulent mixing and diffusion are relatively ineffective in equilibration of propellant concentration (Ref.4-8). Consequently, the c^* potential will be largely dependent on the initial distribution of fuel and oxidizer at the injector end of the chamber. Hence, if by cold-flow techniques the mass and mixture ratio can be determined for local regions within the chamber, the mixing efficiency can be determined by applying simple mass weighted summation techniques.

For this study, the analysis was based on a simplified stream tube model in combination with cold-flow experiments to determine distribution of propellants. The general features of the mixing model permit analytical consideration of an idealized rocket engine composed of N imaginary rocket chambers forming individual, isolated, stream tubes within the main chamber. Each stream tube at its own mass and mixture ratio is allowed to expand isentropically through the chamber and nozzle without heat or mass transfer to adjacent stream tubes. The c^* efficiency due to mixing ($\eta_{c^*,dist}$) is determined by summation of individual mass weighted c^* contributions of each individual stream tube and comparing the total to that theoretically attainable at the injected mixture ratio.

Correction factors for changes in specific heat ratio as a function of mixture ratio may be applied. However, if the effect of γ variation on the sonic point for each individual station can be neglected, the mixing c^* efficiency can be expressed simply as

$$\eta_{c^*,dist} = \frac{\sum_i^n MF_i c^*_i}{c^*_{theo}} \quad (5)$$

where

MF_i = the mass fraction in the individual stream being considered

c^*_i = theoretical c^* corresponding to the mixture ratio of the local stream

c^*_{theo} = theoretical c^* corresponding to the overall mixture ratio

The mixing quality can be expressed by an index, E_m , which defines the mass weighted deviation of local mixture ratio from initially injected overall mixture ratio. The index, E_m , was developed by Rupe (Ref. 9) and is shown below.

$$E_m = \left[1 - \sum_i^N MF_i \frac{(R - r_i)}{R} + \sum_i^N MF_i \frac{(R - \bar{r}_i)}{R - 1} \right] 100 \quad (6)$$

where

E_m = mixing index

MF_i = mass fraction in the stream tube

R = ratio of total oxidizer mass to total oxidizer and fuel mass

r_i = ratio of oxidizer mass to total oxidizer and fuel mass in an individual stream tube for $r_i < R$

\bar{r}_i = ratio of oxidizer mass to total oxidizer and fuel mass in an individual stream tube for $r_i > R$

The foregoing expression for the distribution index is not universal because it is also functionally related to the injected mixture ratio. The c^* efficiency due to propellant distribution, $\eta_{c^*,dist}$, is a function of both the distribution index, E_m , and the initially injected mixture ratio. The actual relationship between E_m , MR, and the resultant mixing c^* efficiency is shown in Fig. 8, in which the mixing c^* efficiency, $\eta_{c^*,dist}$, is shown as a function of E_m for various values of mixture ratio

for the FLOX/LPG propellants considered for this study. It should be noted that the basis of constant mixture ratio would be more correctly expressed as bands because even at a constant mixture ratio, $\eta_{c^*,dist}$ is not uniquely related to the E_m index. Analysis and verification experiments indicate, however, that the band width is normally narrow for most injector-produced spray distributions and the actual error introduced by use of single curves is negligible. The curves illustrated in the referenced figure can be used directly to assess the mixing c^* efficiency of a given injector for which E_m is known. In practice, however, it is often easier to derive an expression for $\eta_{c^*,dist}$ directly from cold-flow experimental data by utilization of the basic $\eta_{c^*,dist}$ expression of Eq. 5. The more universal expression is, however, much more valuable in that it permits a more generalized approach to performance analysis because it permits $\eta_{c^*,dist}$ determination for any injector in which the same propellants are used. In practical use, the figure permits specific determination of the required injector distribution index E_m for a given target level of mixing efficiency, $\eta_{c^*,dist}$, at any desired operating mixture ratio.

In summary, the combustion model analysis disclosed quite clearly that propellant dropsize and chamber geometry were the two most sensitive and important variables affecting propellant vaporization. Chamber pressure was found to have a secondary affect and only becomes important when propellant dropsize or chamber geometry favor reduced vaporization efficiency. Mixture ratio effects were found, also, to be of secondary importance; however, analysis indicated that optimum propellant vaporization would normally occur at slightly less than the nominal optimum mixture ratio. Other input parameters were found to be of minor consequence. The most singularly important finding was that propellant dropsizes of 75 microns or less would be required to attain sufficient vaporization for 97 percent c^* efficiency in the nominal 30 inch L^* thrust chamber. Analysis of propellant mixing effects indicated that uniform mixture ratio distribution

was essential for high c^* efficiency. Further, it was shown that the effect of propellant distribution on c^* efficiency due to mixing was sensitive to the operating mixture ratio of the injector. For FLOX/LPG at the nominal optimum mixture ratio of 5.33, it was found that a mixing uniformity index of at least 90 would be required for eventual attainment of 97 percent c^* efficiency.

EXPERIMENTAL HARDWARE

INJECTORS

The primary objective of this program was to define injector design criteria for high-performance FLOX/LPG injectors. Applicable injector design principles and the basis for selection of the chosen injector types are presented herein in addition to specific injector design details. Two injector types, like and unlike impinging stream, were considered.

Like Impinging Stream Injectors

A review of previous programs in which like impinging stream injector patterns were employed indicated that a like-doublet pattern can be predictably optimized to produce high performance (Ref. 10 and 11). In addition to attaining efficient combustion through proper injector design, this pattern is quite adaptable to design variations which can affect thrust chamber compatibility concerning heat fluxes and/or thermochemical reactions. Like doublet injectors (of relatively simple design) which result in high-performance efficiencies, are durable, and exhibit desirable chamber compatibility characteristics, have been developed at Rocketdyne for a number of fluorinated oxidizers and various fuels (Ref. 10 and 11). These results provided confidence of successful use of the like-doublet pattern for attainment of the program goals. Design details of the like-doublet injectors used are noted in Fig. 9 and Table 1. Table 1 summarizes injector specifications for all of the injectors. Figure 9 illustrates a typical pattern for the like-doublet injectors. The specific like-doublet injector designs are discussed below.

Injector LD-1. Previous experience with other propellant combinations (FLOX/MMH, FLOX/B₂H₆, ClF₅/N₂H₄, and FLOX/butene-1) indicated that the performance objectives of this program could be approached with parallel fan

orientation (i.e., $\alpha = 0$; Fig. 10) optimized in terms of fan spacing only (Ref. 10 and 11). A fan spacing of zero was employed for this injector. In addition to having parallel fan orientation, an intra-element spacing (Y), see Fig. 10, of 0.200 inch was employed. This intra-element spacing was similar to previous designs that had been successfully employed during the above referenced programs. The outer ring of elements (element = pair of oxidizer and fuel doublets) was canted 15 degrees toward the axial centerline of the injector. Resultant propellant direction for the other elements is parallel to the chamber axis.

As noted previously, small mean drop sizes (in addition to uniform mixing) are required to obtain high performance from the FLOX (80-percent F_2)/55 percent CH_4 - 45 percent C_2H_6 LPG blend propellant combination. To obtain the smallest possible propellant mean drop size (D_{30}), minimum orifice diameters and maximum injector ΔP 's (consistent with system requirements) were employed. Selection of the number of elements was based on considerations of injector design complexity, required orifice diameter size for propellant atomization, and injector ΔP 's.

A minimum practical orifice size ($d_f = 0.020$ inch), consistent with present injector fabrication techniques and capabilities and an arbitrarily selected fuel injector ΔP of 100 psi, at optimum mixture ratio, was selected. The oxidizer orifice diameter (0.0292 inch) results in equal injection velocities for the fuel and oxidizer at the design (5.33) mixture ratio. Selection of this orifice size was somewhat arbitrary. Using these orifice sizes and pressure drop, a typical like-doublet injector design contained a total of 112 elements (112 oxidizer and 112 fuel doublets) arranged in six rings. Element placement on the face of the injector was such that propellant mass distribution is essentially uniform in terms of geometric arrangement. Propellant manifolding (feeders) for an injector with significantly more elements than used would present complications in design and fabrication.

Further details of this injector design were:

1. The propellant impingement point was 0.110 inch from the injector face and the impingement angle between opposing streams was 60 degrees, for both oxidizer and fuel elements.
2. Oxidizer/fuel manifold and feeder velocities were less than 10 ft/sec.
3. Oxidizer orifice L/D's are between 8 and 10. Fuel orifice L/D's are 8. Free-stream L/D's for both oxidizer and fuel were between 4 and 7.

The impingement point and angle were selected to provide freedom from injector face burning and efficient atomization. Feeder velocities less than 10 ft/sec, orifice L/D's between 5 and 10, and free-stream jet L/D's less than 10 were selected to provide well defined stable jets. The design values chosen are similar to those successfully employed on previous injector technology programs at Rocketdyne (Ref. 1, 10, and 11).

All injectors were made of nickel 270 because of its high thermal conductivity and compatibility with the propellants. A modification of this injector, injector LD-1-M, was also designed. Injector LD-1-M is injector LD-1 with the oxidizer orifice diameter enlarged to 0.0360 inch. This orifice size results in nearly equal fuel and oxidizer injector pressure drop (~100 psi) at optimum mixture ratio. A photograph of this injectors face, taken after experimental evaluation of the injector, is shown in Fig. 11.

Injector LD-2. This injector differs from LD-1 in that its fan spacing is 0.275 inch instead of zero. Other design parameters for the two injectors were identical. The fan spacing was increased to 0.275 inch by moving the location of the oxidizer doublets 0.275 inch closer to the center of the injector (on the same radii). This variation was made to experimentally define propellant distribution effects on performance for the FLOX/LPG propellant combination.

Injector LD-3. Design of this injector was based on results of cold-flow experiments conducted with "model injectors" to define effects of lateral and angular variations in relative fan orientation between fuel and oxidizer doublets on propellant mixing. Details of the model injectors tested, test conditions, and results of the experiments are presented in the following paragraphs.

Model-injectors with elements, and relative element arrangement, typical of those used in the full-scale injectors were employed. The effects of fan inclination angle and intra-element spacing (Fig. 10) on propellant mixing were defined for the subject injector pattern. Oxidizer and fuel simulants, cold-flow procedures, and methods of data analysis were similar to those for the full-scale injectors (Appendix D).

Results from a recently completed (company funded) experimental study to define like-doublet injector design criteria, for optimization of propellant mixing, were used as a guide in selection of the experiments to be conducted and/or design of the model injectors to be evaluated during this program. During the company-funded program, the effects of both lateral and angular element orientation on propellant mixing were defined for paired fuel and oxidizer doublet elements in a statistically designed experiment. These cold-flow tests were carried out with a single element (one fuel and one oxidizer doublet) self-impinging injector. The geometrical variables studied, and the range of each variable, were: (1) fan spacing, S , with $0 \leq S \leq 0.10$ inch, in increments of 0.020 inch, (2) intra-element spacing, Y , with $0.125 \text{ inch} \leq Y \leq 0.750 \text{ inch}$, in increments of 0.125 inch, and (3) fan inclination angle, α , with $0 \text{ degree} \leq \alpha \leq 40 \text{ degrees}$ in increments of 10 degrees. The fan impingement angle was zero. All experiments were conducted at the same mixture ratio and with injection ΔP 's between 100 and 150 psi. Fuel and oxidizer orifice sizes were 0.0200 and 0.0250 inch, respectively. For the element size and flow conditions considered, which are similar to those for this program, an optimized configuration appears to exist at $S = 0$, $Y = 0.125 \text{ inch}$, and $\alpha \approx 25 \text{ degrees}$.

Two model multielement cold-flow injectors were designed to further define the effect of intra-element spacing (i.e., circumferential spacing between paired adjacent oxidizer and fuel doublets) and fan inclination angle on propellant mixing for the like doublet injector pattern. These model injectors are different than those tested in the above referenced study in that they contain more than a single element (a pair of fuel and oxidizer doublets). Each model injector contained 20 elements arranged in a ring. The basic diameter of the ring of elements was 5.1 inches. Spacing between elements is typical (~0.75 inch) of the like-doublet injectors employed during this program. Each quadrant of both model injectors contains five identical elements and was designed so that each quadrant could be cold-flowed separately. In each quadrant, the spacing between oxidizer and fuel doublets in an element (oxidizer doublet plus fuel doublet) was varied while the distance between adjacent similar elements has been kept constant. These injectors were designed to closely represent the propellant mixing conditions associated with the actual hot-fire injectors. The experiments conducted permitted evaluation of interaction effects between adjacent elements and, thereby, more nearly simulate the actual mixing situation for the hot-fire injectors being employed. The injector design variables studied, and their range are listed in Table II.

Tests were conducted to define the effect of fan inclination angle and intra-element spacing on propellant mixing. Inclination angles of 0, 10, 25, and 40 degrees were employed in conjunction with an intra-element spacing of 0.20 inch to define the effects of fan inclination angle on mixing. To determine the effect of intra-element spacing on propellant mixing, tests were conducted with element spacings of 0.2, 0.3, and 0.4 inch at fan inclination angles of both 0 and 25 degrees. Selection of the variables studied, and their respective range, were based on the results of previously mentioned studies and results presented in Ref. 1.

A typical element from one of the model injectors is shown in Fig. 12. A schematic representation of a typical five-element model injector is presented in Fig. 13.

All of the tests were conducted at the same simulated mixture ratio and injector ΔP 's. Conditions simulated were those for elements operating at the design operating conditions in the full-scale like-doublet injectors (i.e., simulated mixture ratio = 5.33 and thrust per element $\cong 30$ lbf). The test variables were the injector design parameters (fan inclination angle and intra-element spacing).

Results from the experiments conducted with the model injectors are presented in Fig. 14 and 15. In Fig. 14, E_m is plotted as a function of fan inclination angle for an element spacing of 0.2 inch. Optimum mixing was obtained with a fan inclination angle of 25 degrees, as was the case for the single element. As would be expected, the five-element model injector resulted in substantially better mixing than was obtained with the single elements. In Fig. 15, E_m is plotted as a function of element spacing for fan inclination angles of 0 and 25 degrees. E_m increases with decreasing spacing for the 0-degree inclination angle. When an inclination angle of 25 degrees was employed, optimum mixing appears to occur at a spacing of 0.30 inch. An inclination angle of 25 degrees results in considerably (4 to 10 percent) higher values of E_m than a 0-degree inclination angle. It is felt that the 0.20-inch spacing data point (at the 25-degree cant angle) is unreasonably low. However, results from both this study, and the company-funded effort discussed previously, indicate that there is little advantage in decreasing the element spacing below 0.25 inch.

Results from these experiments were used to design the optimized like-doublet injector (LD-3). An element spacing of 0.25 inch was selected for this injector. Improved mixing and resultant performance over the other like-doublet injectors, was attained primarily by inclination of the fuel and oxidizer fans into each other. A fan inclination angle of 25 degrees was employed. Previous injectors had fan inclination angles of zero and intra-element spacings of 0.200 inch. Fan spacing was zero. Fuel and oxidizer orifice diameters were 0.020 and 0.036 inch, respectively. Improved propellant mixing over that for the two preceding like-doublet injectors was attained.

The model injector cold-flow data are summarized in Table III.

Unlike Impinging Stream Injectors

The unlike impinging stream injector pattern selected for study was a 4-on-1 quintuplet (pentad) with fuel injected through the center orifice. Selection of this pattern was based upon: (1) the favorable orifice diameter and/or injector pressure drop ratios required for optimum mixing at the optimum (design) mixture ratio, and (2) its successful use with chemically similar (FLOX/RP-1) propellants (Ref.12).

A review of design requirements for optimum mixing (mass and mixture ratio distribution) with candidate (1-on-1, 2-on-1, and 4-on-1) unlike impinging stream patterns reveals that, of the unlike impinging stream patterns considered, the 4-on-1 quintuplet with fuel injected through the center orifice appears to be most satisfactory. This is primarily because of the pressure drop and diameter ratios (~ 1.3 and 0.85 , respectively) required for optimum mixing at the design (5.33) mixture ratio.

The "design equations" from Ref. 13 were used as design inputs and are presented below:

For a 1-on-1 (or 2-on-2) element:

$$\frac{d_2}{d_1} = \left(\frac{\dot{w}_2}{\dot{w}_1} \right)^{2/3} \left(\frac{\rho_1}{\rho_2} \right)^{1/3} \quad (7)$$

For a 2-on-1 element:

$$\frac{d_2}{d_1} = 1.25 \left(\frac{\dot{w}_2}{\dot{w}_1} \right)^{0.572} \left(\frac{\rho_1}{\rho_2} \right)^{0.286} \quad (8)$$

For a 4-on-1 element:

$$\frac{d_2}{d_1} = 3.06 \left(\frac{\dot{w}_2}{\dot{w}_1} \right)^{0.8} \left(\frac{\rho_1}{\rho_2} \right)^{0.4} \quad (9)$$

where:

d = orifice diameter

ρ = propellant density

\dot{w} = propellant flowrate (total)

Subscripts:

1 = outer orifices

2 = center orifice

For all patterns, the included impingement angle is 60 degrees. These equations were used to calculate the orifice diameter ratio required at the optimum mixture ratio (5.33). The oxidizer-to-fuel pressure drop ratios for these patterns were computed using the continuity equation in conjunction with Eq. 7 through 9. The resulting equations for the injector pressure drop ratios are:

1-on-1 (or 2-on-2) element:

$$\frac{\Delta P_1}{\Delta P_2} = \left(\frac{\dot{w}_2}{\dot{w}_1} \right)^{2/3} \left(\frac{\rho_1}{\rho_2} \right)^{1/3} \quad (10)$$

2-on-1 element:

$$\frac{\Delta P_1}{\Delta P_2} = 0.622 \left(\frac{\dot{w}_2}{\dot{w}_1} \right)^{0.286} \left(\frac{\rho_1}{\rho_2} \right)^{0.143} \quad (11)$$

4-on-1 element:

$$\frac{\Delta P_1}{\Delta P_2} = 5.48 \left(\frac{\dot{w}_2}{\dot{w}_1} \right)^{1.2} \left(\frac{\rho_1}{\rho_2} \right)^{0.6} \quad (12)$$

where:

ΔP = injector pressure drop

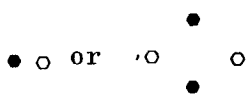


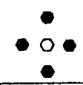
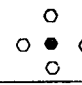
A summary of the orifice diameter, injector pressure drop, and momentum ratios for the various patterns is presented on the page following. As noted in this table, injection of either propellant in the "center" orifice was considered. An inspection of this table indicates that, of the unlike impinging stream patterns considered, only the 4-on-1 quintuplet with oxidizer in the center appears to be completely unsatisfactory (because of the required pressure drop and diameter ratios of ~ 0.04 and ~ 8.0 , respectively). Any of the other patterns, which have pressure drop ratios between 0.44 and 1.31 and diameter ratios between 2.47 and 0.85, could possibly be chosen as the pattern for the injector optimization study.

Patterns which contain a higher number of oxidizer than fuel orifices would appear to be the most satisfactory because the d_{ox}/d_f and/or $\Delta P_{ox}/\Delta P_f$ ratios for these patterns are nearer to unity. Previous experience at Rocketdyne has included injector patterns in which $0.5 \leq d_{ox}/d_f \leq 2.0$.

The 4-on-1 unlike quintuplet, with oxidizer in the outer orifices, pattern was chosen for study during the injector optimization portion of the program. Selection of this pattern was based on the above considerations (diameter and ΔP ratios required for optimum mixing) and the satisfactory employment of the subject pattern with a chemically similar (FLOX/RP-1) propellant combination (Ref. 12).

SUMMARY OF REQUIRED INJECTOR ORIFICE DIAMETER, PRESSURE DROP,
AND MOMENTUM RATIOS (OXIDIZER-TO-FUEL)

(For several unlike impinging stream injector patterns with
FLOX (80 percent fluorine)/55 percent methane-45 percent
ethane LPG blend propellant combination at optimum mixture
ratio of 5.33

Parameter*	Injector Pattern**				
	1-on-1 or 2-on-2 Unlike Impingement Pattern	2-on-1 Unlike Triplet		4-on-1 Unlike Quintuplet	
		Oxidizer Outside 	Oxidizer In-Center 	Oxidizer Outside 	Oxidizer In-Center 
Diameter Ratio	2.22	1.58	2.47	0.85	7.9
ΔP Ratio	0.47	0.44	1.14	1.31	0.044
Momentum Ratio	2.22	2.17	3.56	3.75	0.70

*All propellants in liquid state at -305 F

**For clarity, the oxidizer orifices are shown as black circles, with
the fuel orifices represented by white circles

The "design equation" of Ref. 13 specifies the injection conditions necessary for optimum liquid phase mixing of nonreactive streams. Although it was anticipated that some modification to these cold-flow defined relationships may be necessary when the impinging fluids react, the established influencing parameters have served as effective guides for hot-fire injector optimization during previous Rocketdyne programs (Ref. 10 and 11). In particular, injector optimization results presented in Ref. 10 indicate that for a 4-on-1 quintuplet (the injector type selected herein) the parameters influencing performance in the hot-fire case are the same as those influencing distribution in the cold-flow case. These influencing parameters are the orifice diameter and propellant momentum ratios.

As noted previously, small mean propellant drop sizes (in addition to uniform mixing) will be required to obtain high performance from the FLOX/LPG blend propellant combination. To obtain the smallest possible propellant mean drop size (D_{30}), minimum orifice diameters and maximum injector ΔP 's (consistent with system requirements) were employed.

If a minimum practical orifice diameter ($d_f = 0.018$ inch) is employed, and the highest feasible injector ΔP is arbitrarily selected as 150 psi at optimum mixture ratio, approximately 200 elements would be required. From the standpoint of injector design complexity, it is desirable to minimize the number of elements. Propellant manifolding (feeders) for a 200-element 4-on-1 injector (of the size to be employed herein) would present complicated design/fabrication problems. For this reason, an injector with approximately 100 elements was chosen.

Injector P-1. Design details of this injector are noted in Table I and Fig. 16. Table I summarizes injector specification for all injectors employed. Figure 16 illustrates a typical face pattern for the pentad injectors.

Further design details of the elements are listed below:

1. The propellant impingement point is 0.15 inch from the injector face, and the impingement angle between opposing oxidizer streams is 60 degrees.
2. Oxidizer/fuel manifold and feeder velocities are less than 10 ft/sec.
3. Oxidizer orifice L/D 's are 7. Fuel orifice L/D 's are between 10 and 12, depending on whether $d_f = 0.025$ or 0.0292 inch. Free stream L/D 's for both oxidizer and fuel are between 5 and 9.
4. Element placement on the injector face is such that propellant mass distribution is essentially uniform in terms of geometric arrangement.

The impingement point and angle were selected to provide freedom from injector face burning and efficient atomization. Feeder velocities, orifices L/D 's, and free-stream jet L/D 's were selected to provide well defined stable jets. The design values chosen were similar to those successfully employed on related injector technology programs at Rocketdyne (Ref. 1 and 12).

Injector P-2. This injector differs from P-1 only in the size of the fuel orifice diameter. The fuel and oxidizer orifice diameters for this injector are 0.0292 and 0.0250 inch ($d_{ox}/d_f \cong 0.85$ = optimum design value), respectively.

Two modifications, P-2-M1 and P-2-M2, of this injector were also designed. Injector P-2-M1 is injector P-2 with fuel and oxidizer orifice diameters of 0.0372 and 0.0320 inch ($d_{ox}/d_f \cong 0.85$), respectively. Injector P-2-M2 is injector P-2 with fuel and oxidizer orifice diameter of 0.0465 and 0.0400 inch ($d_{ox}/d_f \cong 0.85$), respectively. A photograph (face view) of injector P-2-M2, taken after experimental evaluation of the injector, is shown in Fig. 17.

Propellant Manifolds

All injectors employed the same manifolding techniques (Fig. 18). Oxidizer manifold and fuel dome designs were identical for all injectors. Both the dome and manifold were made of 321 stainless steel.

Oxidizer Manifold. The oxidizer (FLOX mixtures) was fed into the manifold surrounding the injector proper. The manifold (Rocketdyne drawing No. RID 2665) was welded onto the injector body.

Fuel Manifold. The fuel (55 percent CH_4 - 45 percent C_2H_6 LPG blend) was fed through the dome. The dome (Rocketdyne Drawing RID 2666A) was bolted onto the back of the injector proper.

THRUST CHAMBERS

Uncooled, segmented, calorimetric copper thrust chamber assemblies were employed throughout the experimental program. Provisions were made for measurement of transient circumferential and axial chamber/nozzle heat flux profiles.

Reference Chamber

A single reference ($L^* = 30$ inches; $\epsilon_c = 2$) thrust chamber assembly was employed for evaluation of the various injectors. A schematic representation of this chamber assembly is shown in Fig. 18 and 19. As is noted in Fig. 19, the thrust chamber assembly consists of three essential parts: (1) the cylindrical chamber, (2) the nozzle, and (3) split-ring attachment device.

Dimensions of the reference thrust chamber assembly were established with aid of the following system requirements:

Propellants:	FLOX (80 percent F_2)/55 percent CH_4 - 45 percent C_2H_6 LPG blend
Thrust Level:	3K (3000-pound) thrust at sea level with optimum nozzle expansion
Chamber Pressure:	100 psia
Mixture Ratio:	5.33 = theoretical optimum
A_{exit}/A_t :	1.85 = optimum test site expansion at P_c = 100 psia and MR = 5.33
Performance Level:	97-percent c^* efficiency (shifting equilibrium) in 30-inch L^* chamber

These system requirements were specified in the program work statement (Ref. 14).

Selected nozzle parameters are listed below for the reference thrust chamber assembly.

Nozzle Throat Area = 25.5 in.²

Nozzle Throat Diameter = 5.7 inches

Contraction Area Ratio = $\frac{A_c}{A_t} = \frac{\text{Chamber cross-sectional area}}{\text{Throat area}} = 2$

Nozzle Convergence Angle = 30 degrees

Exit Nozzle = 15-degree cone

$\frac{R_c}{R_t} = 2.0 = \frac{\text{Radius of curvature of nozzle throat}}{\text{Throat radius}}$

A two-to-one contraction ratio (ϵ_c) was chosen for the reference chamber because combustion model results suggested higher performance could be achieved at a given L^* and use of a higher contraction ratio would result in excessively large diameter and costly thrust chambers. The nozzle convergence angle and exit configuration (15-degree cone) are similar to those commonly used in numerous research programs. A radius of

curvature of the nozzle throat to the throat radius ratio (R_c/R_t) of 2.0 was chosen because the nozzle discharge coefficient for the specific configuration is well defined. Lower values of R_c/R_t would result in operation at conditions where the value of the nozzle discharge coefficient has not been specifically defined. If the nozzle discharge coefficient is not well known, performance analysis (based on P_c measurement) will not be well defined. Performance was calculated from both P_c and thrust measurements.

A schematic representation of the reference chamber, with pertinent dimensions noted, is presented in Fig. 19. Detailed drawings of the essential chamber assembly component parts are not presented but are noted in the following engineering drawings:

1. Reference ($\epsilon_c = 2$) nozzle (RID 4246 and RID 4249)
2. Cylindrical Chambers (RID 3394)
3. Attachment Rings (RIC 4247)

The uncooled nozzle and cylindrical chamber were made from high-purity, oxygen-free copper. Copper was selected because of its high thermal conductivity, relatively high specific heat, and satisfactory yield strength at elevated temperatures. The attachment rings were fabricated from 321 stainless steel. These same materials (OFHC copper and 321 stainless steel) were used for all subsequent chamber assemblies.

The split-ring attachment method was employed to attach the nozzle to the cylindrical chamber and, in turn, the chamber to the injector assembly. This attachment method was chosen because it permits fabrication of the chambers/nozzles from relatively small-diameter stock instead of large (and expensive) forged billets. Larger-diameter material would be required if the conventional flange and bolt attachment technique was employed.

Alternate Chamber

To define contraction ratio effects on performance, a 4:1 contraction ratio nozzle (Rocketdyne drawing No. RIC 4251 and RID 4252) was designed and fabricated. Pertinent dimension of this nozzle, with the cylindrical chamber necessary for a 30-inch L^* chamber assembly, are presented in Fig. 20. The chamber diameter of the 4:1 contraction ratio assembly was identical to that of the 2:1 contraction ratio assembly (contraction ratio was increased by decreasing the nozzle throat diameter). The nozzle convergence angle, exit nozzle configuration (15-degree cone), and radius of curvature of nozzle throat-to-throat radius ratio are identical to those of the reference nozzle.

Cylindrical Chamber Segments

The thrust chamber proper (cylindrical chamber plus nozzle) was designed as a two-piece unit to permit maximum use of available hardware while studying the effects of chamber length/ L^* and contraction ratio on performance. The segmented design made variation of chamber length/ L^* possible with one nozzle of each contraction ratio. Variations in chamber length (at each contraction ratio) were accomplished by inserting cylindrical chamber sections of various length between the injector and nozzle assemblies.

Specifically, a cylindrical chamber 11.25 inches in length was fabricated in addition to the 3.75- and 7.50-inch cylindrical chamber sections required for the 30-inch L^* chambers. Depending upon the specific need, three to none of these chamber sections were placed between the nozzle and injector assembly. Specific chamber assemblies employed are listed in Table IV.

A photograph of the assembled engine is presented in Fig. 21. Chamber pressure taps, isolation heat transfer segments, Photocons, etc., are shown in this figure.

Chamber instrumentation and design of the isolation heat transfer segments are presented in subsequent sections of this report.

RESULTS

There were 125 hot-firing and 23 full-scale injector cold-flow experiments conducted to establish design criteria for a high-performance injector using the FLOX/methane-ethane (55-45) LPG blend. The overall program objectives included: (1) development of an injector capable of delivery of 97 percent of theoretical shifting equilibrium characteristic exhaust velocity efficiency at nominal design conditions, and (2) provide sufficient data to allow subsequent extrapolation of the program results to other advanced space storable propellant combinations and operating conditions.

The nominal experimental and thrust chamber design conditions were as follows:

1. Chamber Pressure: 100 psia
2. Oxidizer: F_2-O_2 (80-20)
3. Mixture Ratio: 5.33 (Maximum Theoretical c^*)
4. Thrust Level: 3000 pounds (Sea Level)
5. Chamber Contraction Area Ratio: 2:1
6. Chamber L^* : 30 inches

These nominal conditions were varied over the following ranges:

1. Chamber Pressure: 50 to 200 psia
2. Oxidizer: F_2 (70 to 100 percent)
3. Mixture Ratio: 3 to 7
4. Thrust Level: 1500 to 5000 pounds
5. Chamber Contraction Area Ratio: 2 to 4:1
6. Chamber L^* : 15 to 60 inches

The purpose for variation of the experimental and hardware design conditions was to define the effect of propellant atomization and distribution changes on performance. The injector patterns were employed to study the effects of injector design on propellant atomization and distribution. The two patterns used were an unlike 4-on-1 (four oxidizer streams impinging on a central fuel showerhead) and like-on-like doublet.

The hot-firing experimental results are presented in Table V. Typical parameters such as mixture ratio, chamber pressure, percent FLOX, chamber configuration, etc., are shown. The tabulated corrected c^* efficiency results were obtained by employing the corrections described in Appendix A. The excellent agreement between corrected c^* efficiency, based on thrust and chamber pressure, is illustrated in Fig. 22, which shows c^* efficiency based on chamber pressure plotted against efficiency based on thrust. Data are presented for every seventh test in this figure. The measured heat flux at various chamber locations during each run is presented in Table VI and VII. The cold-flow measured E_m values and predicted losses in c^* efficiency caused by propellant maldistribution are presented in Table VIII.

PERFORMANCE

Initial experimentation was conducted at nominal conditions with mixture ratio and injector design as variables. Two 4-on-1 (pentad) and three like-on-like doublet injector designs were tested. The efficiencies that resulted are shown in Fig. 23. The 4-on-1 results are shown on the upper portion (Fig. 23) and like-on-like results in the lower half (Fig. 23). The two 4-on-1 injectors differed only in respect to the size of the central fuel showerhead orifice size. Injector P-1 and P-2 fuel orifice sizes were 0.0250 and 0.0292 inch, respectively. The design differences between the three like-on-like injectors involved relative fan spacing and angle. Fan spacing for LD-1 and -2 were 0 and 0.275 inch,

respectively; the fan inclination angle was zero. The third injector, LD-3, had aligned fans (zero spacing) and the fans were inclined 25 degrees toward each other.

As indicated in Fig. 23, performance of the two 4-on-1 injectors is about the same and nearly invariant with mixture ratio. The efficiency at low and intermediate mixture ratios (3 to 5) is approximately 97 percent and is about 98 percent at higher values (6 to 7). The performance characteristics of the three like-on-like injectors as a function of mixture ratio are similar. The efficiency of the best design (LD-3) is about 98.5 percent at a mixture ratio of 4; 96.5 percent at 5; and 96 percent at 6. The lowest performing design (LD-2) was about 3 percent less efficient than the LD-3 design.

The cold-flow results obtained using the five injectors are shown in Fig. 24 through 30. Measured distribution efficiency (E_m) and predicted effect of nonuniform distribution on performance are shown plotted as a function of simulated mixture ratio for each injector in Fig. 24 and 25. Mass and mixture ratio distribution profiles for each injector (at the nominal design operating condition) are presented in Fig. 26 through 30.

The upper portion of Fig. 24 and 25 contain a plot of E_m versus simulated mixture ratio; presented in the lower half of the figures is the predicted effect of nonuniform distribution on performance. The 4-on-1 results are shown in Fig. 24 and the like-on-like in Fig. 25. Agreement is excellent between cold-flow predictions and hot-firing results. As expected, the two 4-on-1 injectors performed the same. The predicted and measured differences in performance between the best and worst like-on-like injectors (LD-3 and -2) was about 3 percent.

The left side of Fig. 26 through 30 contains mass distribution profile curves (in two orthogonal planes passing through the center of the injector); presented in the right side of the figures is the "averaged" mixture

ratio distribution profile. Averaged mixture ratio profile was obtained by plotting the arithmetic average of the mixture ratio measured in each row (or column) of the spray collector as the median of that row (or column). The two orthogonal planes so formed are representative cross sections of the entire mixture ratio when the spray patterns are symmetrical, as was the case with these injectors. Mass and mixture ratio profile curves for the two pentad injectors (P-1 and P-2) are shown in Fig. 26 and 27, respectively. Figure 28 through 30 present results for the like doublet injectors (LD-1, LD-2, and LD-3), respectively.

To make interpretation of the mass and mixture ratio distribution profile curves more meaningful, pertinent injector design similarities/differences are reviewed. The two 96-element pentad injectors have an identical geometrical arrangement of their elements. The only difference between these injectors is the size of fuel orifices. Fuel orifice diameters are 0.0250 and 0.0292 inches for the No. 1 and No. 2 injector, respectively. All like doublet injectors have 112 elements (a pair of fuel and oxidizer doublets) arranged into six rings of fuel and oxidizer doublets. The No. 1 and No. 3 like-doublet injectors have the fuel and oxidizer doublet rings on the same diameters (i.e., fan spacing = S = zero). For the No. 2 like doublet injector, the oxidizer doublets are positioned in rings 0.275 inches inside the fuel doublet rings (S = 0.275 inch). All five injectors have the resultant spray from the outer ring of elements canted 15 degrees toward the center of the chamber with the resultant spray from the other elements being directed straight down the chamber.

Cold-flow measured mass and mixture ratio distribution profile curves for the two pentad injectors (Fig. 26 and 27) and the two higher performing like-doublet injectors (Fig. 28 and 30) are quite similar. This result was expected because element distribution/orientation on the injector face and resultant element spray cants are similar for both injector types. Propellant mass fraction next to chamber wall and in the center of the chamber is quite low. These regions of low mass fraction are

caused by the 15-degree inward cant of the outer ring of elements and the element free center portion of the injector, respectively. A region of high mass fraction occurs next to the low mass fraction region adjacent to the chamber walls. This is also caused by the 15-degree inward cant of the spray from the outer ring of elements. An examination of the mixture ratio profile curves for these four injectors reveals that the mixture ratio in the central portion of the spray pattern, comprising the major portion of the mass, is at a nearly uniform mixture ratio equal to that of the overall mixture ratio. In the low mass region near the chamber walls, the mixture ratio of the spray produced by the No. 1 pentad and No. 1 and No. 3 like-doublet injectors is slightly higher than the overall mixture ratio, while that for the No. 2 pentad injector is slightly lower than the overall mixture ratio. Mixture ratios of about 10 percent higher and/or lower than the overall mixture ratio are found in the 10 percent of mass nearest to the chamber wall.

Characteristics of the mass and mixture ratio distribution profile curves for the No. 2 like-doublet injector are presented in Fig. 29. As noted, the mass and mixture ratio distribution profiles for this injector are substantially different than those of the other injectors. As was the case with the other injectors, a region of low mass fraction occurs adjacent to the chamber wall. Other than this similarity, the mass distribution profile for this injector is quite different than that for the other injectors. These differences can be directly correlated with the difference in element orientation on the injector face for this injector. The No. 2 (0.275-inch fan spacing) injector has a considerably lower mixture ratio adjacent to the chamber wall than any of the other injectors. The 10-percent of propellant mass nearest the chamber walls has a mixture ratio 60 percent below that of the overall mixture ratio. The mixture ratio in the central portion of the spray, comprising the major portion of the wall, is at a mixture ratio slightly greater than the overall mixture ratio. The spray mass and mixture ratio distribution from all injectors are exceptionally symmetrical.

Following the initial hot-firing injector evaluation experiments, tests were conducted with variable thrust chamber geometry (L^* and contraction ratio), percent FLOX, and injection conditions (injection velocity was changed by varying total flowrate and orifice size). The best like-on-like doublet injector (LD-3) was selected as the design to be used for these experiments. This selection was based on consideration of performance (Fig. 23), combustion stability (to be discussed later), and chamber heat transfer. Chamber heat flux data obtained using the best performing like-doublet (LD-3) and 4-on-1 (P-2) injectors are shown in Fig. 31. As indicated in the figure, the 4-on-1 injector caused very high flux values throughout the chamber and nozzle as compared with the like doublet. The results shown were measured at the nominal operating conditions described previously. Further details regarding heat transfer rates as a function of design and operating conditions are presented in the following section of this report. In summary, the like-doublet performance was similar, stability was decidedly superior, and resultant chamber heat flux was about 1/2 that of the 4-on-1 designs.

The effects of chamber L^* and contraction ratio (ϵ_c) on performance are shown in Fig. 32, where c^* efficiency is plotted as a function of mixture ratio. Figure 32A presents the $\epsilon_c = 2.0$ data for L^* values of 15, 30, and 60 inches. Figure 32B presents the $\epsilon_c = 4$ data.

A review of Fig. 32 shows that, in general, performance is higher when using a $\epsilon_c = 2.0$ with a given L^* value. For example, at $MR = 5.3$, the efficiencies at $L^* = 60$ and 30 inches are 98.1 and 96.3 percent with $\epsilon_c = 2.0$ contrasted with values of 96.8 and 93.1 percent with $\epsilon_c = 4.0$. The efficiency levels at $L^* = 15$ inches are about the same (~ 90 percent); however, it should be noted that when using the $L^* = 15$ inches and $\epsilon_c = 4.0$ configuration, the injector is bolted directly onto the nozzle so that the effective contraction ratio is appreciably less than 4:1.

The effect of percent FLOX on performance is shown in Fig. 33. In this case, c^* efficiency is plotted as a function of mixture ratio using 100-percent fluorine (Fig. 33A), 80-20F₂-O₂ (Fig. 33B), and (70-30) F₂-O₂ (Fig. 33C) as the oxidizer. All experiments, using the LD-3 injector, were conducted at the nominal condition of $P_c = 100$ psia, $L^* = 30$ inches, and $\epsilon_c = 2.0$.

Examination of these results, shows that the shapes of the curves and level of efficiencies for 100 and 70-30 percent F₂-O₂ (Fig. 33A and 33B) are almost identical. The 80-20 percent curves differ somewhat, especially at lower mixture ratios. At optimum mixture ratio the 100 and 70-30 percent mixtures produced about 1/2 to 1 percent higher efficiencies than the 80-20 mixture. The optimum mixture ratio or point of maximum c^* for the three oxidizers is 3.50, 5.33, and 4.00 for the 100, 80-20, and 70-30 percent F₂-O₂ mixtures, respectively.

The final series of experiments conducted involved evaluation of the effect of injection velocity, orifice size, and chamber pressure on efficiency (Fig. 34). Efficiency versus chamber pressure is presented in Fig. 34A, using an $L^* = 30$ inches and the LD-3 injector. Efficiency versus chamber pressure is shown in Fig. 34B using an $L^* = 30$ and 15 inches and a modified injector (LD-3M). In this case, the orifices of the original injector (LD-3) were enlarged ($d_f = 0.026$ and $d_o = 0.047$ inch compared with $d_f = 0.020$ and $d_o = 0.036$ inch). An 80-20 percent FLOX mixture was used with an $\epsilon_c = 2.0$ chamber. The nominal mixture ratio was 5.33. As indicated in Fig. 34, changing the chamber pressure from 50 to 150 psia resulted in a performance increase of about 2 to 3 percent. Enlarging the orifices resulted in a 1 to 2 percent performance decrease, depending on the chamber pressure. (The effect of orifice size was greater at lower chamber pressures.)

THRUST CHAMBER HEAT TRANSFER

As an integral part of the FLOX/Performance program, complementary investigations were conducted to determine heat transfer characteristics to the chamber and nozzle. Primary emphasis was directed toward providing supplementary evidence to aid in selection of an optimum injector. Supplementary effort was also directed to ascertain the effects of variations in operating conditions, chamber geometry, and FLOX concentration (percent fluorine) on the chamber heat flux. Local chamber heat flux characteristics were determined as a function of both longitudinal and circumferential chamber position at the test conditions. Data were analyzed by the methods outlined in Appendix F. Because this study was limited in scope, only pertinent tests have been selected for analysis and interpretation. However, a complete tabulation of average longitudinal heat flux values for all tests are presented in Table VII. Specific areas considered for analysis were a qualitative assessment of data repeatability, and an analysis of injector design, chamber pressure, and mixture ratio effects. Concluding studies were directed to chamber geometry effects and to a brief analysis of FLOX concentrations (percent fluorine) influence.

Data Repeatability

Calculated heat flux data derived from three different tests conducted at nearly the same operating conditions were compared to establish that measured heat transfer characteristics were repeatable. These tests were conducted with the like-doublet injector (No. 3) in the nominal 30-inch L^* chamber having a 2-to-1 contraction ratio. The calculated local heat flux derived from calorimetric data based on 72 individual temperature measurements are shown in Fig. 35. Each single point defining the curve represents an average value derived from one to three individual heat flux measurements at the indicated axial chamber stations.

Test-to-test variation in heat flux is generally well within ± 10 percent in the chamber and throat section. Point-to-point variation of individual circumferentially located measuring stations indicate similar characteristics as shown in Fig. 36. The scatter of individual heat flux data is more pronounced at the injector end, and may be generally attributed to unstable boundary layer development in the transition regions.

Measured heat flux values (shown in both figures) are substantially higher than would be predicted from the Bartz simplified analysis. Further, chamber heat flux is significantly high compared to the peak heat flux of about $4.5 \text{ Btu/in.}^2\text{-sec}$ near the throat, and also the indicated peak heat flux occurs substantially upstream (approximately 2 inches) of the geometric throat and thereafter undergoes a rapid decrease in a region where persistence of high heat fluxes would normally be expected. In general, the integrated heat load to the thrust chamber appears to be approximately 150 percent of that which would be predicted from simplified analysis. The basic heat flux profile curve shown in Fig. 35 will be employed for subsequent comparison with other pertinent injectors, chambers, and operating conditions. As the basic curve for the optimum like-doublet injector (LD-3) with the nominal 30-inch L^* ($A_c/A_t = 2$) chamber using 80-20 FLOX, it serves as a reference for later comparison to parametric effects of other design and operational variables.

Injector Design

Heat flux characteristics of the injectors evaluated are shown in Fig. 37. In the cases shown, the mixture ratio and chamber pressure were at the nominal design conditions of 5.33 and 100 psia, respectively. The thrust chamber used was the nominal 30-inch L^* ($A_c/A_t = 2$). The injectors evaluated included two 4-on-1 pentad injectors (P-1 and P-2) and three like-doublet designs (LD-1, LD-2, and LD-3). In addition to defining heat transfer characteristics for these injectors, the heat flux level was a

prominant factor in final selection of the optimum design. A review of Fig. 37 clearly shows that the pentad injectors were generally considered unsuitable for further optimization. On the other hand, all three like-doublet injectors display a much milder thermal environment in the chamber and throat. Although greater differences in heat flux are shown for the like-doublet injectors, they are all more moderate than the 4-on-1 (pentad) injectors. Although like-doublet injector No. 2 exhibits a significantly lower heat flux, performance capability was considered inadequate. Heat flux for like-doublet injectors 1 and 3 are higher than that for No. 2, but the realizable performance increment justify their consideration. Specifically, like-doublet injector No. 3 was found to be consistently capable of the target 97-percent combustion efficiency, while only 93 percent could be realized with the No. 2 like doublet. Like-doublet injector No. 1 was found to perform at a slightly lower efficiency level (~96 percent) than the No. 3 injector.

Both pentad injectors gave efficiencies on the order of 97 percent. The heat flux levels, on the other hand, were found to be significantly higher than any demonstrated with the like-doublet injectors. The basic 4-on-1 injector is inherently capable of providing a very uniform propellant distribution which is particularly attractive for maximization of performance. On the other hand, the same factor which promotes efficient propellant mixing is also a negative influence for controlled suppression of heat flux. Because both basic injector types were found to be able to deliver similar performance, injector selection would depend on other significant parameters such as the heat transfer and combustion stability characteristics.

Chamber Pressure

Heat flux data derived from experiments conducted with the optimum (LD-3) like-doublet injector were evaluated to determine heat transfer response to variations in chamber pressure. Although most data were from tests

at nominal 100-psia chamber pressure, selected experiments also were conducted over a limited chamber pressure range using the same test components. The three curves shown in Fig. 38 represent average (of one to three individual circumferential measurements) heat flux values at various axial stations of the nominal 30-inch L^* chamber with the optimum injector at chamber pressure of 150, 100, and 50 psia. Similar characteristic profiles are shown at all three chamber pressures with an indicated convergence of the heat flux curves to a near common lower value at the injector end.

The indicated peak heat flux values of 6.1, 4.4, and 2.8 Btu/in.²/sec at respective chamber pressures of 150, 100, and 50 psia appear to correlate well with analytical considerations for fully developed turbulent flow. Chamber pressure affects Reynolds number due to the corresponding gas density changes with only a minor effect on combustion temperature. The nominal 0.8 power dependence appears to satisfactorily describe the indicated heat flux values at the three chamber pressures. The middle curve (for 100 psia) is the same reference curve shown in Fig. 35. The indicated values of heat flux at mid-chamber also appear to satisfy turbulent-flow heat transfer correlations. It is of specific interest to note that these heat flux profiles are representative of chamber pressure effects when common thrust chamber components are used.

Mixture Ratio

Heat flux data derived from experiments conducted with the optimum like-doublet injector (LD-3) were evaluated to determine the effect of mixture ratio variations on heat transfer response. In addition to chamber pressure variations with the same test components, mixture ratio excursion experiments were conducted with the optimum injector and the nominal 30-inch L^* chamber. The basic reference heat flux profile curve of Fig. 35 is shown superimposed on the average (of one to three individual circumferential measurements) heat flux values for three tests conducted

at mixture ratios of 4.20, 5.33, and 6.70 (Fig. 39). The data scatter is even less than that previously indicated for test-to-test variation (Fig. 35) when all operating conditions were normalized. These results clearly indicate that within the mixture ratio range examined (4.20 to 6.70), there is virtually no effect on either the distribution or magnitude of thrust chamber heat flux. This finding is supported by theoretical chemical equilibrium analysis which discloses virtually no variation for either theoretical gas temperature, density, or specific heat.

Characteristic Chamber Length

The effect of variation in chamber characteristic length, L^* , on chamber heat flux for a constant A_c/A_t is shown in Fig. 40. These test data were derived from experiments conducted with the like-doublet injector (LD-3) using three different chamber lengths with the same throat section ($A_c/A_t = 2$) in each case. The middle curve is the basic reference profile originally shown in Fig. 35. The ordinate scale has been reduced to accommodate the heat flux profile (right side) of the 60-inch L^* chamber. The very peaked heat flux profile for the 15-inch L^* chamber is shown to the left of the reference curve. The abrupt appearance of the heat flux curves for the 15-inch L^* chamber reflects the physical absence of cylindrical length prior to start of convergence.

Because the table (Fig. 40 inset) discloses nearly identical operating conditions for each of the three tests, a similar maximum heat flux value might be anticipated for all three chambers. In fact, however, performance analysis indicates that the reduced heat flux for the shortest chamber can be logically attributed to reduced combustion efficiency resulting primarily from incomplete propellant vaporization. The measured c^* efficiency for the 15-inch L^* chamber was approximately 90 percent as compared to 96.5 and 98 for the two longer chambers. For the 60-inch L^* chamber, the indicated reduced peak heat flux in comparison to the

reference case is slightly more obscure. Although possible reasons could be postulated, an extensive and detailed analysis would be required to explain the apparent attenuation of heat flux for the longer 60-inch L^* chamber. Two obvious reasons for the lower heat flux at the throat of the longer engine may be postulated. First, with the long L/D of the chamber, it is expected that about 8 percent of the total enthalpy of the combustion gases may be lost to the copper chamber. This would result in a similar lowering of heat flux. Secondly, the long chamber allows a thicker boundary layer buildup, which would also decrease the heat flux.

The effect of chamber length variation for the 4-to-1 contraction ratio chambers is somewhat more unusual than that observed for the 2-to-1 chambers. Typical heat flux curves for characteristic lengths of 15-, 30-, and 60-inch L^* are shown in Fig. 41 for an $A_c/A_t = 4$ configuration. The chamber pressure for the 4-to-1 chambers were nominally 200 psia (compensation for reduced throat area to obtain equal thrust). As is evident from the figure, peak heat flux for the $L^* = 15$ chamber is substantially higher than for the 30- and 60-inch L^* chambers. The magnitude of the peak heat flux is much higher than that which may be anticipated from turbulent boundary layer correlations, particularly in light of the relatively low measured combustion efficiency. Without comprehensive analysis, the unusually high peak heat flux may be attributed to unusual boundary layer effects related to the chamber shape. The 15-inch L^* chamber converges almost immediately to the throat without a significant cylindrical region which would normally constitute the combustion chamber.

Similarities and differences in heat flux noted between the 4-to-1 and 2-to-1 contraction ratio chambers at L^* 's of 60 and 30 may be due to several effects. It would seem that the heat flux at 200 psi in the 4-to-1 chamber is not proportionally higher than that observed at 2-to-1 contraction ratio at 100 psi. This is probably due to combustion efficiency and boundary layer buildup effects.

Oxidizer Fluorine Concentration

The effect of fluorine concentration in the FLOX mixture on chamber heat flux is shown in Fig. 42. The test data shown have been derived from experiments conducted with the selected optimum like-doublet injector and the nominal 30-inch L^* ($A_c/A_t = 2$) chamber. The fluorine concentrations of interest were 70 percent and 100 percent in addition to the optimum 80 percent FLOX. Chamber pressure was nominally 100 psia for the three tests; however, the mixture ratio corresponded to optimum conditions for the respective FLOX concentrations in combination with the 55 percent CH_4 45 percent C_2H_6 LPG fuel. Optimum mixture ratio for 70-30 FLOX and for 100-percent fluorine are 4.0 and 3.5, respectively, while that for 80-20 FLOX is nominally 5.33.

Reference to the curves of Fig. 42 will show that the heat flux profile for both the 80-20 and 70-30 FLOX test is characteristically similar, with throat heat flux for the primary 80-20 system slightly higher. The heat flux profile for the 100-percent fluorine system, however, appears distinctly different than either of the two FLOX systems. Specific departure is in the level of heat flux in the cylindrical chamber section and in the expansion region. The reduced chamber heat flux can be attributed primarily to insulative effects of a substantial carbon deposition layer in the thrust chamber. Posttest examination disclosed heavy (up to 1/4-inch thick) carbon layer buildup in the combustion chamber. Some minor carbon deposition was also evident on the throat and expansion nozzle. However, its effect in moderation of heat flux would be substantially less in these regions. As indicated in Fig. 42, the heat flux profile in the nozzle expansion region for the 100-percent fluorine test appears to exhibit a completely different characteristic than any of the preceding experiments with FLOX. The reason for the flattened heat flux profile in the expansion nozzle is not clear without a more detailed heat transfer analysis, but may be found to be related to recombination effects.

Summary

In summary, the supporting heat transfer analysis disclosed that measurements and resultant analysis are based on repeatable and reliable temperature data. It was found that the general group of like-doublet injectors would be favored over the 4-on-1 pentad designs because of the generally lower heat flux characteristics. Heat flux was found to vary with chamber pressure in a well-ordered manner corresponding to convective heat transfer for a fully developed turbulent boundary layer. Mixture ratio over the nominal 4.2 to 6.7 range had virtually no effect on heat flux characteristics for the like-doublet injector. Effects of chamber geometry were found to be generally amenable to analysis. The effects of fluorine concentration were explainable in terms of observed phenomena and supporting theoretical analysis. The effect of carbon deposition (with 100-percent fluoroine) was clearly distinguishable in terms of a marked reduction in chamber heat flux.

COMBUSTION INSTABILITY

Based on reported previous experience, periodic occurrences of combustion instability were expected during the experimental program. Other investigators have experienced instability in a previous program using FLOX and butene-1 (Ref. 21), even with relatively inefficient injectors. In addition, the size of the chamber (8-inch diameter) indicated that the first tangential mode frequency of approximately 4000 Hz was well within the range wherein combustion driving effects could be expected to be large, while damping effects were still small. And perhaps most important, the objective, demonstration of high combustion efficiency, was likely to bring with it a propensity for combustion instability.

Without specific requirements for dynamic stability, emphasis was directed to control of self-initiated instability, i.e., instability which begins without an external trigger source, such as a bomb or pulse gun. Frequently, it has been found in the past that instability was initiated

by a hard start, which served as a trigger for a nonlinear instability. Another possibility is for the oscillation to essentially "grow" out of the normal combustion noise. The latter type of instability is termed "linear" instability. Both of these types are usually observed at the engine start. In the latter case, if a very gradual buildup in chamber pressure is allowed, there will nearly always be a point during this buildup where a resonant mode of the chamber can readily couple with some other resonance such as those of the propellant feed or injection system. In most cases, this type of instability may be avoided by simply using a rapid start transient, and not allowing time for any pair of systems to couple.

Pressure records of a typical unstable test from the Ref. 21 program indicated that a slow start transient had been used because of the injector prechill operation. Analysis of the test records indicated that the probability for spontaneous instability could be avoided by using a rapid start transient. The importance of maintaining a controlled engine start transient was demonstrated in experiments with the normally stable injectors. In two of the tests (28 and 34), inadvertent start sequence abnormalities caused spontaneous instability to occur. In the first case, failure of a normal prestart injector purge resulted in injection of liquid nitrogen into the combustion chamber together with the FLOX/LPG propellants to cause spontaneous instability. In the second, a prolonged oxidizer purge resulted in loss of injector chill and subsequent erratic injection of propellants into the combustion chamber. When starting transients were properly controlled, there was no occurrence of combustion instability with the like-doublet injector.

Later in the program, when testing with the 4-on-1 injector, it was found that the injector was often unstable, regardless of the start sequence. The rapid start sequence which had been successful with the like-doublet injectors was not effective with the unlike 4-on-1 pentad injectors.

Several perturbations on this technique were tried, but the engine was still spontaneously (linearly) unstable, particularly at lower chamber pressures.

Significant instability was experienced only with the pentad injector. Four pentad injectors were used which differed with respect to orifice diameter size and/or diameter ratio. These differences are tabulated below:

Injector	d_{ox} , inch	d_f , inch	d_{ox}/d_f
P-1	0.025	0.025	1.0
P-2	0.025	0.029	0.86
P-2-M1	0.032	0.037	0.86
P-2-M2	0.040	0.047	0.86

The test conditions (chamber pressure, mixture ratio, and injector pressure drops) and observed peak-to-peak chamber pressure oscillations for each of these injectors are shown in Table IX. All like doublets and pentads P-1 and P-2 were stable at nominal conditions ($P_c = 100$ psia) with a noise level of less than 10 percent of chamber pressure. However, at a reduced chamber pressure of about 50 psia, a 30-percent oscillation was observed (with P-2).

After the first pentad modification (P-2-M1), the peak-to-peak amplitude was found to be significantly dependent on chamber pressure; the amplitude varied between 10 and 200 percent of chamber pressure as the chamber pressure was decreased from 150 to 75 psia. The final version of the injector (P-2-M2) was tested at the maximum chamber pressure (175 psia) which had been most stable previously, and peak-to-peak amplitudes of 200 percent of chamber pressure were experienced.

The experienced instability appeared to consist of a mixture of several acoustic modes. The average frequency was ~4000 Hz and three coexistent modes appeared to be present most of the time: the first tangential mode, the first tangential-first longitudinal mixed mode, and the second longitudinal mode.

In an effort to stabilize the motor sufficiently to permit meaningful performance measurements to be made, an acoustic absorber was designed and built. For simplicity and ease of fabrication, the absorber was made up of a single row of Helmholtz resonators around the injector face (actually four slot-like resonators, as shown in Fig. 43). These resonators were machined into a 1-1/2-inch-long ring which formed an extension of the combustion chamber at the injector end. The absorber was designed to have a resonant frequency of 4000 Hz.

The chamber and absorber were tested over a range of chamber pressures from 75 to 175 psia; average peak-to-peak amplitudes of 23 to 33 percent of chamber pressure were observed over this range. Thus, the amplitudes were too high to be regarded as entirely stable (<10 percent) but the influence of the absorber was clearly evident. It is quite possible that the chamber could be fully stabilized by varying the absorber design; however, an extensive stability study was considered beyond the scope of this program.

Because of the nature of the present program, only limited analysis has been done to attempt to understand the instability. Several explanations may be offered but these can only be considered speculation without extensive analysis and experiment. For instance, it may be postulated that somehow these high-energy space storable propellants are "different" in their chemical kinetics than other propellants. This is unlikely because chemical kinetic effects have never been found to be a factor in combustion instability (Ref. 22). An explanation along similar lines involves the effect of liquid reactivity. Because the like-impinging

injector was found to be stable, and the unlike-impinging type was unstable, it is possible that "blowapart" or impinging stream separation may be a factor in the instability. Such a postulate is given (Ref. 23) for earth storable propellants.

Cursory applications of the two most widely accepted combustion instability models is relevant. The Crocco theory, which should be most applicable to a linear instability of the type encountered, predicts, by a rough calculation, instability at frequencies less than about 6000 Hz at 100-psi chamber pressure (Ref. 24). It also predicts that by lowering chamber pressure, the engine would be expected to become more unstable, which was, in fact, observed. Unfortunately, it makes no distinction between the two basic injector types.

The Priem theory (Ref. 25), used predominantly for nonlinear or pulsed instabilities, distinguishes between injector types and generally implies the pentad to be the more unstable. On the other hand, the Priem theory indicates that the instability should be no worse at the low chamber pressure than at high. In summary, a cursory analysis of the instability does not indicate any obvious explanation of the instabilities observed with the pentad injectors; neither does it offer even qualitative reasons to explain differences between injectors and operating conditions.

DISCUSSION OF PERFORMANCE RESULTS

Although the results presented in the previous material illustrate the effects of individual conditions on performance, this type of graphical data display does not provide basic understanding of parameters affecting performance. In an attempt to understand performance variation, these results were analyzed in terms of changes in propellant distribution and dropsizes as a function of design and operating conditions. This analysis was performed using cold flow spray measurement data and correlations to determine if performance can be predicted using this cold flow information as input data for existing computer programs set up to compute propellant vaporization rate and non-uniform distribution effects on performance. Accordingly, the discussion which follows is divided into an analysis of propellant distribution, atomization, and finally overall performance prediction.

EFFECT OF DISTRIBUTION ON PERFORMANCE

When analyzing the effects of nonuniform propellant distribution on performance, the propellant combination and operating mixture ratio must be considered. In addition, for a specific propellant and operating mixture ratio, the effects of injector design parameters must be considered to achieve a given level of uniformity. For this analysis, two figures of merit, E_m and $\eta_{c^*,dist}$, were used. In this case, E_m is the parameter that describes the influence of injector design variables on distribution, whereas $\eta_{c^*,dist}$ depends not only upon uniformity, but also on propellant and operating mixture ratio.

Propellant Combination and Operating Mixture Ratio Effects

Figures 44 and 45 illustrate the effect of propellant combination on performance. In Fig. 44, the ratio of theoretical c^* to c^* at optimum mixture ratio is plotted as a function of actual mixture ratio divided by optimum mixture ratio for the three propellant combinations studied in this program

(100, 80-20, and 70-30 percent FLOX with 55-45 methane-ethane fuel). This figure shows that if a nonuniform mixture occurs in the engine, the performance penalty paid will be the most severe for the 80-20 percent FLOX mixture, especially if local mixture ratios are in excess of optimum.

Figure 45 illustrates the effect of propellant combination and overall operating mixture ratio obtained from cold-flow and hot-firing tests conducted. The upper portion (Fig. 45A) shows the predicted performance loss as a function of mixture ratio divided by optimum mixture ratio for the three FLOX mixtures. The same injector (ID-3) and cold-flow collection data were used in all three cases; only the input theoretical c^* curves differed when performing the stream tube analyses. The predicted performance difference between F_2 or 70-30 percent FLOX and 80-20 percent FLOX at optimum mixture ratio is about 1 percent. As the overall mixture ratio is reduced, this difference diminishes. Figure 45 B shows the actual hot-firing results. The observed difference in performance is again 1 percent at optimum mixture ratio and this difference also diminishes at lower mixture ratios. These results clearly show that if injector cold-flow results are used, performance of the general class of propellants considered to be advanced space storable combinations can be predicted and, therefore, optimized when considering nonuniform distribution effects. Obviously, propellant atomization and subsequent vaporization must also be considered to predict overall performance. (The influence of these parameters on performance is discussed in detail later in this section.)

The effects of overall operating mixture ratio and degree of nonuniformity (E_m) on performance for a given FLOX/LPG propellant combination are shown in Fig. 46. Presented is the predicted c^* efficiency (caused by nonuniformity) as a function of E_m . The predictions are based on the use of 80-20 percent FLOX. Included in this figure are cold-flow results obtained from all five injectors experimentally evaluated. The data shown illustrate the dependency of efficiency on distribution and overall operating mixture ratio. As

indicated, at optimum mixture ratio (5.33), changing E_m by 5 percent (90 to 95 percent) produced a 2 percent performance change (96 to 98 percent), whereas if the mixture ratio is 4.0 the performance increase is about 3/4 percent. Further, at a constant E_m (e.g., 90 percent) the predicted efficiency is 99 percent compared to 96 for the same two mixture ratios (4.0 and 5.33, respectively). It is of interest to note that performance of propellant combinations such as $N_2O_4/50-50$, ClF_3/N_2H_4 , FLOX/MMH, and OF_2/B_2H_6 are considerably less sensitive to E_m . Generally speaking, efficiencies on the order of 98 to 99 percent are predicted with these combinations at an E_m level of about 90 percent at optimum mixture ratio.

Injector Design Effects on Distribution

As indicated previously, the figure of merit currently used in characterizing injector design is E_m . Figures 47 and 48 illustrate the dependency of E_m on injector design variables. During the present program, two injector types, like- (like-on-like doublets) and unlike- (four oxidizer streams impinging on a central fuel jet) impinging stream injectors were investigated.

Like-impinging stream patterns require interfan mixing between oxidizer and fuel fans to provide uniform propellant distribution. In this case, propellant distribution is primarily a function of relative fan position or orientation parameters, such as fan inclination angle and spacing. In addition, distribution is also somewhat dependent on element or fan size and ability of propellant penetration (velocity level and velocity ratio). This latter effect was observed during the present program when a given injector was throttled and the overall mixture ratio was varied. For example, when the third like-on-like doublet injector (LD-3) was drilled out and throttled (the injector pressure drop was changed from 100 to 10 psi), E_m decreased by about 2 percent. This is now denoted as injector LD-3-M. Changing the mixture ratio from 3.0 to 8.0 resulted in a 2-percent E_m change. The effects of relative fan orientation on E_m are shown in Fig. 47. The influence of fan inclination angle and spacing are shown. The greatest effect was noted when fan spacing was varied.

The primary variables affecting the distribution created by unlike stream impingement are propellant momentum and diameter ratio. Typical secondary variables are element size, impingement angle, and proximity to adjacent fans. It should be noted that this latter parameter (fan proximity) can become a primary variable if gross nonuniformities in the individual spray have been created either by improper choice of momentum or diameter ratio or if large jet diameters and/or low pressure drops are used. In the latter situation, the phenomenon termed "hypergolic stream blowapart" can occur, (This same phenomenon is also a function of propellant injection temperature.) However, in the absence of blowapart, distribution (E_m) changes can be correlated in terms of momentum and diameter ratio. This type of correlation is presented in Fig. 48, which shows E_m as a function of K.

$$K = \left[\left(\frac{W_{ox}}{W_f} \right)^2 \left(\rho_f / \rho_{ox} \right) \left(\frac{A_f}{4A_{ox}} \right)^{1.25} \right] \quad (13)$$

where

W = propellant flowrate (total)

ρ = propellant density

A = individual orifice area

Subscripts

f = fuel

ox = oxidizer

This correlation equation was originally developed at JPL (Ref. 13). As indicated in Fig. 48, E_m appears to be a unique function of K (both 4-on-1 injector data are included). In addition, E_m is very sensitive to K despite the fact that the injector contains 96 elements that are quite close to one another and the individual elements are small (about 30 pounds thrust per element).

EFFECT OF VAPORIZATION PERFORMANCE

In the above discussion, the attention was directed toward effects of propellant nonuniformity on performance and efficiency predictions were made assuming no loss due to incomplete vaporization. During the present program, the effect of vaporization on performance was analyzed using the computerized combustion program described previously. In summary, efficiency losses due to incomplete vaporization are primarily a function of propellant physical properties, propellant dropsizes, and thrust chamber geometry. Parameters such as chamber pressure and mixture ratio exert a secondary influence on vaporization rate.

The vaporization rate-limited combustion model was used to define c^* efficiency, $\eta_{c^*, \text{vap}}$, as a function of mean dropsizes (D_{30}), and L^* for the actual test conditions covered during experiment. These results are shown in Fig. 49. Included are the following design and operating conditions:

1. $\epsilon_c = 2.0$; $P_c = 50$ to 150 psia
2. $\epsilon_c = 4.0$; $P_c = 200$
3. Injection velocity = actual experienced ($V_f = 36$ to 108 ft/sec;
 $V_o = 22$ to 66 ft/sec)
4. MR = 5.33

Because dropsizes is the controlling parameter limiting complete vaporization for a given propellant combination and engine size, the influence of injector and chamber design variables on dropsizes must be evaluated if performance predictions are to be made. For some propellant combinations, i.e., $N_2O_4/50-50$, dropsizes of both propellants must be known to predict vaporization efficiency. The propellant combinations studied in this program, however, were found to be fuel vaporization rate limited for equal fuel and oxidizer sizes (see Task I discussion); therefore, the

dropsize analysis performed was directed toward parameters affecting fuel atomization. (Analytical comparison of fuel and oxidizer dropsizes showed that the oxidizer dropsize was always smaller than the fuel because of physical property differences. Hot-firing tests were performed to confirm this analysis. The oxidizer orifices of the first like doublet (LD-1) were enlarged after initial testing (from 0.029 to 0.036 inch), and the before and after measured performance was the same (Table V).

In general, propellant atomization by stream impingement has been found to be a function of:

$$\text{Dropsize} = f \left\{ \begin{array}{l} \text{injection velocity} \\ \text{orifice or jet diameter} \\ \text{impingement angle} \\ \text{propellant physical properties} \\ \text{combustion gas velocity} \\ \text{combustion gas density} \end{array} \right.$$

Like Stream Impingement Atomization

One of the important works performed on the subject of impinging stream atomization was that of Ingebo of NASA some years ago (Ref. 15). His well-known equation shown below was obtained with like-doublet impingement of equally sized jets using n-heptane as a liquid which is similar in physical properties to the ethane-methane blend fuel in this program:

$$D_{30} = \frac{1}{2.64 \sqrt{\frac{V}{D}} + 0.97 / (\Delta V)} \quad (14)$$

where

D_{30} = volume-mean-diameter of resulting droplets, inches

V = injection velocity, ft/sec

D = orifice diameter, inches

ΔV = $(V_g - V_L)$ = relative velocity difference between gas and liquid jet, ft/sec

This equation includes terms that take into account both the primary (hydraulic) and secondary (shear) atomization processes. $\sqrt{\frac{V}{D}}$ is considered the primary atomization term and is controlled by injector design hydraulics. The relative velocity expression ($\Delta V = V_g - V_{inj}$) is considered to be the secondary atomization term and is controlled by high velocity gas forces acting on the liquid.

Other investigators have studied primary and secondary atomization separately. An example of the former is that of Dombrowski and Hooper (Ref. 16), who investigated the effects of injection velocity and impingement angle, again with like-doublet streams of equal size. The latter, secondary atomization, has been studied by several investigators such as Dickerson (Ref. 17), Ingebo and Foster (Ref. 18), Mayer (Ref. 19), and Wolfe and Andersen (Ref. 20). Unfortunately, these investigations have been performed considering either one or the other processes (primary or secondary) only. Ingebo's work (Eq. 15) includes both; however, his results are somewhat limited, especially when considering the effects of fluid physical properties and gas density on secondary atomization. Because of this limitation, the secondary atomization work of Ingebo, Ref. 18 (he studied secondary atomization only, as well as the previously presented combined effort), and Wolfe and Andersen were reviewed relative to gas density and physical properties effects.

Comparing the secondary atomization equations of Wolfe and Anderson and that of Ingebo:

$$D_{30} \propto \frac{1}{\left(\frac{\rho_L^{1/6}}{\mu_L^{1/3} \sigma_L^{1/2}} \right) (\rho_g^{2/3}) (\Delta V^{4/3})} \quad \text{(Wolfe, and Anderson)} \quad (15)$$

$$D_{30} \propto \frac{1}{\left(\frac{\rho_L^{1/4}}{\mu_L^{1/4} \sigma_L^{1/4}} \right) (\rho_g^{1/4}) (\Delta V^{3/4})} \quad \text{(Ingebo)} \quad (16)$$

where

ρ = density

μ = viscosity

σ = surface tension

ΔV = relative velocity between gas and liquid jet/droplet

Subscripts

L = liquid

g = gas

For a given fluid, equivalent gas velocity and characteristic dimensions, the same parameters, fluid physical properties and gas density, appear. The correlating exponents differ considerably. It should be noted, however, that the experimental apparatus also differed. In the case of Ingebo, a showerhead jet was injected normal to the gas flow whereas with Wolfe, a single spherical drop was subjected to the gas flow field.

In attempting to use the experimental work of Ingebo where both atomization mechanisms were evaluated simultaneously (Eq. 14), the most significant limitation occurs when considering gas density differences. (n-heptane and ethane-methane blend liquid property differences result in only about a predicted 10-percent dropsizes change using either of the above equations.) For the present program, it was assumed that Ingebo's secondary atomization experimental work (Ref. 18) more closely modeled the actual conditions encountered (i.e., a partially atomized liquid in the form of ligaments being exposed to combustion gas density). Accordingly, the equation employed to predict fuel dropsizes produced by like-on-like injectors was:

$$D_{30} = \frac{1}{2.64 \sqrt{\frac{V}{D}} + K \left(\frac{\rho_{act}}{\rho_{ref}} \right)^{1/4} / (\Delta V)} \quad (17)$$

where

$$K = 0.97 \times \left[\left(\frac{\mu_L \sigma_L}{\rho_L} \right)_{n\text{-heptane}} / \left(\frac{\mu_L \sigma_L}{\rho_L} \right)_{LPG} \right]^{1/4}$$

$$\rho_{ref} = 10.7 \times 10^{-4} \text{ g/cc}$$

$$\rho_{act} = P_c / RT = \frac{\text{actual chamber pressure}}{\text{theoretical gas constant} \times \text{theoretical flame temperature}}$$

Unlike Stream Impingement Atomization

Until recently, no experimental data existed concerning dropsizes that are produced by impinging jets of differing diameters and fluid properties. The work performed at Rocketdyne by Dickerson et al. (Ref. 17) has shown that considerably differing sizes and size distributions result from un-

like, unequal-size impingement. Of significance to this program, Dickerson found that a 4-on-1 element with fuel in the center jet produced the following correlation:

$$(D_{30})_f \propto \left(\frac{\bar{D}_{\text{orif}}^{1/4}}{V_f^{0.1} V_{\text{ox}}^{0.9}} \right) \quad (18)$$

where

$$\begin{aligned} (D_{30})_f &= \text{volume mean fuel drop size} \\ \bar{D}_{\text{orif}} &= \text{mean orifice diameter} \\ V_f &= \text{fuel injection velocity} \\ V_{\text{ox}} &= \text{oxidizer injection velocity} \end{aligned}$$

These results, obtained in still air (thus minimizing the secondary atomization effects), show that the fuel dropsize is primarily a function of oxidizer injection velocity. This dependency is in agreement with the observed trends in 4-on-1 performance as a function of mixture ratio (Fig. 23), i.e., 4-on-1 performance increases with increasing mixture ratio when performance losses caused by nonuniform distribution are normalized out (Fig. 24).

PERFORMANCE PREDICTION

Previous programs have been conducted wherein consideration of either primary (hydraulic) or secondary (shear) atomization alone were used to successfully predict combustion efficiency. The NASA-sponsored lithium program (Ref. 17) is an example of the latter. In this case, the entire atomization correlation effort involved liquid lithium atomization by a high velocity gas produced in a fluorine-rich gas generator.

An example of the former (correlation of data considering primary atomization only) may be found in Ref. 1. In this Air Force-funded study, the effects of injector design variables on primary atomization were investigated in considerable detail. The objective of the Ref. 1 effort was correlation of spray injector parameters with rocket engine performance. The intent was to define injector design variables that affected atomization and distribution and resultant combustion efficiency. During this effort, the primary atomization process was studied using several impinging patterns. A cold-flow wax system was used to generate original unlike-impinging stream atomization correlations.

The major difference between the present program and that of Ref. 1, aside from propellants, was inclusion of parameters affecting secondary atomization, i.e., chamber pressure (gas density) and contraction ratio (gas velocity). During the Air Force-sponsored program, these two parameters were held constant, and at levels where secondary atomization was diminished. Under these conditions, successful performance predictions resulted by considering only injector hydraulics on atomization. Specific sets of data generated during the current program can also be correlated in this manner, i.e., results obtained with a given contraction ratio and constant chamber pressure. However, a general correlation could not be satisfactorily obtained without inclusion of secondary atomization.

A performance analysis was made using Eq. 14 from which dropsize was predicted for the various configurations tested (includes both primary and secondary atomization effects). The predicted volume mean fuel dropsizes are presented in Table X as a function of injector type, chamber pressure, chamber contraction ratio, injection velocity, and orifice diameter.

It should be noted that use of Eq. 14 required definition of the gas velocity which, at the present state of the art, can only be accomplished by hot-firing experiment. A single test condition was used as a reference point to calculate gas velocity. Calculation of this reference velocity was performed by proceeding backwards using measured overall efficiency adjusted for predicted distribution loss as a starting point. The dropsize required to produce this performance level was determined using the vaporization rate-limited combustion model (Fig. 49). Having defined dropsize, the gas velocity was determined by solving Eq. 14. In all remaining cases, gas velocity (320 ft/sec for $\epsilon_c = 2:1$, $L^* = 30$ inches, $MR = 5.33$) was assumed invariant, being only proportional to contraction area ratio.

The predicted and actual performance efficiencies for 16 differing design or operating conditions are presented in Table XI. This prediction was made on the basis that overall efficiency is a product of distribution and vaporization efficiencies, i.e., $\eta_{c*} = \eta_{c*,dist} \times \eta_{c*,vap}$. A comparison between these efficiencies is shown in Fig. 50, which is a plot of predicted versus actual c^* efficiency. The agreement is excellent. As indicated in Table XI, several injector modifications are considered as well as propellant combination, chamber pressure, contraction ratio, and chamber length. The results shown in Fig. 50 and Table XI are for an operating mixture ratio of 5.33 (optimum c^*) using like-doublet injectors.

Excellent agreement between predicted and actual efficiencies was also obtained at other mixture ratios. However, additional mixture ratios were not included in the present tabulation because of lesser interest in off-design operation.

While the available 4-on-1 injector data agrees with predictions, experiments were not conducted with variable thrust chamber geometries and useful results were not obtained at differing chamber pressures due to combustion instability. Because of this, it was felt that the range of data available was too narrow for confirmation of predicted performance by actual results.

In summary, the program objectives have been achieved. High performance using FLOX/LPG propellants has been demonstrated. Further, because predicted performance agrees with that actually observed within about $\pm 1/2$ percent over a very wide design and operating range, sufficient data exist to allow extrapolation of the program results to other advanced space storable propellant combinations and operating conditions. In addition, cold-flow results have been presented which show the effects of injector design variables on distribution and dropsizes. Generally speaking, it was shown that a mixing index value (E_m) of about 95 percent is required for high performance and the dropsizes needed for high performance is dependent upon the chamber geometry used.

CONCLUDING REMARKS

An analytical and experimental program has been conducted to establish a sound technical base for predictable, high combustion performance of advanced space-storable propellant combinations. The propellants considered consisted of mixtures of fluorine and oxygen oxidizers and light hydrocarbon fuels such as ethane and methane. Cold-flow spray information results were used as input data for combustion performance prediction using computerized combustion model programs involving propellant vaporization and nonuniform distribution effects on delivered performance. The program results have shown that performance predicted on this basis agrees very well with actual observed efficiencies.

The data obtained have shown that present cold-flow correlations coupled with a single, typical, hot-firing data point allow prediction and extrapolation of performance over a rather broad spectrum of design and operating conditions. Evaluation of other FLOX/LPG propellant combinations may now be analytically performed with a high degree of confidence.

Previous programs conducted at Rocketdyne (Ref. 1) have also shown that the use of cold-flow data and combustion model analysis will result in successful prediction of performance. It is felt, however, that the wider scope of the present program resulted in more generally useful correlations in certain respects. The major difference between this and the Air Force-sponsored program (Ref. 1) was inclusion of parameters affecting secondary atomization, i.e., chamber pressure (gas density) and contraction ratio (gas velocity). In reviewing these two programs, it is felt that previous effort was more useful in understanding injector design influences on performance whereas the present results are more generally applicable for extrapolation to other operating conditions and thrust chamber geometries.

Present results have several limitations. For instance, specific design criteria do not exist in the area of injector-chamber compatibility when using LPG fuels. The familiar "fix" of injecting film cooling near the

outer periphery to reduce heat flux or improve ablative chamber life will probably result in unsatisfactory performance. Performance is very sensitive to nonuniform distribution as evidenced by the shape of the theoretical c^* curve versus mixture ratio. Further, present results are limited to liquid-liquid injection. Injecting the fuel as a gas does not present any unique combustion modeling problem; however, quantitative gas-liquid distribution data as a function of injector design do not exist.

Finally, when cold-flow spray data are used as computer input, it is obviously restricted to injector designs amenable to cold-flow spray characterization. For instance, designs that are particularly sensitive to high combustion gas cross-flow velocities (radial winds) caused by very localized mass injection will be difficult, if not impossible to analyze. Further, inappropriate feed system designs which have high manifold cross velocities and/or very short orifice L/D ratios cannot be expected to produce reliable or reproducible cold-flow correlation results. In this case, ambient versus actual chamber pressure environments will obviously cause differing distributions.

REFERENCES

1. AFRPL-TR-68-147, Correlation of Spray Injector Parameters With Rocket Engine Performance, R. Dickerson et al., Rocketdyne, a Division of North American Rockwell Corporation, Canoga Park, California, June 1968.
2. Lambiris, S., L. P. Combs, and R. S. Levine: "Stable Combustion Processes in Liquid Propellant Rocket Engines," Combustion and Propulsion, Fifth AGARD Colloquium: High Temperature Phenomena, The MacMillan Company, New York, N. Y., 1962, 596-636.
3. Priem, R. J. and Heidmann, M. F., Propellant and Vaporization as a Design Criterion for Rocket Engine Combustion Chambers, NASA TR R-67, 1960.
4. Pieper, J. L., L. E. Dean, and R. S. Valentine, "Mixture Ratio Distribution--Its Impact on Rocket Thrust Chamber Performance," J. Spacecraft Rockets, Vol. 4, No. 6, pp 786-789, June 1967.
5. Rupe, J. H., A Correlation Between the Dynamic Properties of a Pair of Impinging Streams and the Uniformity of Mixture-Ratio Distribution in the Resulting Spray, Progress Report No. 20-209, Jet Propulsion Laboratory, Pasadena, California, 28 March 1956.
6. Rupe, J. H., An Experimental Correlation of the Nonreactive Properties of Injection Schemes and Combustion Effects in a Liquid-Propellant Rocket Engine, Technical Report No. 32-255, Jet Propulsion Laboratory, Pasadena, California, 15 July 1965.
7. Riebling, R. W., "Criteria for Optimum Propellant Mixing in Impinging Jet Injection Elements," J. Spacecraft Rockets, Vol. 4, No. 6, pp 817-819, June 1967.
8. Wrobel, J. R., "Some Effects of Gas Stratification on Choked Nozzle Flows," AIAA Paper 64-266, 1964.
9. Rupe, J. H., The Liquid Phase Mixing of a Pair of Impinging Streams, Progress Report No. 20-195, Jet Propulsion Laboratory, Pasadena, California, 6 August 1953.

10. Technical Documentary Report No. TR-65-107, Performance Characteristics of Compound "A"/Hydrazine Propellant Combinations, Rocketdyne, a Division of North American Aviation, Inc., Canoga Park, California, May 1965, CONFIDENTIAL.
11. Contract NAS7-304, Chamber Technology for Space Storable Propellants, Third Interim Report, Rocketdyne, a Division of North American Aviation, Inc., Canoga Park, California, May 1967.
12. Kirsch, J. W., Rocket Injector Design Optimization for the $\text{OF}_2/\text{RP-1}$ Combination, Research Report No. 64-40, Rocketdyne, a Division of North American Aviation, Inc., Canoga Park, California, September 1964.
13. Elverum, G. W., Jr. and T. F. Morey, Criteria for Optimum Mixture Ratio Distribution Using Several Types of Impinging-Stream Injector Elements, JPL Memo No. 30-5, 25 February 1959.
14. Rocketdyne General Order No. 9006, Deal RC67-1209, Space Storable Propellant Performance Program ... Statement of Work for General Order 9006, 3 August 1967.
15. Ingebo, R. E., Dropsizes Distributions for Impinging-Jet Breakup in Airstreams Simulating the Velocity Condition in Rocket Combustors, NACA TN 4222, 1958.
16. Dombrowski, N. and P. Hooper, A Study of the Sprays Formed by Impinging Jets in Laminar and Turbulent Flow, Journal of Fluid Mechanics, V18, Part 3, pp 392-400, 1964.
17. R-7257, Lithium-Fluorine-Hydrogen Propellant Study, H. A. Arbit, et al., Rocketdyne, a Division of North American Rockwell Corporation, Canoga Park, California, October 1967 (NASA CR-72325).
18. Ingebo, R. D., et al., Dropsizes Distribution for Crosscurrent Breakup of Liquid Jets in Airstreams, NACA TN 4087, 1957.
19. Mayer, E., "Theory of Liquid Atomization in High Velocity Gas Streams," ARS Journal, V31, N12, December 1961, p 1783.
20. Wolfe, H. and W. Anderson, Kinetic Mechanism and Resultant Droplet Sizes of the Aerodynamic Breakup of Liquid Drops, Report 0395-04(18) SP, Aerojet-General Corporation, Downey, California, April 1964.

21. Colbert, J.E.: "Use of an Acoustic Liner to Attenuate FLOX-Light Hydrocarbon Instability," Fourth ICRPG Combustion Conference, Menlo Park, California, October 1967.
22. Wood, J.S., D. R. Hardesty, I. Glassman, and D. T. Harrje: "Possible Relationships Between Chemical Kinetics and Liquid Propellant Rocket Combustion Instability," Fifth ICRPG Combustion Conference, Howard County, Maryland, October 1968.
23. Lawver, B.R.: "An Experimental Study of the N_2O_4/N_2H_4 Jet Separation Phenomena," 5th ICRPG Combustion Conference, Howard County, Maryland, October 1968.
24. Reardon, F.H.: "Correlations of the Sensitive Time Lag Theory Combustion Parameters with Thrust Chamber Design Parameters," 5th ICRPG Combustion Conference, Howard County, Maryland, October 1968.
25. Campbell, D.T. and W.D. Chadwick: Combustion Instability Analysis At High Chamber Pressure, AFRPL TR-68-179, November 1968.

TABLE I

SUMMARY OF INJECTOR ASSEMBLY SPECIFICATIONS

Injector Identification Number	Injector Type	Orifice Diameter		Number of Elements *	Nominal Injector ΔP (psi) at Design Conditions		Pattern Specifications**					Rocketdyne Drawing Number
		Fuel, d _f , inch	Oxidizer, d _{ox} , inch				d _{ox} /d _f	Fan Spacing, inch	Fan Inclination Angle, degrees	Intra-Element Spacing, inch	Fan Impingement Angle, degrees	
					Oxidizer	Fuel						
LD-1	Like Doublet	0.0200	0.0292	112	290	100	1.46	0.00	0	0.20	0	R1E 2676-3
LD-1-M			0.0360		85		1.80					↓
LD-2			0.0292		290		1.46	0.275				R1E 2676-5
LD-3				0.0360		85		1.80	0.00	25	0.25	R1E 2741
LD-3-M			0.0260	0.0469	↓	30	30	↓	↓	↓	↓	↓
P-1	Pentad***	0.0250	0.0250	96	190	240	1.00	NA	NA	NA	NA	R1E 2665
P-2		0.0292	↓		190	130	0.86	↓	↓	↓	↓	↓
P-2-M1		0.0372	0.0320		60	45						
P-2-M2		0.0465	0.0400	↓	30	25	↓	↓	↓	↓	↓	↓

*Like-doublet element is pair of fuel and oxidizer doublets.

**All injectors contain six rings of elements. For each injector, the outer ring of elements are canted so that the resultant propellant spray is directed 15 degrees toward the axial centerline of the injector. Resultant propellant spray direction for the remaining elements is parallel to the chamber axis. See Fig. 9 and 16 for illustration of typical face patterns for like-doublet and pentad injectors, respectively.

***Four oxidizer streams impinging on a center fuel stream.

TABLE II

MODEL INJECTOR DESIGN SPECIFICATIONS*

Injector Quadrant	Fan Inclination Angle, degrees	Element Spacing (between paired fuel and oxidizer doublets), inch
R1D2692-1	0	0.20
R1D2692-2	0	0.30
R1D2692-3	0	0.40
R1D2692-4	25	0.20
R1D2716-1	25	0.30
R1D2716-2	25	0.40
R1D2716-3	10	0.20
R1D2716-4	40	0.20

* $D_f = 0.0200$ inch; $D_{ox} = 0.0292$ inch; injector
 $100 \text{ psi} \geq \Delta P \geq 200 \text{ psi}$; spacing between elements
 is constant for all quadrants (~ 0.75 inch); fan
 spacing and impingement angles were zero.

TABLE III

SUMMARY OF MODEL INJECTOR COLD-FLOW DATA*

Injector Quadrant	Fan Inclination Angle, degrees	Intra-Element Spacing, inch	E _m , percent
R1D2692-1	0	0.20	79.4
R1D2692-1	0	0.20	77.4
R1D2716-3	10	0.20	80.5
R1D2692-4	25	0.20	83.3
R1D2716-4	40	0.20	79.0
R1D2692-2	0	0.30	78.7
R1D2692-3	0	0.40	75.3
R1D2716-1	25	0.30	85.4
R1D2716-1	25	0.30	88.0
R1D2716-2	25	0.40	86.5

*Nominal mixture ratio = 5.33 for all tests.

TABLE IV
CHAMBER ASSEMBLY SPECIFICATIONS

Nozzle Contraction Ratio	Chamber Assembly L*, inches	Distance to Start of Convergence, inches	Distance to Geometric Throat, L _t , inches	Number and Length of Cylindrical Chamber Sections Employed
2 (See Fig. 19) ↓	15 30 60	4.687 12.187 27.187	8.267 15.767 30.767	None One; 7 inches long Three; 3.75, 7.50, and 11.25 inches long
4 (See Fig. 20) ↓	15 30 60	1.083 4.833 12.333	5.653 9.403 16.903	None One; 3.75 inches long Two; 3.75 and 7.50 inches long

TABLE V

SUMMARY OF PERFORMANCE DATA

Test Number	Injector Assembly Number	Chamber Assembly, L*, in./ ϵ_c	Oxidizer ¹	Stagnation Chamber Pressure ² , psia	Mixture Ratio, w_{ox}/w_f	Total Propellant Flowrate, \dot{w}_t , lbm/sec	Throat Area, A_t , in. ²	Measured Thrust, F_{meas} , lbf	F_{vac} , lbf	c^* theo, ft/sec	Corrected c^*_{Eff} (Based on P_c), percent	Corrected c^*_{Eff} (Based on P), percent	Remarks ³
1*	P-1	30/2	FLOX (70% F_2)	100.0	5.33	-	25.39	-	-	-	-	-	No usable data. Fuel flowrate not recorded.
2*				100.0	5.33	-		-	-	-	-	-	No usable data. Fuel flowrate not recorded.
3*				100.0	5.33	-		-	-	-	-	-	No usable data. Fuel flowrate not recorded.
4				103.8	5.18	12.990	25.42	2997	3643	6703.0	99.2	98.9	
5				104.1	6.99	13.509		3091	3737	6425.0	99.9	100.4	
6				97.8	4.02	12.482		2853	3499	6805.0	95.9	97.1	
7	LD-1			99.4	4.76	12.369		2834	3480	6750.0	98.1	97.6	
8				103.8	3.75	12.948		3008	3654	6800.0	97.1	97.2	
9				105.6	5.20	13.208		3079	3725	6700.0	98.4	98.6	
10*				100.0	6.50	-		-	-	-	-	-	No usable performance data obtained. Ran out of fuel.
11			FLOX (80% F_2)	103.0	5.13	12.915		2896	3542	6916.0	95.1	92.9	
12				102.0	5.43	12.779		2940	3586	6910.0	95.4	95.1	
13				104.0	3.95	12.962		3090	3736	6758.0	97.8	98.4	
14				100.3	6.40	12.918		2896	3542	6712.0	95.8	95.6	
15				97.4	4.97	12.053		2800	3446	6909.0	96.5	96.9	
16	P-1			100.7	5.18	12.639	25.47	2890	3536	6918.0	96.1	95.2	
17				102.6	6.36	13.012		2986	3632	6725.0	97.7	97.8	
18				101.9	5.30	12.764		2965	3611	6920.0	96.3	96.4	
19				104.2	6.96	13.414		3046	3692	6575.0	98.4	98.7	
20				99.5	4.06	12.691		2865	3511	6780.0	96.3	96.2	
21				102.4	8.97	14.424		2975	3621	6035.0	98.1	98.1	
22	P-2			101.3	5.31	12.682	25.52	2957	3603	6920.0	96.6	96.8	
23				101.4	5.32	12.779		2946	3592	6920.0	96.4	95.8	
24				102.9	6.42	13.080		3001	3647	6707.0	98.3	98.1	
25				102.6	7.97	13.781		2990	3636	6295.0	99.4	98.8	
26				103.0	3.83	13.023		3009	3655	6736.0	98.4	98.3	
27*				100.0	4.00	-							No usable data. Run duration too short. Fuel main valve closed prematurely.

Test Number	Injector Assembly Number	Chamber Assembly, in. ²	Oxidizer ¹	Stagnation Pressure ² , psia	Total Propellant Flowrate, lbm/sec	Measured Thrust, lbf	c^* , ft/sec	Corrected c^* , lbf (Based on P_c), percent	Corrected c^* , lbf (Based on P), percent	Remarks
28	P-2	30/2	FLOX (60% F_2)	100.9	12.718	2920	6742.0	98.6	98.1	Unstable at start caused by improper sequence, but damped out. Pretest purges were not turned on, thus, IAG injected with FLOX/LFG into chamber at start of test.
29				102.6	12.804	2979	6920.0	97.0	96.5	
30				99.0	12.999	2823	6606.0	96.5	95.5	
31				100.7	12.558	2912	6915.0	97.0	96.6	
32				48.1	6.097	1094	6822.0	96.5	98.5	
33	ID-2			76.6	9.653	2067	6890.0	96.4	96.1	No usable data. Run duration too short. (RCC) instability caused by improper line/injector chill.
34				100.0	5.55	2713	6890.0	96.4	96.1	
35				97.1	5.21	2786	6920.0	95.2	95.2	
36				100.6	4.04	2899	6778.0	96.2	95.9	
37				96.9	6.31	2773	6735.0	95.0	92.4	
38				97.6	5.17	2792	6919.0	95.2	92.8	
39				100.9	4.01	2912	6770.0	96.1	96.1	
40	P-2-M1			99.7	5.50	2885	6920.0	95.5	94.5	
41				98.7	5.47	2835	6905.0	95.1	95.7	
42				99.1	5.58	2847	6880.0	95.4	95.6	
43a				50.0	5.35					No usable data. (RCC)
44a				50.0	5.35					No usable data. (RCC)
45a				50.0	5.35					No usable data. (RCC)
46a				67.2	5.54	1811	6848.0	95.9	96.9	
47a				50.0	5.35					Data questionable
48				98.7	5.40	2820	6915.0	94.5	95.0	No usable data. (RCC)
49a				74.5	6.25	2076	6710.0	96.0	96.4	Data questionable
50a				50.0	5.35					No usable data. (RCC)
51				148.5	5.58	4657	6953.0	94.0	94.6	No usable data. (RCC)
52				150.6	5.37	4684	6950.0	94.4	94.7	No usable data. (RCC)
53a				50.0	5.35					No usable data. (RCC)
54a				50.0	5.35					No usable data. (RCC)

TABLE V
(Continued)

Test Number	Injector Assembly Number	Chamber Assembly, L*, in/ε _c	Oxidizer ¹	Stagnation Chamber Pressure ² , psia	Mixture Ratio, w _{ox} /w _f	Total Propellant Flowrate, ṁ _t , lbm/sec	Throat Area, A _t , in. ²	Measured Thrust, F _{meas} , lbf	F _{vac} , lbf	c* _{theo} , ft/sec	Corrected c* _{Eff} (Based on P _c), percent	Corrected c* _{Eff} (Based on F), percent	Remarks ³
55*	P-2-M2	30/2	FLOX (80% F ₂)	150.0	5.33		25.52						No Usable Data (RCC)
56*													No Usable Data (RCC)
57*													No Usable Data (RCC)
58*													Tests conducted with acoustic absorber fabricated from mild steel. Edges of acoustic cavity were burned. (RCC) No Usable Data.
59*													Tests conducted with OFHC copper acoustic absorber. Performance data questionable (See Footnote)
60*													
61*				173.0	5.33								
62**				174.2	5.57	21.734		3692	6338	6885.0	96.1	96.9	
63**				150.5	5.00	18.750		4714	5360	6915.0	96.3	96.6	
64**				99.1	5.61	12.732		2916	3562	6873.0	96.8	95.7	
65**				71.2	5.30	9.149		1939	2585	6885.0	96.3	97.0	
66*	LD-1-M			100.0	5.333		25.56						No Usable Data. Flowmeter Problems
67*													
68				101.0	5.50	12.792		2886	3532	6895.4	95.3	94.8	
69				101.2	5.47	12.872		2942	3588	6901.4	95.0	95.2	
70				101.2	6.77	13.330		2947	3593	6626.7	95.4	95.6	
71				102.7	3.97	12.948		3036	3682	6761.8	97.8	97.8	
72				101.3	5.25	12.799		2978	3624	6921.5	95.4	95.5	
73*	LD-3			100.0	5.33								No Usable Data. Fuel Flowrate Unsteady.
74				99.9	5.40	12.578		2899	3545	6915.9	96.1	96.0	
75				102.3	4.20	12.786		2987	3633	6807.6	97.8	98.0	
76				99.0	6.70	12.896		2875	3521	6641.4	96.5	96.6	
77				99.5	5.33	12.428		2877	3523	6918.6	96.4	96.0	
78				98.3	5.22	12.356		2850	3496	6919.1	96.3	96.4	
79				152.0	5.23	18.607		4752	5398	6956.4	97.8	97.5	
80*				50.0	5.33								No usable data. Fuel flowrate unsteady.
81				48.3	5.60	6.234		1119	1765	6805.7	95.2	98.4	Possible nozzle flow separation. Consequently performance value based on thrust should be used judiciously.
82		60/2		100.4	5.29	12.535		2959	3605	6920.9	98.0	98.6	
83				100.8	5.44	12.648		2963	3609	6907.3	98.1	98.3	
84				100.3	6.78	13.069		2948	3594	6622.4	98.8	99.3	
85				102.6	4.10	12.866		3038	3684	6787.4	99.9	100.6	

TABLE V
(Continued)

Test Number	Injector Assembly Number	Chamber Assembly, L*, in./ c_c	Oxidizer ¹	Stagnation Chamber Pressure ² , psia	Mixture Ratio, w_{ox}/w_f	Total Propellant Flowrate, \dot{w}_t , lbm/sec	Throat Area, A_t , in. ²	Measured Thrust, F_{meas} , lbf	F_{vac} , lbf	c^* theo, ft/sec	Corrected c^*_{Eff} (Based on P_c), percent	Corrected c^*_{Eff} (Based on F), percent	Remarks ³
86	1D-3	60/4	FLOX (80% F_2)	199.2	5.27	12.354	12.91	3324	3839	6993.4	96.2	96.8	
87				200.7	5.31	12.415		3359	3874	6994.3	96.9	97.6	
88				205.6	4.15	12.631		3463	3978	6855.6	99.3	100.2	
89				198.8	6.47	12.792		3306	3821	6754.2	96.6	97.1	
90				199.0	5.22	12.218		3314	3829	6993.3	97.4	97.4	
91				206.1	4.10	12.668		3464	3979	6850.8	99.3	99.9	
92		15/2		99.0	5.47	12.534	25.56	2712	3358	6901.1		89.5	c^* efficiency based on P_c is not presented because it would be in error (high) because appreciable amounts of combustion occur in the nozzle for this configuration.
93				101.1	5.33	12.721		2780	3426	6920.1		89.8	Test duration was too short to determine steady-state perf. (Runs 96 & 97)
94				100.5	6.82	13.168		2786	3432	6612.2		90.9	
95				102.1	4.16	12.786		2835	3481	6799.7		92.2	
96*		30/4		200.0	5.33		12.91						Same as Test No. 96*
97*				200.0	5.33								
98				197.2	6.32	12.998		3244	3759	6791.2	92.9	92.6	
99*				200.0	4.00								
100				194.2	5.68	12.494		3186	3701	6949.4	93.1	97.3	
101*		15/4		200.0	5.33								Same as Test No. 96*
102				203.5	4.91	12.732		3189	3704	6971.9		90.5	See Remark for Tests 92-95
103*				200.0	4.00								Same as Test No. 96*
104				199.2	6.63	13.040		3109	3624	6717.6		90.0	See Remark for Tests 92-95
105				201.5	5.16	12.719		3142	3657	6993.7		89.2	See Remark for Tests 92-95
106		30/2	FLOX (70% F_2)	95.8	4.10	12.113	25.56	2759	3405	6803.0	97.2	97.7	
107				97.8	3.94	12.282		2806	3452	6804.0	97.4	97.8	
108				99.0	5.38	12.612		2827	3473	6677.0	97.9	97.5	
109				97.2	3.06	12.551		2798	3444	6635.0	97.3	97.8	
110*			FLOX (100% F_2)	100.0	4.00								No Usable Data (RCC)
111*				100.0	4.00								No Usable Data. Flowrates Unsteady
112				98.4	4.46	13.105		2879	3525	6489.0	97.0	97.0	
113				97.1	6.43	13.411		2834	3480	6157.0	98.5	98.7	
114				98.9	3.50	12.971		2880	3526	6537.0	97.1	97.0	

TABLE V
(Concluded)

Test Number	Injector Assembly Number	Chamber Assembly, L*, in./ ϵ_c	Oxidizer ¹	Stagnation Chamber Pressure ² , psia	Mixture Ratio, w_{ox}/w_f	Total Propellant Flowrate, w_t , lbm/sec	Throat Area, A_t , in. ²	Measured Thrust, F_{meas} , lbf	F_{vac} , lbf	c^*_{theo} , ft/sec	Corrected c^*_{Eff} (Based on P_c), percent	Corrected c^*_{Eff} (Based on F), percent	Remarks ³
115*	LD-3-M	30/2	FLOX (80% F_2)	100.0	5.33		25.56						No usable data. (RCC)
116*				100.0	5.33								No usable data. (RCC)
117				130.2	4.42	18.581		4709	5355	6871.6	97.6	98.0	
118				149.9	4.99	18.612		4683	5329	6941.6	96.3	96.4	
119				99.2	4.04	12.468		2858	3505	6775.6	97.7	97.5	
120				100.0	5.24	12.687		2919	3565	6920.6	95.4	95.8	
121				46.7	6.06	6.295		1069	1715	6701.2	93.2	95.5	See remark for Test 81.
122		15/2		150.5	5.25	18.842		4486	5132	6955.5		90.3	See remark for Tests 92-95.
123				100.8	5.38	12.893		2788	3434	6917.2		88.8	See remark for Tests 92-95.
124				101.1	5.37	12.923		2804	3450	6917.9		89.0	See remark for Tests 92-95.
125				47.9	5.05	6.385		1052	1698	6836.5		89.7	See remark for Tests 92-95- and 81.

1. Fuel for all tests was 55 percent CH_4 -45 percent C_2H_6 LPG blend.

2. Derived from P_c near start of convergence.

3. RCC = Test cut by rough combustion cut system.

* Nominal target test conditions shown.

** Test not cut by RCC system but peak-to-peak P_c oscillations greater than 25 percent of P_c (Perf. data questionable.)

TABLE VI

LOCATION KEY FOR HEAT FLUX DATA IN TABLE VII

Station Code	Axial Distance From Injector, inches	Station Code	Axial Distance From Injector, inches	Station Code	Axial Distance From Injector, inches	Station Code	Axial Distance From Injector, inches
1	1.88	21	7.05	41	11.35	61	18.05
2	2.03	22	7.07	42	12.10	62	18.30
3	2.50	23	7.39	43	12.53	63	18.62
4	2.57	24	7.60	44	13.13	64	18.85
5	3.01	25	7.93	45	13.28	65	19.60
6	3.19	26	7.96	46	13.57	66	20.00
7	3.50	27	8.27	47	13.82	67	20.03
8	3.64	28	8.35	48	14.07	68	25.69
9	3.75	29	8.50	49	14.26	69	28.57
10	4.18	30	8.78	50	14.57	70	29.07
11	5.00	31	8.84	51	14.89	71	29.57
12	5.30	32	9.05	52	15.43	72	30.46
13	5.65	33	9.34	53	15.46	73	30.77
14	5.78	34	9.40	54	15.77	74	31.34
15	6.07	35	9.88	55	16.34	75	31.84
16	6.32	36	10.15	56	16.55	76	32.38
17	6.40	37	10.55	57	16.84	77	33.05
18	6.50	38	10.69	58	16.90	78	33.62
19	6.57	39	10.80	59	17.38		
20	6.76	40	11.12	60	17.85		

SUMMAR

1	2	3	4	5	6	7	8	9
No Usable Data	No Usable Data	No Usable Data	3/4.39	3/4.52	3/3.14	3/2.19	3/2.74	3/3.19
			9/4.63	9/4.93	9/3.99	9/2.23	9/3.18	9/3.45
			11/5.03	11/5.01	11/3.78	11/2.86	11/3.37	11/3.74
			38/3.46	38/3.26	38/2.82	38/2.87	38/2.89	38/2.81
			46/3.98	46/3.82	46/3.09	46/3.33	46/3.17	46/3.42
			48/3.50	48/3.27	48/3.21	48/2.31	48/2.65	48/3.46
			50/4.02	50/3.60	50/3.74	50/3.16	50/3.06	50/3.50
			53/4.27	53/3.82	53/3.59	53/2.09	53/2.47	53/3.03
			54/3.76	54/3.60	54/3.47	54/2.69	54/2.57	54/2.63
			55/4.57	55/3.51	55/3.78	55/1.85	55/2.14	55/2.54
			57/3.20	57/2.91	57/2.62	57/2.05	57/1.98	57/2.00
			59/3.20	59/2.85	59/2.42	59/1.48	59/1.67	59/2.05
			61/2.87	61/2.68	61/2.06	61/1.76	61/1.59	61/1.73
			63/2.79	63/2.54	63/2.36	63/1.45	63/1.40	63/1.89

*Table values are station code/heat flux; values of heat flux are in Btu/in.²-sec

TABLE VII

OF HEAT FLUX DATA*

TEST NUMBER										
10	11	12	13	14	15	16	17	18	19	20
No Usable Data	3/3.08	3/3.45	3/3.17	3/3.62	3/3.19	3/4.70	3/5.04	3/4.65	3/5.10	3/3.63
	9/2.64	9/2.93	9/2.51	9/3.26	9/2.91	9/5.06	9/5.46	9/5.12	9/5.62	9/4.44
	11/2.40	11/2.83	11/2.19	11/3.31	11/2.76	11/5.37	11/5.84	11/5.38	11/5.89	11/3.66
	38/2.65	38/3.64	38/2.96	38/3.75	38/2.82	38/5.61	38/4.95	38/5.12	38/4.65	38/4.15
	46/2.92	46/3.90	46/3.39	46/4.12	46/3.40	46/6.11	46/5.44	46/5.88	46/4.83	46/4.75
	48/3.15	48/3.96	48/3.32	48/4.07	48/3.40	48/5.75	48/4.79	48/5.36	48/4.22	48/4.32
	50/3.22	50/4.35	50/3.87	50/4.05	50/3.68	50/6.04	50/5.02	50/5.73	50/4.40	50/5.02
	53/3.15	53/4.02	53/3.82	53/3.75	53/3.52	53/5.76	53/4.67	53/5.39	53/4.18	53/4.98
	54/2.95	54/3.70	54/3.59	54/3.56	54/3.38	54/5.47	54/4.33	54/5.05	54/3.96	54/4.93
	55/2.63	55/3.11	55/3.07	55/3.02	55/3.01	55/5.07	55/4.05	55/4.43	54/4.22	55/4.16
	57/2.28	57/2.76	57/2.69	57/2.55	57/2.55	57/4.15	57/3.15	57/3.71	57/2.85	57/3.68
	59/1.98	59/2.21	59/2.23	59/2.11	59/2.22	59/3.67	59/3.02	59/3.45	59/2.79	59/3.22
	61/1.67	61/1.98	61/1.87	61/1.92	61/1.89	61/3.35	61/2.61	61/3.17	61/2.41	61/3.34
	63/1.49	63/1.62	63/1.79	63/1.64	63/1.89	63/3.24	63/2.61	63/2.94	63/2.33	63/2.90

TABLE VII
(Continued)

										TEST NUMBER
21	22	23	24	25	26	27	28	29	30	31
3/4.92	3/4.72	3/4.85	3/5.34	3/5.23	3/4.38	No Usable Data	3/4.94	3/4.98	3/3.70	3/5.08
9/5.24	9/5.18	9/5.46	9/5.78	9/5.53	9/4.85		9/5.24	9/5.49	9/4.29	9/5.37
11/5.10	11/5.48	11/5.80	11/6.11	11/5.54	11/5.11		11/5.35	11/5.71	11/4.55	11/5.76
38/3.24	38/5.57	38/6.04	38/5.20	38/3.87	38/5.12		38/5.33	38/5.54	38/3.87	38/5.32
46/3.49	46/5.41	46/6.16	46/5.38	46/4.04	46/5.60		46/5.86	46/6.15	46/4.30	46/6.32
48/3.32	48/5.21	48/6.13	48/5.15	48/4.08	48/5.76		48/5.22	48/6.05	48/4.07	48/5.90
50/3.36	50/5.20	50/5.72	50/4.82	50/4.04	50/5.36		50/5.01	50/5.66	50/4.64	50/5.23
53/3.28	53/4.23	53/4.97	53/4.12	53/3.66	53/5.49		53/4.43	53/4.94	53/5.41	53/4.92
54/3.20	54/4.17	54/4.96	54/4.05	54/3.87	54/4.90		54/4.74	54/4.52	54/4.89	54/4.32
55/3.01	55/3.51	55/4.08	55/3.26	55/3.06	55/4.83		55/4.05	55/3.88	55/4.59	55/3.85
57/2.30	57/3.24	57/3.73	57/2.96	57/2.80	57/3.93		57/3.70	57/3.32	57/4.02	57/3.22
59/2.23	59/2.62	59/3.00	59/2.44	59/2.33	59/3.80		59/3.27	59/2.96	59/3.62	59/2.90
61/1.95	61/2.53	61/3.06	61/2.47	61/2.33	61/3.40		61/2.96	61/2.67	61/3.47	61/2.70
63/2.01	63/2.12	63/2.60	63/2.44	63/2.05	63/3.44		63/3.05	63/2.58	63/3.15	63/2.52

*Table values are station code/heat flux; values of heat flux are in Btu/in.²-sec.

32	33	34	35	36	37	38	39	40
3/2.46	3/3.62	No Usable Data	3/2.55	3/2.04	3/2.92	3/2.35	3/1.96	3/3.88
9/2.81	9/4.02		9/2.27	9/1.84	9/3.03	9/2.38	9/1.70	9/3.82
11/2.98	11/4.40		11/2.90	11/1.58	11/3.13	11/2.60	11/1.45	11/4.98
38/3.37	38/4.40		38/2.68	38/1.80	38/3.43	38/2.36	38/1.39	38/5.30
46/4.14	46/5.06		46/2.56	46/2.31	46/3.51	46/2/30	46/2.19	46/5.15
48/3.69	48/5.06		48/2.65	48/1.93	48/3.33	48/2.46	48/1.84	48/4.99
50/3.49	50/2.41		50/2.75	50/1.97	50/3.34	50/2.63	50/2.03	50/5.22
53/2.99	53/2.20		53/2.62	53/1.99	53/3.30	53/2.55	53/2.03	53/4.98
54/2.61	54/2.93		54/2.44	54/2.04	54/2.87	54/2.41	54/2.02	54/4.74
55/2.26	55/2.58		55/2.19	55/1.96	55/2.42	55/2.15	55/1.97	55/4.49
57/1.83	57/3.68		57/1.93	57/1.63	57/2.12	57/1.92	57/1.62	57/3.70
59/1.65	59/3.47		59/2.00	59/1.65	59/1.78	59/1.63	59/1.66	59/3.42
61/1.40	61/4.50		61/1.43	61/1.29	61/0.89	61/1.39	61/1.30	61/3.10
63/1.31	63/4.47		63/1.28	63/1.50	63/0.44	63/1.26	63/1.48	63/2.94

41	42	43	44	45	46	47	48	49
3/3.83	3/4.03	3/3.60	3/3.94	3/3.79	3/5.53	3/4/25	3/3.44	3/5.13
9/4.52	9/4.02	9/3.81	9/4.04	9/3.95	9/4.92	9/4.24	9/3.46	9/4.51
11/5.00	11/5.35	11/3.96	11/3.68	11/3.83	11/4.40	11/4.02	11/4.29	11/4.15
38/5.14	38/5.43	38/3.45	38/2.96	38/3.25	38/3.27	38/3.13	38/4.61	38/2.73
46/5.34	46/5.44	46/3.54	46/3.04	46/3.17	46/3.42	46/3.42	46/4.88	46/3.10
48/5.35	48/5.63	48/3.33	48/2.74	48/3.03	48/3.37	48/3.14	48/4.72	48/3.30
50/5.50	50/5.45	50/3.30	50/2.71	50/2.88	50/3.02	50/3.01	50/4.87	50/2.86
53/5.37	53/5.29	53/2.77	53/1.97	53/2.47	53/2.58	53/2.21	53/4.78	53/2.53
54/5.23	54/5.13	54/2.67	54/1.95	54/2.28	54/2.25	54/2.20	54/4.52	54/2.26
55/4.79	55/4.76	55/2.15	55/1.46	55/1.89	55/1.87	55/1.65	55/4.20	55/2.02
57/4.05	57/3.81	57/1.85	57/1.25	57/1.51	57/1.48	57/1.52	57/3.51	57/1.65
59/3.68	59/3.55	59/1.54	59/0.96	59/1.33	59/1.44	59/1.08	59/3.22	59/1.51
61/3.45	61/3.34	61/1.53	61/0.94	61/1.18	61/1.14	61/1.07	61/2.97	61/1.38
63/3.13	63/3.03	63/1.33	63/0.79	63/1.10	63/1.29	63/0.86	63/2.81	63/1.42

*Table values are station code/heat flux; values of heat flux are in Btu/in.²-sec.

TABLE VII

(Continued)

TEST NUMBER										
50	51	52	53	54	55	56	57	58	59	60
No Usable Data	3/5.79	3/5.75	No Usable Data	No Usable Data	No Usable Data	No Usable Data	No Usable Data	No Usable Data	No Usable Data	3/4.81
	9/5.38	9/5.41								9/5.21
	11/6.73	11/6.53								11/5.31
	38/5.75	38/5.60								38/5.14
	46/5.00	46/5.15								46/5.15
	48/5.26	48/5.63								48/5.56
	50/5.93	50/6.28								50/6.49
	53/6.17	53/6.75								53/6.64
	54/6.06	54/6.50								54/6.67
	55/5.15	55/5.67								55/5.41
	57/4.46	57/4.90								57/5.13
	59/3.89	59/4.36								59/4.10
	61/3.66	61/4.05								61/4.19
	63/3.26	63/3.66								63/4.19

TABLE VII
(Continued)

										TEST NUMBER
61	62	63	64	65	66	67	68	69	70	71
No Usable Data	3/4.86	3/4.06	3/3.59	3/3.06	No Usable Data	No Usable Data	3/3.38	3/3.64	3/3.17	3/3.17
	9/5.15	9/4.75	9/3.96	9/3.33			9/3.99	9/3.99	9/4.08	9/4.08
	11/5.26	11/4.62	11/4.08	11/3.43			11/3.92	11/4.08	11/3.38	11/4.08
	38/4.93	38/4.70	38/4.04	38/3.36			38/4.23	38/4.84	38/3.94	38/4.08
	46/6.17	46/5.95	46/4.82	46/3.82			46/4.48	46/4.97	46/4.20	46/4.08
	48/6.02	48/6.27	48/5.34	48/4.72			48/4.32	48/4.95	48/4.10	48/4.08
	50/6.25	50/5.77	50/4.71	50/3.95			50/4.16	50/4.89	50/4.01	50/4.08
	53/6.67	53/6.27	53/4.18	53/3.19			53/3.89	53/3.90	53/3.70	53/4.08
	54/6.81	54/5.98	54/3.83	54/2.83			54/3.44	54/3.83	54/3.17	54/3.08
	55/5.81	55/5.59	55/3.64	55/2.53			55/3.18	55/3.21	55/3.08	55/3.08
	57/5.11	57/4.69	57/2.87	57/2.04			57/2.59	57/2.76	57/2.24	57/2.08
	59/4.49	59/4.28	59/2.81	59/1.88			59/2.42	59/2.48	59/2.39	59/2.08
	61/4.31	61/3.91	61/2.53	61/1.72			61/2.11	61/2.39	61/1.89	61/1.08
	63/3.90	63/3.77	63/2.49	63/1.72			63/2.11	63/2.39	63/2.28	63/1.08

*Table values are station code/heat flux; values of heat flux are in Btu/in.²-sec.

	72	73	74	75	76	77	78	79	80
45	3/3.57	No Usable Data	3/2.80	3/2.87	3/2.88	3/2.78	3/2.84	3/3.46	3/1.62
17	9/3.87		9/2.83	9/2.97	9/2.95	9/3.22	9/2.90	9/3.85	9/1.58
12	11/4.14		11/3.21	11/3.21	11/3.27	11/3.32	11/3.39	11/4.23	11/1.84
52	38/4.62		38/3.79	38/3.23	38/3.55	38/3.37	38/3.76	38/4.74	38/2.04
42	46/4.95		46/4.23	46/4.25	46/4.54	46/4.39	46/4.87	46/6.36	46/2.31
28	48/4.76		48/4.91	48/3.88	48/4.54	48/3.98	48/4.12	48/5.33	48/2.61
14	50/4.58		50/3.94	50/4.16	50/4.20	50/4.08	50/4.53	50/6.02	50/2.16
11	53/4.12		53/3.82	53/3.71	53/3.30	53/3.24	53/3.32	53/4.55	53/1.93
44	54/3.64		54/3.13	54/3.45	54/3.18	54/3.18	54/3.41	54/5.34	54/1.68
25	55/3.19		55/2.95	55/2.90	55/2.55	55/2.59	55/2.56	55/3.81	55/1.54
46	57/2.63		57/2.19	57/2.32	57/2.25	57/2.35	57/2.36	57/4.13	57/1.18
34	59/2.42		59/2.10	59/2.01	59/1.82	59/1.83	59/1.80	59/2.83	59/1.09
82	61/2.04		61/1.61	61/1.70	61/2.01	61/1.81	61/1.83	61/3.55	61/0.85
97	63/2.26		63/1.78	63/1.67	63/1.61	63/1.51	63/1.44	63/2.47	63/0.86

81	82	83	84	85	86	87	88	89	
38/1.80	3/2.71	3/2.88	3/3.32	3/3.31	3/0.29	3/2.17	3/1.87	3/2.29	
46/2.37	18/2.47	18/2.75	18/3.29	18/2.84	11/3.10	11/2.86	11/2.43	11/3.06	1
48/4.36	44/2.77	44/3.64	44/3.93	44/3.17	29/2.15	29/3.10	29/2.68	29/3.47	2
50/2.81	66/2.60	66/3.24	66/3.35	66/3.63	45/3.37	45/4.87	45/4.48	45/4.64	4
53/2.44	68/2.71	68/2.81	68/2.72	68/4.24	47/3.81	47/3.55	47/4.32	47/4.22	4
54/2.17	69/3.79	69/3.72	69/3.46	69/4.51	49/4.43	49/4.78	49/4.41	49/4.79	4
55/1.79	70/3.60	70/3.44	70/3.32	70/4.53	51/4.12	51/4.12	51/3.67	51/4.16	5
57/0.95	71/3.29	71/3.25	71/3.13	71/4.11	52/6.44	52/4.57	52/4.54	52/4.86	5
59/0.66	72/2.84	72/2.70	72/2.69	72/3.51	56/6.04	56/4.37	56/4.89	56/4.49	5
61/0.99	73/2.57	73/2.42	73/2.37	73/3.07	58/5.39	58/3.38	58/3.48	58/4.18	5
63/0.62	74/2.10	74/2.17	74/2.17	74/2.70	60/4.92	60/3.74	60/3.87	60/3.55	6
	75/1.92	75/1.72	75/1.75	75/2.13	62/4.45	62/2.33	62/2.49	62/3.11	6
	76/1.52	76/1.65	76/1.76	76/1.86	64/2.13	64/2.53	64/2.65	64/2.60	6
	77/1.52	77/1.49	77/1.70	77/1.57	65/3.35	65/2.20	65/2.24	65/2.78	6
	78/1.49	78/1.63	78/1.84	78/1.54	67/1.26	67/2.12	67/2.18	67/2.36	6

*Table values are station code/heat flux; values of heat flux are in Btu/in.²-sec.

TABLE VII
(Continued)

TEST NUMBER										
90	91	92	93	94	95	96	97	98	99	100
/2.22	No Usable Data	6/2.89	6/3.13	6/3.03	6/2.97	1/7.32	1/7.62	1/3.32	1/8.81	1/3.30
/2.92		15/3.76	15/3.85	15/4.19	15/3.87	14/4.64	14/4.95	14/3.70	14/6.30	14/3.10
/3.80		19/3.18	19/3.67	19/3.42	19/3.46	16/4.41	16/5.03	16/4.16	16/6.19	16/2.62
/4.95		22/3.82	22/3.98	22/4.27	22/3.81	20/4.59	20/5.43	20/4.11	20/6.68	20/3.35
/4.68		26/2.84	26/3.52	26/3.31	26/2.97	23/5.35	23/5.93	23/4.67	23/7.15	23/3.60
/5.11		27/3.20	27/3.62	27/3.79	27/3.34	25/5.37	25/5.63	25/4.73	25/6.93	25/4.14
/4.57		31/2.44	31/3.03	31/2.85	31/2.45	32/4.84	32/5.76	32/4.64	32/6.47	32/4.35
/4.94		33/2.60	33/2.73	33/2.84	33/2.55	34/4.38	34/4.91	34/4.09	34/5.65	34/3.82
/5.23		35/1.81	35/2.35	35/2.13	35/1.80	36/4.08	36/4.98	36/3.41	36/5.32	36/3.30
/3.58		37/2.14	37/2.39	37/2.45	37/2.06	39/3.80	39/3.98	39/2.65	39/4.18	39/2.52
/3.87		40/1.61	40/2.20	40/1.95	40/1.54	41/3.99	41/4.43	41/2.50	41/4.31	41/2.41
/2.66						42/3.84	42/4.00	42/2.07	42/3.52	42/1.97
/2.60						43/3.97	43/4.00	43/2.23	43/3.72	43/2.19
/2.49										
/2.27										

TABLE VII
(Concluded)

TEST NUMBER										
101	102	103	104	105	106	107	108	109	110	111
2/6.63	2/2.89	2/7.18	2/3.21	2/2.98	3/2.51	3/2.83	3/2.77	3/2.79	No Usable Data	No Usable Data
4/5.65	4/2.31	4/7.24	4/3.00	4/2.84	7/2.39	7/2.68	7/2.63	7/2.55		
5/5.65	5/3.49	5/7.38	5/3.65	5/2.92	11/2.92	11/3.43	11/3.27	11/3.15		
8/6.58	8/4.39	8/7.70	8/5.09	8/5.45	38/2.99	38/3.11	38/3.07	38/2.79		
10/6.16	10/5.91	10/7.71	10/5.99	10/5.36	46/3.49	46/3.68	46/3.68	46/2.91		
12/6.60	12/6.83	12/6.88	12/6.87	12/7.76	48/2.82	48/2.09	48/3.50	48/2.77		
13/5.15	13/6.71	13/6.08	13/6.50	13/7.54	50/3.45	50/3.73	50/3.34	50/2.66		
17/5.19	17/6.00	17/5.42	17/4.36		53/2.54	53/2.67	53/2.94	53/2.34		
21/4.65	21/5.30	21/4.43	21/4.90	21/5.90	54/2.63	54/2.70	54/2.69	54/2.04		
24/4.90	24/4.70	24/4.27	24/5.06	24/3.43	55/2.19	55/2.26	55/2.50	55/1.98		
28/4.56	28/4.68	28/3.91	28/4.34	28/5.51	57/2.01	57/2.06	57/2.07	57/1.62		
30/4.34	30/4.00	30/3.59	30/4.38	30/2.54	59/1.74	59/1.76	59/2.03	59/1.55		
					61/1.75	61/1.82	61/1.91	61/1.36		
					63/2.99	63/2.94	63/3.39	63/2.57		

*Table values are station code/heat flux; values of heat flux are in Btu/in.²-sec.

112	113	114	115	116	117	118	119	120-125
3/1.91	3/1.93	3/1.54	No Usable Data	No Usable Data	No Usable Data	No Usable Data	No Usable Data	No Usable Data
7/1.77	7/1.84	7/1.83						
11/1.78	11/2.16	11/1.77						
38/2.51	38/4.26	38/2.41						
46/4.43	46/5.26	46/3.62						
48/3.81	48/5.04	48/3.26						
50/3.17	50/3.91	50/3.05						
53/4.56	53/4.77	53/3.63						
54/4.23	54/4.61	54/3.19						
55/4.13	55/4.08	55/3.29						
57/3.58	57/3.66	57/2.67	No Usable Data	No Usable Data	No Usable Data	No Usable Data	No Usable Data	No Usable Data
59/3.28	59/3.06	59/2.74						
61/2.91	61/2.90	61/2.17						
63/3.66	63/4.56	63/2.42						

Run No.	Injector Identification Number	No Sim Ch Pre p
1	LD-1	
2	↓	
3		
4	LD-2	
5	↓	
6		
7	LD-3	
8	↓	
9		
10		
11	↓	
12	LD-3M	
13	↓	
14		
15	P-1	
16	↓	
17		
18		
19	↓	
20	P-2	
21	↓	
22		
23	↓	

TABLE VIII

SUMMARY OF COLD-FLOW DATA

Initial diluted number pressure, psia	Actual Cold-Flow Mixture Ratio, $\dot{w}_{\text{tric}}/\dot{w}_{\text{H}_2\text{O}}$	Simulated Mixture Ratio		$E_m, \%$	η_{c*} , distribution		K
		FLOX (80% F_2)	FLOX (70% F_2)		FLOX (80% F_2)	FLOX (70% F_2)	
00	2.09	3.78	3.68	90.24	99.27	98.61	N/A
	2.60	4.71	4.58	93.38	98.32	98.88	
	3.20	4.79	5.63	94.81	98.38	99.10	
	2.12	3.83	3.73	87.25	98.33	96.85	
	2.83	5.12	4.98	88.21	95.53	96.97	
	3.41	6.17	6.00	89.11	95.66	96.86	
	3.07	5.55	5.40	97.16	98.64	99.46	
	2.76	5.00	4.86	95.26	98.67	99.40	
	2.01	3.64	3.54	94.06	99.64	99.36	
50	3.00	5.43	5.28	96.91	98.16	98.95	
50	2.58	4.67	4.54	96.17	99.16	99.27	0.89
	2.74	4.97	4.83	93.03	97.36	98.12	
	2.63	4.76	4.63	94.27	98.35	98.83	
00	2.52	4.57	4.44	95.92	98.94	98.72	
	2.72	3.66	3.61	90.44	99.33	98.01	
	3.78	5.09	5.02	95.55	98.36	99.39	
	5.00	6.73	6.64	95.71	97.69	98.36	
	5.83	7.85	7.74	94.03	98.29	98.19	
	4.28	5.76	5.69	95.95	98.42	99.00	
	2.26	3.04	3.00	89.94	99.89	99.59	
	3.82	5.15	5.07	95.73	98.33	99.24	1.72
	5.18	6.97	6.86	92.72	97.45	98.17	
50	3.67	4.94	4.87	97.27	98.87	99.53	3.01
							4.09
							2.20
							0.91
							2.59
							4.76
							2.39

TABLE 1A

COMPARISON OF COMBUSTION STABILITY OF PENTAD AND LIKE DOUBLET INJECTORS

Run No. (1)	Injector Employed	Stagnation Chamber Pressure, psia	Mixture Ratio, \dot{w}_{ox}/\dot{w}_f	Injector ΔP , psi		Index of Stability
						Nominal Peak-to-Peak ⁽²⁾ Chamber Pressure Oscillation as Percentage of P_c
				Oxidizer	Fuel	
16	P-1	100.7	5.18	197	237	<10
23	P-2	102.4	5.32	183	127	<10
33	↓	77.3	5.23	107	70	20
32	↓	48.6	4.76	50	33	30 (U)
51	P-2-M1	150.6	5.38	131	102	10
42	↓	100.1	5.58	61	46	25
46	↓	67.8	5.54	54	43	200 (U)
61	P-2-M2	175.0	5.33	77	61	200 (U)
62	↓	175.8	5.57	74	60	30 (U)
63	↓	151.9	5.00	53	51	30 (U)
64	↓	101.2	5.50	30	26	30 (U)
65	↓	71.8	5.19	21	19	30 (U)
79	LD-3	153.5	5.23	200	224	<10
77	↓	100.5	5.33	86	100	<10
81	↓	48.8	5.60	24	25	<10
118	LD-3-M	151.3	4.99	64	71	<10
120	↓	100.9	5.24	31	31	<10
121	↓	47.2	6.06	9	8	(marginal)*

(1) Runs 62 through 65 were conducted with the acoustic absorber in the chamber

(2) U-denoted tests considered sufficiently unstable that meaningful performance data were not obtained

*Intermittent bursts of high-frequency, high-amplitude pressure oscillations occurred

TABLE X

PREDICTED FUEL DROPSIZE VARIATION AS A
 FUNCTION OF INJECTOR DESIGN AND
 OPERATING CONDITIONS
 (MR = 5.33; FLOX-80% F₂)

Injector Number	Nominal Chamber Pressure, psia	Contraction Area Ratio	Fuel Injection Velocity, ft/sec	Fuel Orifice Diameter, inch	Predicted Mean Fuel Dropsizes* (D ₃₀), μ
LD-1	100	2:1	122	0.0200	75
LD-2	100	↓	122	↓	75
LD-3	50	↓	61	↓	86
↓	100	↓	122	↓	75
↓	150	↓	183	↓	72
↓	200	4:1	122	↓	107
LD-3M	50	2:1	108	0.0260	98
↓	100	↓	72	↓	83
↓	150	↓	36	↓	78

V_g determined using L = 30 inches, P_c = 100 psia, ε_c = 2:1 data in conjunction with modified Ingebo equation, vaporization rate limited combustion model, and distribution data.

TABLE XI

PREDICTED AND ACTUAL PERFORMANCE AT OPTIMUM MIXTURE RATIO FOR FLOX/LPG PROPELLANTS
AS A FUNCTION OF INJECTOR AND THRUST CHAMBER DESIGN AND OPERATING CONDITIONS

Injector Number	Propellant Combination (Oxidizer)	Nominal Chamber Pressure, psia	Contraction Area Ratio	L*, inch	D ₃₀ (see Table X)	Measured E _m , %	$\eta_{c*,dist}$	$\eta_{c*,vap}$ (Fig. 31)	$\eta_{c*,pred}^*$	$\eta_{c*,act}$
LD-1	FLOX (80% F ₂)	100	2:1	30	75	94.3	98.2	97.5	95.7	95.5
LD-2				30		88.5	95.6	97.5	93.2	93.3
LD-3				15		96.1	98.7	92.8	91.6	89.8
				30				97.5	96.2	96.3
				60				99.5	98.2	98.1
		200	4:1	30	107			93.2	92.0	93.1
		200	4:1	60	107			97.7	96.4	96.8
		50	2:1	30	86	96.9	98.2	96.2	94.5	95.2
		150		30	72	96.2	99.2	97.9	97.1	97.8
	FLOX (70% F ₂)	100			74	94.3	99.4	97.6	97.0	97.3
	LF ₂	100			79	94.1	99.4	97.1	96.5	97.0
LD-3M	FLOX (80% F ₂)	50			98	93.0	97.4	94.4	91.9	93.2
		100			83	94.3	98.4	96.9	95.0	95.4
		150			78	95.9	98.9	97.2	96.1	96.4
		100		15	83	94.3	98.4	90.6	89.2	88.9
		150		15	78	95.9	98.9	92.0	91.0	90.3

$$* \eta_{c*,pred} = \eta_{c*,dist} \times \eta_{c*,vap}$$

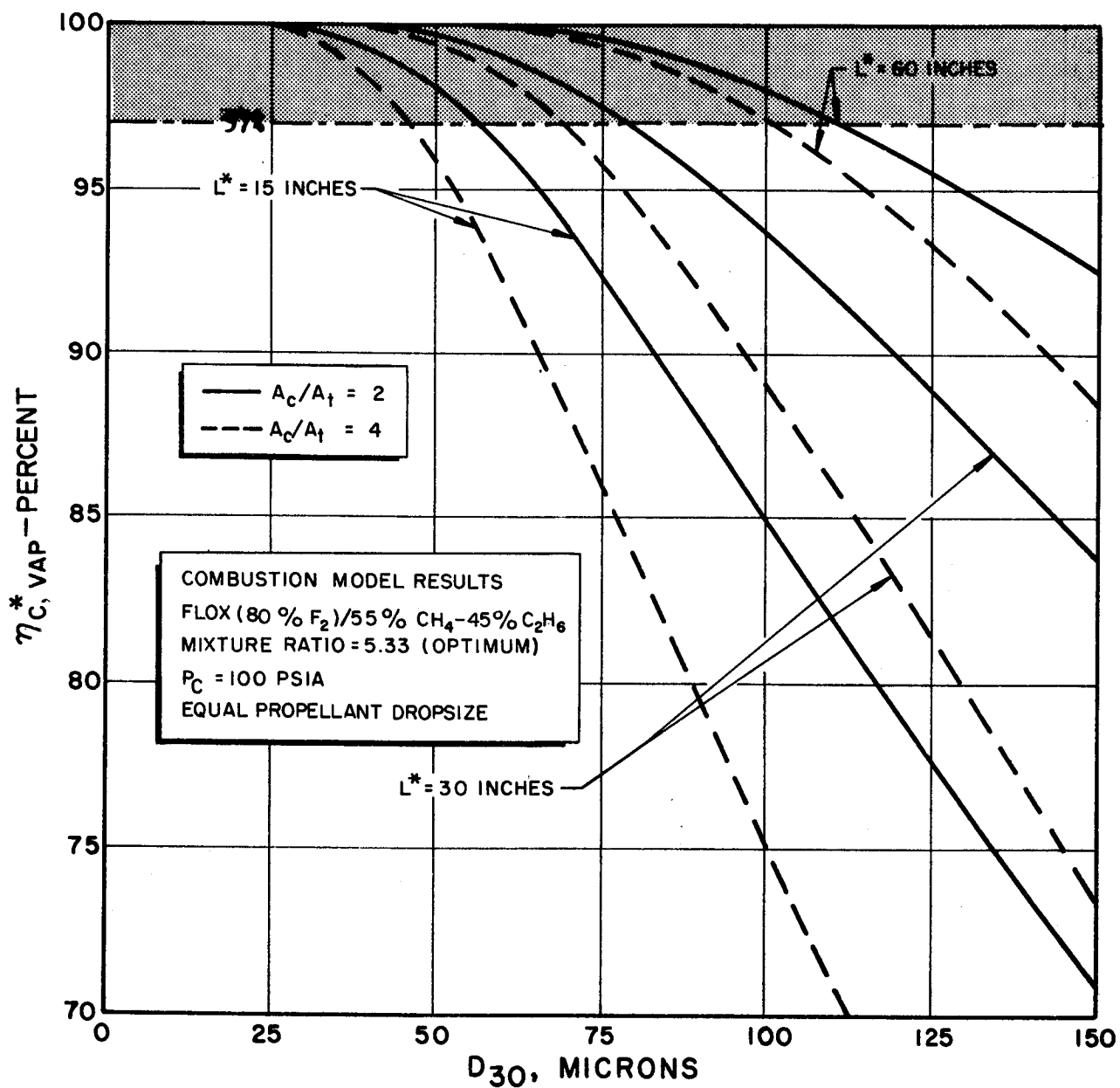


Figure 1. The Effect of Dropsize on Characteristic Velocity Efficiency (due to vaporization) for Various Chamber Geometries

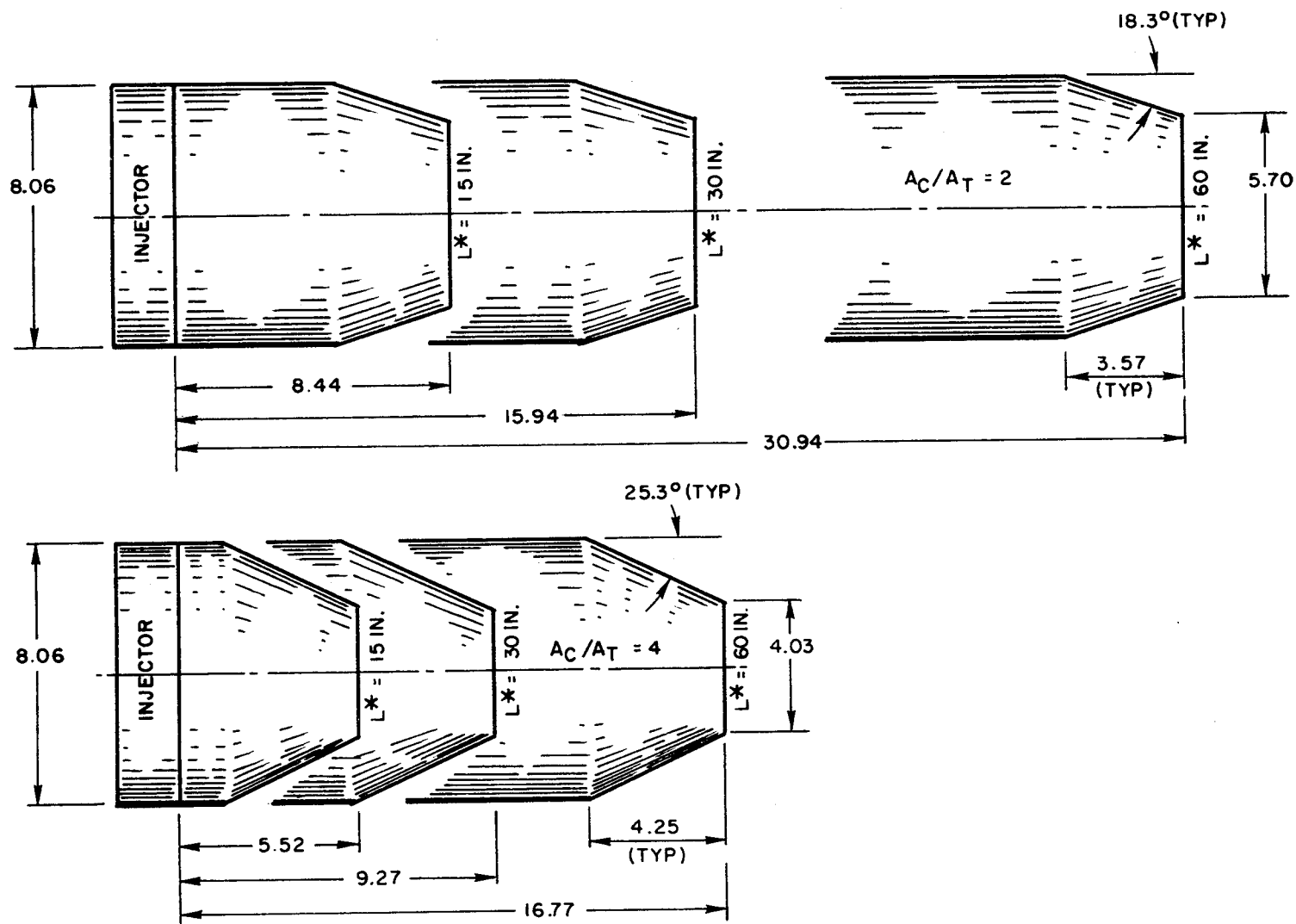


Figure 2. Simplified Schematics of Thrust Chamber Geometries Considered for Combustion Model Analysis (similar to actual design geometries for hot-fire experiments)

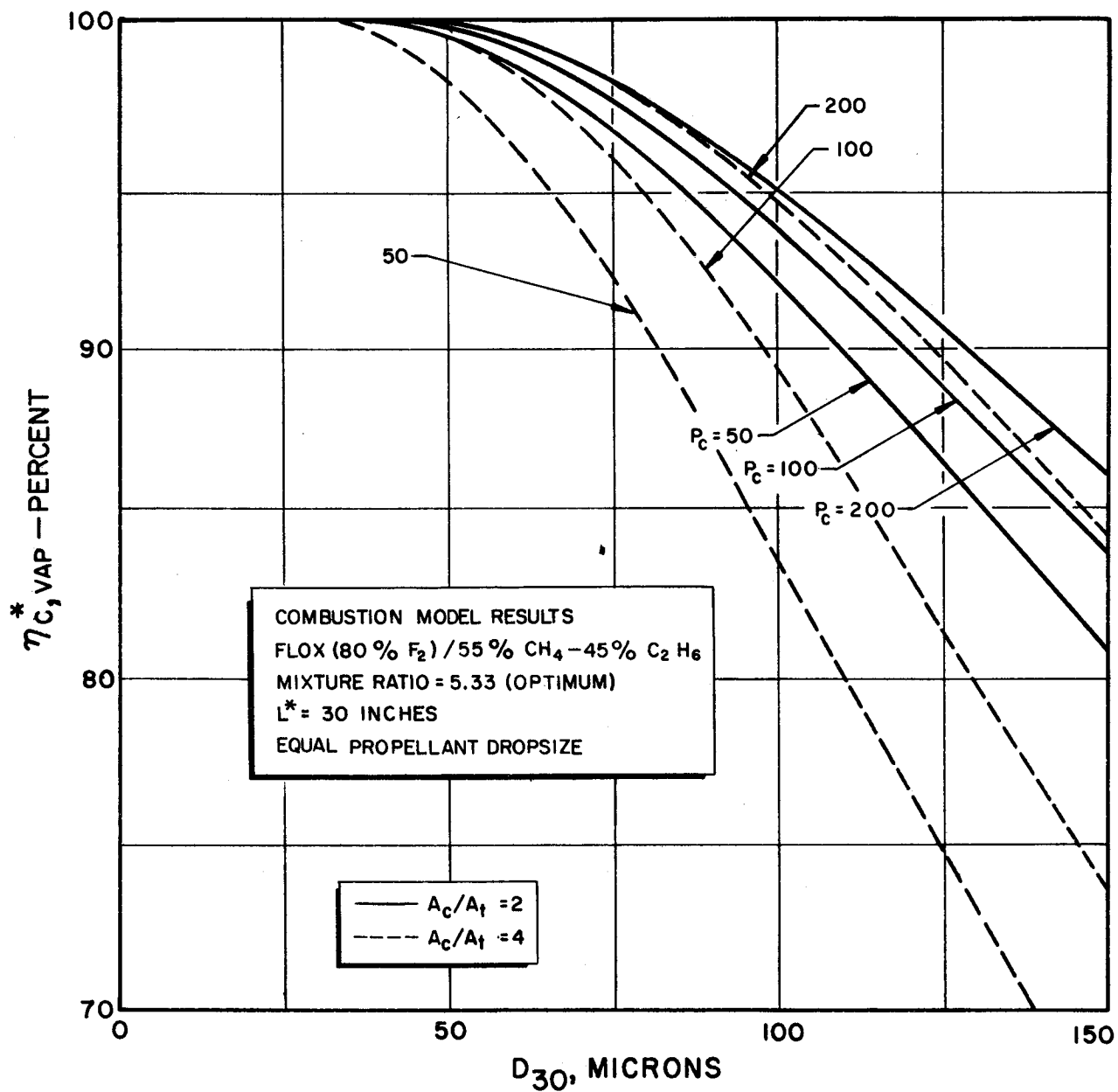


Figure 3. The Effect of Dropsizes on Characteristic Velocity Efficiency (due to vaporization) for Various Chamber Pressures. The Effect of Chamber Contraction Area Ratio is Also Shown.

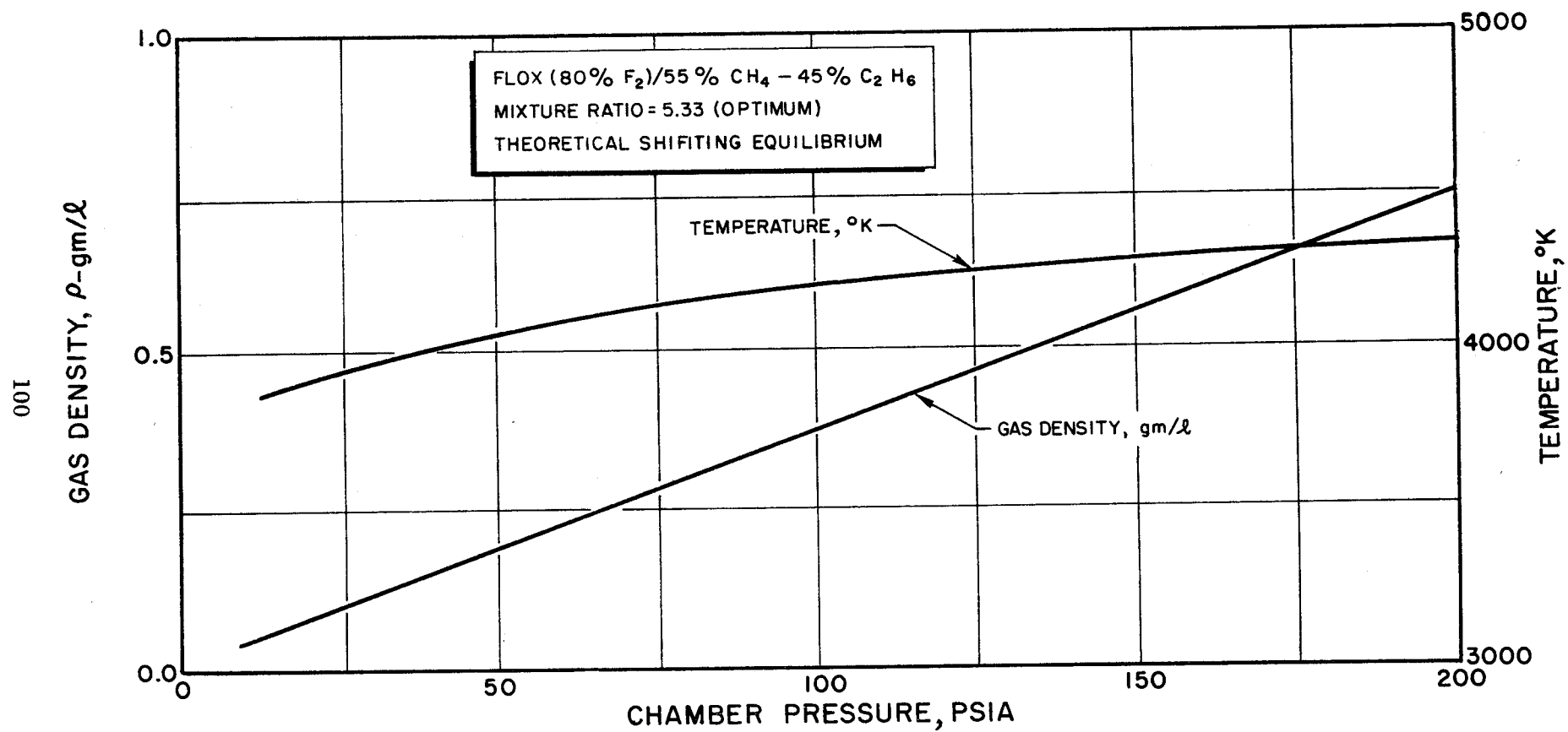


Figure 4. Effect of Chamber Pressure on Combustion Gas Property Variation

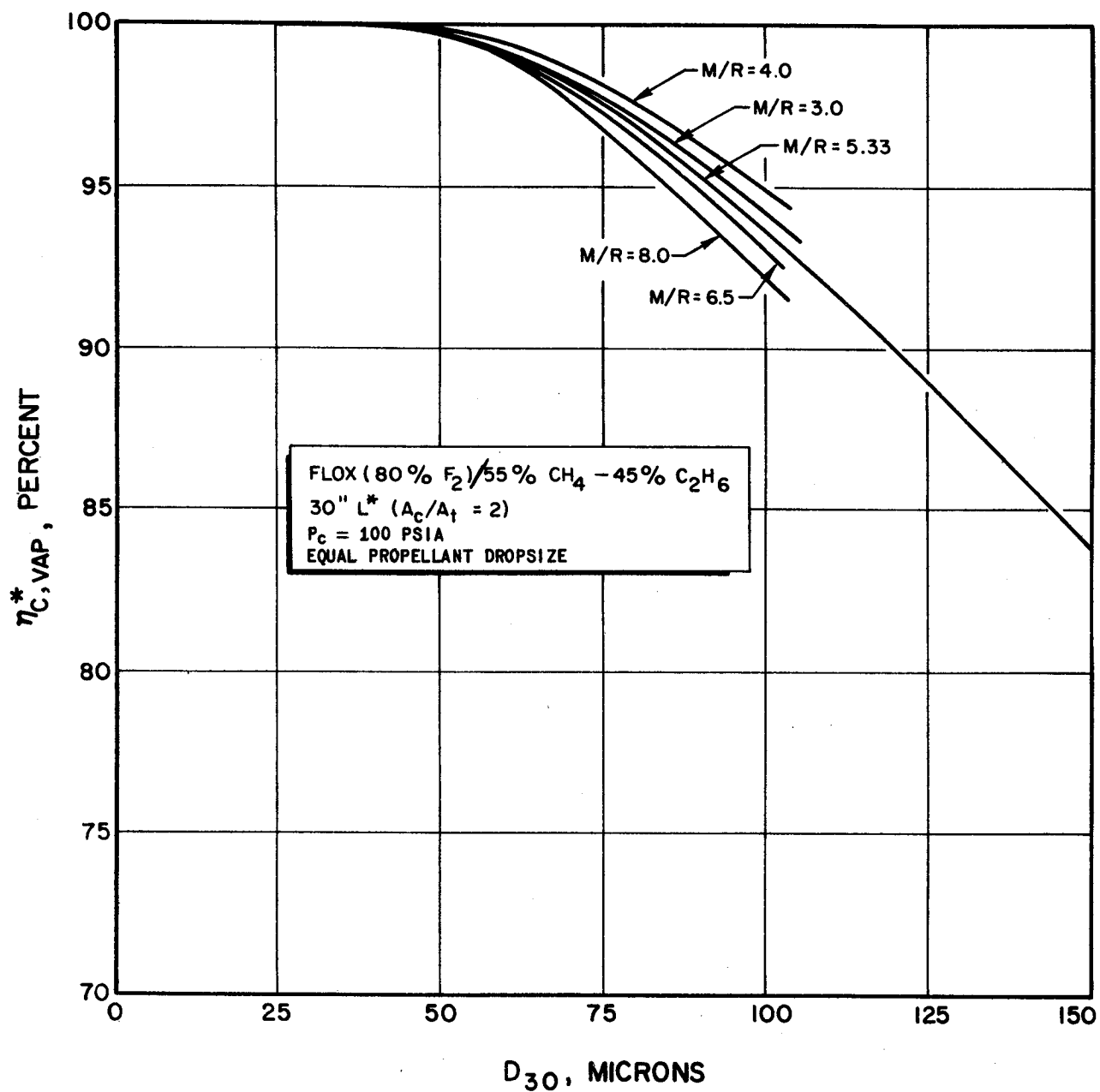


Figure 5. Effect of Propellant Drop size on c^* Efficiency (Due to Vaporization) for Various Injected Mixture Ratios

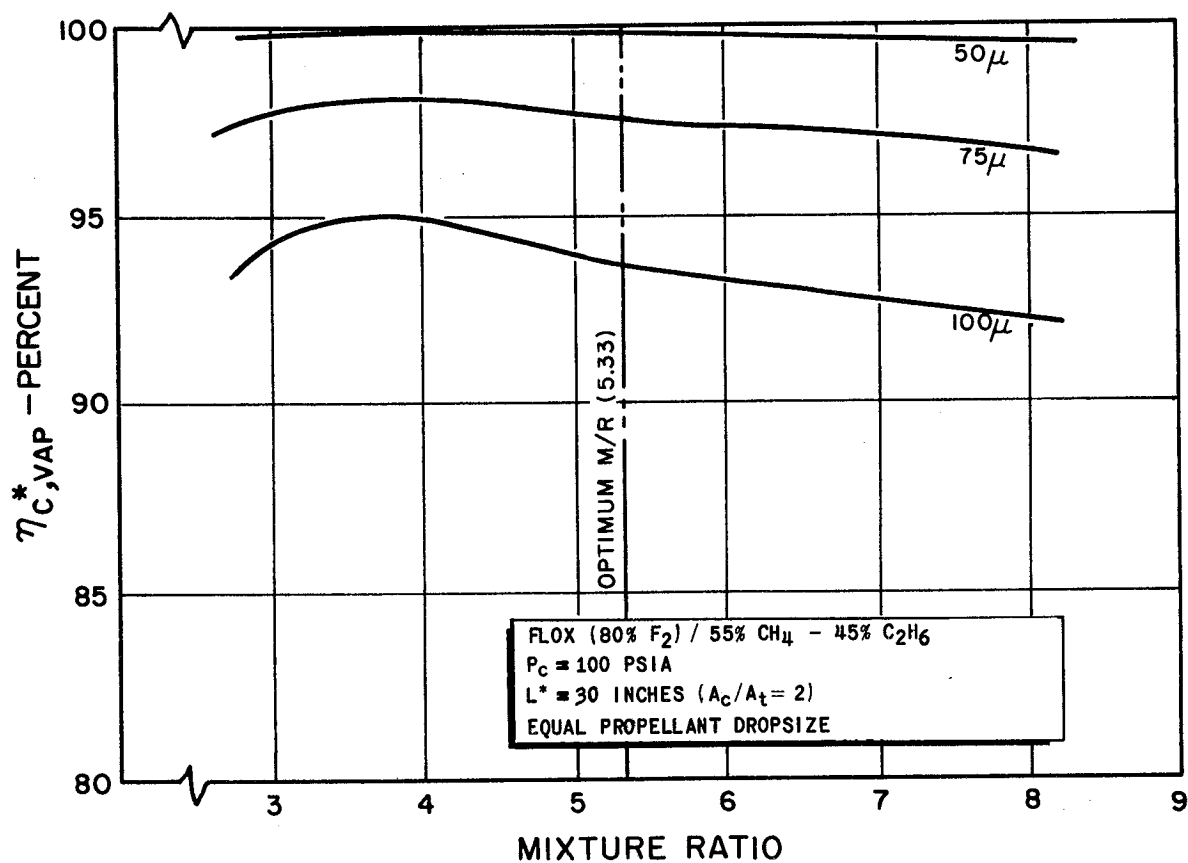


Figure 6. The Effect of Mixture Ratio on Characteristic Velocity Efficiency (due to vaporization) for Various Initial Propellant Drop Sizes

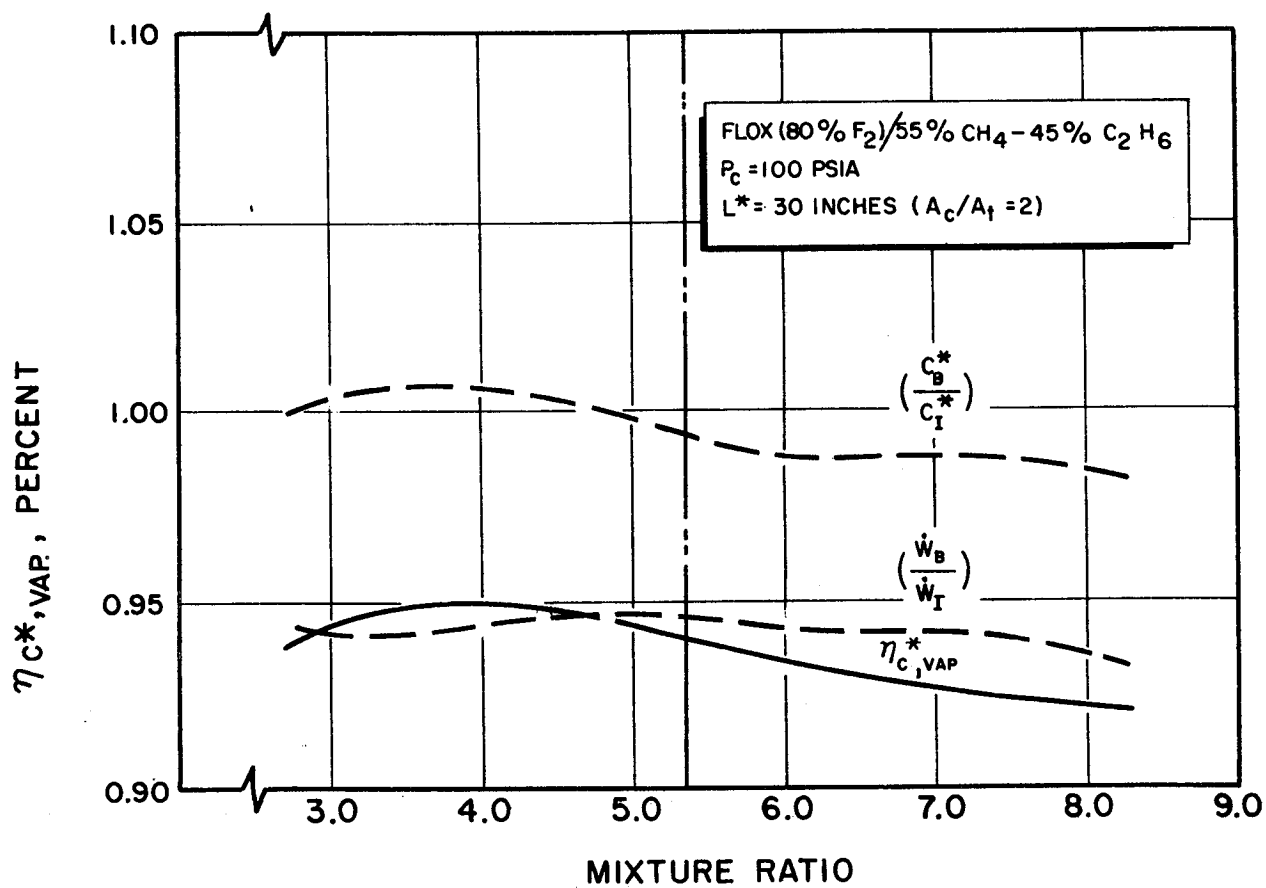


Figure 7. Effect of Mixture Ratio on c^* Efficiency (Due to Propellant Vaporization) for Initial Equal Propellant Dropsize of 100 Microns

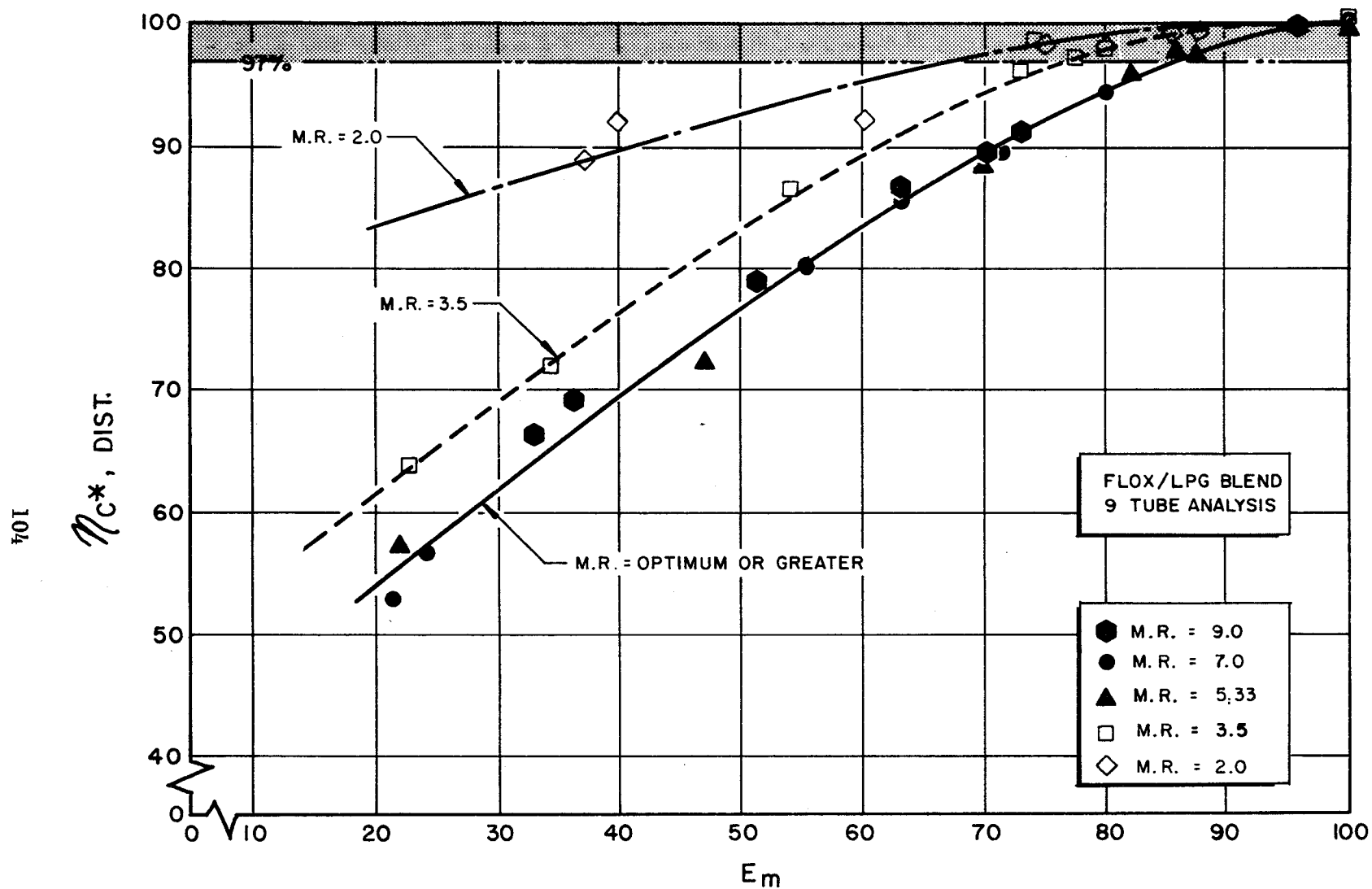
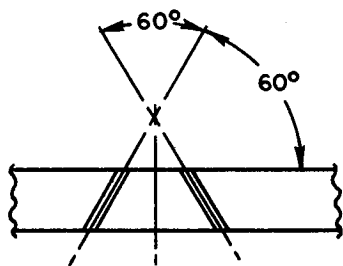
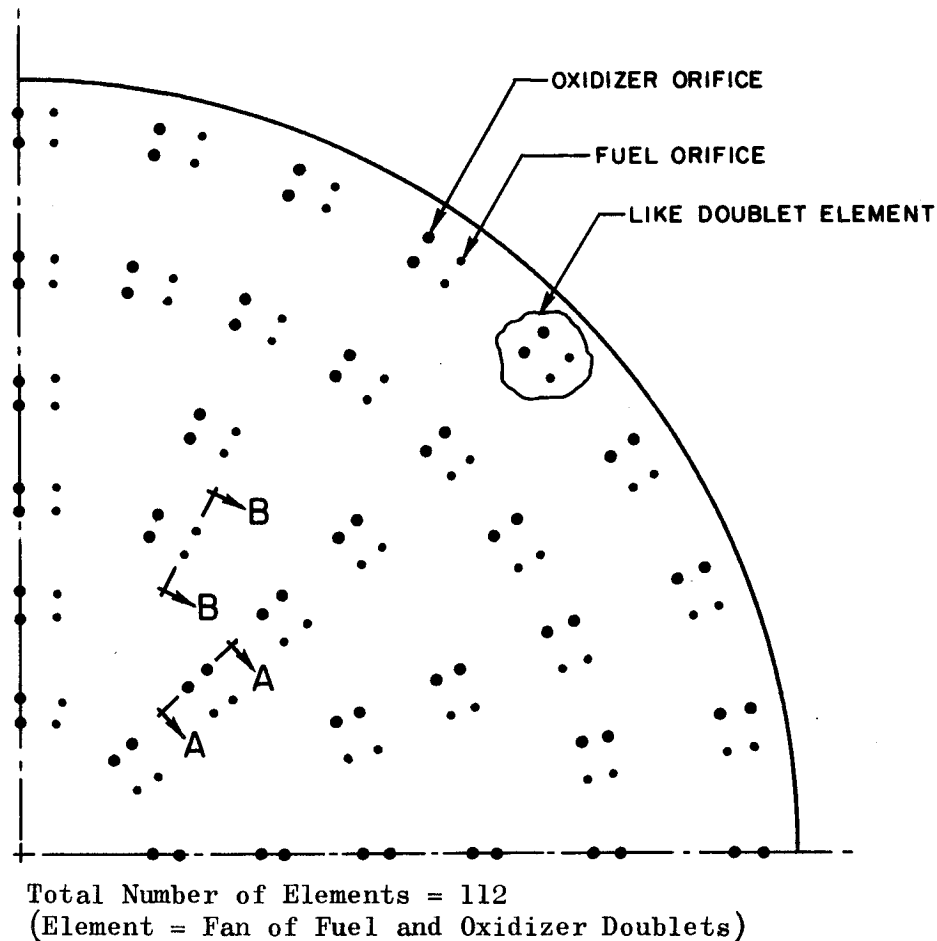


Figure 8. Predicted Effect of Nonuniform Distribution on Performance for Several Mixture Ratios. FLOX (80 Percent Fluorine)/55 Percent Methane-45 Percent Ethane LPG Blend Propellant Combination (assuming 100 percent c^* efficiency for each tube and no intertube mixing)



SECTION A-A OR B-B

Typical for Five Inner Rings
of Elements
(Outer Ring of Elements is Canted
15 Degrees Toward Axial Centerline of Injector)

Figure 9. Schematic Representation of Injector Face Pattern for Typical Like-Doublet Injector (Differences Between Specific Injectors are Noted in Table I ; Design Variables are Illustrated in Fig. 10). Quarter Segment of Symmetrical Pattern Shown

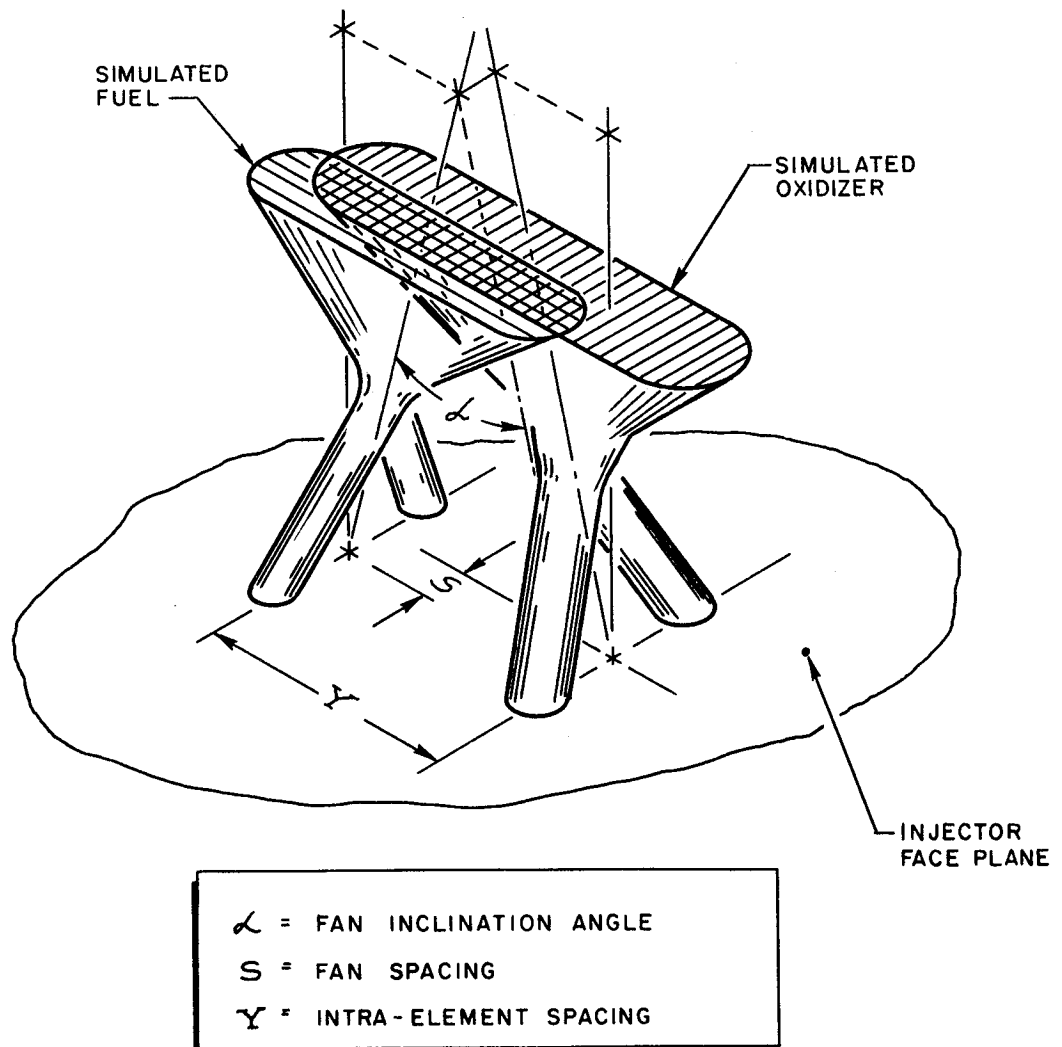


Figure 10. Geometric Factors Affecting Propellant Distribution for Like-Doublet Injector Elements

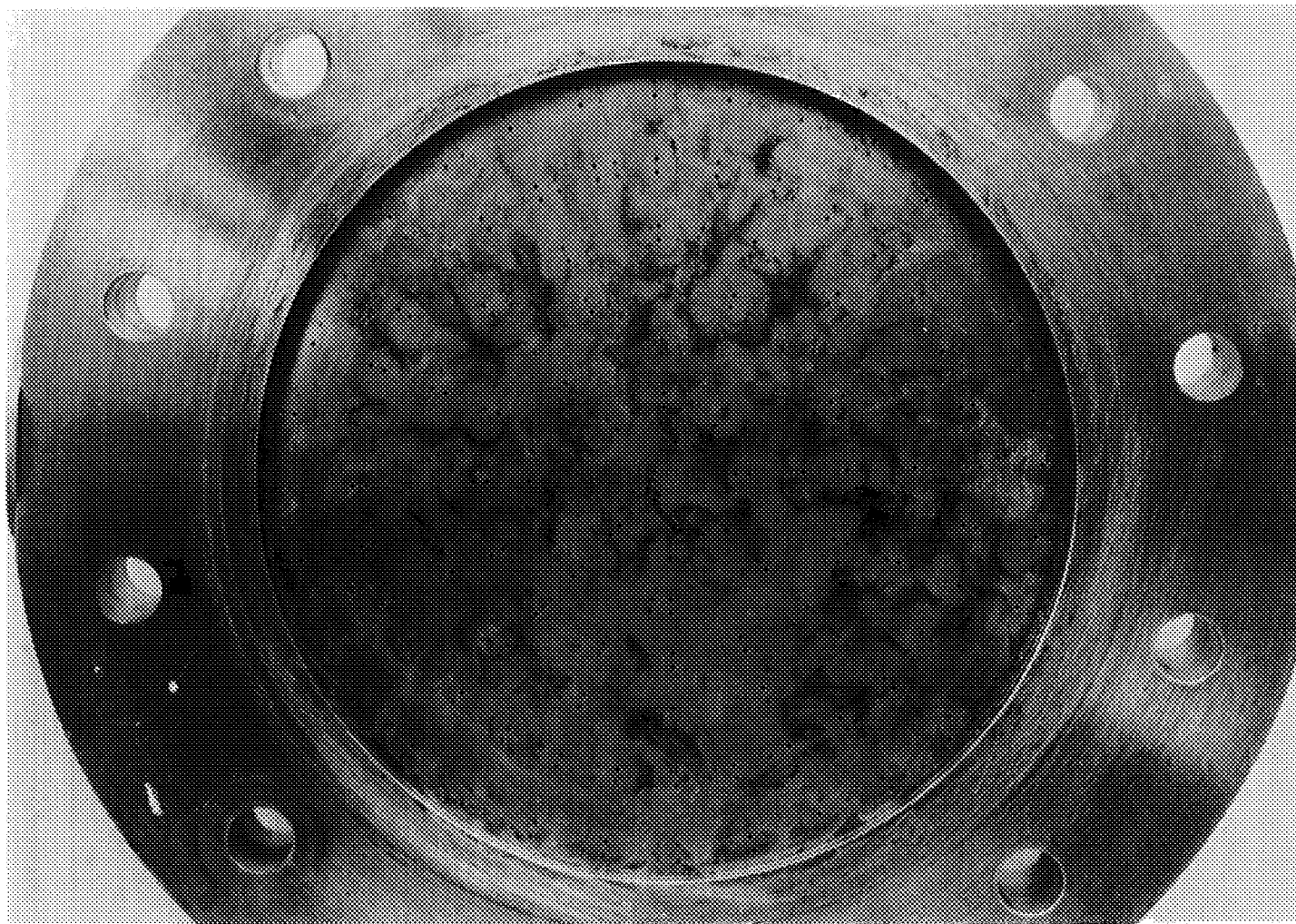
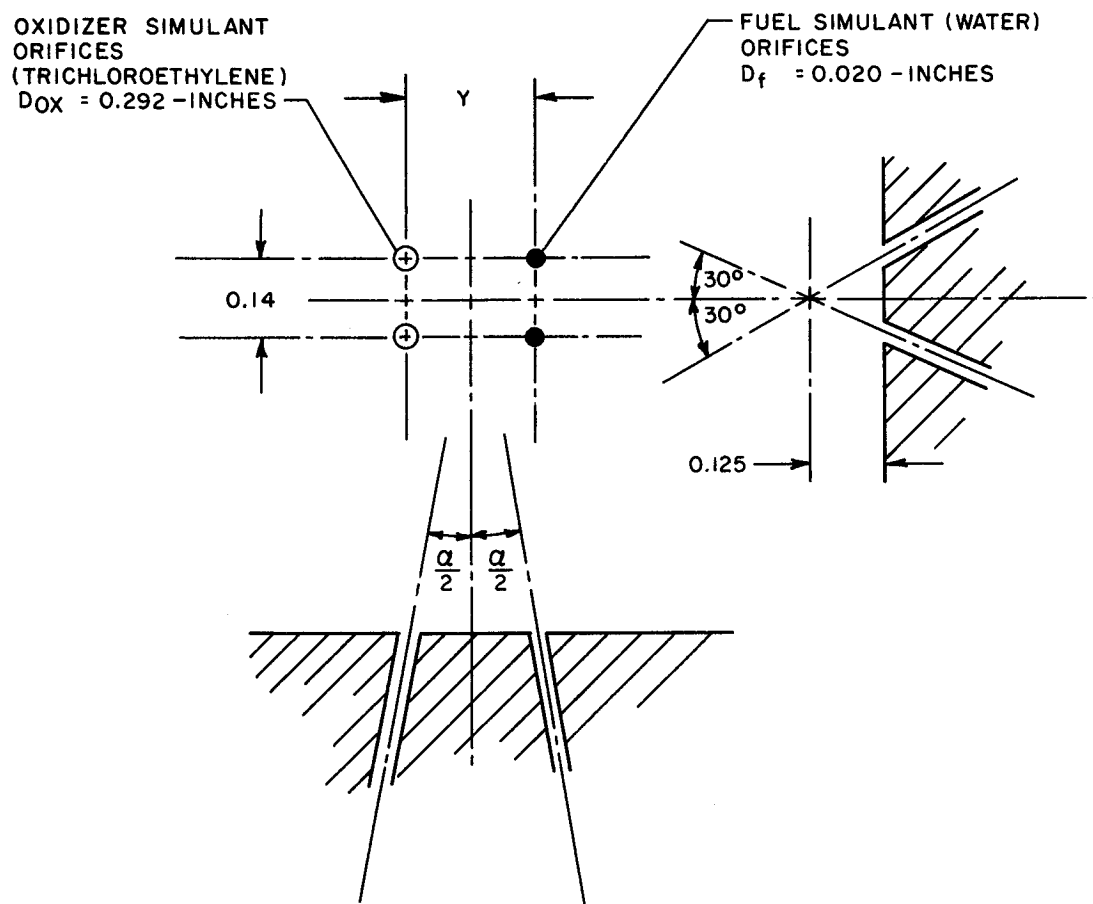


Figure 11. Face View of Like Doublet Injector No. LD-1-M Showing Orifice Pattern. Large Orifices, Oxidizer; Small Orifices, Fuel. (Photo taken after experimental evaluation.)



FAN SPACING AND IMPINGEMENT ANGLE ARE ZERO

$Y = \text{INTRA-ELEMENT SPACING}$
 $(0.20\text{-INCHES} \leq Y \leq 0.40\text{-INCHES})$

$\alpha = \text{FAN INCLINATION ANGLE}$
 $(0 \text{ DEGREES} \leq \alpha \leq 40 \text{ DEGREES})$

Figure 12. Typical Element in Model Self-Impinging Doublet Injectors

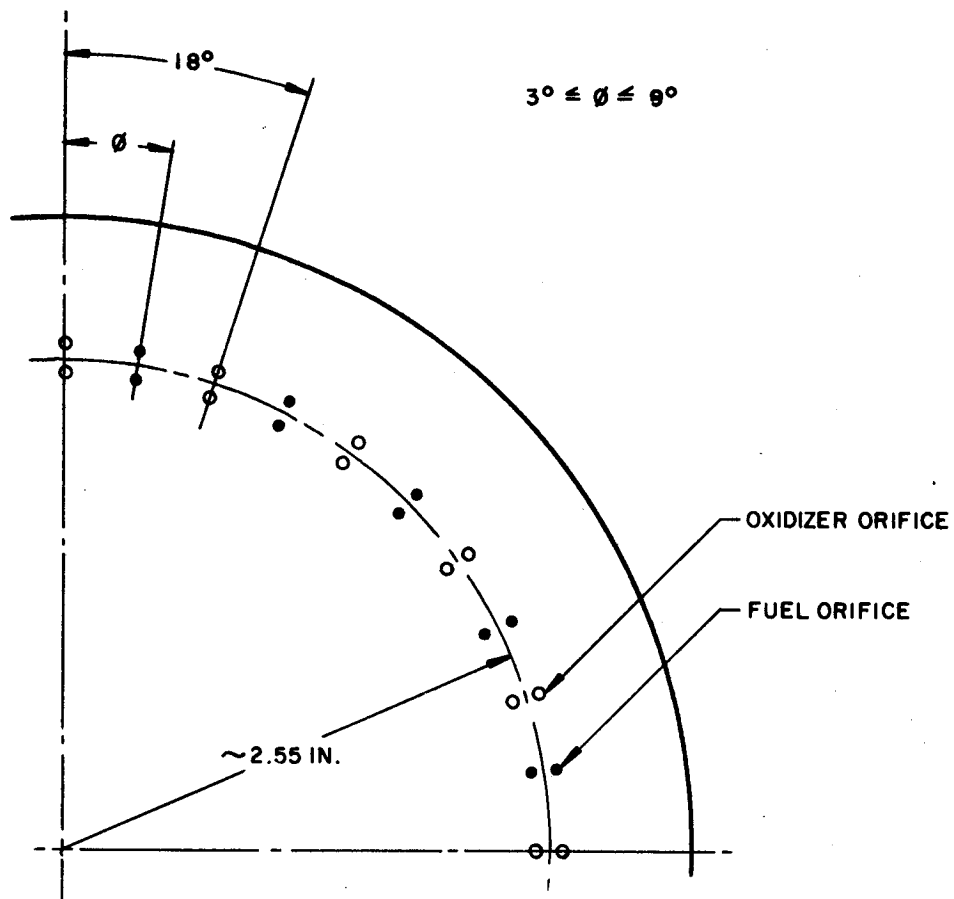


Figure 13. Schematic Representation of Face Pattern for Typical Five-Element Model Injector

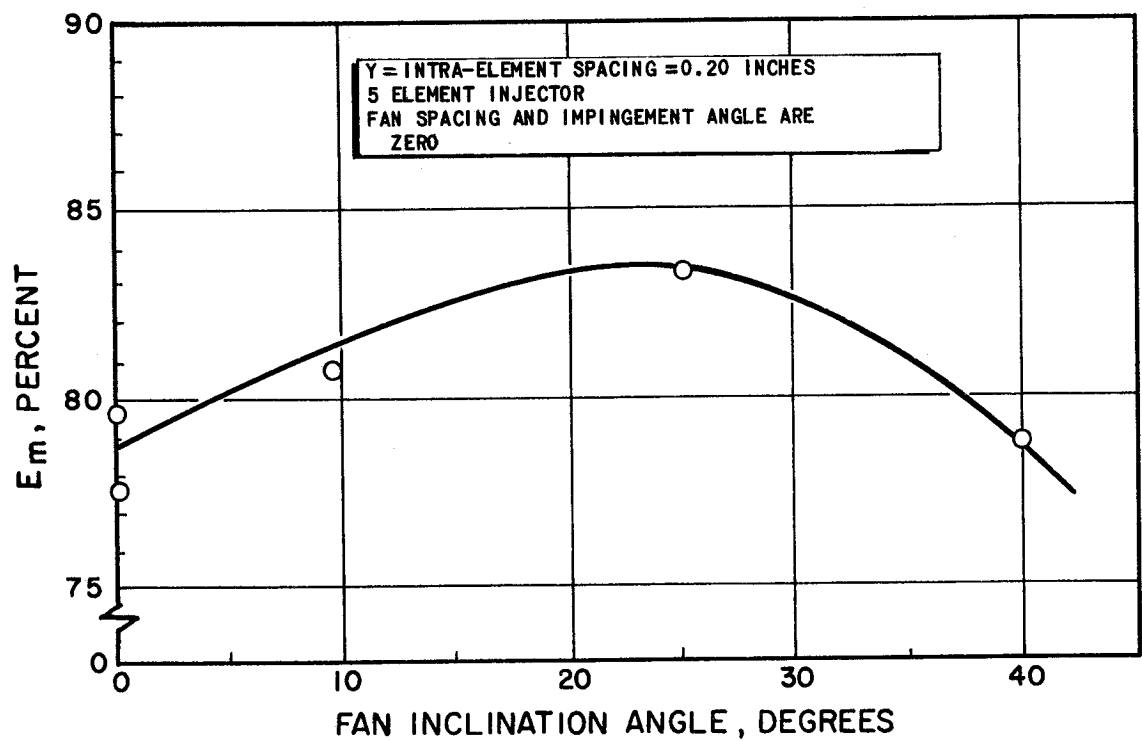


Figure 14. Effect of Fan Inclination Angle on Propellant Mixing for the Like-Doublet Injector Pattern

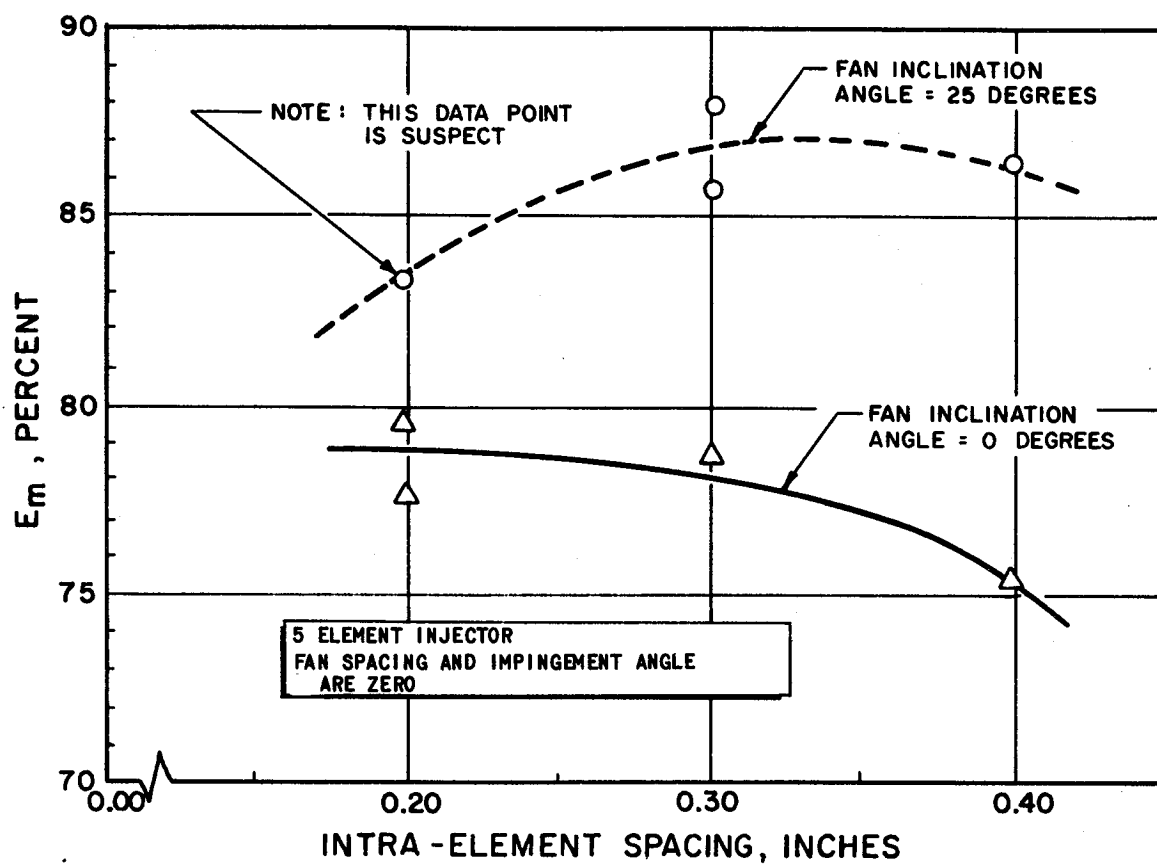
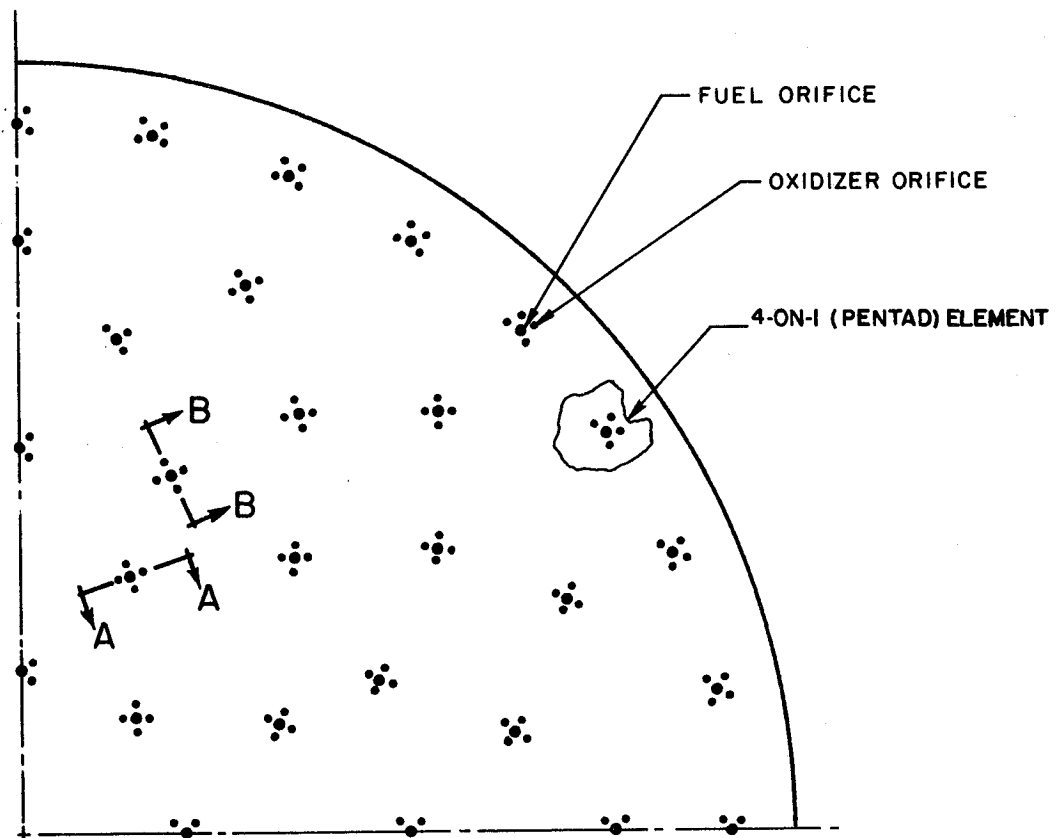


Figure 15. Effect of Fan Inclination Angle and Intra-Element Spacing on Propellant Mixing for the Like-Doublet Injector Pattern



Total Number of Elements = 96
 Fuel Injected Through Center Orifices

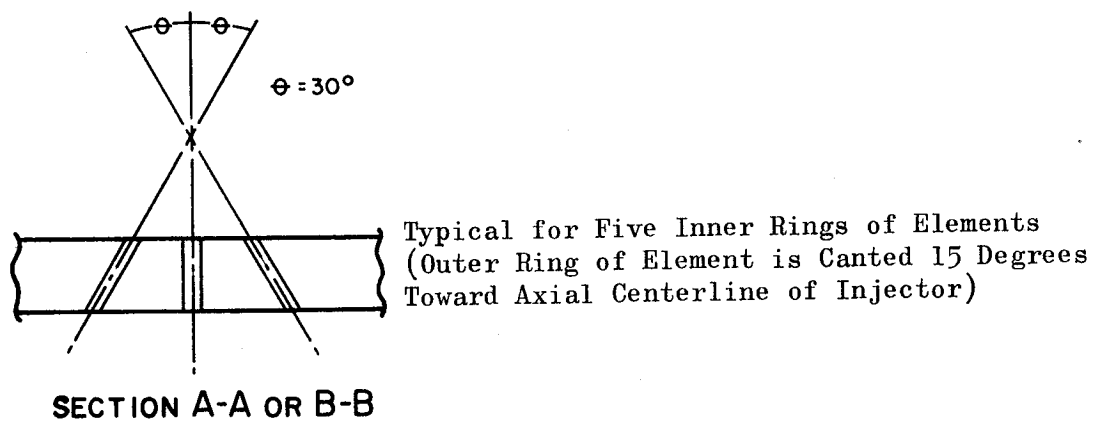


Figure 16. Schematic Representation of Typical Face Pattern for Pentad Injectors. Quarter Segment of Symmetrical Pattern shown

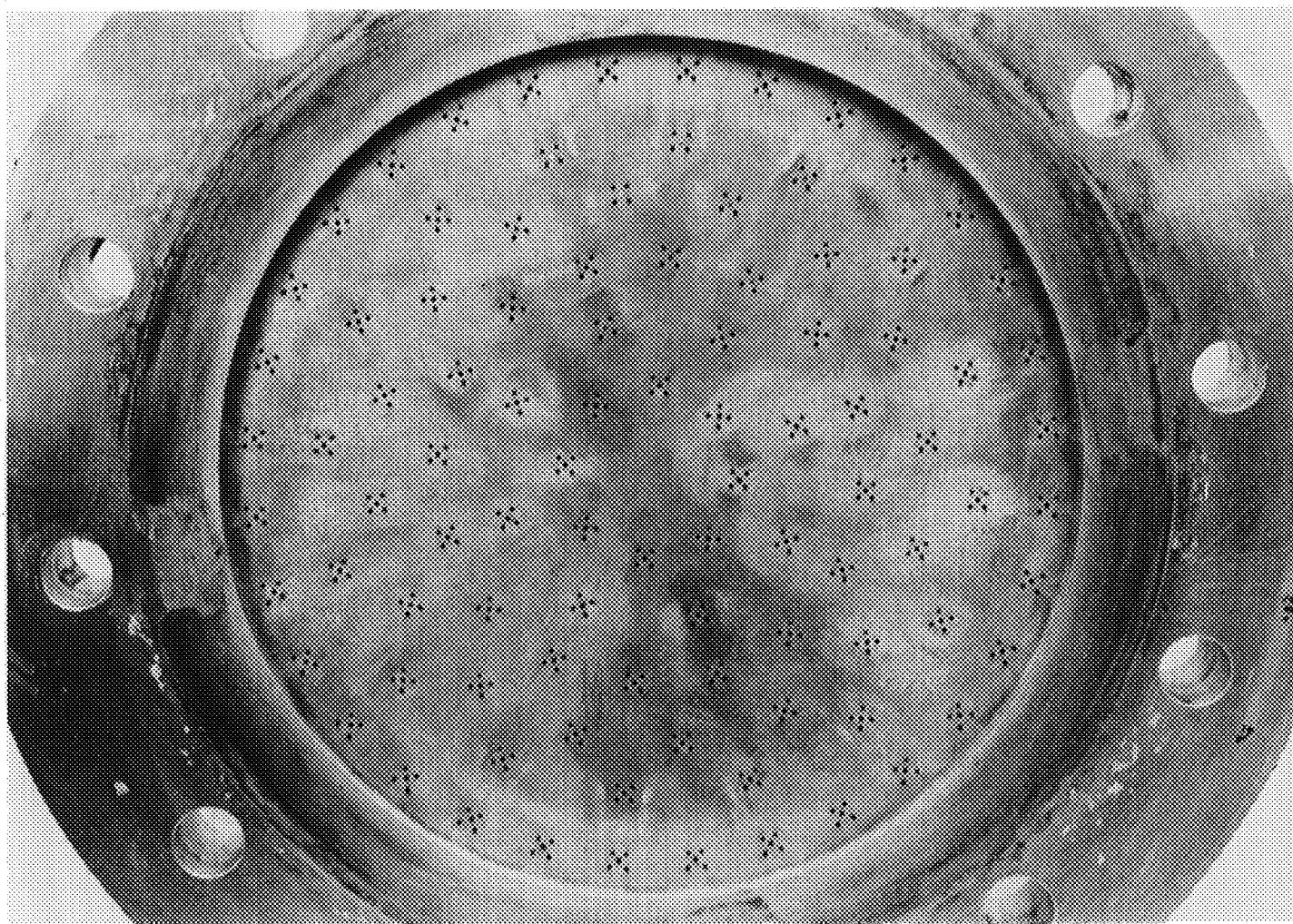


Figure 17. Face View of Pentad Injector No. P-2-M2 Showing Orifice Pattern.
Center Orifice of Element, Fuel; Outer Orifices, Oxidizer.
(Photo taken after experimental evaluation.)

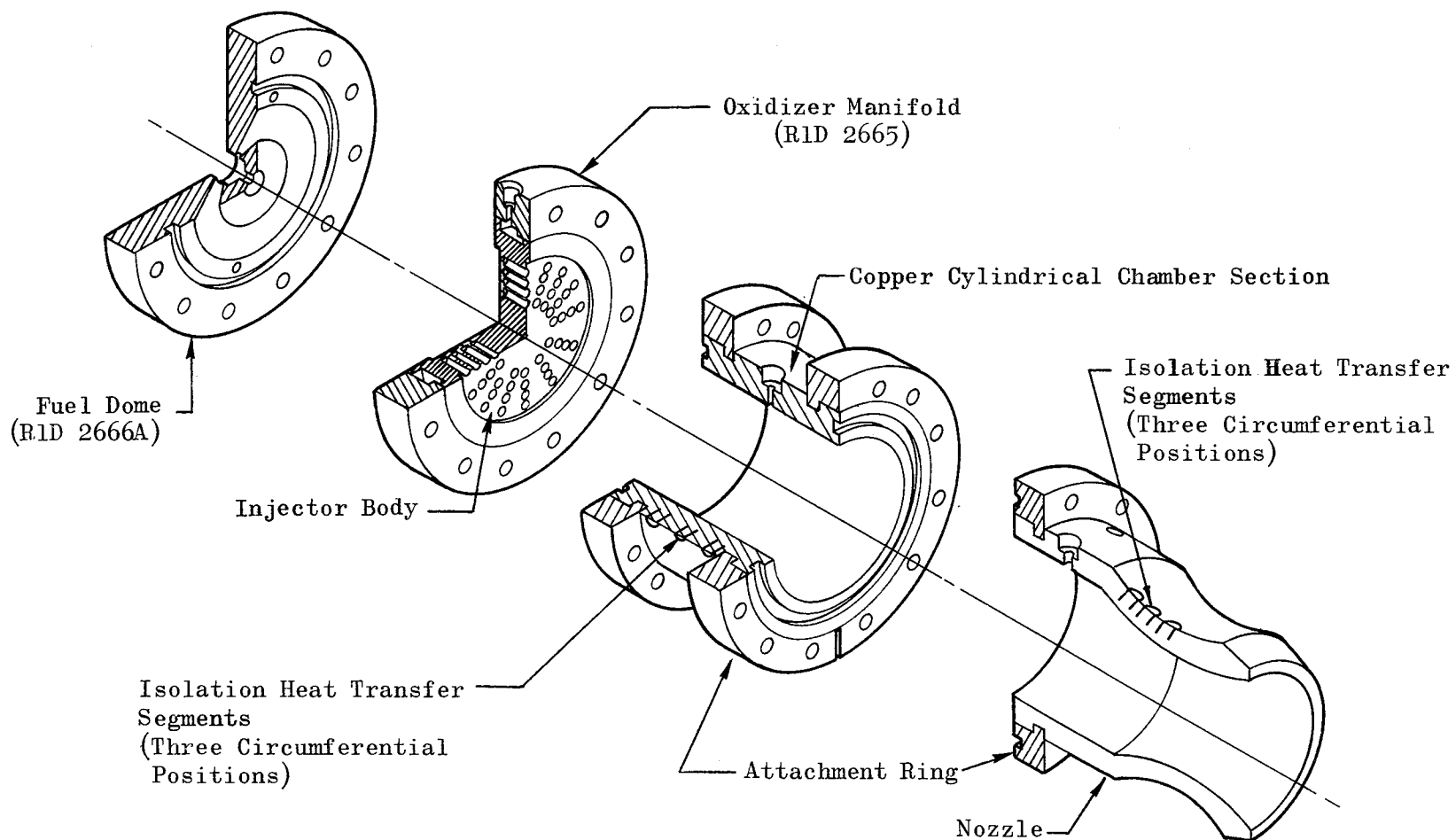


Figure 18. Schematic Representation of Reference ($L^* = 30$ Inches; $\epsilon_c = 2$) Thermally Instrumented Uncooled Motor Used for Injector Optimization Studies

CHAMBER PARAMETER	DIMENSION
D_c , INCHES	8.06
D_t , INCHES	5.70
D_e , INCHES	7.75
L_1 , INCHES	7.50
L_2 , INCHES	4.687
L_t , INCHES	15.767
L_r , INCHES	20.298
σ , DEGREES	15
β , DEGREES	60
Δx , INCHES	0.80
Δy , INCHES	1.0
R , INCHES	1.0
R_c , INCHES	5.70
ϵ_c	1.85

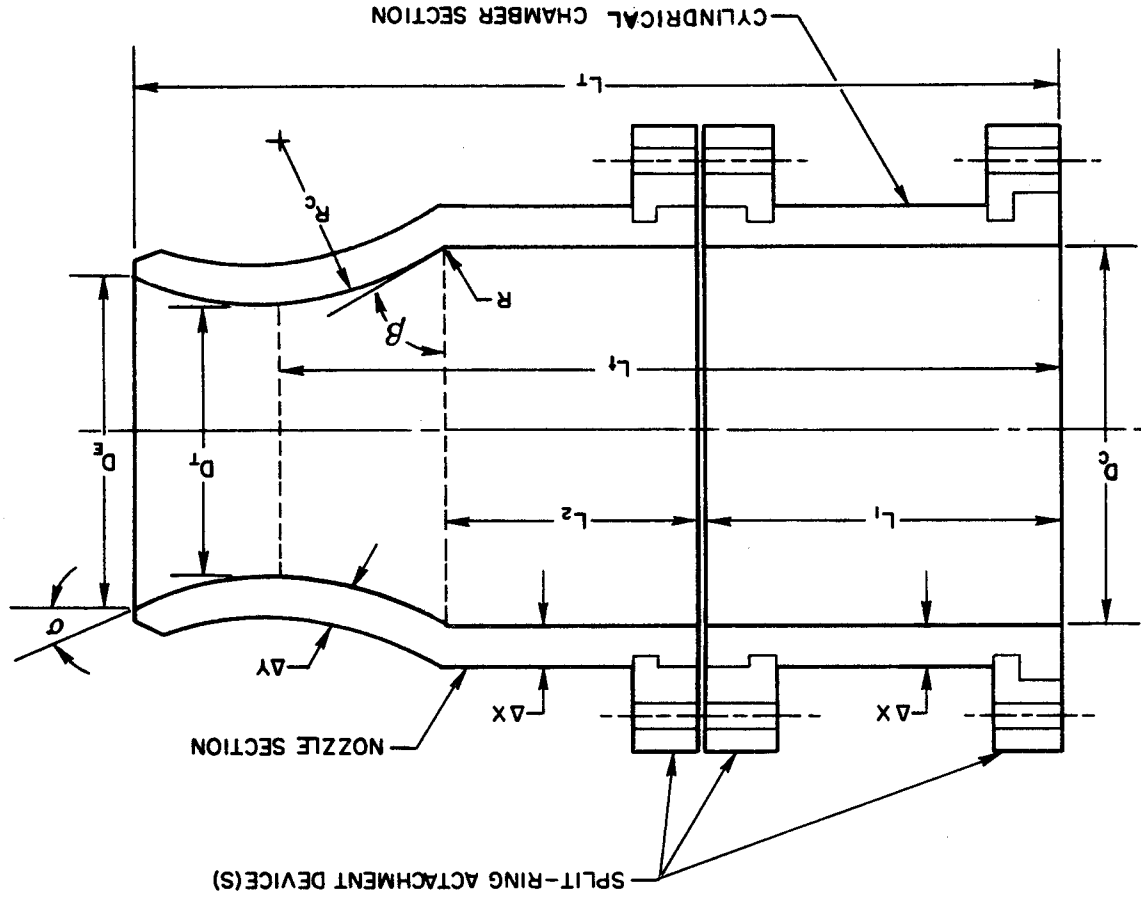


Figure 19. Schematic Representation of Reference ($L^* = 50$ Inches; $\epsilon_c = 2$) Chamber Assembly Showing Segmented Design and Dimensions

CHAMBER	PARAMETER	DIMENSION
	D_C , INCHES	8.06
	D_T , INCHES	4.03
	D_E , INCHES	6.91
	L_1 , INCHES	3.75
	L_2 , INCHES	1.083
	L_1 , INCHES	9.403
	L_T , INCHES	15.308
	σ , DEGREES	15
	β , DEGREES	60
	ΔX , INCHES	0.80
	ΔY , INCHES	1.0
	R , INCHES	1.0
	R_C , INCHES	4.03
	ϵ_e	2.94

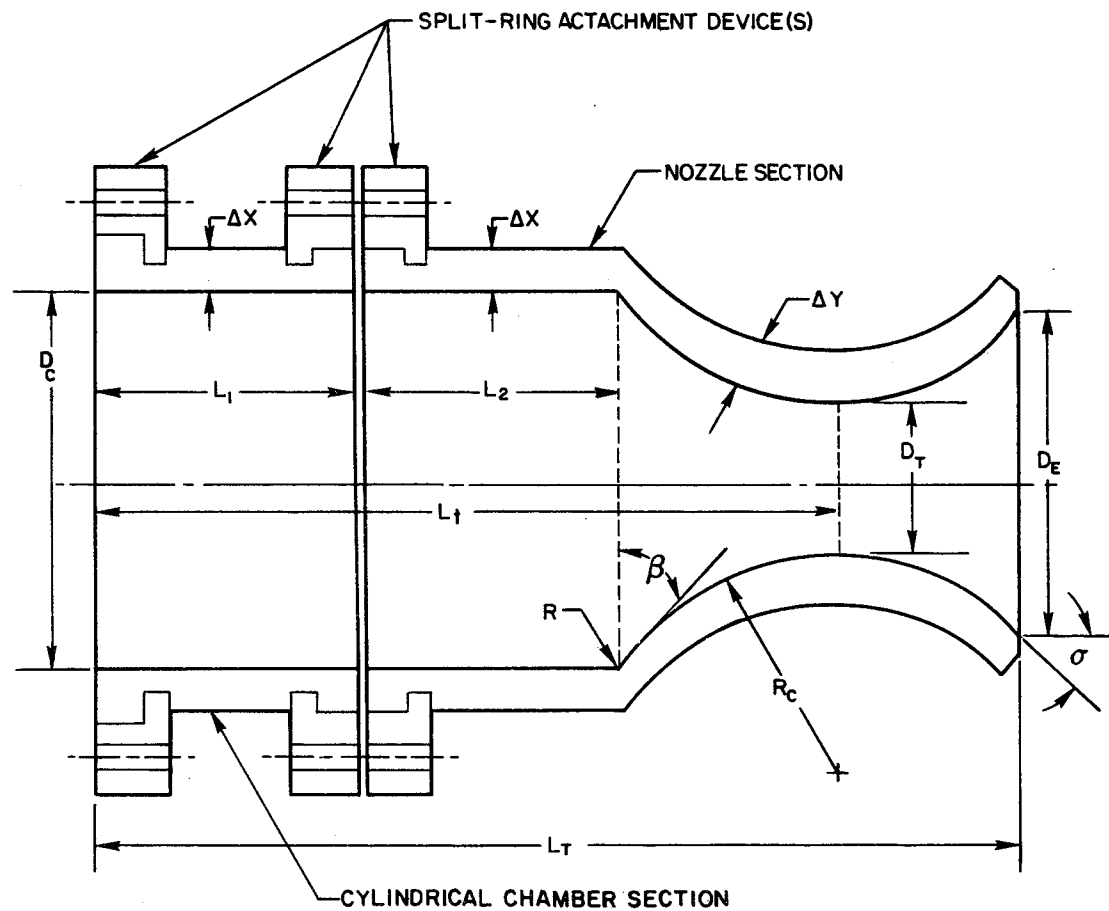
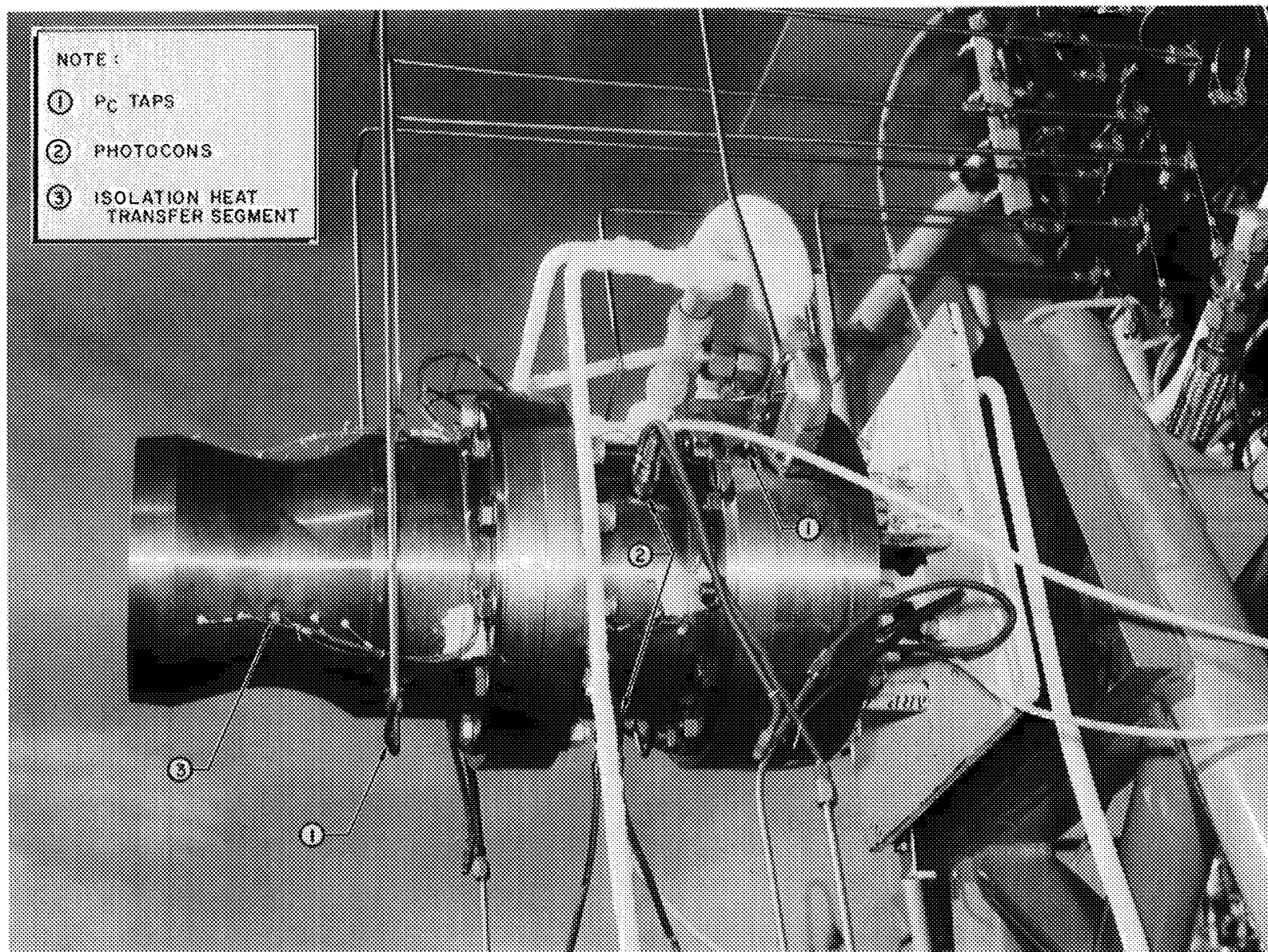


Figure 20. Schematic Representation of Alternate Contraction Ratio ($L^* = 30$ Inches; $\epsilon_c = 4$) Chamber Assembly Showing Segmented Design and Dimensions



5AA21-1/7/68-S1B

Figure 21. Photograph of 30-Inch L* Thrust Chamber Assembly Mounted on Thrust Stand

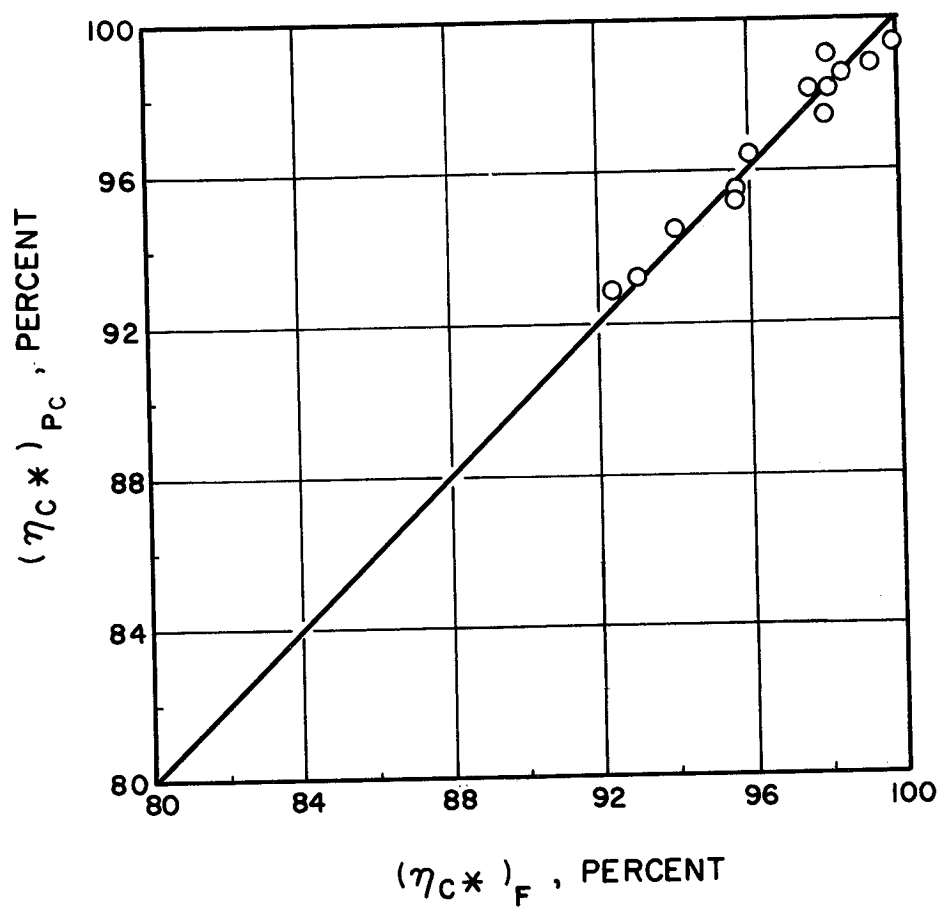


Figure 22. Comparison of Corrected c^* Efficiencies Based on Measurement of Chamber Pressure and Thrust

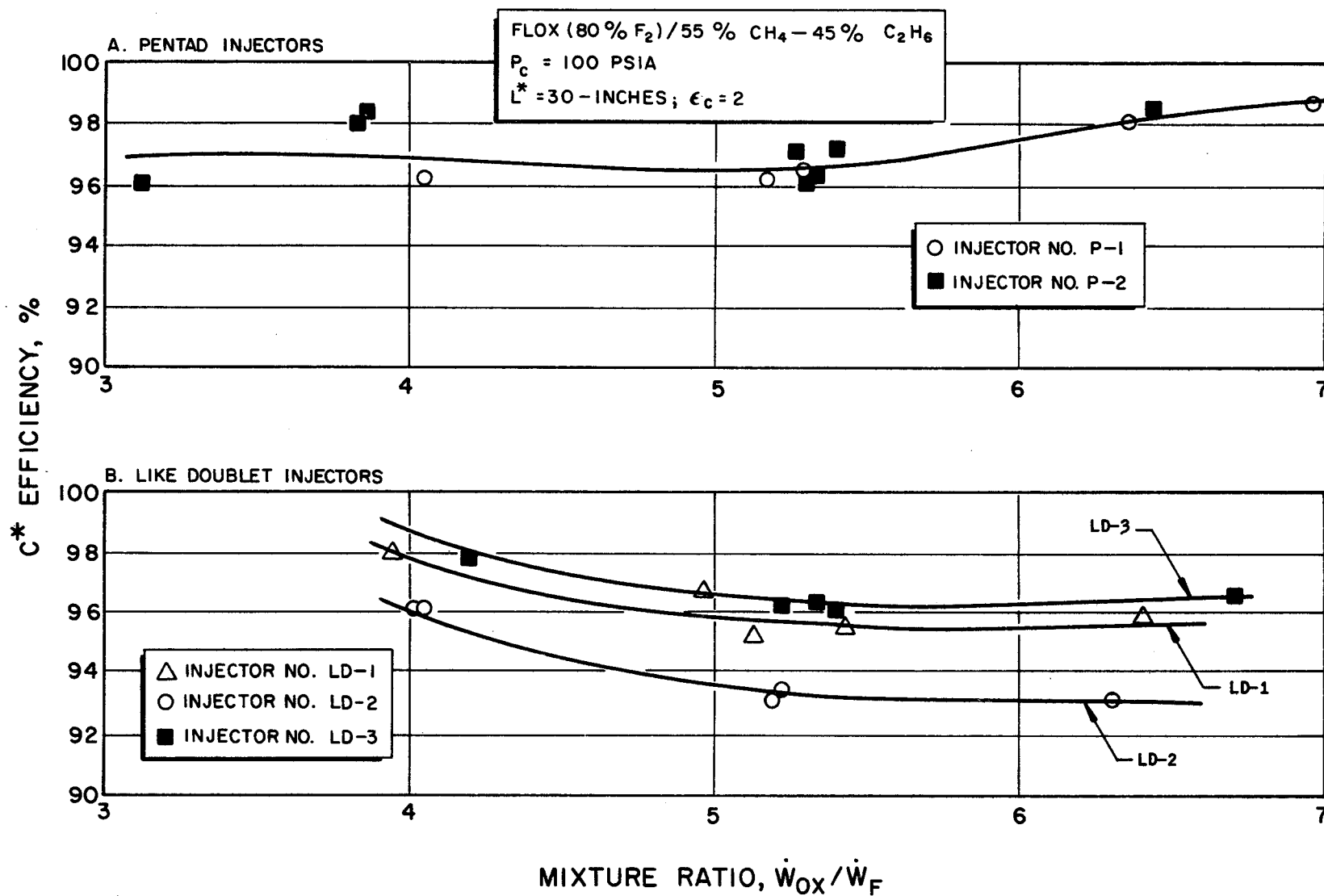


Figure 23. Corrected c* Efficiency as a Function of Mixture Ratio for Two Pentad and Three Like-Doublet Injectors

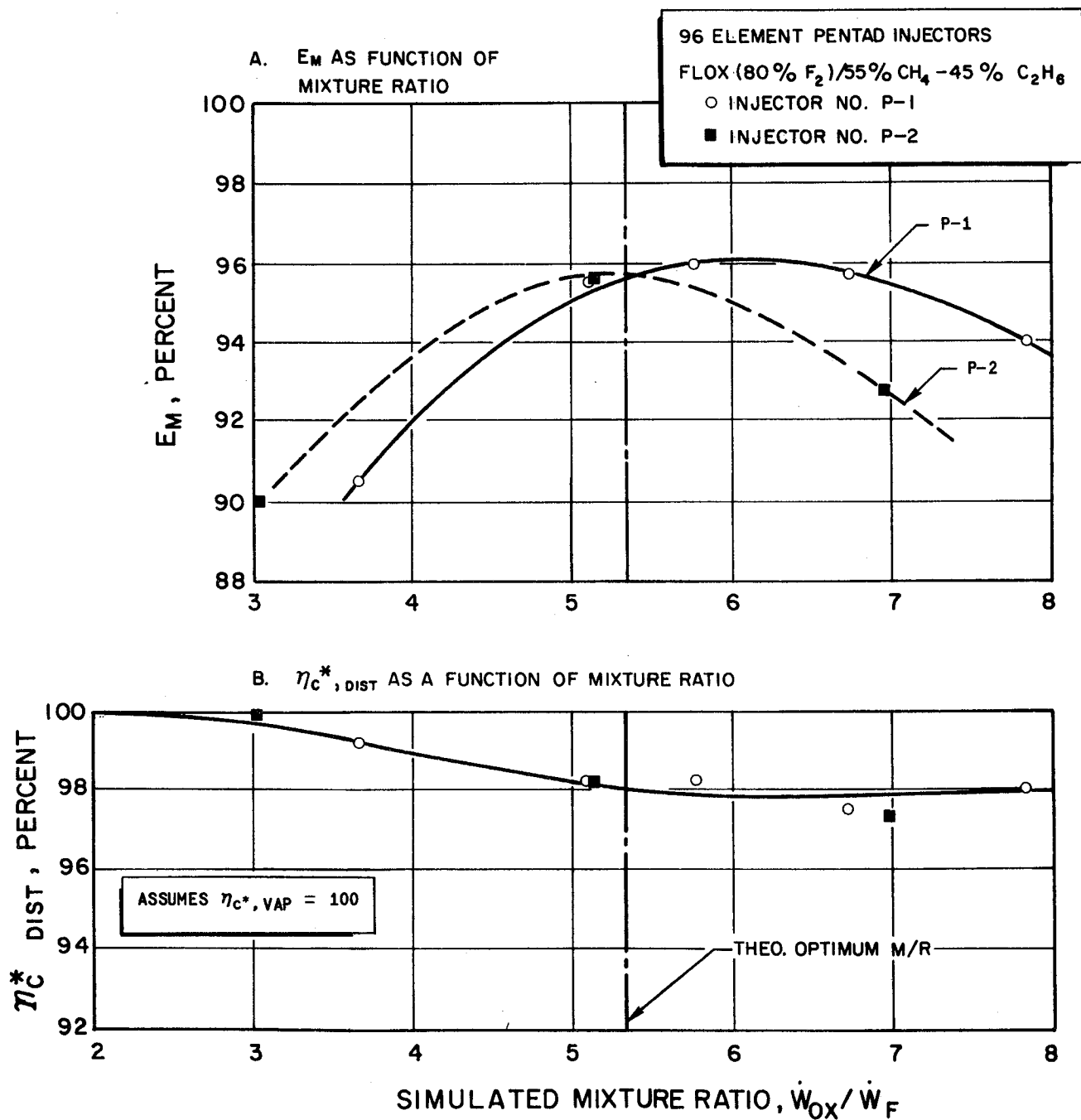


Figure 24. Measured Distribution Efficiency, E_m , and Predicted Effect of Nonuniform Distribution, $\eta_{c^*,dist}$, on Performance as a Function of Mixture Ratio for Two Pentad Injectors

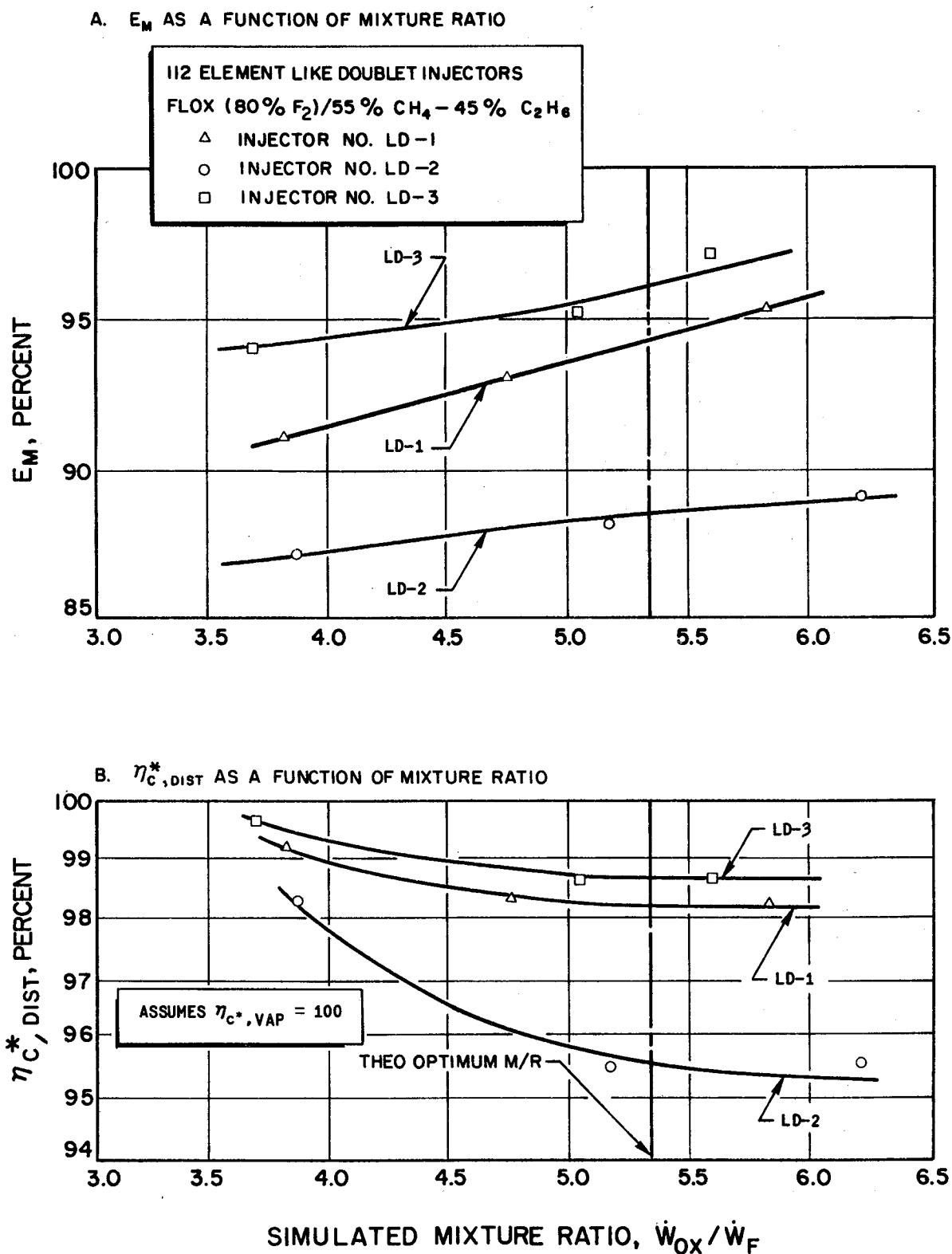


Figure 25. Measured Distribution Efficiency, E_m , and Predicted Effect of Nonuniform Distribution, $\eta_{c^*,dist}$, on Performance as a Function of Mixture Ratio for Three Like-Doublet Injectors

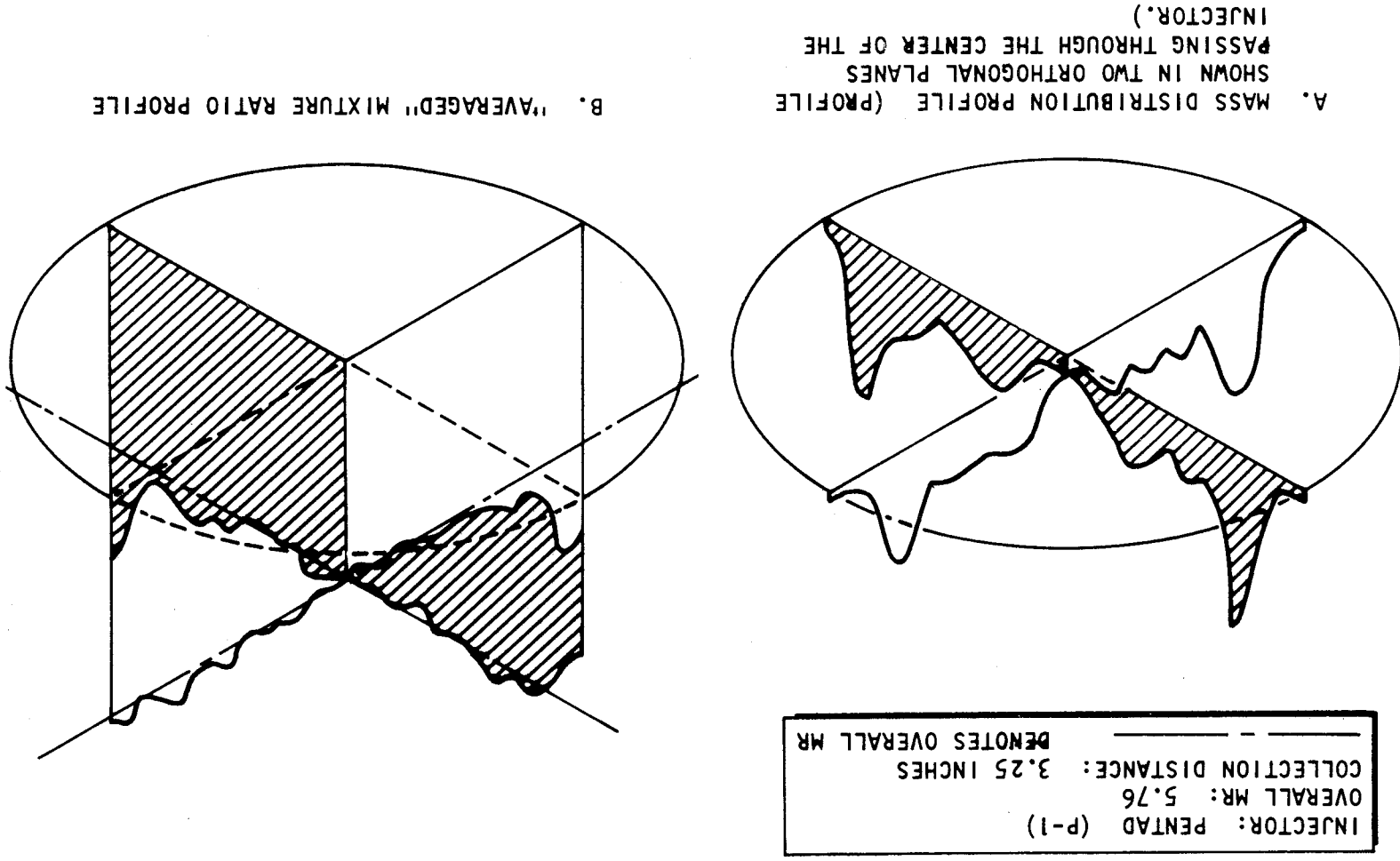
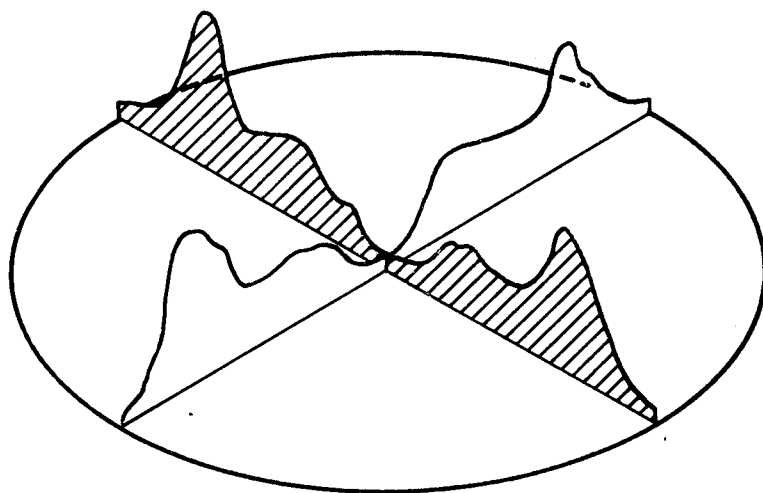
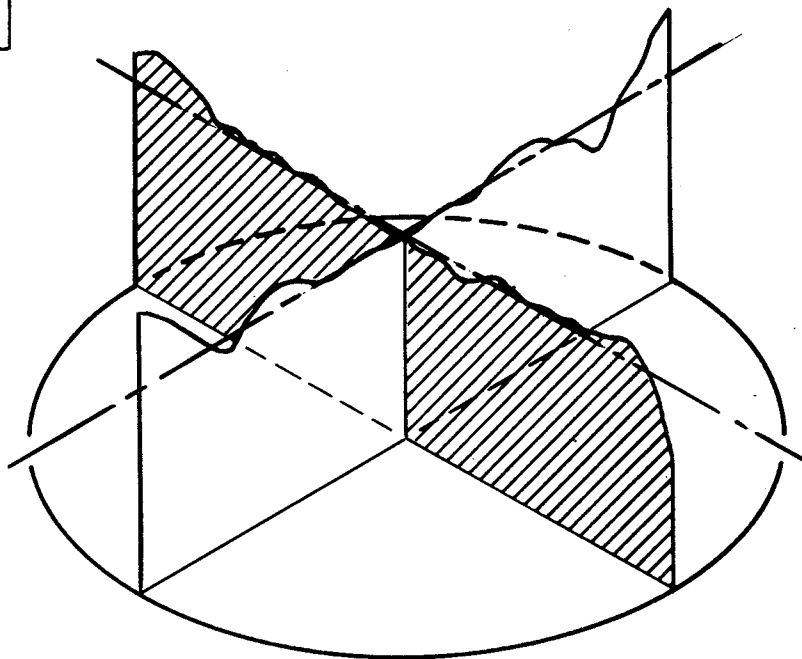


Figure 26. Mass and Mixture Ratio Distribution Profiles for Spray From Pentad Injector P-1

INJECTOR: LIKE DOUBLET (LD-1)
OVERALL MR: 4.71
COLLECTION DISTANCE: 3.25 INCHES
----- DENOTES OVERALL MR



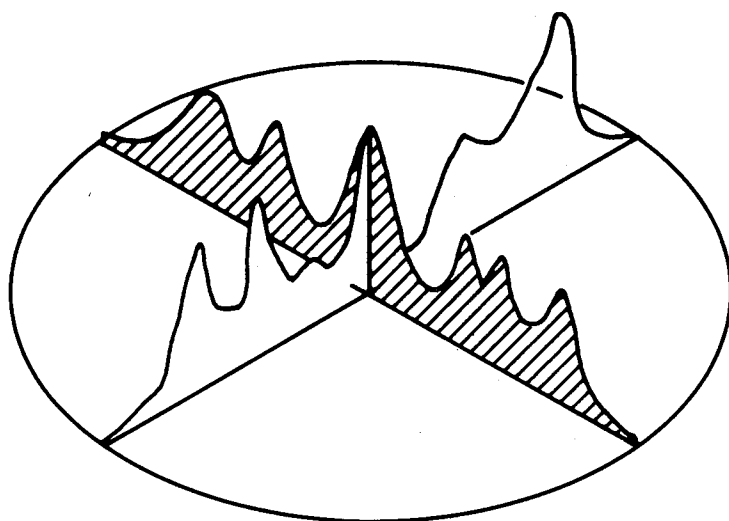
A. MASS DISTRIBUTION PROFILE (PROFILE SHOWN IN TWO ORTHOGONAL PLANES PASSING THROUGH THE CENTER OF THE INJECTOR.)



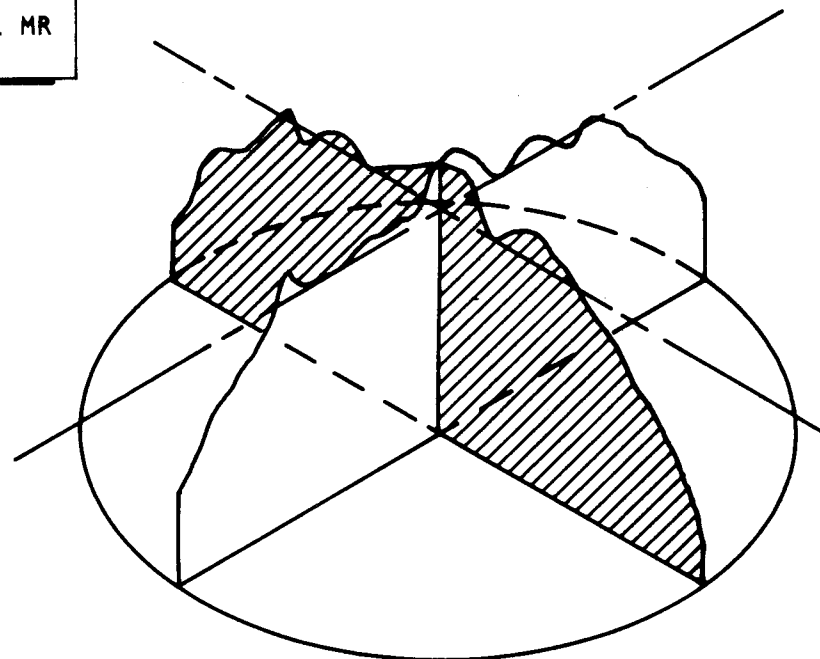
B. "AVERAGED" MIXTURE RATIO PROFILE

Figure 28. Mass and Mixture Ratio Distribution Profiles for Spray From Like Doublet Injector LD-1

INJECTOR: LIKE DOUBLET (LD-2)
OVERALL MR: 5.12
COLLECTION DISTANCE: 3.25 INCHES
— — — — — DENOTES OVERALL MR



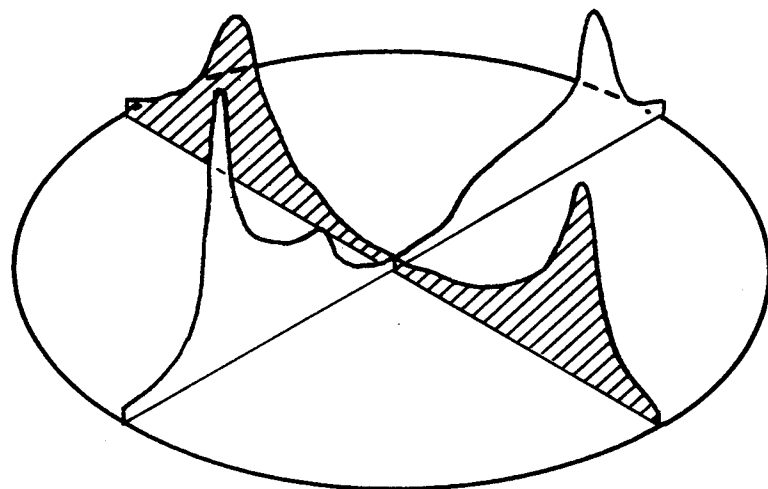
A. MASS DISTRIBUTION PROFILE (PROFILE SHOWN IN TWO ORTHOGONAL PLANES PASSING THROUGH THE CENTER OF THE INJECTOR.)



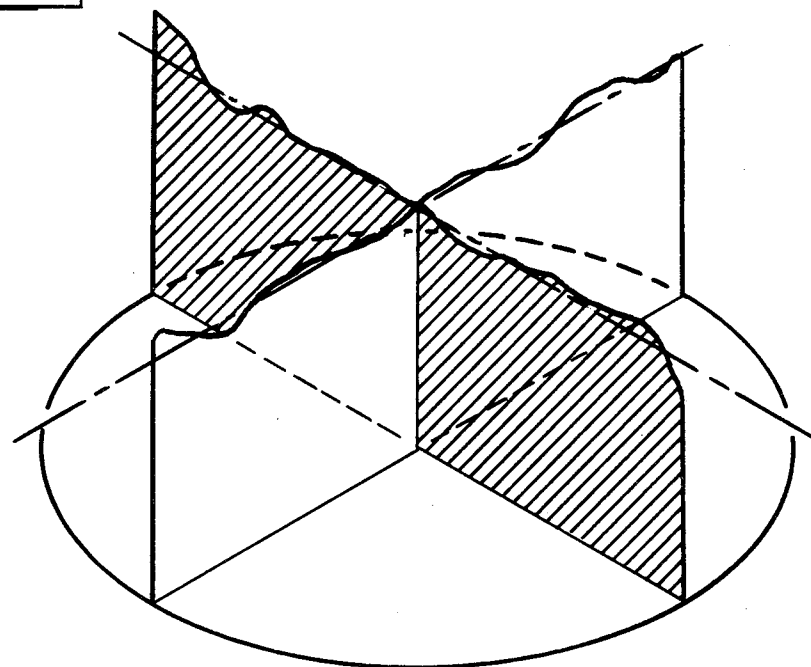
B. "AVERAGED" MIXTURE RATIO PROFILE

Figure 29. Mass and Mixture Ratio Distribution Profiles for Spray From Like Doublet Injector LD-2

INJECTOR: LIKE DOUBLET (LD-3)
 OVERALL MR: 5.55
 COLLECTION DISTANCE: 3.25 INCHES
 ----- DENOTES OVERALL MR



A. MASS DISTRIBUTION PROFILE (PROFILE
 SHOWN IN TWO ORTHOGONAL PLANES
 PASSING THROUGH THE CENTER OF THE
 INJECTOR.)



B. "AVERAGED" MIXTURE RATIO PROFILE

Figure 30. Mass and Mixture Ratio Distribution Profiles for Spray From Like Doublet Injector LD-3

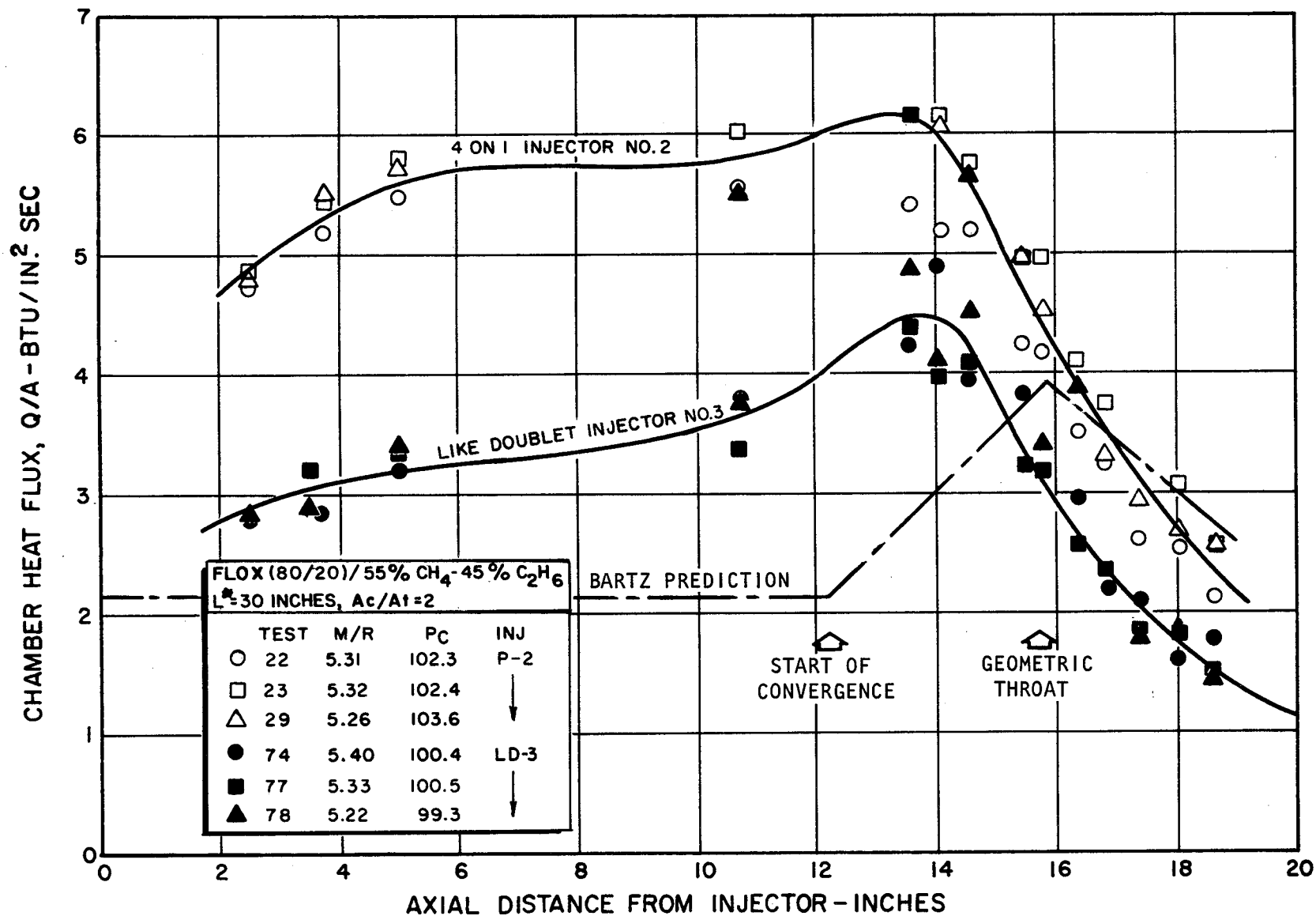


Figure 31. Characteristic Heat Flux Curves for the 4-on-1 Pentad Injector and Like-Doublet Injector at Common Test Conditions

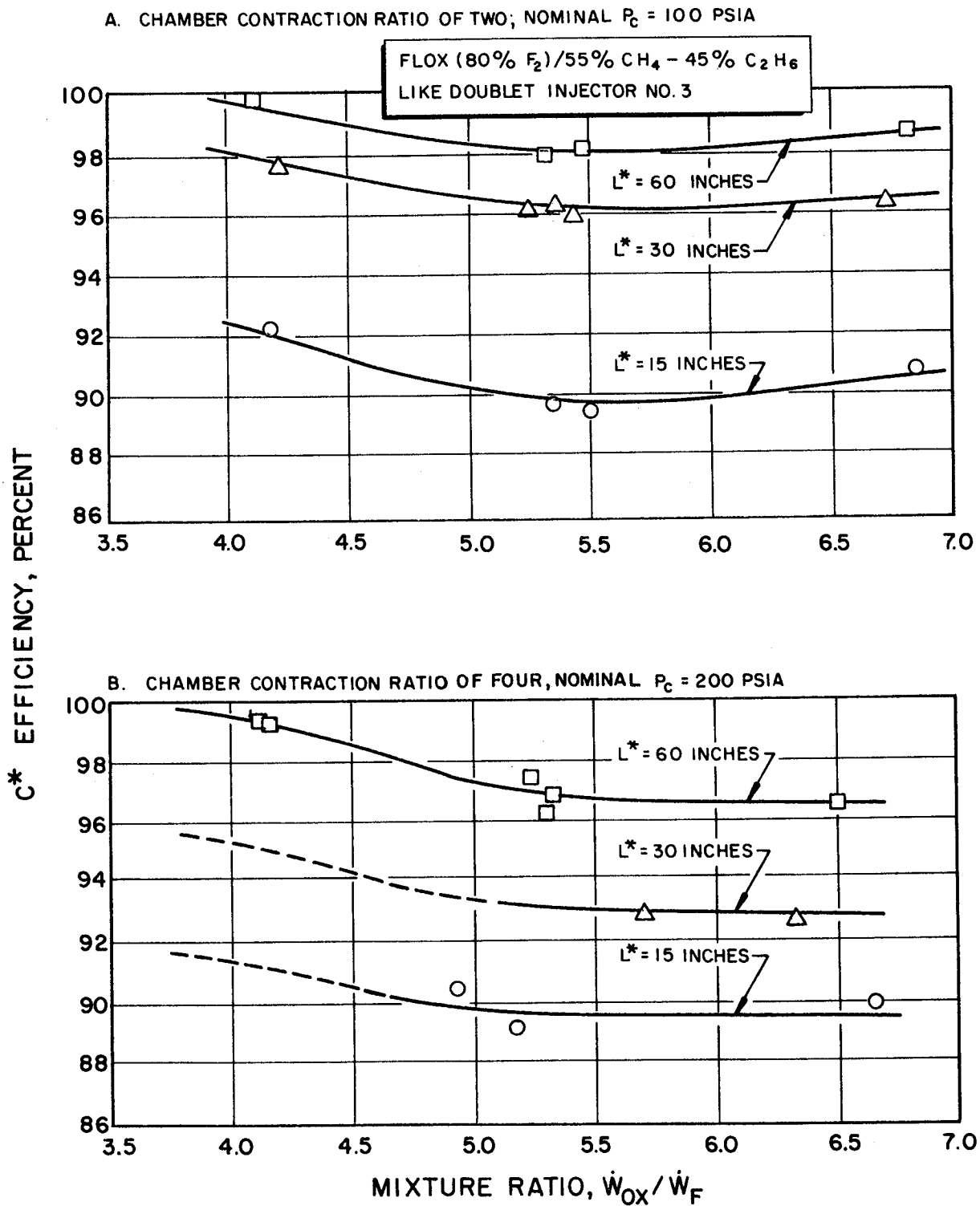


Figure 32. Corrected c^* Efficiency as a Function of Mixture Ratio for Three Characteristic Chamber Lengths and Two Chamber Contraction Ratios

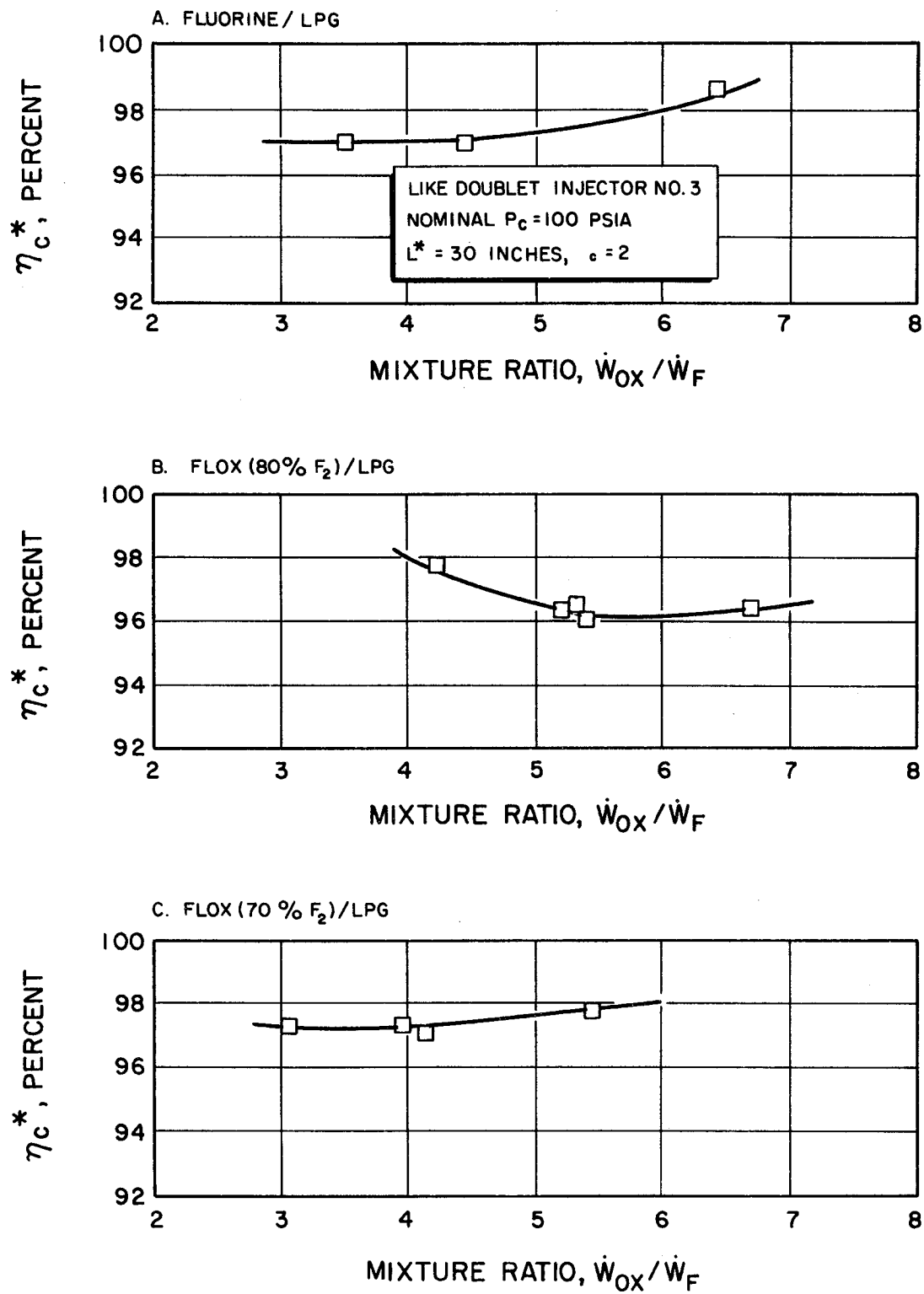


Figure 33 . Corrected c^* Efficiency as a Function of Mixture Ratio for Several Fluorine Oxidizers With 55 Percent CH_4 -45 Percent C_2H_6 LPG Blend

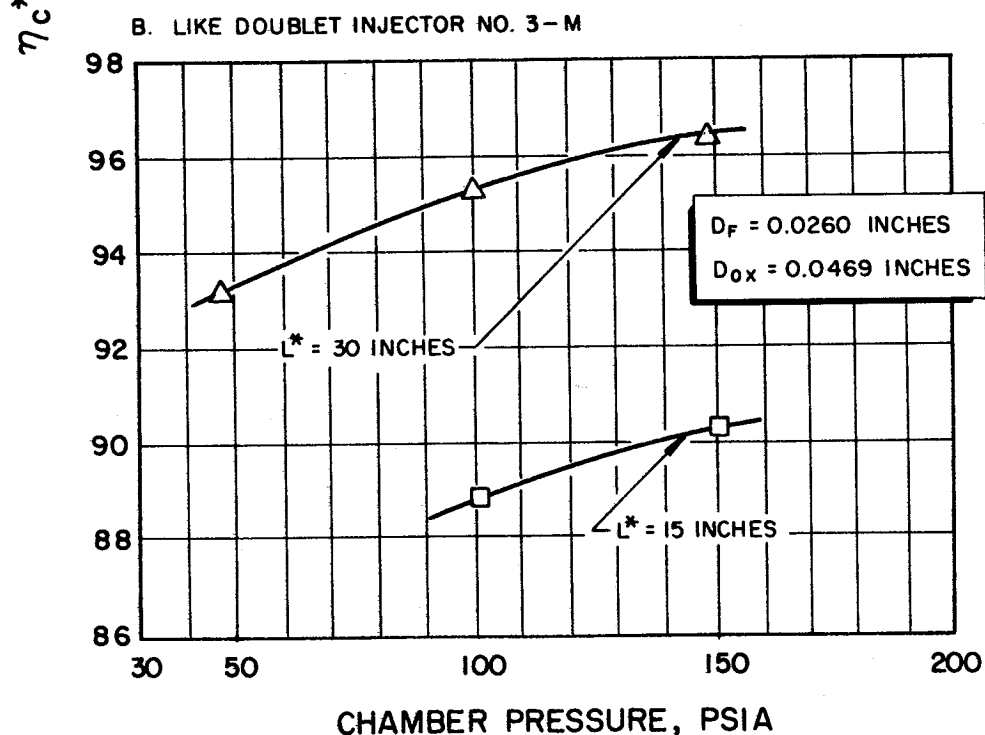
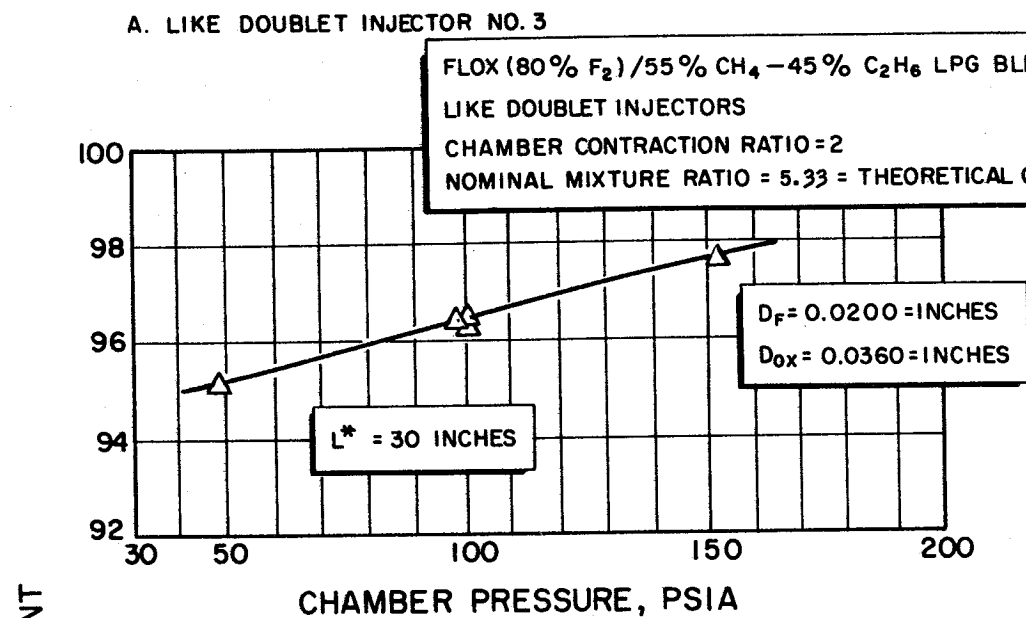


Figure 34. Corrected c^* Efficiency as a Function of Chamber Pressure for Two Like-Doublet Injectors

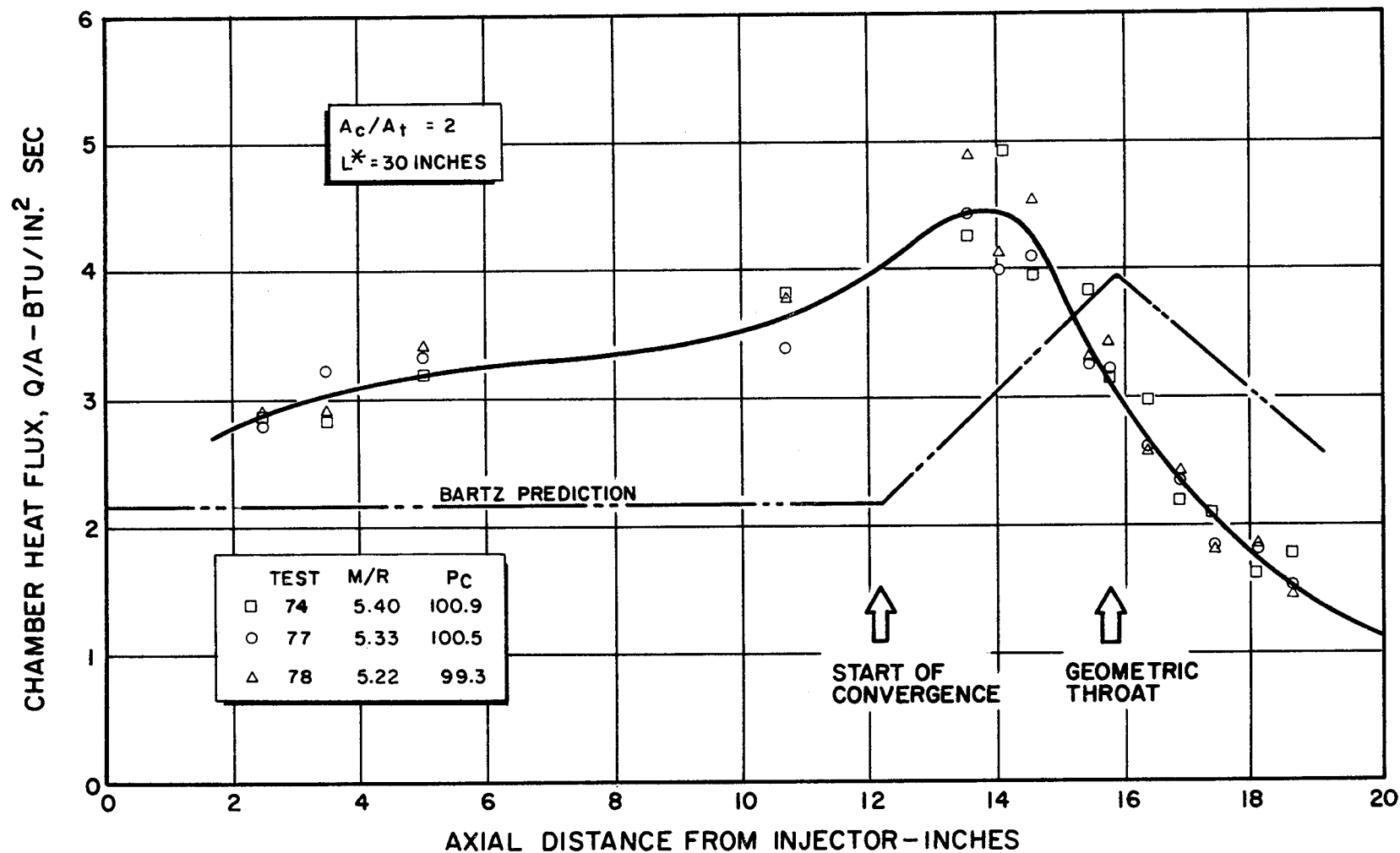


Figure 35. Heat Flux Characteristics for Optimum Like-Doublet Injector Showing Data Repeatability Based on Average Circumferential Measurements From Three Tests. (Data shown are for experiments conducted with FLOX (80/20)/55 percent CH_4 - 45 percent C_2H_6)

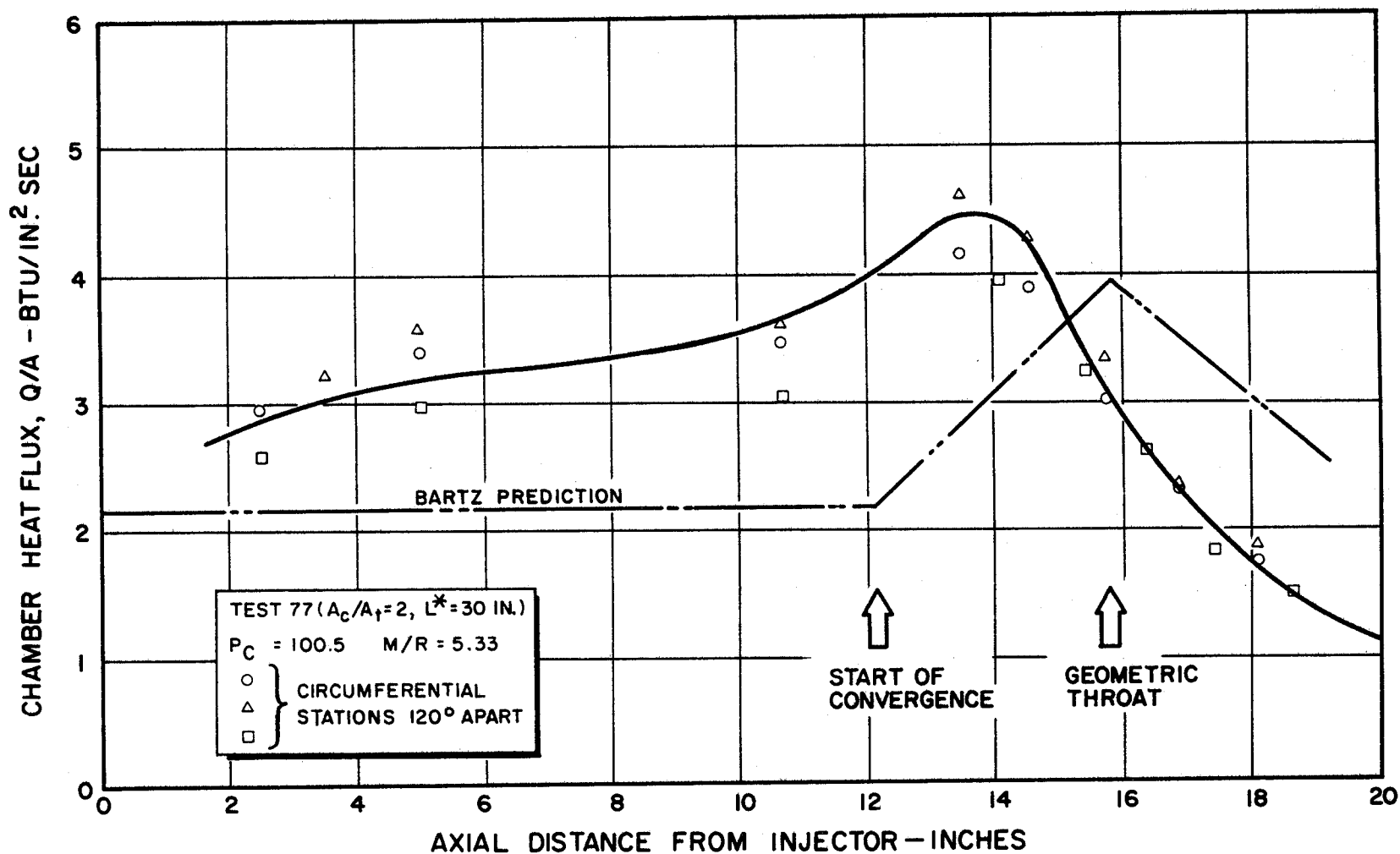


Figure 36. Heat Flux Characteristics for Optimum Like-Doublet Injector Based on Individual Circumferential Measurements (Test was conducted with FLOX (80/20)/55 percent CH_4 -45 percent C_2H_6)

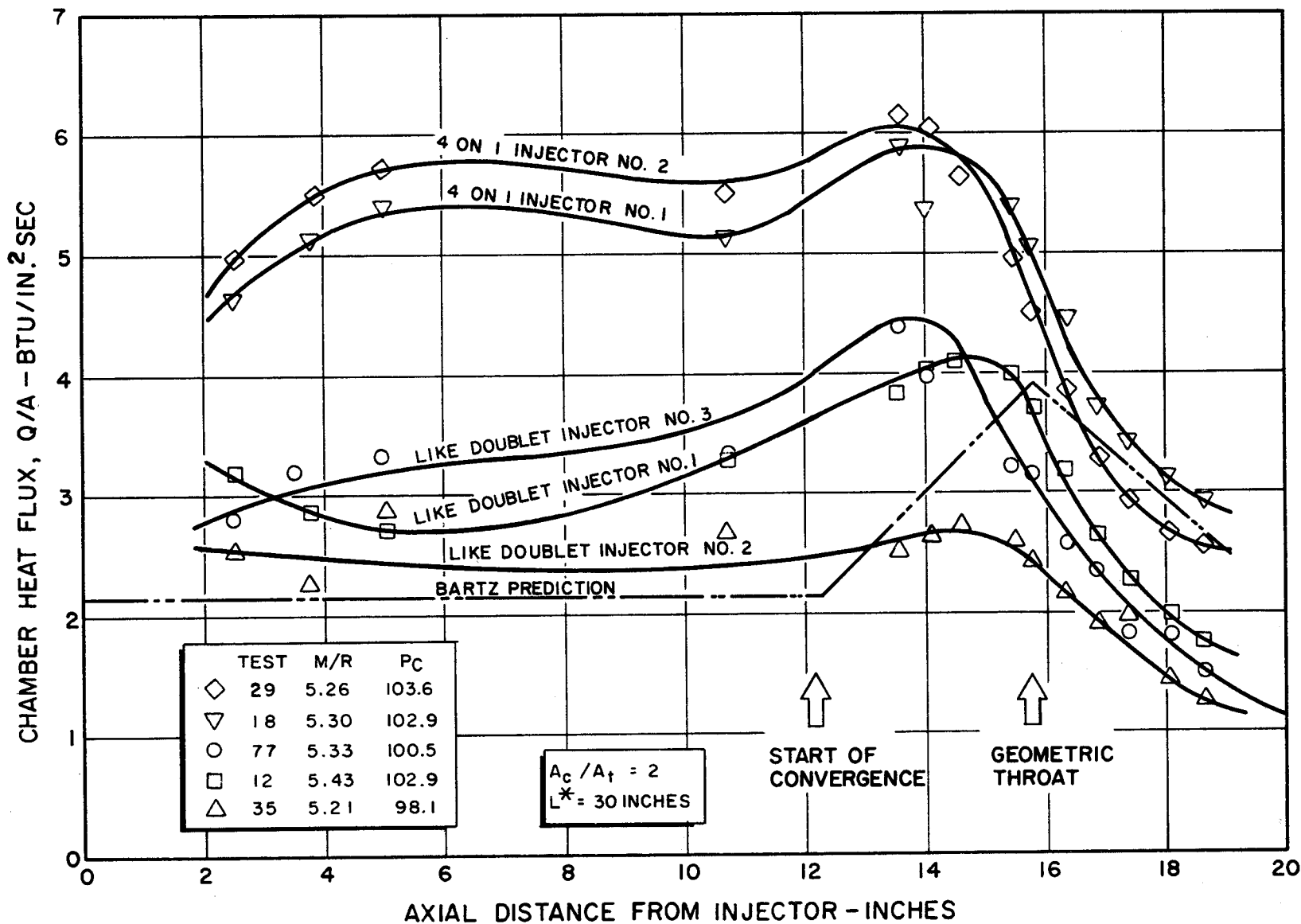


Figure 37. Characteristic Heat Flux Curves for Five Basic Candidate Injectors Evaluated With FLOX (80/20)/55 Percent CH_4 -45 Percent C_2H_6 at Nominal Design Conditions

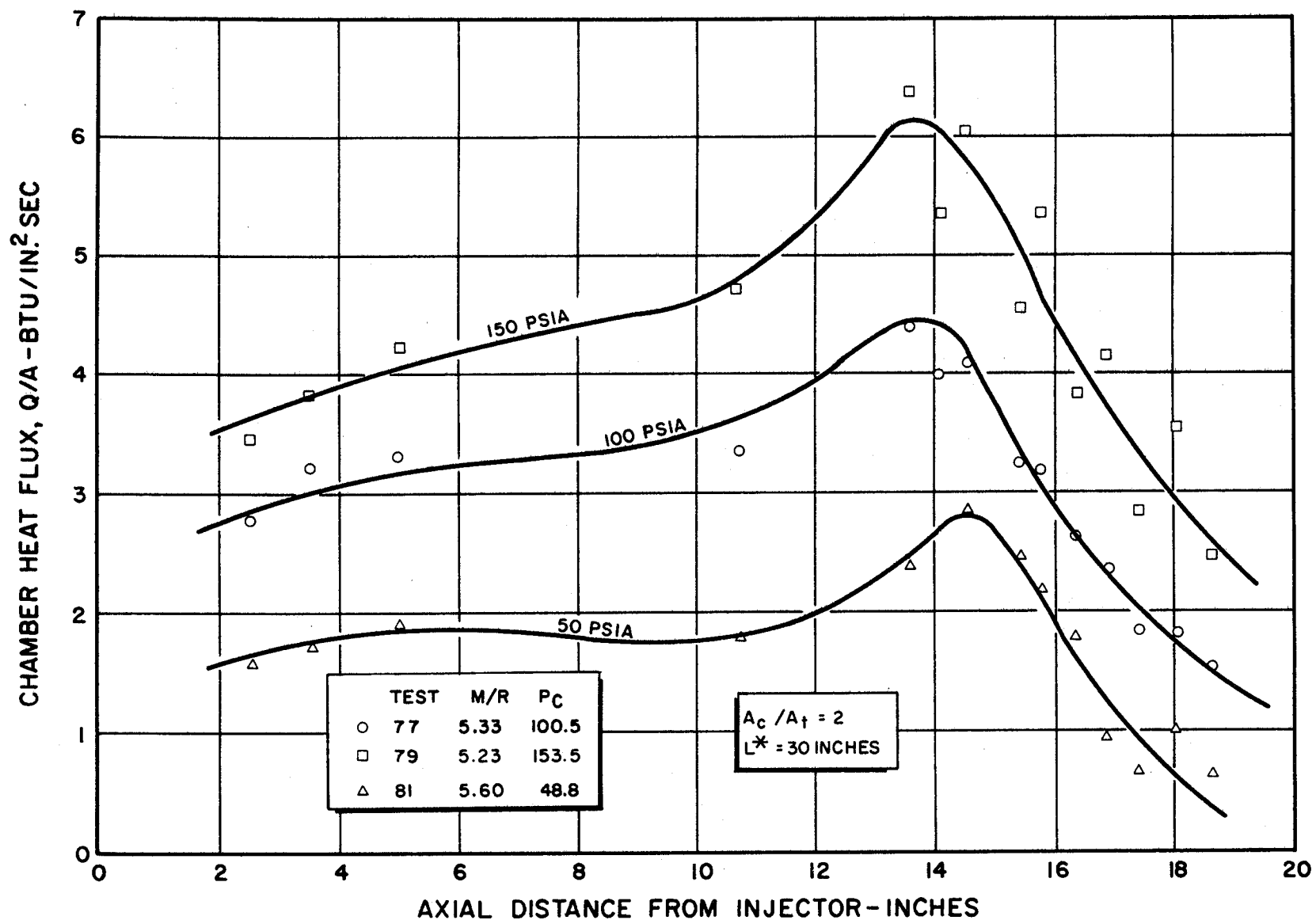


Figure 38. Heat Flux Characteristics for Optimum Like-Doublet Injector With Variation in Chamber Pressure (Tests were conducted with FLOX (80/20)/55 percent CH_4 -45 percent C_2H_6)

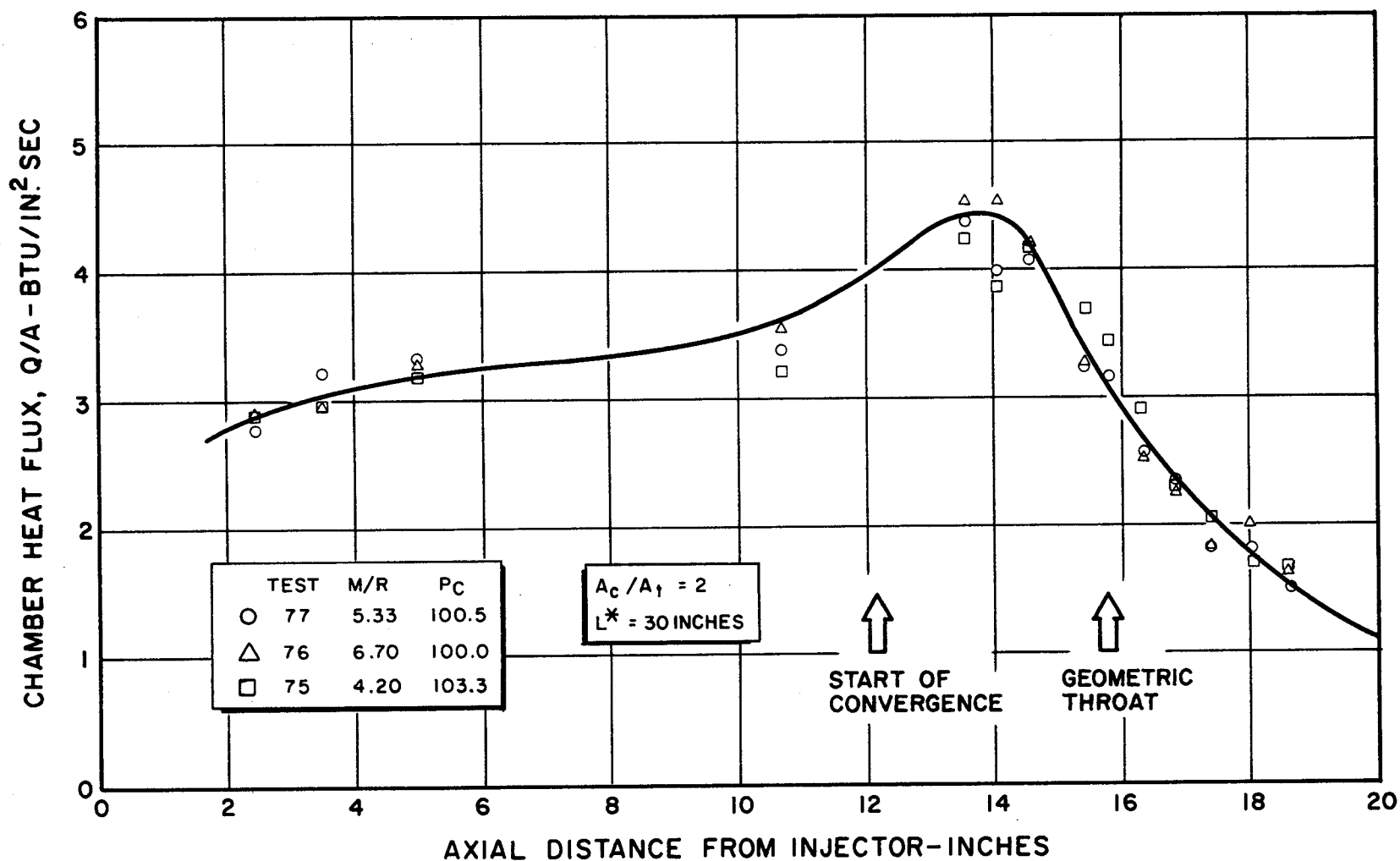


Figure 39. Characteristic Heat Flux Curve Showing Effect of Mixture Ratio Variation
(Tests were conducted with FLOX (80/20)/55 percent CH_4 -45 percent C_2H_6)

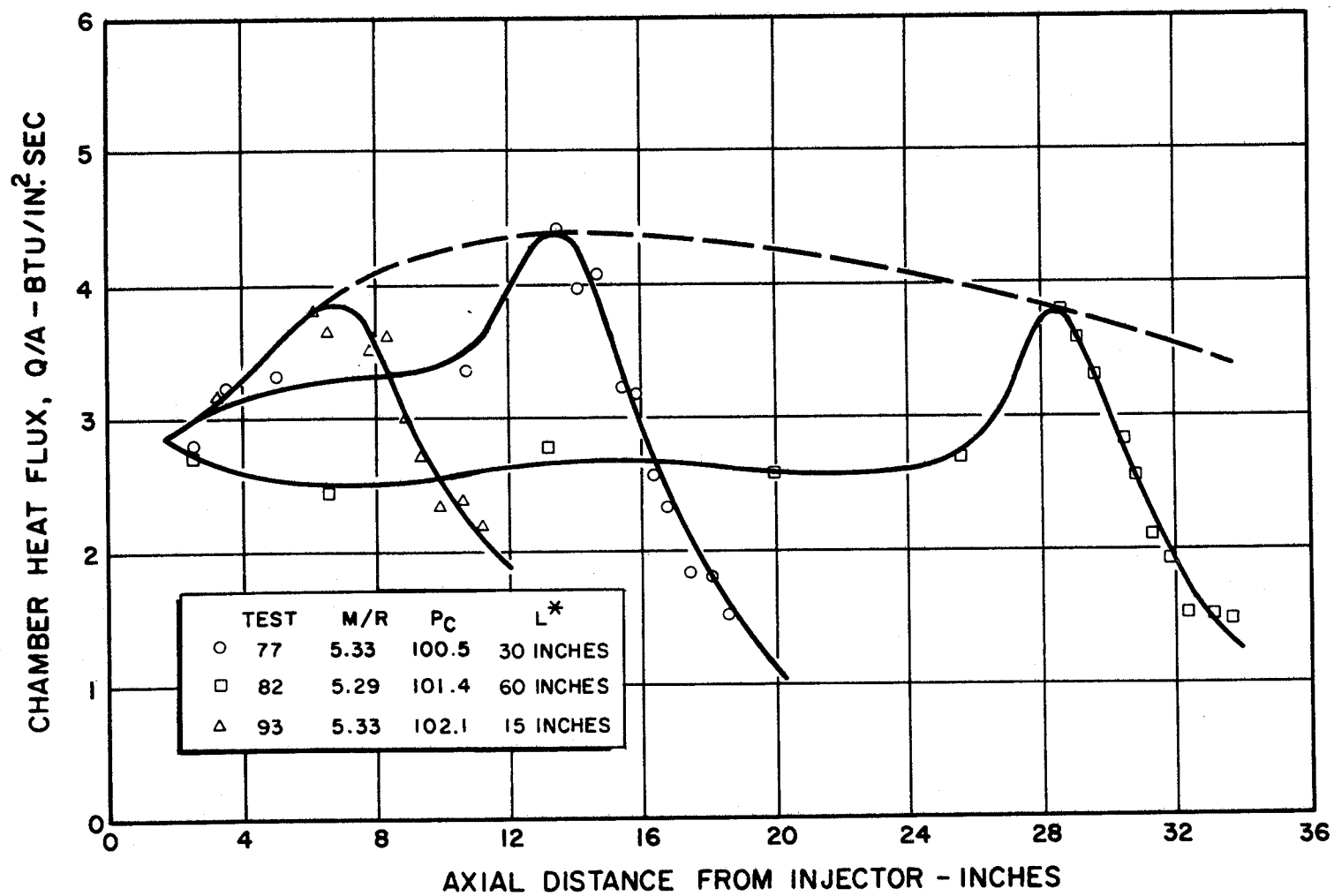


Figure 40. Characteristic Heat Flux Curves Showing Variation With Chamber Characteristic Length (Tests were conducted with FLOX(80/20)/55 percent CH_4 /45 percent C_2H_6 at nominal design conditions)

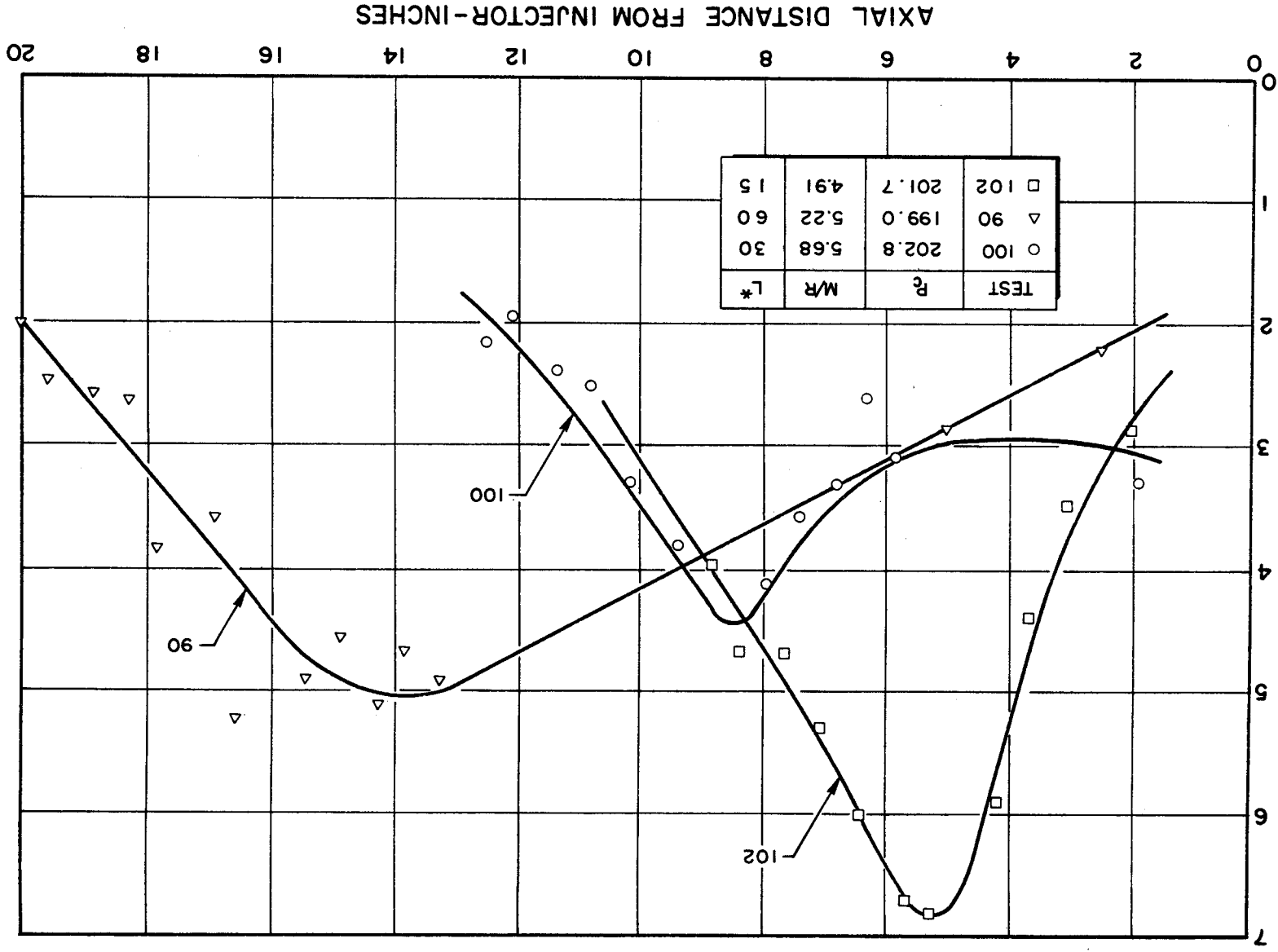
CHAMBER HEAT FLUX, $Q/A \sim \text{BTU}/\text{IN}^2\text{-SEC}$ 

Figure 41. Characteristic Heat Flux Curves for the Like-Doublet Injector and 4-to-1 Contraction Area Ratio Chambers (all tests were conducted with FLOX (80-20)/55 percent methane-45 percent ethane)

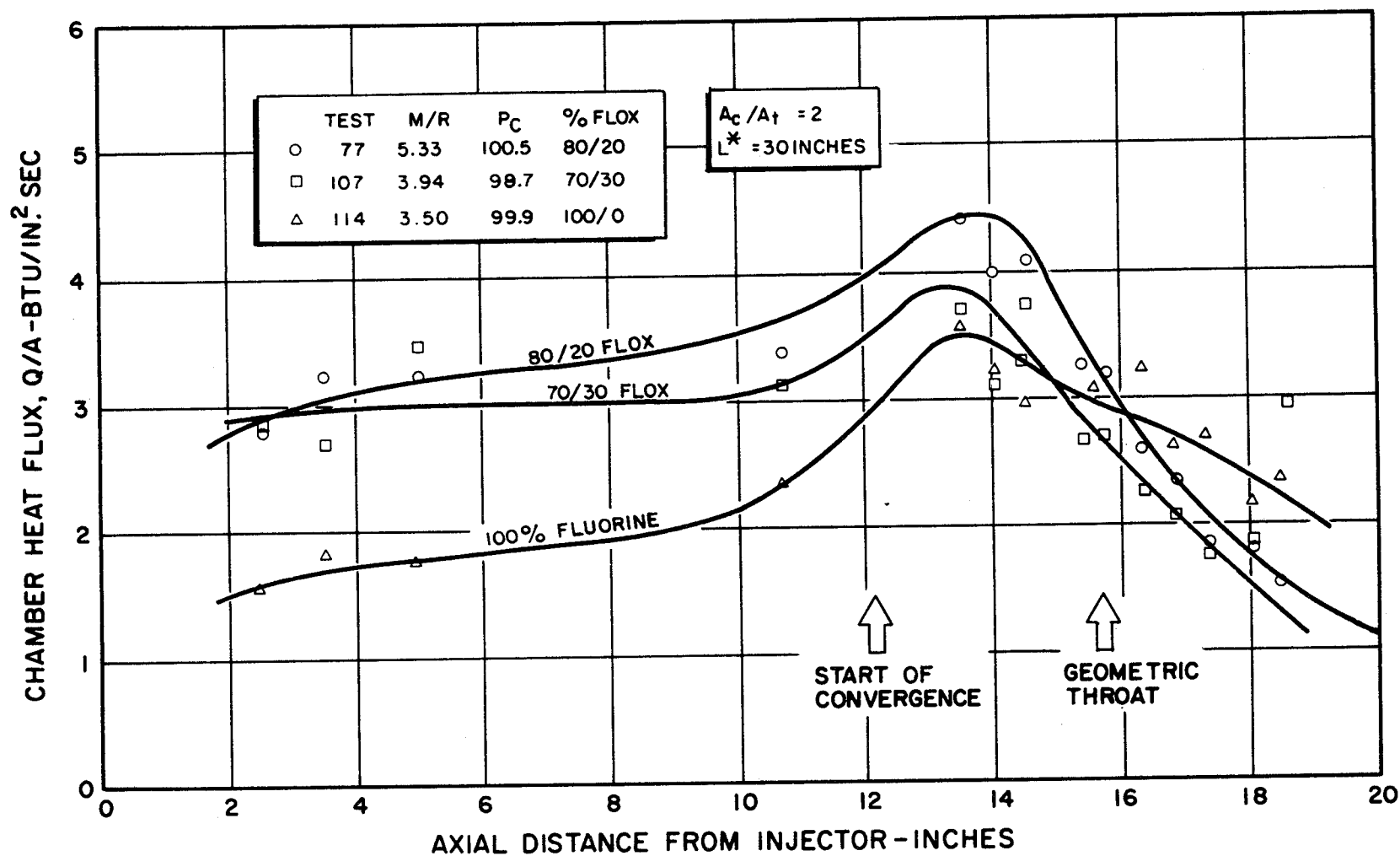


Figure 42. Characteristic Heat Flux Curves Showing Effect of Oxidizer Fluorine Concentration
(Tests were conducted at optimum mixture ratio for specific oxidizer in combination
with 55 percent CH_4 -45 percent C_2H_6)

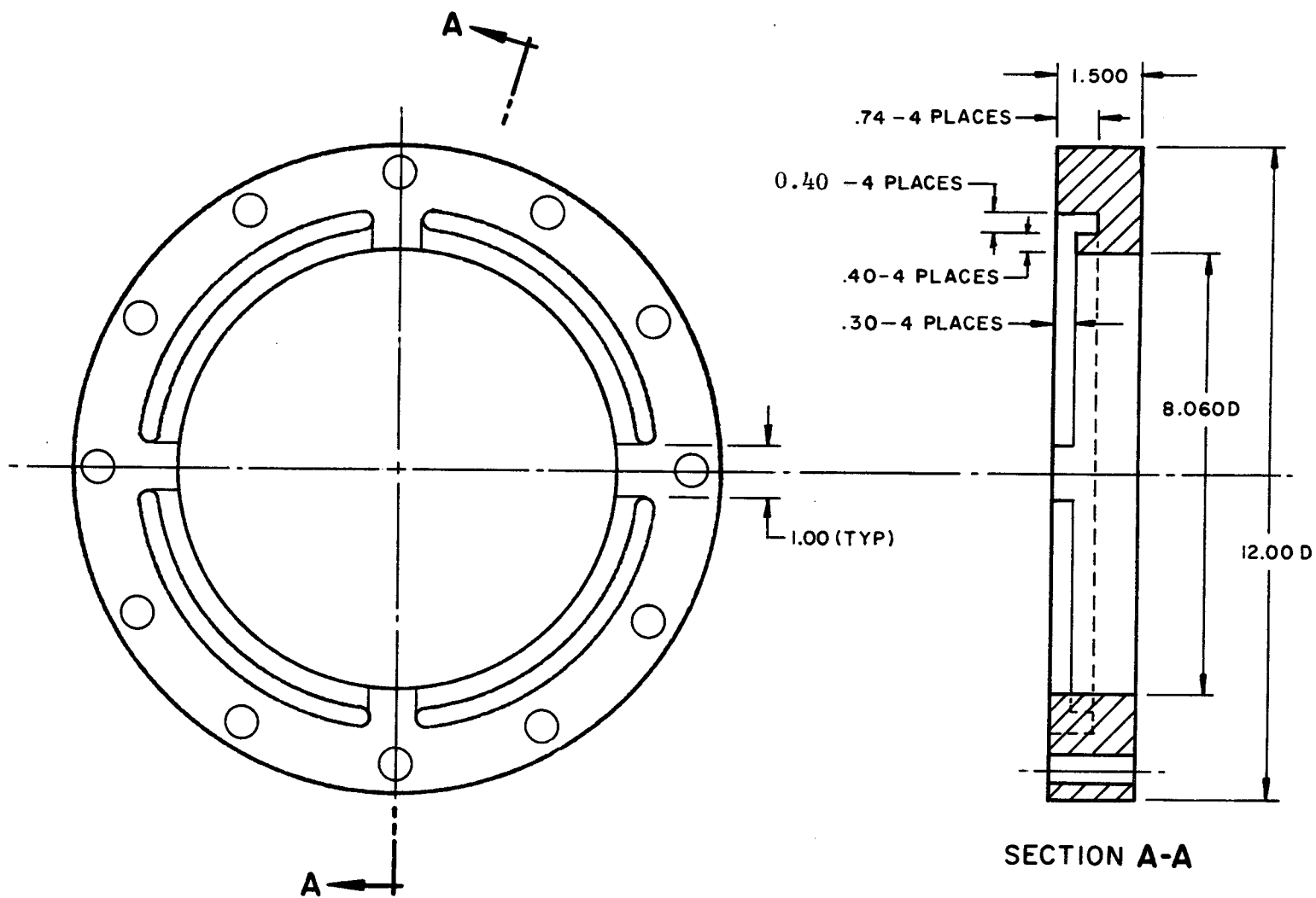


Figure 43. Sketch of Acoustic Absorber Used With Injector P-2-M2

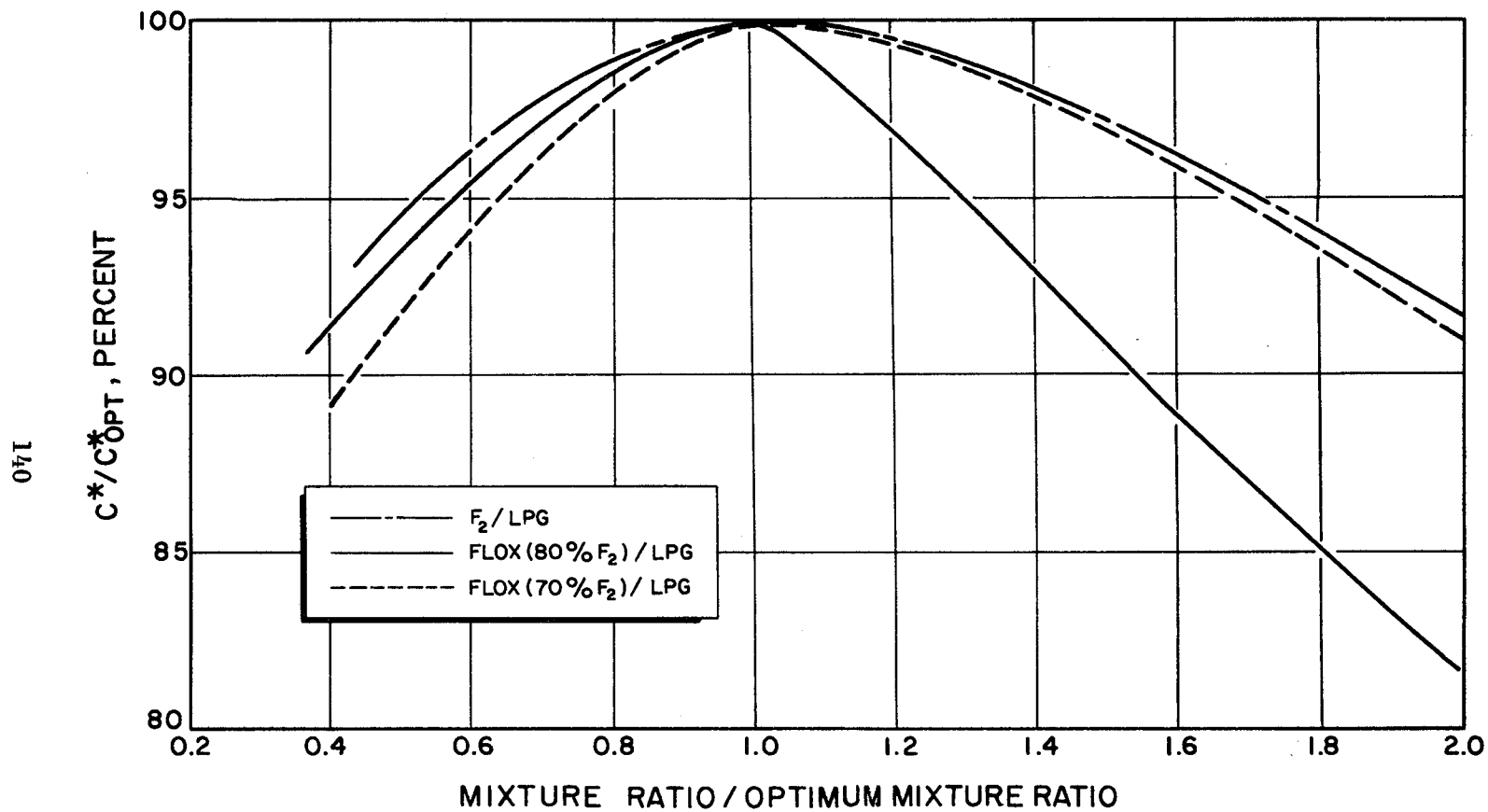


Figure 44. Percent of Optimum c^* as a Function of (Mixture Ratio/Optimum Mixture Ratio) for Several FLOX Mixtures With 55 Percent CH_4 -45 Percent C_2H_6 LPG Blend

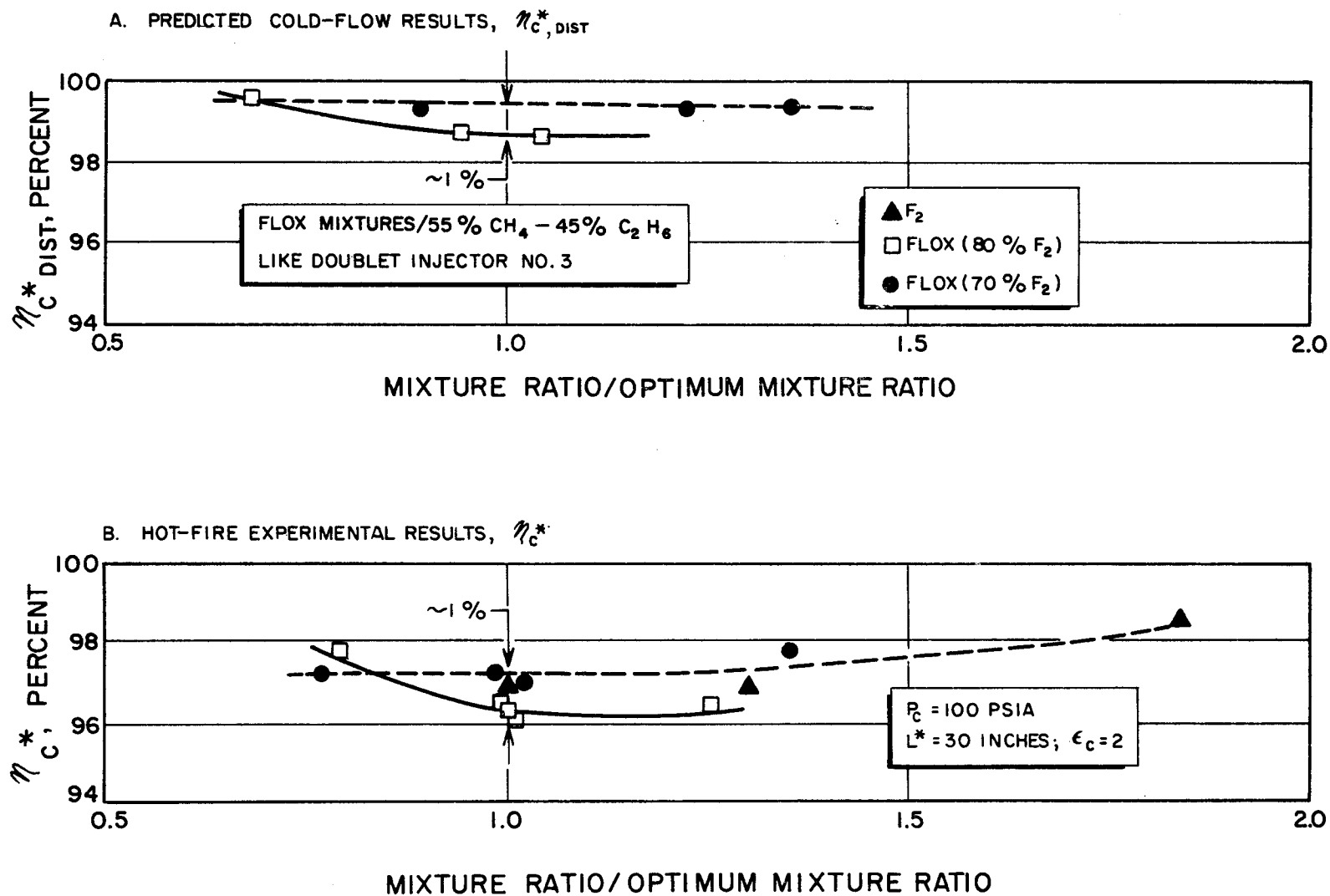


Figure 45. Effect of Nonuniform Distribution on Performance for Several FLOX Mixtures/LPG as a Function of Operating Mixture Ratio/Optimum Mixture Ratio

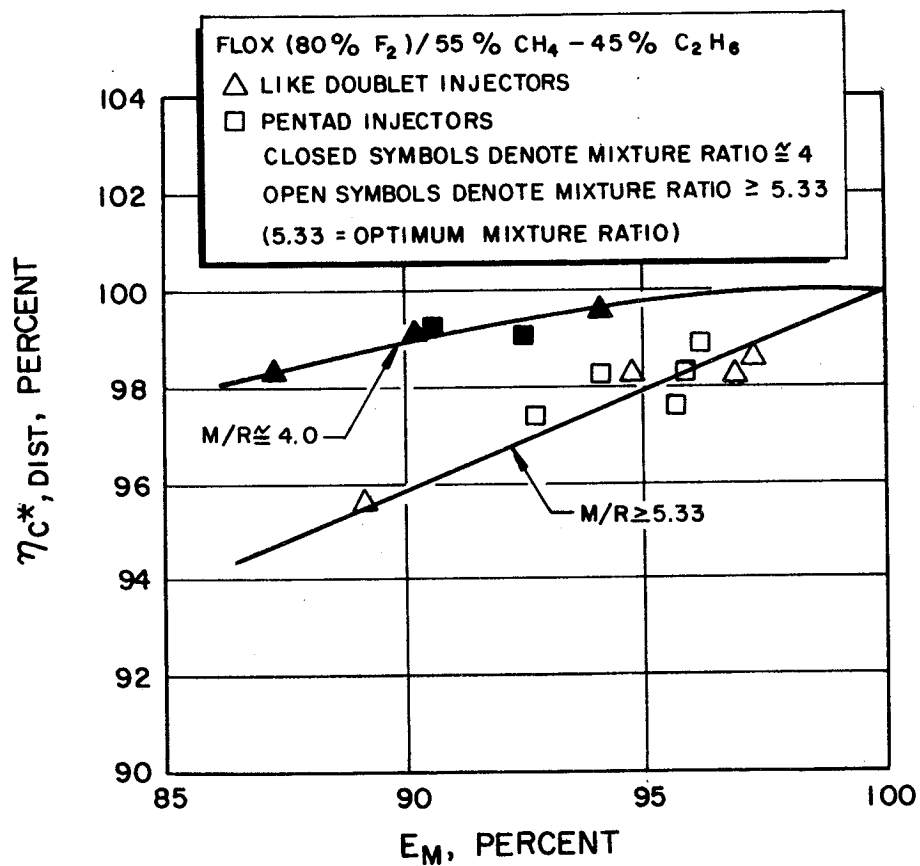
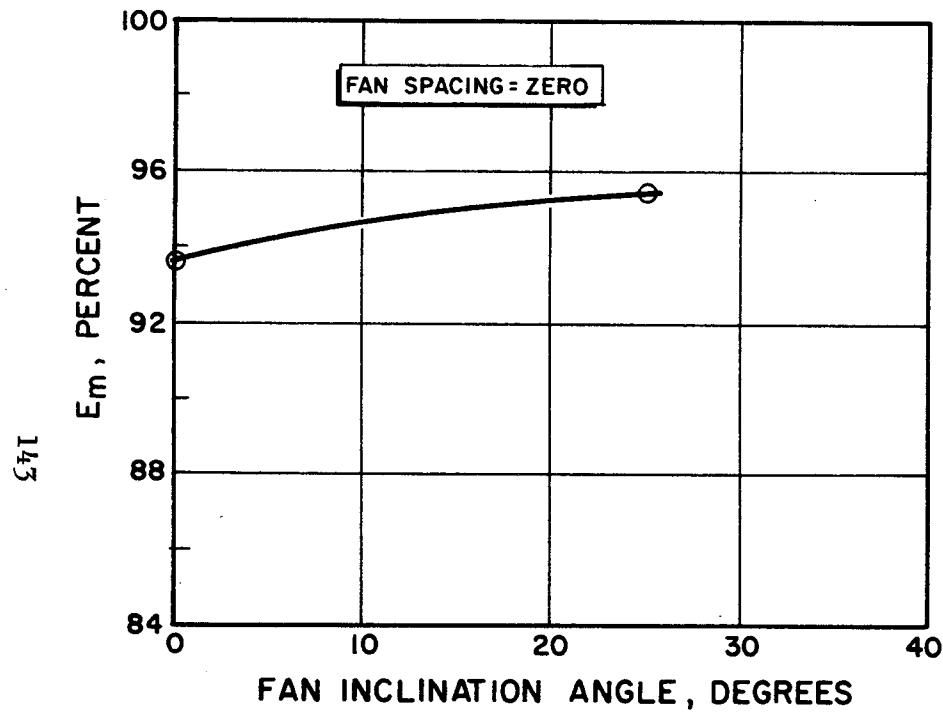
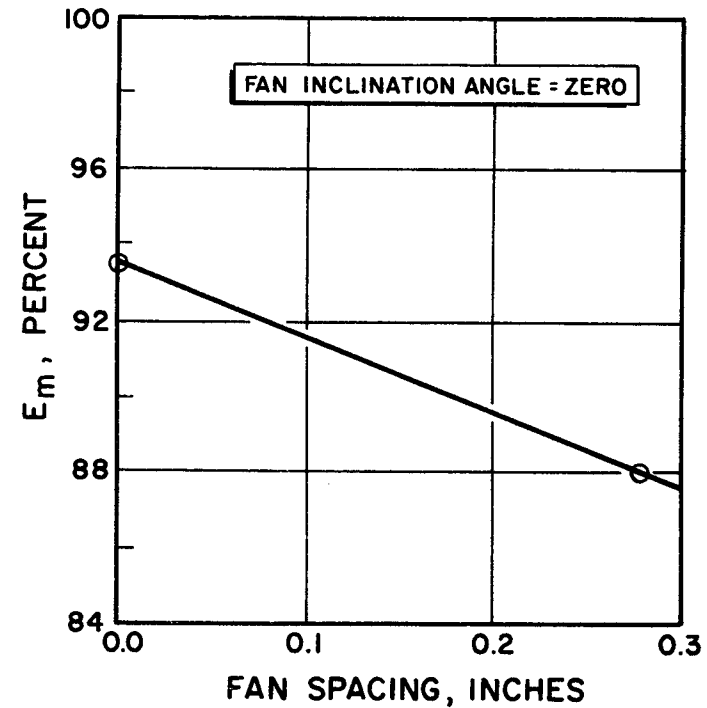


Figure 46. Predicted Effect of Nonuniform Distribution on Performance, $\eta_{c^*, \text{dist}}$, as a Function of Measured Distribution Efficiency, E_m , and Mixture Ratio

FULL SCALE (112 ELEMENTS) INJECTORS



A. E_m AS A FUNCTION OF FAN INCLINATION ANGLE



B. E_m AS A FUNCTION OF FAN SPACING

Figure 47. Measured Mixture Ratio Distribution Efficiency, E_m , as a Function of Fan Inclination Angle and Fan Spacing for Like-Doublet Injectors

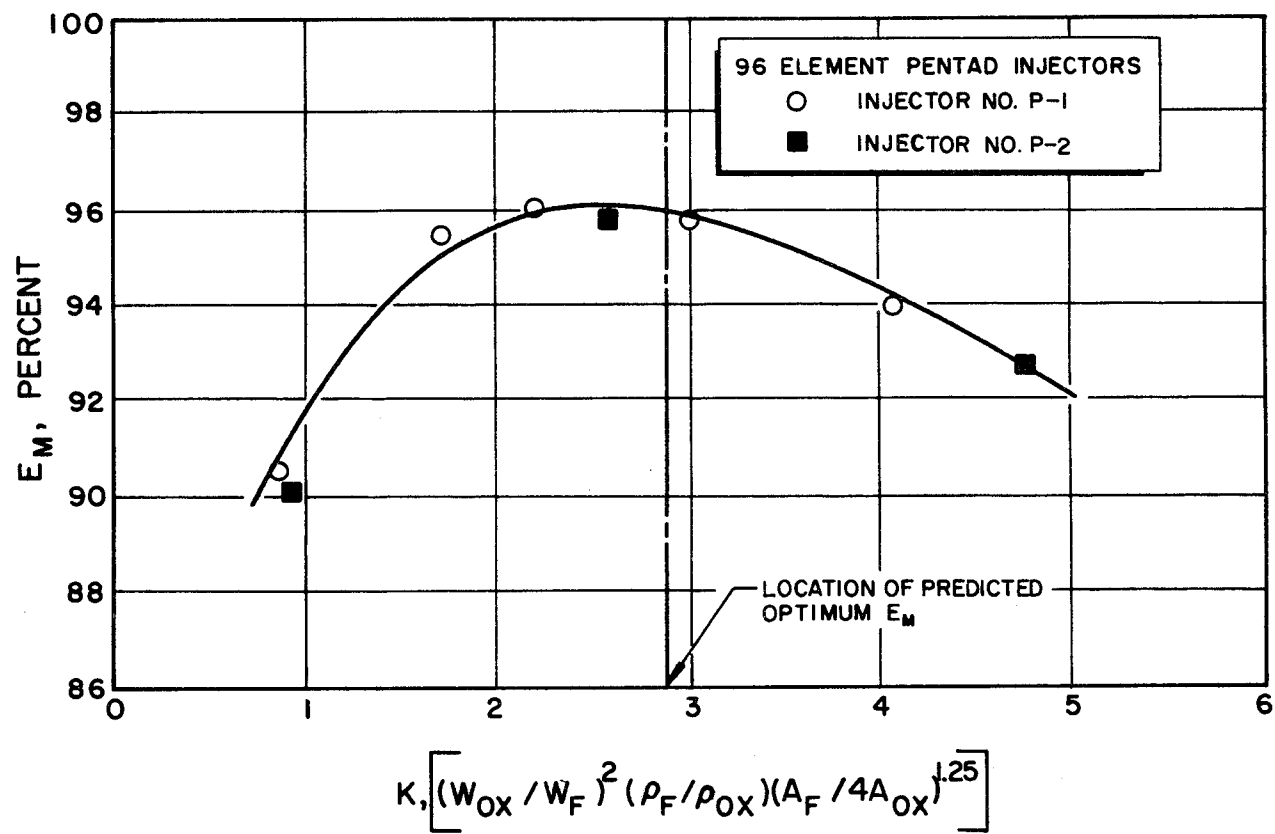


Figure 48. Measured Distribution Efficiency, E_m , as a Function of Distribution Parameter, K , for Two Pentad Injectors

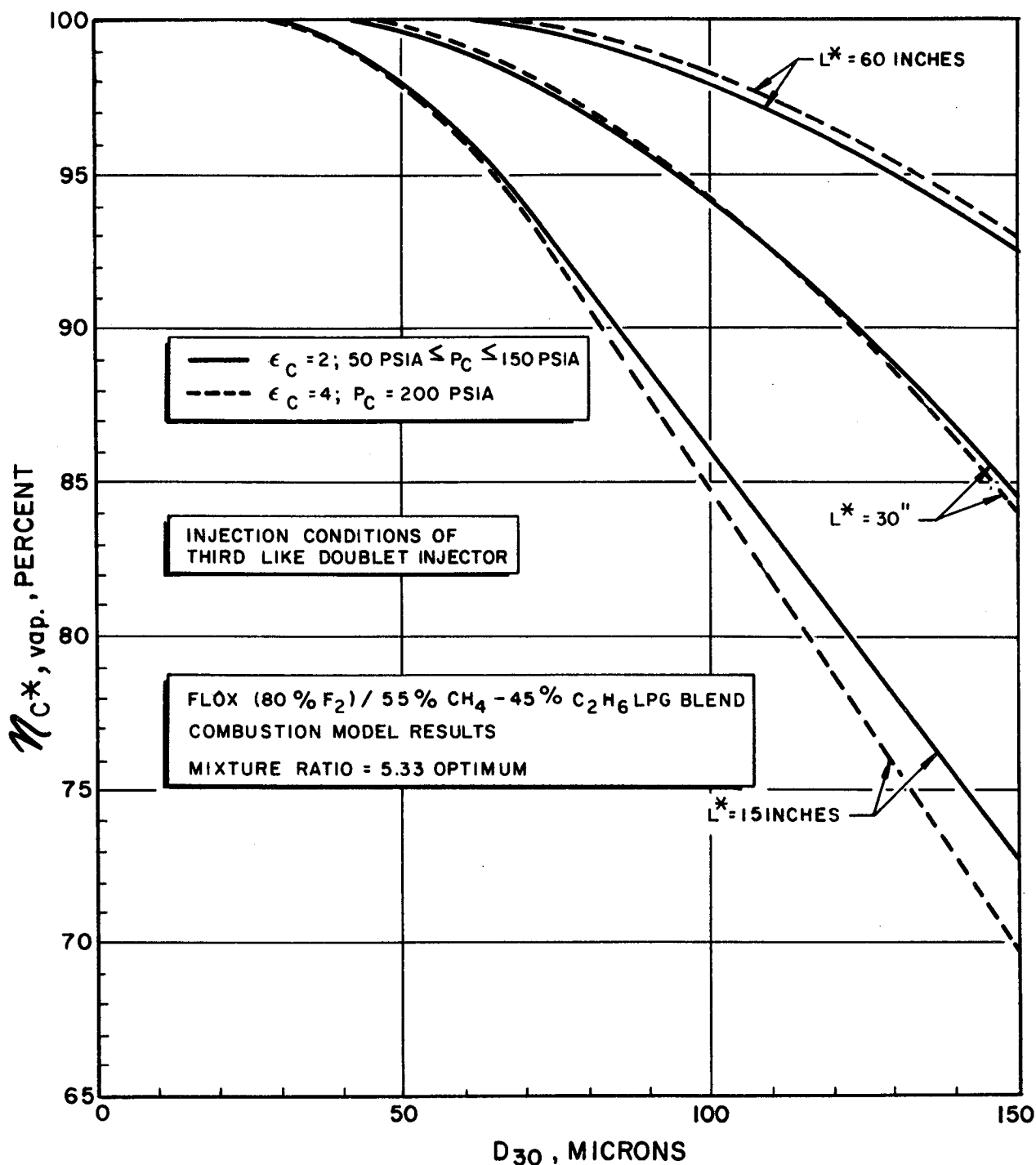


Figure 49. Effect of Propellant Dropsize and Chamber Geometry on Characteristic Velocity Efficiency (due to vaporization) for FLOX/LPG

FLOX MIXTURES / 55% CH₄ - 45% C₂H₆ LPG BLEND
 50 PSIA ≤ P_c ≤ 200 PSIA
 15-INCHES ≤ L* ≤ 60-INCHES
 NOMINAL MIXTURE RATIO = THEORETICAL OPTIMUM
 OPEN SYMBOLS : ε_c = 2 (P_c = 100 PSIA)
 CLOSED SYMBOLS : ε_c = 4 (P_c = 200 PSIA)
 ● P_c = 50 PSIA
 ● P_c = 150 PSIA

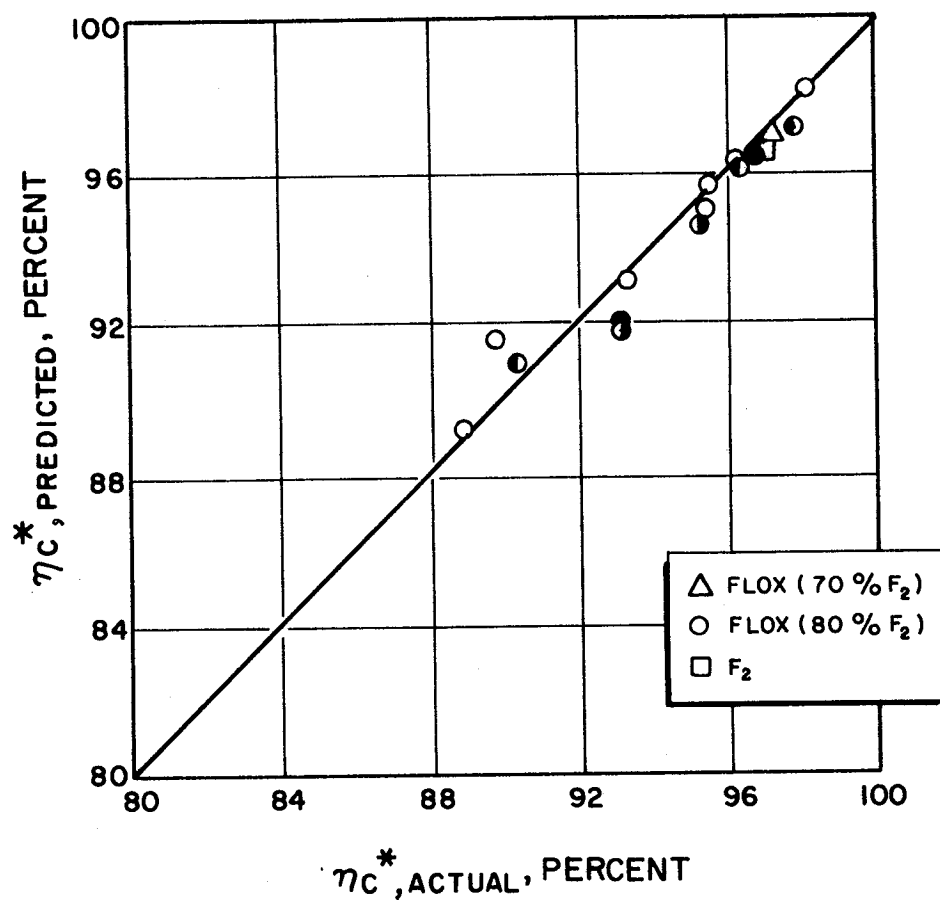


Figure 50. Comparison of Predicted and Actual Performance for Like-Doublet Injectors

APPENDIX A

CALCULATION OF CORRECTED c^* EFFICIENCY

INTRODUCTION

The index of injector performance used in this experimental program was corrected c^* efficiency. This parameter was calculated by two independent methods, one based on measurement of chamber pressure and the other on measurement of thrust. Details of the computational procedures and of the corrections applied are given in this appendix. A numerical example is included.

CALCULATIONS BASED ON CHAMBER PRESSURE

Characteristic velocity efficiency based on chamber pressure is defined by the following equation:

$$\left(\eta_{c^*}\right)_{P_c} = \frac{(P_c)_o (A_t)_{\text{eff}} g_c}{(\dot{w}_T) (c^*)_{\text{theo}}} \quad (\text{A-1})$$

where

- $(P_c)_o$ = stagnation pressure at the throat, psia
- $(A_t)_{\text{eff}}$ = effective thermodynamic throat area, in.²
- g_c = conversion factor (32.174 lbm-ft/lbf-sec²)
- \dot{w}_T = total propellant weight flowrate, lbm/sec
- $(c^*)_{\text{theo}}$ = theoretical characteristic velocity based on shifting equilibrium, ft/sec

Values calculated from Eq. A-1 are referred to as "corrected" c^* efficiencies, because the factors involved are not measured directly, but are obtained by application of suitable corrections to measured parameters. Thus, stagnation pressure at the throat was obtained from measured static

pressure near the start of nozzle convergence by assumption of isentropic expansion; effective throat area was estimated from measured geometric area by allowing for radius changes during firing and for nonunity discharge coefficient; and chamber pressure was corrected to allow for energy losses from the combustion gases to the chamber wall by heat transfer and friction. Equation A-1 may therefore be written as follows:

$$\left(\eta_{c*}\right)_{P_c} = \frac{P_c A_t g_c f_p f_{TR} f_{DIS} f_{FR} f_{HL}}{(\dot{w}_o + \dot{w}_f) (c^*)_{theo}} \quad (A-2)$$

where

- P_c = measured static pressure near the start of nozzle convergence, psia
- A_t = measured geometric throat area, in.²
- \dot{w}_o = oxidizer weight flowrate, lbm/sec
- \dot{w}_f = fuel weight flowrate, lbm/sec
- f_p = factor correcting observed static pressure to throat stagnation pressure
- f_{TR} = factor correcting for change in throat radius during firing
- f_{DIS} = factor correcting throat area for effective discharge coefficient
- f_{FR} = factor correcting measured chamber pressure for frictional drag of combustion gases at chamber wall
- f_{HL} = factor correcting measured chamber pressure for heat losses from combustion gases to chamber wall

Methods of estimation of the various correction factors are described in the following paragraphs.

Pressure Correction (f_p)

Measured static pressure near the start of convergence was converted to stagnation pressure at the throat by assumption of no combustion in the nozzle and application of the isentropic flow equations.

For calculation of a "valid" performance value, care must be taken to ensure measurement of a "valid" static chamber pressure near the start of nozzle convergence. Experience gained on this and related programs (Ref. A-1) at Rocketdyne indicate that a definite increase in static pressure can occur near the start of convergence. This increase in pressure appears to be caused by the subsonic decelerating effects associated with the turning of the combustion gases by the converging walls prior to acceleration in the nozzle. The magnitude of this increase is dependent upon the geometric configuration of the nozzle. Measurement of the static chamber pressure must be taken sufficiently upstream of the start of convergence so that its value is not affected by the subsonic decelerating effects discussed above. Furthermore, chamber pressure must be measured where combustion is nearly complete. During this program, procedures were followed which accounted for these effects and, thereby, produced valid static pressure measurements for calculation of performance. These procedures are discussed in the following paragraphs.

To ensure that the proper static pressure measurement was being employed for calculation of performance, the hot-firing static pressure profile along the wall of the combustion chamber was determined. Static pressure taps were located axially along the combustion chamber wall so that the pressure profile in the region near the start of convergence would be well-defined. The combustion chamber geometry and axial location of the chamber pressure taps are noted in the upper portion of Fig. A-1 for the reference ($L^* = 30$ inches; $\epsilon_c = 2$) chamber configuration.

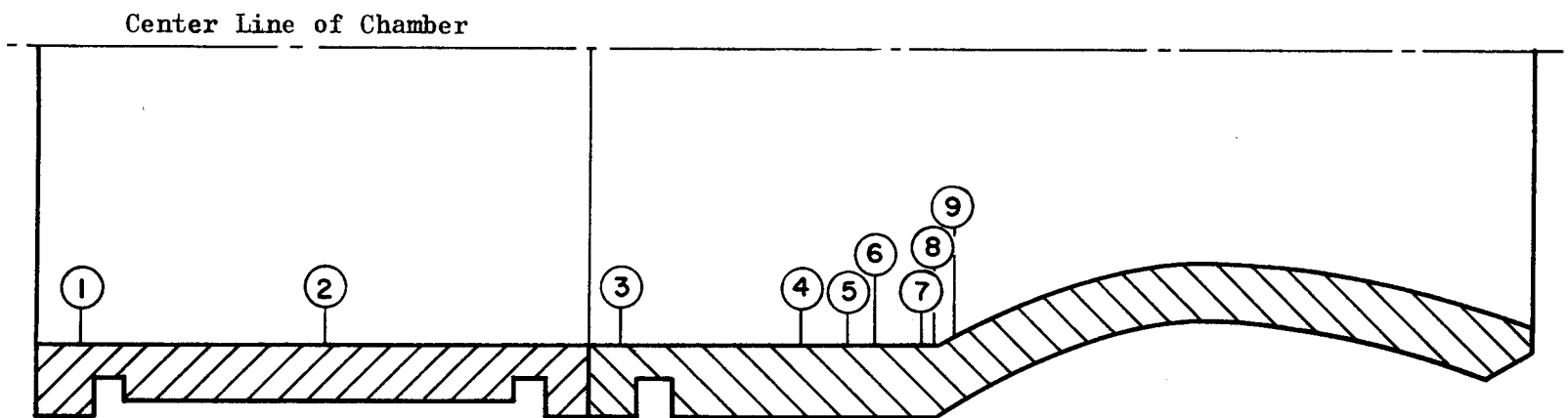
The static pressure profile for a typical (representative) hot-fire test is shown in the bottom portion of Fig. A-1. All pressure are referenced to the stagnation pressure at Position No. 6 (~ 0.75 -inch upstream of the start of convergence). The region of rapidly decreasing pressure represents the region where the majority of combustion is occurring. Reasons for the increase in pressure near the start of convergence were discussed above. To obtain a valid static pressure for calculation of performance, the static pressure corresponding to that measured at pressure tap 5 was used. This tap is located approximately 1 inch prior to start of convergence.

Static pressure was measured $1/2$ inch before the start of convergence in the 4:1 contraction ratio chambers. This should result in valid static chamber pressure measurements (for calculation of performance) for the subject chamber configurations because of the low chamber gas velocity associated with these chambers.

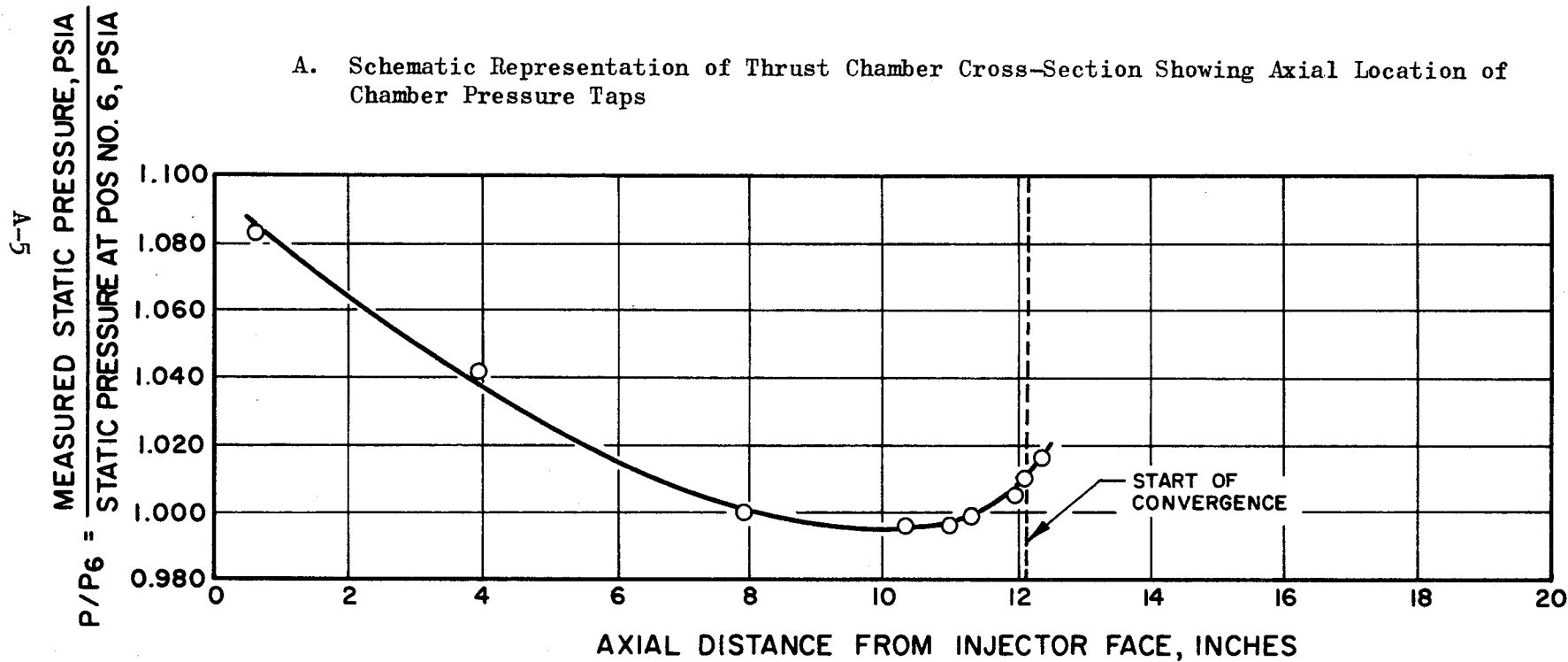
The values of f_p , the stagnation-to-static pressure ratios, were estimated to be 1.058 and 1.013 for the 2-to-1 and 4-to-1 contraction ratio chambers, respectively. Variations in the shifting-equilibrium specific heat ratio were minor over the range of test conditions (chamber pressure, mixture ratio, and percent F_2 in FLOX) employed. These same correction factors ($f_p = 1.058$ for $\epsilon_c = 2$ and 1.013 for $\epsilon_c = 4$) were therefore considered applicable over the entire test matrix.

Throat Radius Correction (f_{TR})

Temperature gradients produced in an uncooled nozzle wall by radiative and convective heat transfer from the hot combustion gases result in thermal stresses which can affect the throat radius. Consequently, the geometric throat diameter measured in an ambient-temperature nozzle is not necessarily the same as that which exists during firing. Furthermore, throat diameter during firing will be a function of time, as well as of the physical properties of the throat material, the temperature and pressure of the combustion gases, and the nozzle geometry (i.e., wall thickness, etc.).



A. Schematic Representation of Thrust Chamber Cross-Section Showing Axial Location of Chamber Pressure Taps



B. Chamber Pressure Profile for Reference ($L^* = 30$ Inches; $\epsilon_c = 2$) Chamber

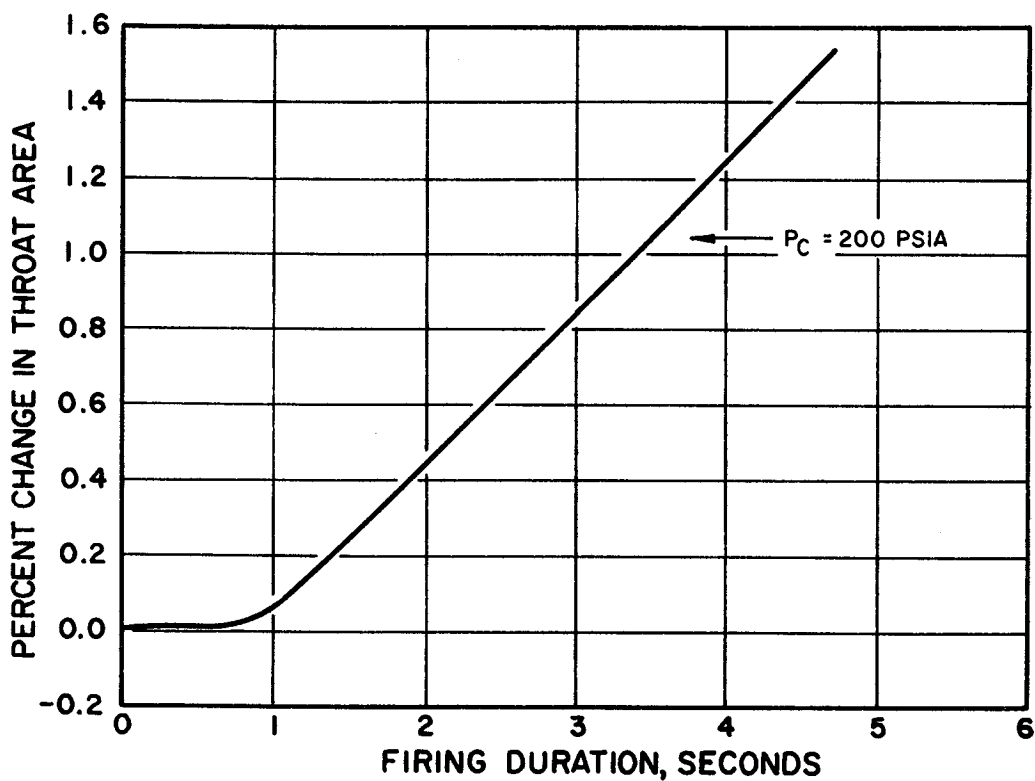
Figure A-1. Axial Location of Chamber Pressure Taps and Chamber Pressure Profile for Reference Chamber Configuration

A Rocketdyne computer program is available which estimates the change in throat radius as a function of time (Ref. A-2). This computation is based on numerical integration of the transient thermal stress equation for a hollow cylinder (Ref. A-3). A cubic temperature distribution is assumed in the wall, plastic as well as elastic strain in the material is considered, and allowance is made for stress caused by combustion gas pressure. Convective film coefficients at the throat based on the Bartz (Ref. A-4) method of calculation and gas temperatures based on 97-percent combustion efficiency were used for program input.

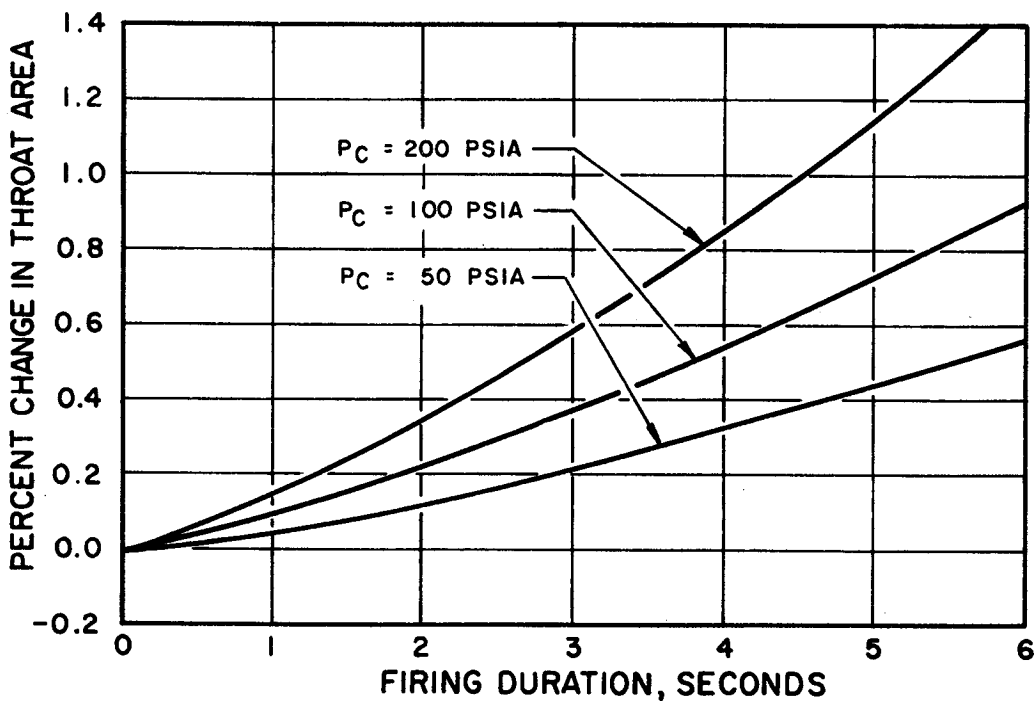
Results of the calculations are presented in Fig. A-2, which indicates the change in geometric throat area as a function of firing duration. The upper portion of the figure presents results for the 4:1 contraction ratio nozzle. Results for the 2:1 contraction ratio nozzle are presented in the bottom portion of the figure. Differences in the values at each of the three nominal chamber pressures (lower portion of Fig. A-2) are not primarily due to pressure effects as such, which are minor, but rather to the corresponding variations in convective film coefficients. For all cases, the throat area change is minor over the time interval of interest. Performance was calculated at approximately 1.5 to 2.0 seconds into the test.

Throat Discharge Coefficient (f_{DIS})

The discharge coefficient is defined as the ratio of actual flowrate through the throat to the theoretical maximum based on geometric throat area and ideal, uniform, one-dimensional flow with no boundary layer. Values of the discharge coefficient may be estimated either analytically or from correlations of the results of experimental studies of gas flow through nozzles. Its value is quite sensitive to the ratio of the upstream wall radius of curvature at the throat-to-the throat radius (R_c/R_t) for values of $R_c/R_t \leq 1.0$. In the present program, R_c/R_t was large (2:1), so that the discharge coefficient could be well-defined by either of the two methods.



A. Four-to-One Contraction Ratio Nozzle



B. Two-to-One Contraction Ratio Nozzle

Figure A-2. Change in Throat Area as a Function of Firing Duration for 2:1 and 4:1 Contraction Ratio Nozzles

In a recent investigation (Ref. A-5) at Rocketdyne, a critical review of available analytical and experimental techniques/results for estimation of f_{DIS} was conducted. Correlations were developed to define the throat discharge coefficient as functions of R_c/R_t and throat Reynolds number. For the nozzles and test conditions employed during this program the value of f_{DIS} is 0.995.

Frictional Drag Correction (f_{FR})

Calculation of c^* efficiency based on chamber pressure is concerned with chamber phenomena up to the nozzle throat. Drag forces to this point are generally small. For the present application, measured chamber pressure should be, and was, corrected for frictional losses only from the injector to the point where the chamber pressure was measured. Details of the method of estimation of f_{FR} are presented below. This discussion is general and applies to frictional losses for performance based on thrust as well as chamber pressure. Differences between the values of frictional losses for thrust and chamber pressure calculated performance are associated with the different regions over which the frictional losses are integrated.

This factor (f_{FR}) corrects for the energy losses caused by drag forces resulting from the viscous action of the combustion gases on the thrust chamber walls. Its magnitude, which is the integral of the local friction forces over the chamber inside wall, was estimated by a boundary layer analysis utilizing the integral momentum equation for turbulent flow. This analysis accounts for boundary layer effects from the injector to the nozzle exit by suitable description of the boundary layer profile and local skin friction coefficient. A computer program was used to carry out a numerical integration of the equation, including effects of pressure gradient, heat transfer, and surface roughness. The program required a potential core solution of the nozzle flow which was obtained from the variable-property, axisymmetric method of characteristics calculation of the flow field outside the boundary layer; corresponding properties for the subsonic combustion chamber flow field were also calculated.

The computed value of f_{FR} in the reference ($L^* = 30$ inches; $\epsilon_c = 2$) chamber was 1.004 at the design operating conditions ($P_c = 100$ psia; $MR = \text{optimum} = 5.33$). Frictional losses for the other chamber configurations are presented in Fig. A-3. The f_{FR} at design operating conditions is plotted as a function of chamber L^* for both contraction ratio chambers in this figure.

Operating mixture ratio and chamber pressure effects on f_{FR} are presented in Fig. A-4. As is noted in Part B of this figure, f_{FR} is essentially independent of mixture ratio over the range of interest (3 to 7). In Part A of Fig. A-4, f_{FR} is plotted as a function of chamber pressure ($L^* = 30$ inches; $MR = 5.33$). Frictional losses decrease slightly with increasing chamber pressure.

These same frictional losses were employed for the tests conducted with FLOX (70 percent F_2) and LF_2 .

Heat Loss Correction (f_{HL})

Heat transfer from the combustion gases to the walls of an uncooled thrust chamber results in loss of enthalpy and thus decreases chamber pressure and thrust. This enthalpy loss is substantially reduced in an ablative chamber and is effectively recovered in a chamber cooled regeneratively by one of the propellants, whose initial enthalpy is raised by the heat absorbed. To obtain a true indication of performance efficiency in an uncooled chamber, measured chamber pressure must be corrected by a factor which accounts for heat loss to the walls. Heat transfer to the injector was neglected in this correction because the injector surface area was small relative to that of the chamber and because a major portion of injector heat flux is absorbed by the injected propellants.

FLOX (80% F₂) / 55% CH₄ - 45% C₂ H₆
 CHAMBER PRESSURE = 100 PSIA
 MIXTURE RATIO = 5.33 = OPTIMUM

— $\epsilon_c = 2$; UPPER LINE FOR PERF BASED ON F
 LOWER LINE FOR PERF BASED ON P_C
 - - - $\epsilon_c = 4$; UPPER LINE FOR PERF BASED ON F
 LOWER LINE FOR PERF BASED ON P_C

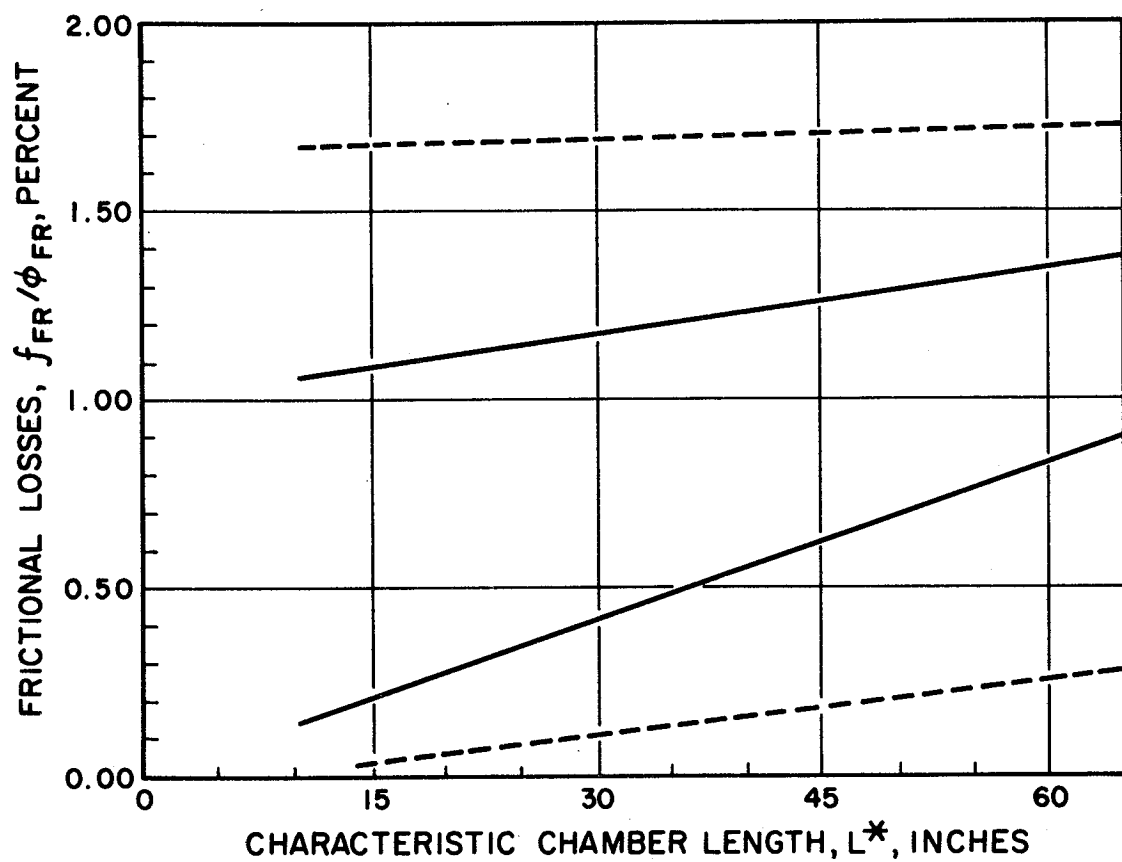
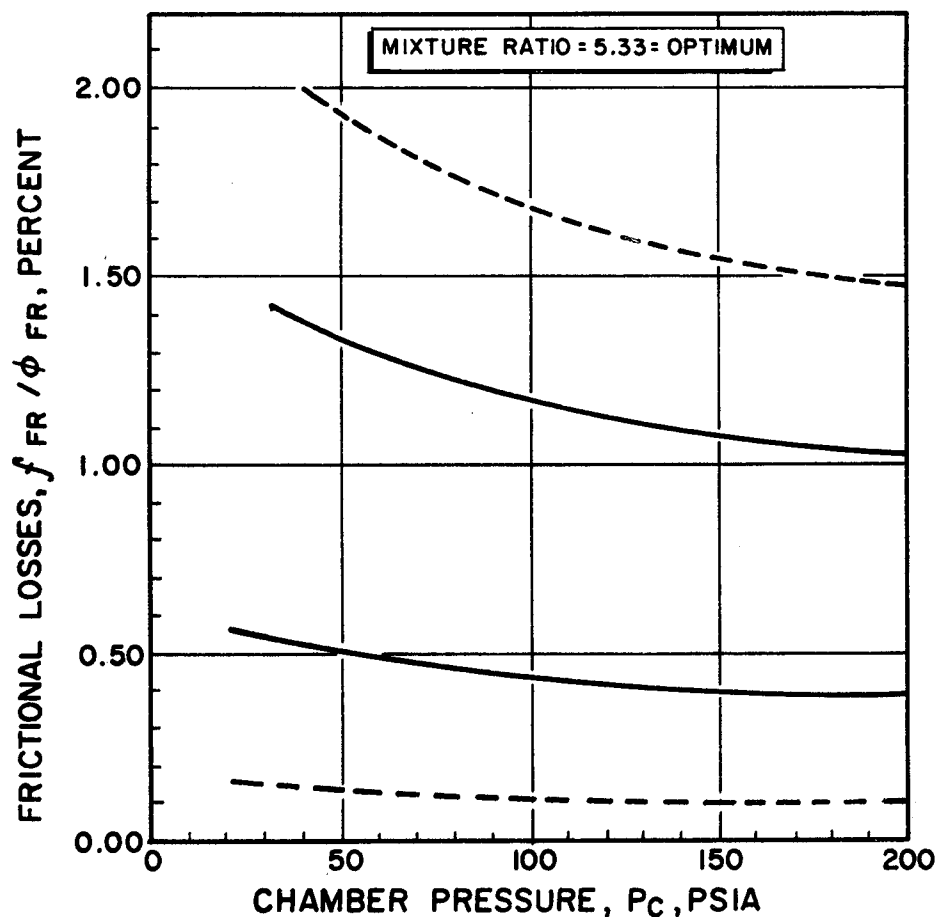


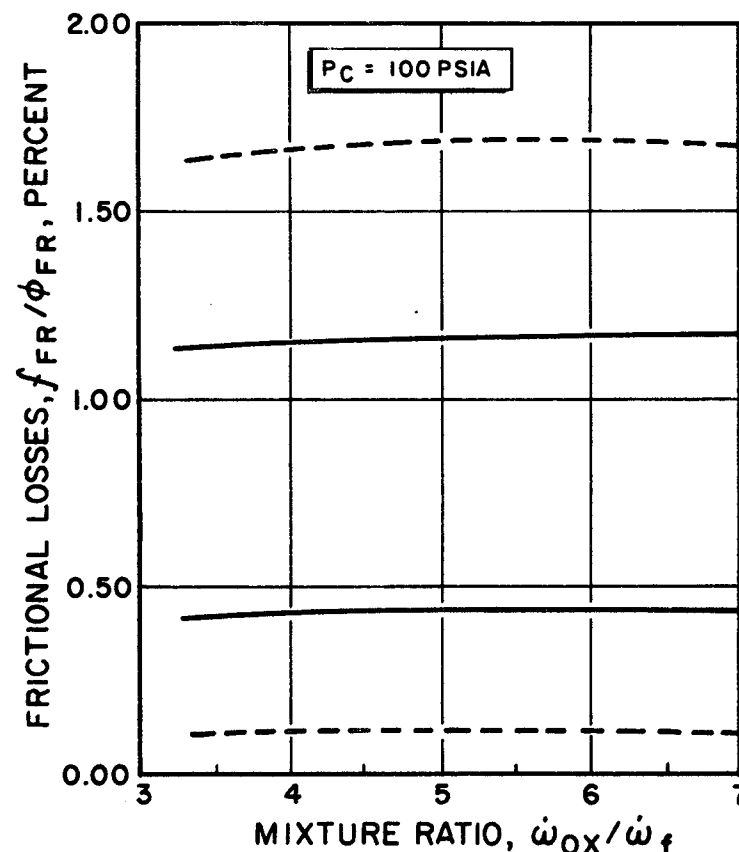
Figure A-3. Performance Frictional Loss Correction as a Function of Characteristic Chamber Length and Contraction Ratio for FLOX/LPG

FLOX (80% F_2) / 55% CH_4 - 45% - C_2H_6
 $L^* = 30$ INCHES

— $\epsilon_c = 2$; UPPER LINE FOR PERF BASED ON F
 LOWER LINE FOR PERF BASED ON P_c
 --- $\epsilon_c = 4$; UPPER LINE FOR PERF BASED ON F
 LOWER LINE FOR PERF BASED ON P_c



A. f_{FR}/ϕ_{FR} as a Function of P_c and ϵ_c



B. f_{FR}/ϕ_{FR} as a Function of Mixture Ratio and ϵ_c

Figure A-4. Performance Frictional Loss Correction as a Function of Chamber Pressure, Mixture Ratio, and Contraction Ratio for FLOX/LPG

Using the following equation, f_{HL} was estimated:

$$f_{HL} = \left\{ 1 + \left[\frac{c_{theo}^*}{c_{meas}^*} \right]^2 \left[\frac{\sum (q/A)A}{\dot{w}_T c_{p_m} T_c} \right] \right\}^{1/2} \quad (A-3)$$

where

- c_{theo}^* = theoretical characteristic velocity at test conditions, based on full shifting equilibrium
- c_{meas}^* = measured characteristic velocity, corrected for the previously discussed losses.
- $\sum (q/A)A$ = observed heat loss to chamber walls
- \dot{w}_T = total propellant flowrate
- c_{p_m} = mean specific heat of combustion chamber gases at test conditions
- T_c = theoretical combustion gas temperature at test conditions

The basis for use of this equation is presented in Ref. A-6 and A-7.

Total heat loss to the chamber walls, in Btu/lb of propellant, was obtained by summation of measured heat fluxes over the appropriate areas:

$$\text{Heat loss} = \frac{\sum (q/A)A}{\dot{w}_T} \quad (A-4)$$

where

- q/A = experimentally observed heat flux
- A = area applicable to each q/A value
- \dot{w}_T = total propellant flowrate

Only heat losses to the chamber wall between the injector and the chamber pressure tap employed for calculation of performance based on chamber pressure are included in Eq. A-3 or A-4.

A Rocketdyne computer program was used to calculate f_{HL} from measured heat flux values. In the reference chamber, at design operating conditions, the value of f_{HL} was approximately 1.013 for the optimized like-doublet injector. Its value was relatively independent of operating chamber pressure and mixture ratio.

CALCULATIONS BASED ON THRUST

An alternate determination of corrected c^* efficiency is based upon the following defining equation:

$$(\eta_{c^*})_F = \frac{F_{vac} g_c}{(C_F)_{vac} \dot{w}_T (c^*)_{theo}} \quad (A-5)$$

where

- F_{vac} = measured thrust corrected to vacuum conditions by the equation: $F_{vac} = F + P_a A_e$, lbf
- F = measured thrust, lbf
- P_a = ambient pressure, psia
- A_e = area of nozzle exit, in.²
- g_c = conversion factor (32.174 lbf-ft/lbm-sec²)
- $(C_F)_{vac}$ = theoretical shifting thrust coefficient (vacuum)
- \dot{w}_T = total propellant flowrate, lbm/sec
- $(c^*)_{theo}$ = theoretical shifting-equilibrium characteristic velocity, ft/sec

Corrected values of vacuum thrust may be obtained by application of suitable corrections to measurements of thrust made at sea level. With these values, which include allowances for all important departures from ideality, theoretical thrust coefficients may be used for calculation of c^* . That is, C_F coefficient is 100 percent if there is no combustion in the nozzle, if chemical equilibrium is maintained in the nozzle expansion process, and if energy losses from the combustion gases are taken into account.

Applicable corrections to measured thrust are specified in the following equation:

$$(\eta_{c*})_F = \frac{(F + P_a A_e) g_c \phi_{FR} \phi_{DIV} \phi_{HL}}{(C_F)_{vac} (\dot{w}_o + \dot{w}_f) (c^*)_{theo}} \quad (A-6)$$

where

- $(C_F)_{vac}$ = theoretical shifting thrust coefficient (vacuum)
- \dot{w}_o = oxidizer weight flowrate, lbm/sec
- \dot{w}_f = fuel weight flowrate, lbm/sec
- ϕ_{FR} = correction for frictional losses
- ϕ_{DIV} = correction for nozzle divergence
- ϕ_{HL} = correction for heat losses to chamber and nozzle walls

The correction factors in Eq. A-6 were applied to vacuum thrust $(F + P_a A_e)$ instead of to measured site thrust (F) because, for convenience, the correction factors were calculated as changes in efficiency based on theoretical vacuum parameters, so that the total correction was of the form $\Delta F/F_{vac}$.

Although they do not appear explicitly in Eq. A-6, corrections to geometric throat area and to measured static chamber pressure at start of nozzle convergence are implicit in the use of theoretical C_F values. Thus, calculation of corrected c^* efficiency from thrust measurement includes all the corrections described above for calculations from chamber pressure measurement plus an additional one to account for nonparallel nozzle exit flow. However, because $(C_F)_{vac}$ is essentially independent of the very small changes in chamber pressure and contraction ratio which are involved in corrections to P_c and A_t , these corrections are of no practical significance in calculation of c^* from thrust measurements.

Corrections for Frictional Drag (ϕ_{FR})

The basis for and method of calculation of this factor were discussed under calculation of performance based on chamber pressure.

The computed value of ϕ_{FR} in the reference chamber was 1.012 at the design operating conditions. Frictional losses for the other chamber configurations are presented in Fig. A-3. The effects of mixture ratio and chamber pressure on ϕ_{FR} are presented in Fig. A-4.

Correction for Nozzle Divergence (ϕ_{DIV})

The one-dimensional theoretical performance calculations assume that flow at the nozzle exit is uniform and parallel to the nozzle axis. The correction factor, ϕ_{DIV} , allows for nozzle divergence (i.e., for nonaxial flow) and for nonuniformity across the nozzle exit plane. It was calculated by a computer program which utilized the axisymmetric method of characteristics for a variable-property gas.

The geometric efficiency was essentially independent of chamber pressure and mixture ratio for the entire test matrix. Its value, $\phi_{DIV} = 1.018$, was identical for both contraction ratio nozzles.

Correction for Heat Losses (ϕ_{HL})

Heat loss correction factors for performance calculated from measured thrust are similar to those for performance calculated from chamber pressure, except that heat fluxes in the nozzle are included in the calculations. Thus, Eq. A-3 and A-4 were employed with the measured heat flux summed from the injector to nozzle exit.

A Rocketdyne computer program was used to calculate ϕ_{HL} from the measured heat flux values. In the reference chamber, at design operating conditions, the value of ϕ_{HL} was approximately 1.025. Its value was relatively independent of operating pressure and mixture ratio.

NUMERICAL EXAMPLE

The method of performance data reduction and correction are illustrated by the following numerical example. This example is typical of all tests. Data from test No. 77 are analyzed in this example. The subject test was conducted in the reference chamber ($L^* = 30$ inches; $\epsilon_c = 2$) at nominal design operating conditions ($P_c = 100$ psia; mixture ratio = 5.33 = optimum; FLOX (80-percent F_2)/LPG). Pertinent steady-state raw data (static chamber pressure, propellant flowrates, measured thrust) from this test are presented in Table A-1. Figure A-5 presents the chamber heat flux characteristics and pressure profile for the subject test. CRT printouts of the pertinent parameters (as a function of time) were used to determine when steady-state had been achieved. Beckman traces of static chamber pressure, measured thrust, oxidizer flowrate, and fuel flowrate for test No. 77 are shown in Fig. A-6 through A-9. The data slice interval for calculation of performance is noted. Steady-state performance was determined at approximately 2.0 seconds into the 2.5 second test. These traces are representative of the hot-fire tests conducted during the program. Beckman data were used for calculation of performance values.

TABLE A-1
DATA FROM TEST NO. 77

Parameter	Numerical Value of Parameter
Static Chamber Pressure ¹	$(81.42 + 80.95 + 81.42)/3 = 81.26$ psig = 94.96 psia
Oxidizer Flowrate ²	$(10.532 + 10.399)/2 = 10.466$ lbm/sec
Fuel Flowrate ²	$(1.962 + 1.961)/2 = 1.962$ lbm/sec
Measured Thrust	2877.0 lbf
D_t/A_t ³	5.705 in./25.562 in. ²
Mixture Ratio	5.33
c_{theo}^*	6918.6 ft/sec

¹Average value of the static chamber pressure measured at three circumferential locations (120 degrees apart) at Position No. 7 (see Fig. A-1).

²Value is average of two flowmeters in series.

³Measured with hardware at ambient temperature (~ 70 F).

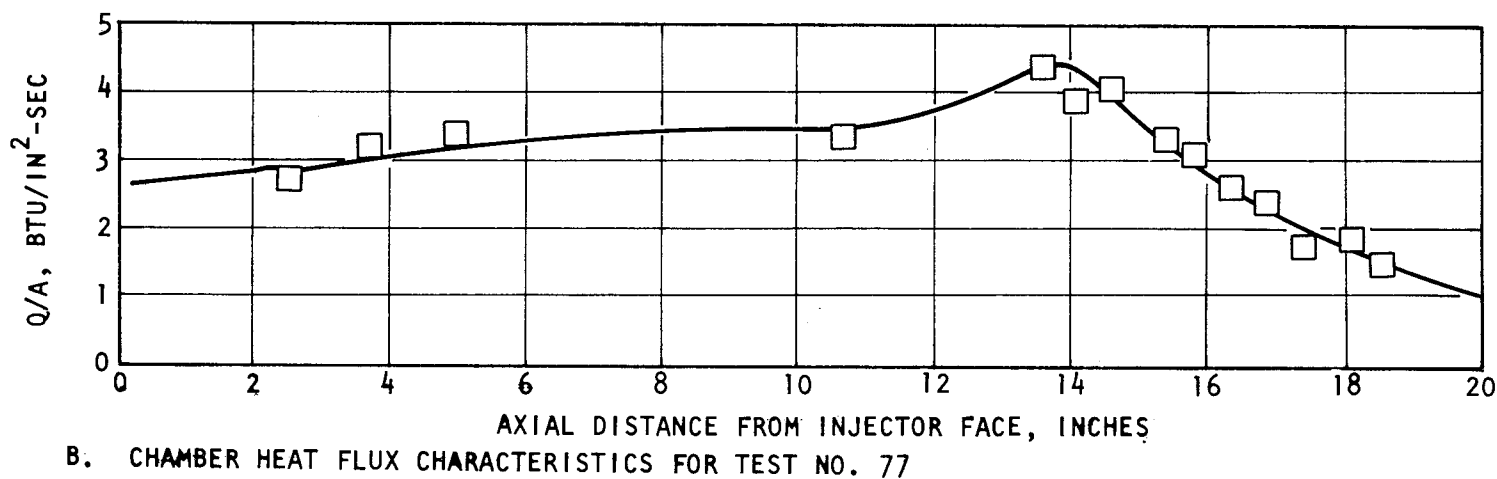
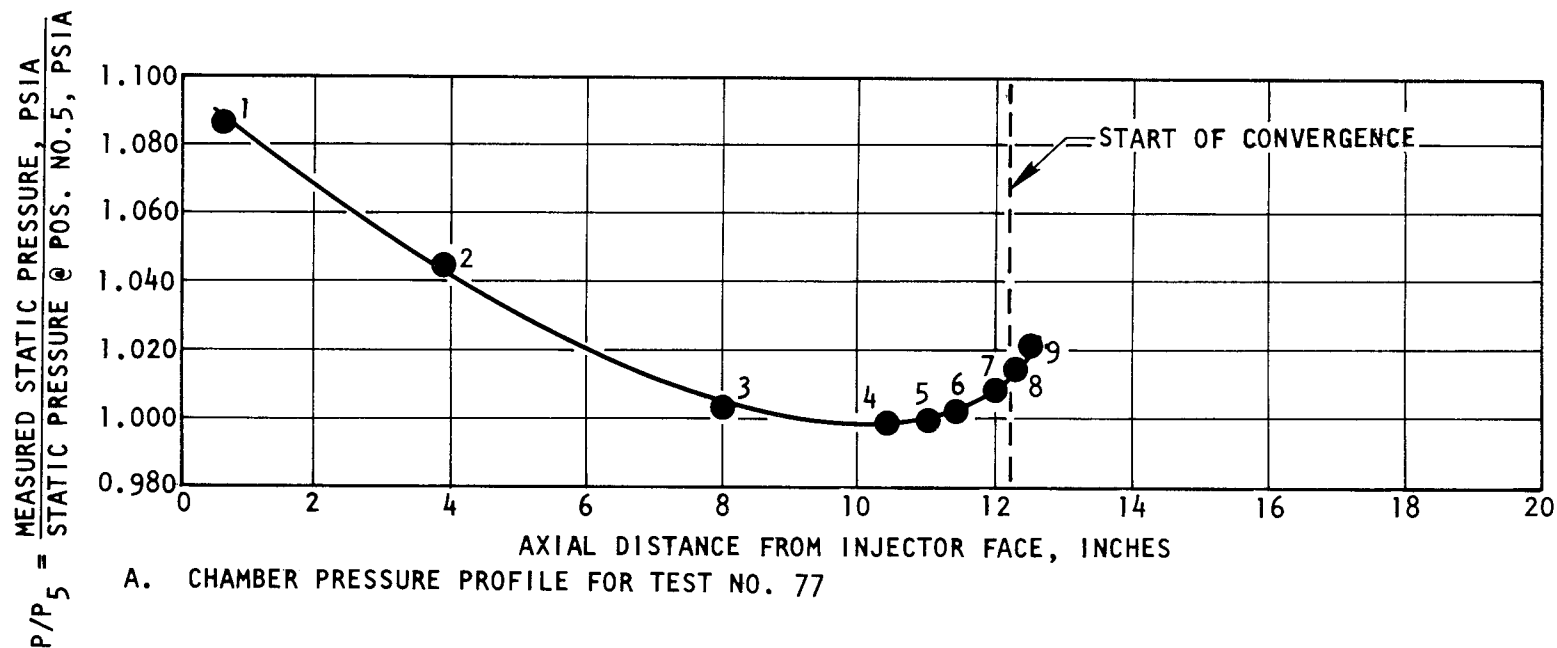
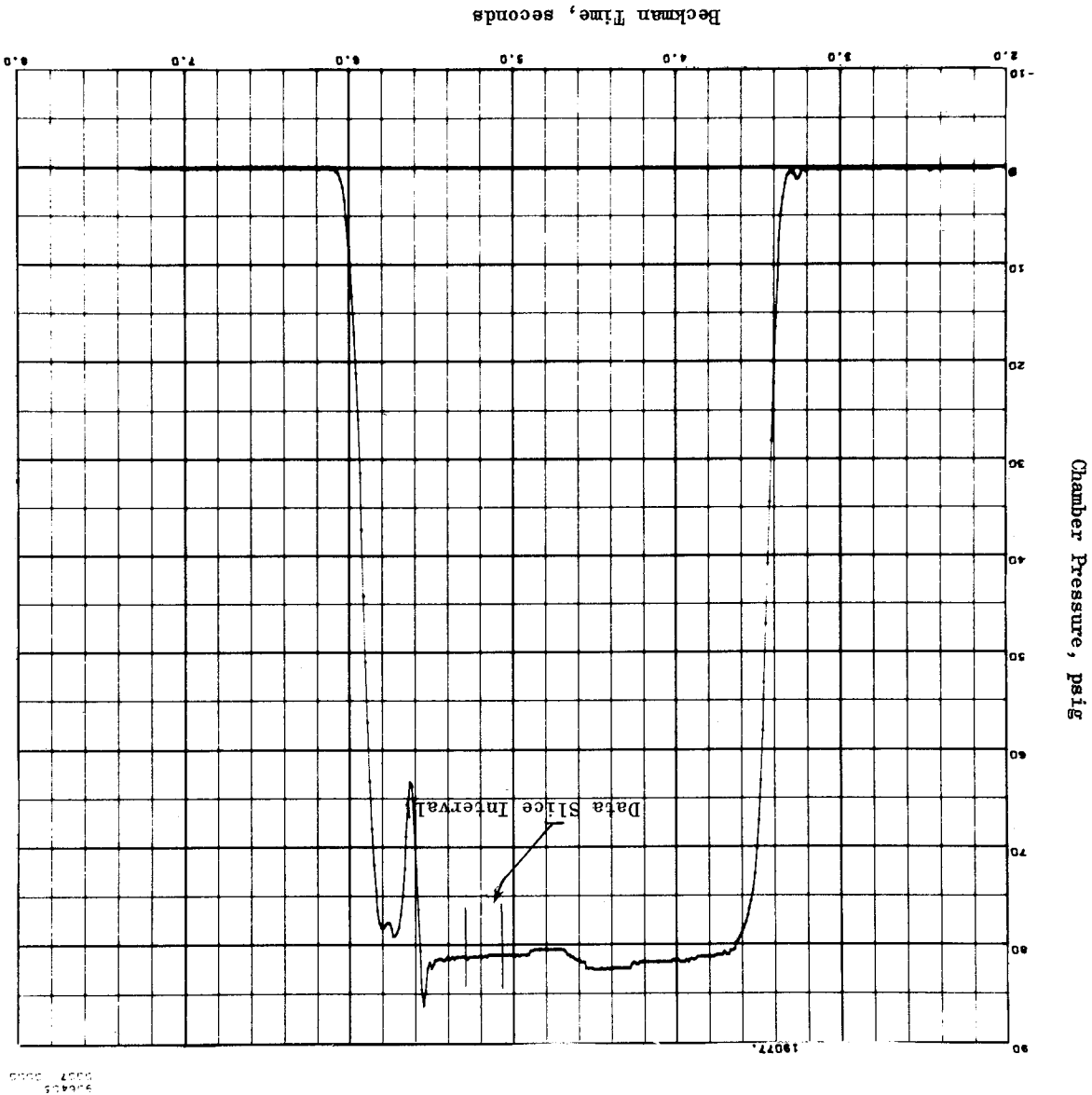


Figure A-5. Chamber Pressure Profile and Heat Flux Characteristics for Test No. 77
 ($L^* = 30$ inches; $\epsilon_c = 2$; Nominal $P_c = 100$ psia; Nominal MR = 5.33 = opt.)

Figure A-6. Static Chamber Pressure (at Position No. 7) as a Function of Beckman Time for Test No. 77



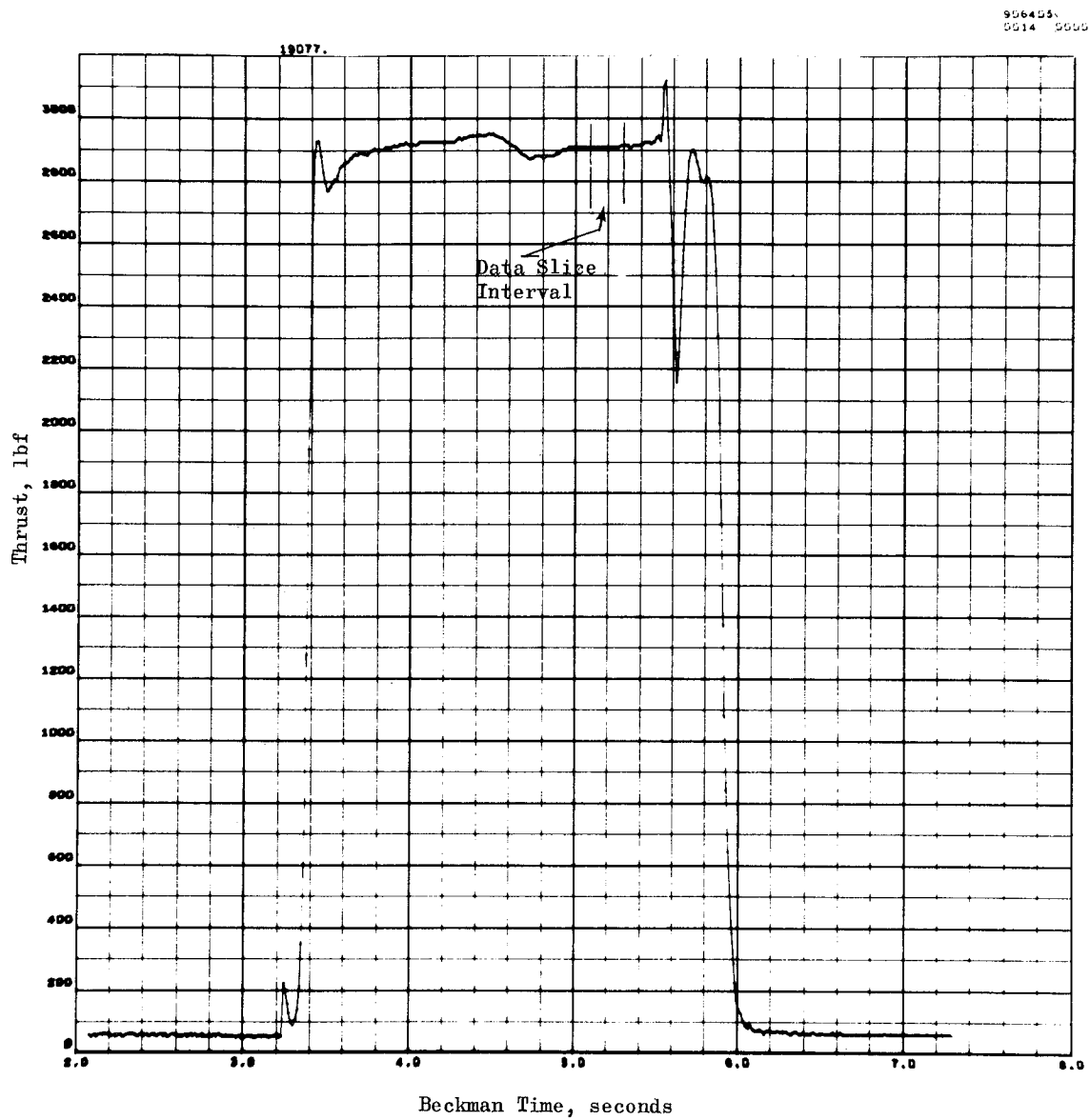


Figure A-7. Measured Thrust as a Function of Beckman Time for Test No. 77

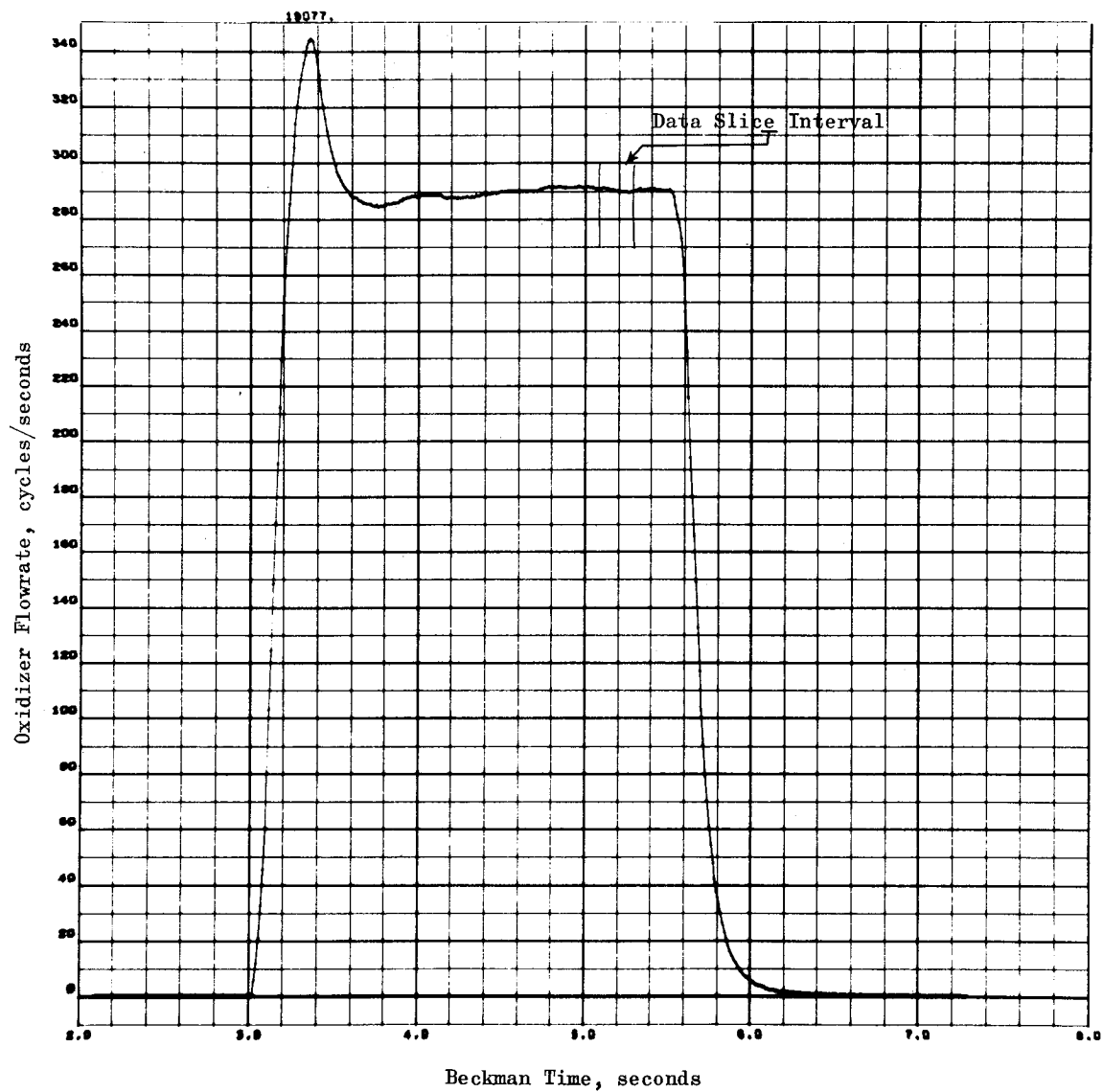


Figure A-8. Oxidizer Flowrate (Cycles/Second) as a Function of Beckman Time for Test No. 77

956453
0021 5555

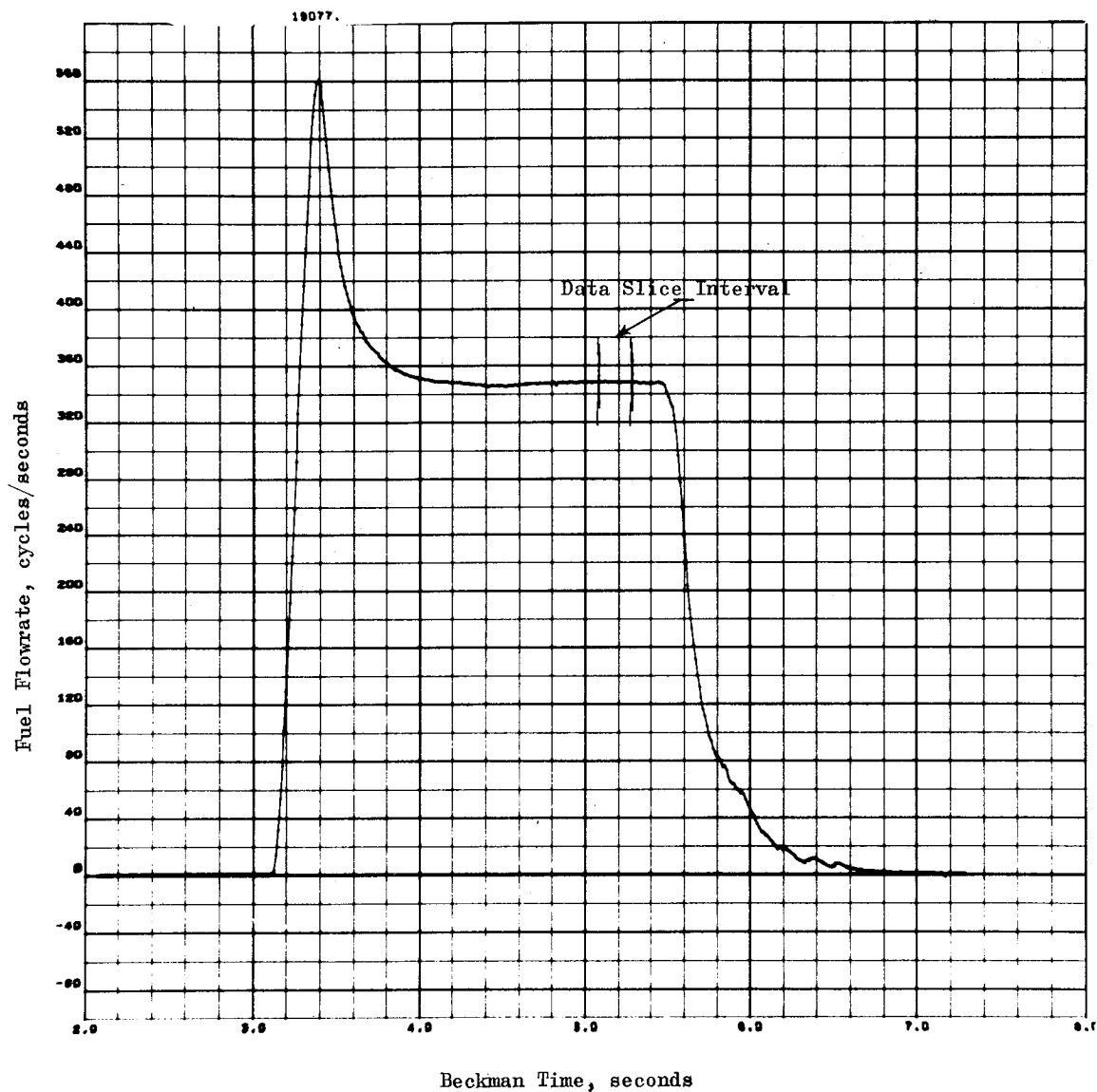


Figure A-9. Fuel Flowrate (Cycles/Seconds) as a Function of Beckman Time for Test No. 77

Performance Based on Chamber Pressure

Corrected c^* efficiency based on chamber pressure measurement was calculated using Eq. A-2. Values of the measured parameters (\dot{w}_o , \dot{w}_f , and A_t) and the theoretical c^* used in Eq. A-2 are shown in Table A-1. As was noted on page A-4, to obtain a valid static chamber pressure measurement for calculation of performance, the static pressure corresponding to that measured at Position No. 5 (Fig. A-1) should be used. For most tests conducted in the 2:1 contraction ratio chambers, static chamber pressure was measured at only one axial position. (Position No. 7 at three circumferential locations 120 degrees apart). This value was converted to the static pressure corresponding to Position No. 5 as follows:

$$\begin{aligned}(P_c)_{\text{Position No. 5}} &= \text{static chamber pressure to be used in Eq. A-2} \\ &= \text{measured static pressure at Position No. 7 times} \\ &\quad \text{the ratio of the static pressures at Positions 5} \\ &\quad \text{and 7. This ratio is 0.99 for the 2:1 contraction} \\ &\quad \text{ratio chambers (see Fig. A-1 or A-5).}\end{aligned}$$

The static chamber pressure measured 1/2-inch from the start of nozzle convergence was used for calculation of performance in the 4:1 contraction ratio chambers.

Methods of estimation of the various connection factors in Eq. A-2 were outlined previously. Estimation of these correction factors for test No. 77 is described in the following paragraphs.

Pressure Correction (f_p). Measured static pressure was converted to stagnation pressure at the throat by assumption of no combustion in the nozzle and application of the isentropic flow equations. The value of f_p , the stagnation-to-static pressure ratio, was estimated to be 1.058 for the 2:1 contraction ratio chambers.

Throat Radius Connection (f_{TR}). Throat area changes were minor over the time interval of interest. The value of the f_{TR} was obtained from Fig. A-2.

For the subject configuration/operating conditions ($\epsilon_c = 2:1$; $P_c = 100$ psia), f_{TR} was estimated to be 1.002.

Throat Discharge Coefficient (f_{Dis}). For all experiments, the throat discharge coefficient was estimated to be 0.995.

Frictional Drag Correction (f_{FR}). Frictional losses were estimated from Fig. A-3 and A-4. For the subject test conditions, f_{FR} was estimated to be 1.004.

Heat Loss Correction (f_{HL}). The heat loss correction was estimated from the measured performance and observed chamber heat flux values by use of Eq. A-3. Terms in Eq. A-3 were calculated and defined as follows:

c^*_{theo} = theoretical characteristic velocity at test conditions
(based on full shifting equilibrium) = 6918.6 ft/sec

c^*_{meas} = measured characteristic velocity (corrected for the previously
determined losses) = $\frac{P_c f_p A_t g_c F_{TR} f_{Dis} f_{FR}}{\dot{w}_t}$

= 6588.5 ft/sec

T_c = 7566 R

C_{p_m} = 0.420 Btu/lbm R

\dot{w}_T = 12.428 lbm/sec

$\Sigma (q/A) (A)$ = heat losses to the chamber wall between the injector face and the P_c tap upon which performance is based (i.e., between the injector face and P_c tap Position No. 5 which is 11-inches from the injector face).
= 884.9 Btu/sec

Heat losses to the chamber wall were calculated by dividing its inside surface area into segments (regions) of relatively constant heat flux and then summing the products of these surface areas times their respective average heat values. Table A-2 presents a tabulation of the regions into

TABLE A-2

TABULATION OF REGIONS INTO WHICH THE CHAMBER WAS DIVIDED FOR CALCULATION OF HEAT LOSSES TO THE CHAMBER WALLS. MEASURED AVERAGE HEAT FLUX AND HEAT LOSSES ASSOCIATED WITH EACH REGION ARE NOTED FOR TEST NO. 77

Chamber Region Code Number	Location of Chamber Region, Axial Distance From Injector, Face, inches	Surface Area, in. ²	Measured Average* Heat Flux, Btu/in. ² -sec	Heat Losses to Chamber Wall, Btu/sec
1	0.00 to 3.00	75.96	2.78	211.2
2	3.00 to 4.00	25.32	3.22	81.5
3	4.00 to 8.00	101.28	3.32	336.2
4	8.00 to 11.00	75.96	3.37	256.0
5	11.00 to 12.00	25.32	3.65	92.4
6	12.00 to 13.00	27.20	3.95	107.4
7	13.00 to 14.00	22.00	4.30	94.6
8	14.00 to 15.00	19.40	4.00	77.6
9	15.00 to 16.00	17.90	3.25	58.2
10	16.00 to 17.00	18.80	2.55	47.9
11	17.00 to 18.00	20.40	2.00	40.8
12	18.00 to 19.00	22.00	1.55	34.1
13	19.00 to 20.30	31.40	1.15	36.1
				1474.0
				884.9

*Determined from Fig. A-5

which the chamber was divided for calculation of chamber heat losses. Average heat flux values (determined from Fig. A-5) and heat losses for each region are also presented in this table for test No. 77. The sum of the chamber heat losses between the injector face and P_c tap upon which performance was based was 884.9 Btu/sec (i.e., the sum of the heat losses in the first four chamber heat flux regions).

The heat loss correction factor, f_{HL} , for this test is calculated below.

$$f_{HL} = \left\{ 1 + \left[\frac{c^*_{theo}}{c^*_{meas}} \right]^2 \left[\frac{\sum (q/A) (A)}{\dot{w}_T C_{P_m} T_c} \right] \right\}^{1/2}$$

$$f_{HL} = \left\{ 1 + \left[\frac{6918.6}{6588.5} \right] \left[\frac{884.9}{12.428 \times 0.420 \times 7566} \right] \right\}^{1/2}$$

$$f_{HL} = \sqrt{1.025} = 1.012$$

Corrected c^* efficiency (based on chamber pressure) for the test was 96.4 percent.

Equation A-2 with the appropriate numerical values shown is presented below for test No. 77:

$$(\eta_{c^*})_{P_c} = \frac{P_c A_t g_c f_p f_{TR} f_{DIS} f_{FR} f_{HL}}{(\dot{w}_o + \dot{w}_f) (c^*)_{theo}}$$

$$(\eta_{c^*})_{P_c} = \frac{(94.96 \times 0.99)(25.562)(32.174)(1.058)(1.002)(0.995)(1.004)(1.012)}{(10.466 + 1.962)(6918.6)}$$

$$(\eta_{c^*})_{P_c} = 96.4$$

Performance Based on Thrust

Corrected c^* efficiency based on thrust measurement was calculated using Eq. A-6. Initially, vacuum thrust was calculated from the measured thrust, ambient pressure, and nozzle exit area as follows:

$$F_{\text{vac}} = F_{\text{meas}} + P_a A_e = 2877.0 + (13.7) (47.15) = 3523.0 \text{ lbf}$$

This was necessary because the corrections to be applied were calculated as changes in efficiency based on theoretical vacuum parameters.

Methods of estimation for the correction factors to be applied to the vacuum thrust in the calculation of c^* efficiency were presented previously. Estimation of the values used for test No. 77 are described below in the following paragraphs.

Corrections for Fractional Drag (ϕ_{FR}). Frictional losses were estimated from Fig. A-3 and A-4. For the subject test conditions, ϕ_{FR} was estimated to be 1.012.

Nozzle Divergence Correction (ϕ_{div}). For all experiments, the nozzle divergence losses were estimated to be 1.8 percent (i.e., $\phi_{\text{div}} = 1.018$).

Heat Loss Correction (ϕ_{HL}). As was the case for the heat loss correction factor for performance based on chamber pressure, (f_{HL}), the heat loss correction factor was estimated using Eq. A-3. For this case, however, the measured c^* is based on thrust and total chamber heat losses are employed (i.e., heat losses are summed from injector face to nozzle exit). Terms in Eq. A-3 were calculated and defined as follows:

$$c_{\text{theo}}^* = 6918.6 \text{ ft/sec}$$

$$T_c = 7566 \text{ R}$$

$$C_{p_m} = 0.420 \text{ Btu/lbm R}$$

$$\dot{w}_T = 12.428 \text{ lbm/sec}$$

$$(C_F)_{\text{vac}} = 1.446$$

$$c^*_{\text{meas}} = \frac{F_{\text{vac}} g_c \phi_{\text{FR}} \phi_{\text{Div}}}{(C_F)_{\text{vac}} \dot{w}_T}$$

$$= \frac{3523.0 \times 32.174 \times 1.012 \times 1.018}{1.446 \times 12.428}$$

$$= 6496.4 \text{ ft/sec}$$

$\Sigma(q/A)(A)$ = heat losses to the chamber wall between the injector face and nozzle exit.

$$= 1474 \text{ Btu/sec (see Table A-2)}$$

The heat loss correction factor, ϕ_{HL} , was calculated as follows:

$$\phi_{\text{HL}} = \left\{ 1 + \left[\frac{c^*_{\text{theo}}}{c^*_{\text{meas}}} \right]^2 \left[\frac{(q/A)(A)}{\dot{w}_T C_{p_m} T_c} \right] \right\}^{1/2}$$

$$= \left\{ 1 + \left[\frac{6918.6}{6496.4} \right]^2 \left[\frac{1474}{12.428 \times 0.420 \times 7566} \right] \right\}^{1/2}$$

$$= \sqrt{1.044} = 1.022$$

Corrected c^* efficiency (based on thrust) for this test was 96.0 percent. Equation A-6 with the appropriate numerical values shown is presented below for test No. 77:

$$(\eta_{c^*})_F = \frac{(F + P_a A_e) g_c \phi_{\text{FR}} \phi_{\text{Div}} \phi_{\text{HL}}}{(C_F)_{\text{vac}} (\dot{w}_o + \dot{w}_f) (c^*)_{\text{theo}}}$$

$$(\eta_{c^*})_F = \frac{(3523.0)(32.174)(1.012)(1.018)(1.022)}{(1.446)(10.446 + 1.962)(6918.6)}$$

$$(\eta_{c^*})_F = 96.0$$

REFERENCES

- A-1. LAP 68-411 (RC): Static Pressure Measurement for Contract NASw-1229 Combustion Chamber, Rocketdyne, a Division of North American Rockwell Corporation, 19 August 1968.
- A-2. Havenstein, C. A.: Alternate Throat Development Program for the Apollo Command Module Reaction Control Engines, Report No. R-5941, Rocketdyne, a Division of North American Aviation, Inc., Canoga Park, California, 16 November 1964.
- A-3. Timoshenko, S. and J. N. Goodier: Theory of Elasticity, McGraw-Hill Book Company, New York, N. Y., 1951.
- A-4. Bartz, D. R.: "A Simple Equation for Rapid Estimation of Rocket Nozzle Convective Heat Transfer Coefficients," Jet Propulsion, January 1957.
- A-5. Singer, H. A.: Discharge Coefficients of Nozzles Having Sharp Throat Curvature, LAP 66-518, Rocketdyne, a Division of North American Rockwell Corporation, Canoga Park, California, 18 October 1966.
- A-6. Arbit, H. A. and S. D. Clapp: Fluorine-Hydrogen Performance Evaluation. Part I: Analysis, Design, and Demonstration of High-Performance Injectors for the Liquid Fluorine-Gaseous Hydrogen Propellant Combination, Research Report No. 66-10, Rocketdyne, a Division of North American Rockwell Corporation, Canoga Park, California, April 1966.
- A-7. Chamber Technology for Space Storable Propellants - Task II, Prepared for National Aeronautics and Space Administration, Contract NAS7-304, Report No. R-6028-2, Rocketdyne, a Division of North American Rockwell Corporation, Canoga Park, California, 13 October 1965.

APPENDIX B

PERFORMANCE DATA MEASUREMENT ERROR ANALYSIS

INTRODUCTION

Because it is not possible to measure the true value of any physical property or parameter, the error limits, or uncertainty interval, associated with any experimental measurement should be specified. It is the purpose of this appendix to indicate the reliability of the experimental results of this program by estimation of the errors inherent in the data acquisition processes and/or in the calculation procedures. This will permit determination of the range within which, at a given confidence level, the true values of the measured or calculated parameters may be expected to fall.

If error is defined as departure of an experimental measurement from the "true" value, its magnitude can never be completely known; if it were known, it would become a correction which could be systematically applied. Hence, error limits can only be stated within probability limits. Performance data (c* efficiency) precision was estimated by two separate methods; one based on static calibration of the individual transducers, and the other based on analysis of repeated firings of the rocket engine.

In the present application, the data precision analysis based on static calibration of the individual transducers was made by an error analysis procedure which consisted of the following steps:

1. Estimation of the uncertainty intervals of the individual transducers, including the measuring systems in which they were used.
2. Combination of the uncertainty intervals of duplicate or redundant sensors into an uncertainty interval for the measurement.

3. Combination of the uncertainty intervals of several measurements (e.g., flowmeter frequency and propellant density) into an uncertainty interval for the parameter they determine (e.g., flowrate).
4. Combination of the uncertainty intervals of the parameters (e.g., chamber pressure, flowrate, and throat area) entering into calculation of the value of the desired variable (e.g., characteristic velocity efficiency) to estimate the uncertainty interval of the calculated result.

As noted above, the second method used to estimate the uncertainty (confidence) interval associated with the experimental determination of characteristic velocity efficiency was by analysis of data from repeated firings of the rocket motor. For this case, the test data were analyzed as a completely randomized design, by use of the analysis of variance technique.

Two types of error are possible in any measurement:

1. Systematic Errors. These are associated with the particular system, with the experimental techniques employed, or with the calibration procedures. They cannot be estimated by statistical methods, and are minimized primarily by careful calibration with the best available standards, by requirements for consistency and traceability of the experimental and calibration techniques, and by critical examination of experimental data.
2. Random Errors. These arise from unpredictable and unknown variations in the experimental situation and are generally assumed to follow a normal distribution to permit simple statistical analysis. Error analysis is concerned only with random errors and implicitly assumes that systematic errors can be eliminated in a carefully conducted experimental program.

SENSOR PRECISION

A measurement analysis program (Random Walk measurement analysis program) is employed at Rocketdyne which uses transducer calibrations to provide appropriate factors for test data reduction. In addition, statistical histories for each transducer are developed so that estimates of short-term and long-term deviations can be made and probable error bands calculated. This program is discussed in detail in Appendix C.

The precision of a measurement obtained as the output of a physical instrument or sensor is a quantitative estimate of the uncertainty associated with that measurement. (By sensor is meant not only the transducer itself but the complete system which converts the transducer signal to a numerical value of its physical parameter analog.) This estimate is made by statistical analysis of the outputs of the sensor when repeatedly acted upon by known inputs. The known inputs, of course, have uncertainty limits of their own, but for practical purposes it is assumed that they are accurate (i.e., identical to true values) within the limits required by the experimental situation. Ultimately, these inputs must be directly traceable to established standards, such as those of the National Bureau of Standards.

When a sensor is calibrated against known inputs, precision may be considered as the certification of an error band within the calibrated interval and within a given confidence level. Thus, it provides a measure of "closeness to truth" of the reduced data. Precision may be numerically expressed as the standard deviation of a measurement, which has the same units as the measurement itself, or as the coefficient of variation (C_v), which permits valid comparisons between measurements in different units. It also permits valid comparisons to be made between large and small things. Coefficient of variation (C_v) is the standard deviation (σ) expressed as a percentage of the mean, thus making it dimensionless:

$$C_v = \frac{\sigma}{\mu} 100 \quad (B-1)$$

where

σ = the standard deviation

μ = sample mean value

C_v = coefficient of variation

Pressure

The coefficients of variation of the pressure transducers were obtained by application of the Random Walk measurement analysis program to the calibration data. Chamber pressure values ranged from 0.25 to 0.53 percent for static calibrations made on a pressure manifold mounted on the thrust stand.

For all tests, redundant sensors were used to measure the chamber pressure. Two or three independent transducers were used to measure this important parameter in order to increase the measurement reliability.

Other errors in pressure measurement may arise in addition to the random statistical uncertainty limits. In measurement of chamber pressure through a drilled wall tap, as herein, erroneous values of stream pressure may be indicated because of the effect of the hole itself upon the flow. Estimated magnitudes of this error, which is a function of stream velocity, were based on experimental data obtained with water and gas (Ref. B-1). For the experimental situation herein, these errors are insignificant. Coupling errors, arising from effects of the tubing joining the pressure taps to the transducers were also insignificant in the present series of experiments (Ref. B-2). As was noted in Appendix A, the location of the pressure tap from which combustion chamber throat stagnation pressure (or performance) is calculated is quite critical. Procedures were followed (Appendix A) to ensure that the proper static pressure measurement was employed. Thus, this source of error is assumed to be insignificant.

Thrust

Values of coefficient of variation obtained by application of the Random Walk measurement analysis program to thrust calibrations were in the 0.23- to 0.35-percent range. A possible source of error in thrust measurement arose from the necessity of taking system prerun zeros with the same degree of propellant line chill as existed during the firings. The procedure for doing this is described in Appendix D. On the basis of thrust calibrations made with chilled and unchilled propellant lines, the above C_v values should be applicable. The coefficient of variation increase due to line chill variations between tests should (and is assumed to) be negligible.

Throat Area

Geometric throat diameter was measured with an expansion micrometer by at least two observers prior to, and following, each days firings. The maximum coefficient of variation of the calculated areas was 0.42 percent. As was noted in Appendix A, throat area variation during firing was small.

Volumetric Flowrate

The coefficients of variation of the turbine flowmeters used to measure the propellant flowrates were determined from flow-bench calibration data. Each meter was calibrated prior to the start, and at the end, of the program. The meters were calibrated in both Freon 113 and water. Redundant (two) flowmeters, in series, were placed in each propellant line. C_v values for the oxidizer flowmeters were 0.05 and 0.02. C_v values for the fuel flowmeters were 0.03 and 0.01. Corrections for viscosity and temperature differences between the calibration fluid and the cryogenic propellants are discussed in Appendix D. In addition, however, there are unpredictable water-to-cryogenic calibration shifts (Ref. B-3) which introduce additional sources of error. The coefficient of variation arising from this course is approximately 0.5 percent (Ref. B-4).

Temperature

The platinum resistance thermometers (Rosemount bulbs) were precision calibrated by the manufacturer. These calibrations were checked by taking several emf readings with the sensors immersed in LN_2 and in LO_2 at atmospheric pressure; they were correct within the limits of readability. Root-sum-square (RSS) error limits of these sensors based on specifications of repeatability, insulation, time lag, friction heating, and interchangeability are approximately 0.1 percent (Ref. B-5). Voltage readout of the transducers was adjusted to calibration values by means of a standard decade resistance box with error limits of 0.2 percent.

COMBINED ERROR ESTIMATION

Redundant Measurements

Redundant transducers were used to measure the most important parameters in order to increase the measurement reliability. The most probable value of a redundant measurement is the weighted average. The variance of the weighted mean value, σ_m^2 , is given by the following equation:

$$\frac{1}{\sigma_m^2} = \frac{1}{\sigma_1^2} + \frac{1}{\sigma_2^2} + \dots + \frac{1}{\sigma_n^2} = \sum_{i=1}^n \frac{1}{\sigma_i^2} \quad (\text{B-2})$$

where

σ_m^2 = the variance of the weighted mean

σ_i^2 = the variance of the i^{th} measurement

Clearly, the variance of a weighted mean is less than any of the individual variances.

Combined Measurements

When several measured variables are combined algebraically to yield an experimental result, the standard deviation of the result, which takes into account the propagation of the individual error, is given by the following equation (Ref. B-6):

$$\sigma_R = \sqrt{\left[\left(\frac{\partial R}{\partial X_1}\right) (\sigma_1)\right]^2 + \left[\frac{\partial R}{\partial X_2} (\sigma_2)\right]^2 + \dots + \left[\left(\frac{\partial R}{\partial X_n}\right) (\sigma_n)\right]^2} \quad (B-3)$$

where

σ_R = the standard deviation of the calculated result

X_1, X_2, \dots, X_n = measured variables

$R = f(X_1, X_2, \dots, X_n)$

$\sigma_1, \sigma_2, \dots, \sigma_n$ = standard deviations of X_1, X_2, \dots, X_n
respectively

When the individual measurements are combined by addition, and are independent, the standard deviation is given by (Ref. B-6):

$$\sigma_R = \sqrt{\sigma_1^2 + \sigma_2^2 + \dots + \sigma_n^2} \quad (B-4)$$

DATA PRECISION

Static Calibration Precision Analysis

Characteristic velocity can be calculated by two methods, one based on chamber pressure (P_c) measurement and one based on thrust (F) measurement, as given below:

$$c^* = \frac{(P_c) A_t g_c}{w_t} \quad (B-5)$$

or

$$c^* = \frac{F_{vac} g_c}{(C_F)_{vac} w_t} \quad (B-6)$$

where

- c^* = characteristic velocity (calculated), ft/sec
- $(P_c)_o$ = stagnation pressure at the throat, psia
- A_t = measured geometric throat area, in.²
- g_c = conversion factor (32.174 $\frac{\text{lbm-ft}}{\text{lbf-sec}^2}$)
- w_t = total propellant mass flowrate, lbm/sec
- $(C_F)_{vac}$ = theoretical shifting thrust coefficient (vacuum)
- F_{vac} = measured thrust corrected to vacuum conditions by the equation: $F_{vac} = F + P_a A_e$, lbf
- F = measured thrust, lbf
- P_a = ambient pressure, psia
- A_e = area of nozzle exit, in.²

It should be noted that these expressions yield uncorrected characteristic velocity.

The standard deviation of the characteristic velocity based on both methods of calculation can be determined by application of Equation (B-3) to Equations (B-5) and (B-6). The standard deviation of the uncorrected characteristic velocity (based on chamber pressure) is calculated as follows:

$$(\sigma_{c^*})_{P_c} = \sqrt{\left[\left(\frac{A_t g_c}{w_t} \right) \sigma_{P_c} \right]^2 + \left[\left(\frac{(P_c)_o g_c}{w_t} \right) \sigma_{A_t} \right]^2 + \left[\left(\frac{(P_c)_o g_c}{w_t^2} \right) \sigma_{w_t} \right]^2} \quad (B-7)$$

The resulting expression for the standard deviation of the characteristic velocity, based on thrust, is:

$$(\sigma_{c^*})_F = \sqrt{\left[\left(\frac{g_c}{(C_F)_{vac} w_t} \right) \sigma_{F_{vac}} \right]^2 + \left[\left(\frac{F_{vac} g_c}{(C_F)_{vac} w_t^2} \right) \sigma_{w_t} \right]^2} \quad (B-8)$$

Substitution of numerical values into these expressions yield the resulting standard deviations. As far as random errors only are concerned, there was no significant difference in the estimated standard deviations based on chamber pressure or thrust. The standard deviation of the uncorrected characteristic velocity was approximately 35 ft/sec. This corresponds to a coefficient of variation of approximately 0.5 percent for the uncorrected c^* efficiency. Therefore, the uncorrected c^* efficiencies determined in the present program are estimated to have an error band of approximately ± 1.0 percent at the 95 percent (2σ) confidence level.

Application of the corrections to measured uncorrected characteristic velocities could cause an increase in the error associated with corrected characteristic velocities. Assuming proper application of these corrections, however, the resulting characteristic velocity efficiencies reported herein are estimated to be within ± 1.0 percent of the true value.

Calculation of appropriate values for σ_{P_c} , σ_{A_t} , and $\sigma_{F_{vac}}$ for use in Eq. B-7 and B-8 are straightforward. Estimation of σ_{w_t} is more complicated and is therefore discussed briefly herein.

For each meter, the propellant mass flowrate (W_i) is a function of the flowmeter frequency (f_i) and the propellant density (ρ_i):

$$W_i = \phi(f_i, \rho_i) \quad (B-9)$$

In particular,

$$W_i = f_i \rho_i (\text{flowmeter constant})_i (K) \quad (\text{B-10})$$

where

f_i = flowmeter output frequency, cps

ρ_i = propellant density, lbm/ft³

$(\text{flowmeter constant})_i$ = flowmeter constant, gal/cycle

K = conversion factor = $(\frac{1}{7.48}) \text{ ft}^3/\text{gal}$

Therefore, the standard deviation of each meters flowrate is given by

$$\sigma_{w_i} = \sqrt{\left(\frac{\partial w_i}{\partial f_i} \sigma_{f_i}\right)^2 + \left(\frac{\partial w_i}{\partial \rho_i} \sigma_{\rho_i}\right)^2} \quad (\text{B-11})$$

$$\sigma_{w_i} = \left[K (\rho_i) (\text{flowmeter constant})_i (\sigma_{f_i}) \right]^2 + \left[(f_i) (\text{flowmeter constant})_i (\sigma_{\rho_i}) K \right]^2$$

Actually, flowrate is a function of flowmeter frequency and propellant temperature (assuming no significant error in conversion of propellant temperature to equivalent density). Thus, Eq. B-11 may be written as follows:

$$\sigma_{w_i} = \left[K (\rho_i) (\text{flowmeter constant})_i (\sigma_{f_i}) \right]^2 + \left[(f_i) (\text{flowmeter constant})_i (\sigma_T)_i K \right]^2 \quad (\text{B-12})$$

Standard deviation is converted to coefficient of variation by use of Eq. B-1. The standard deviation of each propellant flowrate is then determined by application of Eq. B-2 to the redundant measurements. The coefficient of variation of the total propellant flowrate may be obtained from the coefficients of variation of its component parts by use of the following equation:

$$(C_v)_{\dot{w}_t} = \sqrt{\frac{r^2(C_v)_{\dot{w}_o}^2 + (C_v)_{\dot{w}_f}^2}{(r + 1)^2}} \quad (B-13)$$

where

$$r = \text{mixture ratio} = \dot{w}_o / \dot{w}_f$$

The standard deviation of the total propellant flowrate can then be obtained from Eq. B-1.

Dynamic Precision Analysis

The estimates of expected standard deviations in characteristic velocity calculated above are based on static calibrations of pressure/thrust sensors, and hence may not be strictly applicable to the dynamic system represented by a firing rocket motor. It is generally assumed, however, that such calibration data may be extended without significant change to dynamic systems oscillating at very low frequencies and amplitudes and that steady-state stable combustion is such a system.

An indication of the possible magnitude of the uncertainty interval associated with the experimental determination of characteristic velocity efficiency may be obtained by analysis of repeated firings of a rocket motor with the same set of transducers. If systematic errors are assumed to be insignificant, variations from indicated "correct" values (i.e., those which are on the best curve through the experimental points) may be ascribed to random errors and hence are subject to statistical analysis. The usefulness of such an analysis is a direct function of the number of data points used to obtain the correct or average values. With only three or four data points available for determination of efficiency at a given condition, statistical calculation of measurement reliability has no great absolute value but may be used for comparisons with those estimated from transducer calibrations.

During this program, many different test conditions were duplicated. (Several were duplicated four times.) These test data were analyzed as a completely randomized design (Ref. B-7) by use of the analysis of variance technique. (This is, perhaps, the most powerful and widely used statistical technique.) On the basis of this analysis, the experimental c^* efficiencies determined in the present program are estimated to have an error band of approximately ± 1.0 percent at the 95 percent confidence level.

SUMMARY

Both methods of estimation of the performance data precision indicate that the experimental c^* efficiencies determined in the present program have an error band of approximately ± 1.0 percent at the 95 percent (2σ) confidence level. Of course, both of these estimates are based on the assumption that the corrections applied to the uncorrected c^* efficiencies (Appendix A) are valid. Because good correlation (agreement) was obtained between the independently calculated performance values (i.e., c^* efficiency based on P_c and F ; Fig. 18), this assumption appears to be valid.

REFERENCES

- B-1. Dean, R. C., Jr., Aerodynamic Measurements, Gas Turbine Laboratory, Massachusetts Institute of Technology, Cambridge, Massachusetts Institute of Technology, Cambridge, Massachusetts, 1953.
- B-2. Thomson, D. B., The Effect of Tubing on Dynamic Pressure Recording, TN-61-3, Rocketdyne, a Division of North American Aviation, Inc., Canoga Park, California, 28 February 1961.
- B-3. Bucknell, R. L., "Calibration Systems and Turbine-Type Flow Transducers for Cryogenic Flow Measurements," Advances in Cryogenic Engineering, Vol. 8, Plenum Press, New York, 1963, pp 360-369.
- B-4. Alspach, W. J. and T. M. Flynn, "Considerations When Using Turbine-Type Flowmeters in Cryogenic Service," Advances in Cryogenic Engineering, Vol. 10, Plenum Press, New York, 1965, pp 246-252.
- B-5. Research Report No. 66-10, Fluorine-Hydrogen Performance Evaluation. Part I: Analysis, Design, and Demonstration of High-Performance Injectors for the Liquid Fluorine-Gaseous Hydrogen Propellant Combination, Arbit, H. A., and Clapp, S. D., Rocketdyne, a Division of North American Aviation, Inc., Canoga Park, California, April 1966.
- B-6. Arkin, H., and Colton, R. R., Statistical Methods, Barnes & Nobel, Inc., New York.
- B-7. Ostle, B., Statistics in Research, The Iowa State College Press, Ames, Iowa.

APPENDIX C

RANDOM WALK MEASUREMENT ANALYSIS PROGRAM

INTRODUCTION

The primary purpose of a sensor measurement analysis program is to provide a function which relates observed sensor outputs to estimates of corresponding system inputs, together with quantitative indications of the precision of this conversion. The function and the precision estimates are established on the basis of sensor calibration history, that is, upon a sequence of periodic calibrations of the sensor and its associated measuring and recording system against known inputs.

Because calibrations must of necessity be made at a time differing from the actual firing time by several hours to several days, the changes in random sensor error with time must be established. In the Random Walk measurement analysis program (Ref. C-1) this is accomplished by assuming that the input-to-output ratio at a particular input level performs a random walk in time which has normal distribution and variance. It assumes also that there is a random measurement error in the observed datum which is independent of the random walk and which is also normally distributed. Mathematical foundations and development of the program are given in Ref. C-2 and C-3.

On the basis of a sequence of periodic calibrations, the Random Walk program provides the following:

1. A function, either linear or cubic, which converts observed system outputs into estimates of true system inputs;
2. Coefficients of short-term and random walk variations, as well as a combined value valid at specified times; and
3. A decision, based upon the calculated coefficient of variation and a prespecified imprecision limit, as to whether the sensor should be used as is, recalibrated immediately, or discarded, and the maximum allowable interval to next calibration.

MEASUREMENT PROGRAM OUTPUT

A typical Random Walk computer program output is shown in Table C-1. The first line of output gives the test stand name and number (Willie, 0019), recording system (Beckman), transducer serial number (671755), range (230 psi), ID number for data cards (018056), and the physical parameter being calibrated ($P_c - 2$).

The next set of numbers ("Latest Output") is the most recent raw calibration data. On the left are the readings (in Beckman counts) for the listed calibration input steps ("Input"); on the right are the precalibrate throw zero (Z1), the calibrate throw reading (CT), the postthrow zero (Z2), the precalibration zero (Z3), the postcalibration zero (Z4), and the date of calibration ("Time").

The first two zeros (Z1 and Z2) are averaged and subtracted from the throw to obtain a reduced throw. For each calibration step, a linear interpolation is made between the last two zeros (Z3 and Z4) and the interpolated result is subtracted from the reading to obtain a reduced reading. Each reduced reading is then divided by the reduced throw to obtain a scaled output. All scaled output values from all calibrations in the system history are then listed ("Scaled Output") under the appropriate input pressures, with one calibration per line and its date ("Time") listed at the right of each line.

The first three lines following the scaled output table are estimates of the measurement variance (σ_m^2) in the input-to-scaled output ratio, the random walk variance (σ^2) in the input-to-scaled output ratio, and the ratio (k) of the former (short-term) variance to the latter (long-term) variance. The variances (σ_m^2 and σ^2) are used in computing the data reduction imprecision, which is defined as the standard deviation of an estimated input about the true input.

TABLE C-1

TYPICAL COMPUTER OUTPUT FOR TRANSDUCER CALIBRATIONS USING
RANDOM WALK MEASUREMENT ANALYSIS PROGRAM

WILLIE 0019 8KM 671755 230 019056 PC-2

LATEST OUTPUT

	Z1	CT	Z2	Z3	Z4	TIME
222 594 964 1334 1704	4	2951	4	4	6	5-28-68

INPUT

30 80 130 180 230				

SCALED OUTPUT

					TIME
0.0739	0.2000	0.3254	0.4509	0.5763	5-28-68
0.0741	0.1995	0.3255	0.4505	0.5759	5-23-68
0.0743	0.1992	0.3258	0.4514	0.5770	5- 8-68
0.0746	0.2008	0.3274	0.4523	0.5771	4- 1-68
0.0746	0.2006	0.3269	0.4530	0.5786	3-11-68
0.0732	0.1973	0.3221	0.4458	0.5702	2- 8-68
0.0731	0.1981	0.3223	0.4466	0.5708	1-24-68
0.0734	0.1980	0.3233	0.4468	0.5717	1-16-68
0.0738	0.1980	0.3229	0.4471	0.5720	1- 2-68
0.0738	0.1984	0.3238	0.4480	0.5726	12-18-67
0.0738	0.1985	0.3233	0.4483	0.5731	12-11-67
0.0730	0.1982	0.3224	0.4470	0.5726	12- 5-67
0.0736	0.1989	0.3235	0.4485	0.5727	12- 1-67
0.0730	0.1973	0.3222	0.4465	0.5698	11-13-67
0.0736	0.1978	0.3223	0.4461	0.5703	11-13-67
0.0735	0.1980	0.3221	0.4458	0.5699	11-13-67
0.0736	0.1978	0.3220	0.4459	0.5708	11-13-67

MEASUREMENT VARIANCE IN INPUT-TO-SCALED OUTPUT RATIO = 0.156820 01

RANDOM WALK VARIANCE IN INPUT-TO-SCALED OUTPUT RATIO = 0.920910-01

RATIO OF SHORT-TERM VARIANCE TO RANDOM WALK VARIANCE = $\frac{1}{2}$ = 0.170290 02 (DAYS)

COEFFICIENT OF SHORT-TERM VARIATION = 0.313 (PERCENT)

COEFFICIENT OF RANDOM WALK VARIATION = 0.0757 (PERCENT/DAY**0.5)

REQUIREMENT FOR COEFFICIENT OF VARIATION OF REDUCED DATA = 1.500 (PERCENT)

SYSTEM NOW PASSES TEST FOR LINEARITY (TYPE I ERROR= 0.05).

DATA REDUCTION FORMULA IS

$$(INPUT) = (3.99290 02) * (SCALED OUTPUT)$$

ABOVE OUTPUT-INPUT MODEL IS SATISFACTORY (TYPE I ERROR= 0.05).

SYSTEM SHOULD BE CALIBRATED ON OR BEFORE 6-27-68

COEFFICIENT OF VARIATION OF REDUCED DATA IN 6-27-68 = 0.52 PERCENT

COEFFICIENT OF VARIATION OF REDUCED DATA IN 5-30-68 = 0.34 PERCENT

DATA REDUCTION MATRIX

(1.13953D-01	0.0)
(0.0	0.0)

The next line of output gives the coefficient of short-term variation, which is the standard deviation (σ_m) expressed as a percentage of the average input-to-scaled output ratio. This quantity is generally the largest component of data reduction imprecision. The following entry gives the coefficient of random walk (long-term) variation, which is the standard deviation (σ) also expressed as a percentage of the average input-to-scaled output ratio. This item is meaningful only after calibrations are obtained over a period of time. The final listing in this block is the prespecified maximum limit of data reduction imprecision expressed as coefficient of variation.

The program now calculates revised scaled output values corresponding to the state of the system at the time of the most recent calibration. These values are then fit by least squares with either a linear or cubic function by the following procedure. The null hypothesis is that the function is linear, and the specified error (the probability that a truly linear function is mistakenly concluded to be nonlinear) is printed out. If the linearity hypothesis is rejected, a cubic fit is made. In either case, the formula for converting scaled outputs to estimated inputs is then given, and, if the relationship is cubic, an input-output table is printed out for convenience in data reduction.

The next line gives the result of the second test, which checks whether or not the input-output model is consistent with the estimate of σ_m (the root-mean-square estimate for the calibration curve fit and σ_m should be approximately equal). If it is, then the model is labeled "SATISFACTORY"; if not, the model is labeled "UNSATISFACTORY," indicating a significant intercept or an error in the input data.

The following item indicates the ability of the system to meet the specified imprecision requirement. On the basis of the calibration data, three situations are recognized:

1. The system can never meet required precision, and should be replaced;

2. The system will fail the requirement within the next two days and should be recalibrated immediately; or
3. The system will meet the requirement up to a certain date (30 days maximum), on or before which it should be recalibrated. In this case, the estimated data reduction imprecision is given for test data taken two days after the most recent calibration and on the specified recalibration date.

In the present program, the system transducers were calibrated weekly, regardless of the leeway allowed by reason of little or no random walk variation and consequent minimum degradation in precision.

The final item is a 2 by 2 matrix, denoted by R, which is used to estimate data reduction imprecision at any other time of interest and for any scaled output by the following expression:

$$P = \left[V + s^2 (h \sigma^2 + \sigma_m^2) \right]^{1/2} \quad (C-1)$$

where

P = estimated standard deviation for a reduced datum

s = scaled output

h = number of days after most recent calibration

V = matrix product: $(s, s^3) R \begin{pmatrix} s \\ s^3 \end{pmatrix}$

Application of the results of this sensor measurement analysis program to estimation of random experimental errors and to measurement reliability is given in Appendix B.

REFERENCES

- C-1. Rothman, D.: Random Walk Program for Measurements Analysis of Static Systems, RM-1119-351, Rocketdyne, a Division of North American Aviation, Inc., Canoga Park, California, 25 January 1965.
- C-2. Rothman, D.: A Random Walk Model for Non-Uniform, One-Parameter, Static, Linear Measurement Systems, RR-59-47, Rocketdyne, a Division of North American Aviation, Inc., Canoga Park, California, 15 December 1959.
- C-3. Rothman, D.: Gaussian Random Walk with Gaussian Measurement Errors, SORUM-63-9, Rocketdyne, a Division of North American Aviation, Inc., Canoga Park, California, 24 September 1963.

APPENDIX D

EXPERIMENTAL FACILITIES AND PROCEDURES

Detailed descriptions of the test stands, instrumentation, data recording (test documentation) procedures, and pertinent experimental procedures utilized during this program are presented in this appendix. The hot-fire and cold-flow experimental facilities and procedures are discussed under separate headings.

HOT-FIRE TEST FACILITY, INSTRUMENTATION, AND PROCEDURES

Test Facility

The hot-fire experimental portion of the program was conducted on test stand Willie at Rocketdyne's Propulsion Research Area test complex. A schematic flow diagram of the stand is shown in Fig. D-1.

The liquid FLOX mixtures were loaded into the run tank from the storage tank/trailer prior to each days testing. Liquid fluorine was obtained by condensation of GF_2 from the PRA storage tank. Procedures for condensation, transfer, and handling of the FLOX mixtures had been established on previous programs at Rocketdyne. Following completion of each days testing, the oxidizer remaining in the run tank was returned to its storage vessel. The fuel (55 w/o methane-45 w/o ethane mixture) was stored in the gaseous state. It was stored in the cylinders (size 1A) in which it was purchased. The fuel was liquified by condensation of the gaseous blend into the run tank prior to each days testing.

Both propellant systems were completely chilled with liquid nitrogen from the condenser (on top of the run tank) to the engine, as shown in Fig. D-1. In addition, use of three-way main valves permitted prerun chilldown of the manifolds and injector by means of a liquid nitrogen

Figure D-1. Schematic Flow Diagram of Test Stand Willie, Propulsion Research Area, as Used in FLOX/LPG Experimental Program

bleed directly through the injector and thrust chamber, thus preventing the propellant from flashing in the initial portion of the firing and minimizing flow transients.

The engine was mounted horizontally. Tank and purge pressures were set by motorized Dome loaders in conjunction with electrically operated tank vent and control valves. Filtered dry helium was used as the run tank pressurant. Gaseous dry nitrogen purges were used on the propellant lines.

Instrumentation

A schematic diagram indicating the location of system instrumentation is shown in Fig. D-2. Redundant measurements were made on the most important experimental parameters (e.g., chamber pressure, flowrates, etc.) to increase data reliability. The data recording systems and particular transducers used for the various types of measurements are described and discussed below.

Data Recording Systems. Pertinent pressure, temperature, and flow measurements were recorded on tape during each firing by means of a Beckman Model 210 Data Acquisition and Recording System. This system acquires analog data from the transducers, which it converts to digital form in binary-coded decimal format. The latter are recorded on tapes which are then used for computer processing.

The Beckman Data Acquisition Unit sequentially samples the input channel at a rate of 5625 samples per second. Programmed computer output consists of tables of time versus parameter value (in engineering units) printed out at approximately 10-millisecond intervals during the firing, together with calibration factors, prerun and postrun zero readings, and related data. The same computed results are machine-plotted and displayed as CRT outputs on appropriately scaled and labeled grids for simple determination of gradients, establishment of steady state, etc.

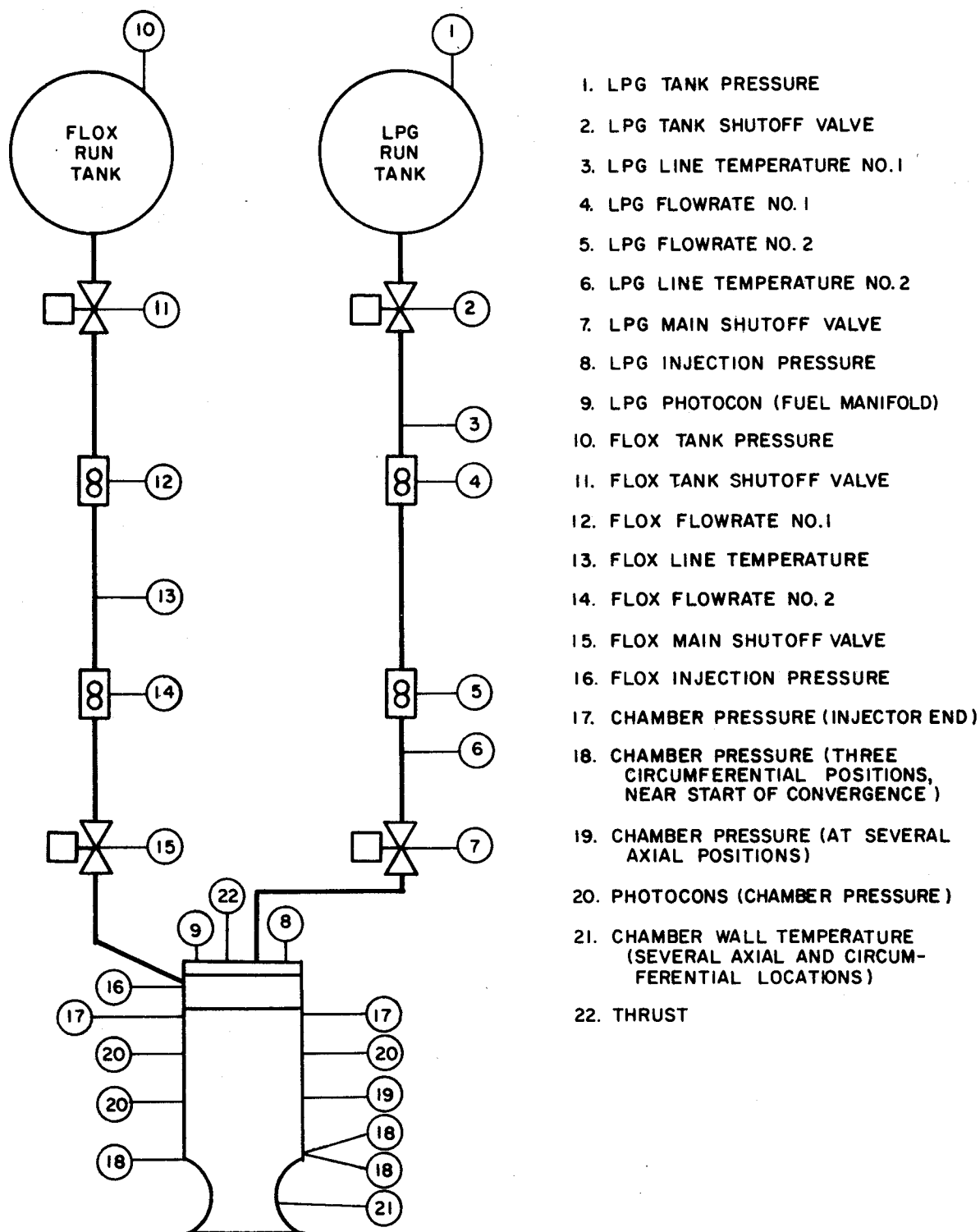


Figure D-2. Schematic Flow Diagram of Hot-Fire Experimental Test Facility Showing Location of Instrumentation

Primary data recording for these firings, and subsequent calculation of performance, was on the Beckman 210 system. In addition, the following auxiliary recording systems were employed:

1. An 8-channel, Brush, Mark 200 recorder was employed in conjunction with the Beckman unit, primarily to establish time intervals for computer data reduction and, additionally, for "quick-look" information on the most important parameters. This is a direct-inking system, with display on high-gloss, graduated paper moving at 20 mm/sec.
2. A CEC, 36-channel, direct-reading oscillograph was used as backup for the Beckman 210 system and for indication of any oscillatory combustion.
3. Direct-inking graphic recorders (DIGR's), either Dynalog rotary chart or Esterline-Angus strip chart, were used to set prerun propellant supply pressures, for recording of propellant manifold pressures, to provide quick-look information, and as secondary backup to the Beckman and oscillograph recorders.
4. An Esterline-Angus, 20-channel event recorder was used for direct-inking recording of main propellant valve signal and travel, as well as for chart drive and camera actuations.

Thrust. The thrust chamber mount was supported on flexures, which will allow free movement parallel to the engine axis (horizontally), restrained in the thrust direction by a Baldwin-Lima-Hamilton double-bridge load cell. Thrust was recorded on the Beckman and Dynalog recorders.

Pressures. Pressures were measured with bonded strain-gage transducers (Taber "Teledyne" Series 206 or equivalent). As noted in Appendix A, chamber pressure was measured at several circumferential and axial positions in the chamber. Redundant measurements were made at pertinent axial locations. Chamber pressure was recorded on the Beckman, oscillograph, and Dynalog recorders. Tank pressures were recorded on Dynalog recorders. Injector pressures were recorded on Beckman and Dynalog recorders.

Flowrates. All propellant flowrates were measured by means of Fischer-Porter turbine flowmeters which measure the volumetric flowrate. Each propellant line had two flowmeters in series to measure the volumetric flowrate. The flowrates were recorded on Beckman, oscillograph, and Esterline-Angus recorders.

Temperatures. Reliable measurement of cryogenic propellant flowrates requires accurate determination of liquid density as well as of volumetric flowrate. Density of cryogenic propellants is a sensitive function of temperature; therefore, it is important to make careful measurements of propellant temperature as close to the flowmeters as practical. This can be done by use of shielded platinum resistance bulbs (Rosemount Model 176) immersed in the liquid stream. These instruments are very sensitive to temperature changes in the cryogenic region and are the preferred method of measurement. It has been shown in previous F_2/H_2 programs (Ref. D-1) that iron-constantan thermocouples in wells give erratic, nonduplicating readings, whereas platinum resistance bulbs give consistent measurements. Rosemount bulbs were used to measure the cryogenic propellant temperatures. Fuel temperature was measured at two positions; upstream of the flowmeter nearest the run tank, and downstream of the flowmeter nearest to the engine. The two temperatures were generally less than 2 degrees apart. Oxidizer temperature was measured between the two flowmeters. Propellant temperatures were recorded on the Beckman and Esterline-Angus recorders.

Temperature histories of the heat transfer isolation segments on the chamber and/or nozzle were measured by means of 10-mil, chromel-alumel thermocouples peened to the outside of the chamber wall. These temperatures were recorded on the Beckman recording unit. The wall sections of the chamber that were expected to attain the highest temperature were also recorded on graphic dynalog charts for visual monitoring during the tests.

Special Instrumentation. Photocon pressure transducers were used to monitor high-frequency pressure oscillations in the combustion chamber and fuel manifold. One of the chamber pressure Photocons was connected to a rough combustion cutoff (RCC) system. This device was set to cut off any test in which the peak-to-peak chamber pressure oscillations were greater than 100 psi for 80 milliseconds. Photocon outputs were recorded on the oscillograph and tape recorders.

Calibration Procedures

Transducer calibrations were employed not only to obtain appropriate factors for test data reduction, but to develop statistical histories for each transducer, so that estimates of short-term and long-term deviations could be made, and probable error bands calculated (see Appendixes B and C for detailed discussions). The calibration methods used for the various types of transducers are described below.

Thrust. The thrust-measuring load cell was calibrated in-place by means of a permanently mounted, manually operated, hydraulic force cell, which deflects the load cell exactly as does the engine; i.e., through a yoke tension rod system. Known loads were applied to the force cell through a Morehouse compression-type, temperature-compensated, proving ring calibrated by the National Bureau of Standards (NBS). A thrust calibration was conducted prior to testing on each test day.

The "end-to-end" calibration technique (i.e., one in which the complete measuring system is included, in addition to the transducer itself) provides for reliable determination of the thrust force acting on the load cell. For this thrust to be equal to that actually resulting from a firing, free movement of the engine mount is desirable; hence, flexible metallic tubing is generally used for propellant supply lines to the manifolds. Such tubing was used in the fuel feed line. For the FLOX

inlet line, special monel-lined flexible tubing was specified, because of previous experience in which flexible lines with stainless-steel inner corrugations failed unpredictably in LF_2 service. However, because of long lead time for delivery of this item, rigid stainless-steel tubing was used instead.

An extensive series of thrust calibrations was made with the lines in place, chilled and unchilled, pressurized and unpressurized, to determine possible effects of line temperature and pressure on the thrust readings. The only significant effect found was that of line chill, which changed the zero setting, in effect preloading the cell. Net transducer outputs (actual output less zero reading) over the entire calibration range were not affected by line condition (ambient, unpressurized; ambient, pressurized; chilled, unpressurized; chilled, pressurized). Line pressurization to run level had no significant effect on load cell output with either chilled or ambient temperature lines. These results indicated that load cell calibrations could be made with the inlet lines at ambient temperature, but that prerun zero readings should be taken with the line chilled to the same extent as during firing. This was done by bleeding LN_2 through the main valves and engine to chill the inlet lines prior to each test while monitoring the output of an iron-constantan thermocouple soldered to the line. When the desired temperature was reached, the LN_2 flow was stopped and the prerun thrust zero was recorded. Thus, thrust was calibrated with all lines at ambient temperature, to obtain the thrust/load cell output curve. Zero readings were obtained immediately before and after every firing, with inlet lines chilled to run temperature. Because the thrust/output factors were not changed by the ambient-chilled zero shift, the ambient calibration was valid.

Pressures. Pressure transducers were calibrated end-to-end by mounting them on stand manifolds in which pressures were read with high-precision Heise-Bourdon tube gages. The latter were calibrated periodically on Ruska dead-weight testers. Maximum length of pickup line from pressure tap to transducer was less than 3 feet. The pressure transducers were calibrated weekly.

Flowrates. The turbine flowmeters used to measure volumetric flowrates were calibrated prior to the initial testing and at the end of the test schedule. The initial calibration was conducted using water as the calibration fluid. Use of these calibrations for the cryogenic propellants required that allowances be made for the difference in temperature and viscosity between water and the cryogenic propellants. Manufacturer-furnished information (Ref. D-2) was used to define the extent of the temperature correction. Actual flowrate was approximately 1 percent lower than that calculated using the water calibration data (i.e., actual flowrate $\cong 0.99 \times$ flowrate calculated using water calibration determined flowmeter factor). The final calibration was conducted using Freon 113. This fluid has a viscosity similar to the cryogenic propellants. Results of these calibrations indicated that the viscosity effects correction is negligible, and no significant change in the flowmeter factors occurred between calibrations.

Temperature. Resistance of the platinum thermometers used in the cryogenic propellant lines was converted to millivolt output by a triple-bridge system. This was calibrated by substituting a decade resistance box for the sensor and setting it at various resistances corresponding to a temperature-resistance calibration for each instrument. These precision platinum resistance sensors had no significant calibration drift. Chamber thermocouples were used on the basis of the standard NBS millivolt/temperature tables. Thermocouple recorders were electrically calibrated.

Firing Procedures

Fluorine System Passivation. Prior to assembly, fluorine system components were carefully and thoroughly cleaned in accordance with standard prescribed procedures (Ref. D-3). Passivation of the assembled system (to main oxidizer valve), by provision of protective fluoride

films on exposed surfaces, was carried out as follows: low-pressure gaseous fluorine was introduced into the system and maintained for successive 15-minute periods at 5, 10, and 15 psi; finally, 20 psi was maintained for several hours.

The feed line/thrust chamber system downstream of the main valve was passivated immediately before each set of firings by flowing the oxidizer (FLOX mixture) through the system for short intervals of time.

Run Procedure. A console within the Propulsion Research Area blockhouse and a sequential timer supplied the controls for firing the experimental propulsion system. All remotely controlled valves, such as main valves, purges, vents, firex, short drive, etc., were operated from this console. Critical functions requiring precise timing were operated by the timer system with their respective time setting established prior to firing. All other functions were manually actuated from the console.

Before each firing, LN_2 was bled through the main valves and engine to chill the inlet lines and injector to the temperature which would be maintained by the propellants during the run. After chilldown, the following sequence of events were carried out in rapid succession:

1. LN_2 flow through the main valve and engine was stopped
2. Prerun thrust zero was taken
3. GN_2 purges were turned on to clear the LN_2 from the propellant lines
4. Automatic sequencer was activated to fire the engine

These events were conducted in approximately a 5- to 10-second interval; thus, the test was initiated before the system was allowed to warm up.

Test durations were from 1.5 to 3.0 seconds, depending upon the test conditions. A slight oxidizer lead (approximately 40 milliseconds) on start and simultaneous shutdown was employed throughout the program. The engine was purged preceding each firing. Wall sections of the chamber that were expected to attain the highest temperatures were instrumented with thermocouples and the temperatures recorded on graphic dynalog charts for close visual monitoring of the temperature rise during the test runs. Motion picture coverage, primarily for hardware monitoring, included Fastax and Bell and Howell cameras.

COLD-FLOW FACILITY AND PROCEDURES

Test Facility

The description of the cold-flow facility is divided into two distinct parts: (1) the flow system, and (2) the collection system.

Flow System. The basic components of the flow system are shown in Fig. D-3. The system contains two high-pressure (maximum rated pressure = 1000 psig) supply tanks. Each can be remotely pressurized. The propellant lines are stainless-steel tubing. Pneumatic (Annin) valves were used for tank shutoff and main valves.

Flow system instrumentation consists of four Taber "Teledyne" series bonded strain gage pressure transducers, and two Fischer-Porter turbine-type volumetric flowmeters. Measurements of propellant tank pressures and propellant injection pressures were made. These measurements were recorded on Dynalog direct-inking graphical recorders. The volumetric flowmeter signals were recorded on a CEC multichannel oscillograph.

Cold-flow propellant simulants were trichloroethylene and water, which simulated the oxidizer and fuel, respectively. These simulants were chosen on the basis of: (1) availability, being employed on a related program at Rocketdyne using the same facility, (2) ease of handling, and (3) maintaining the oxidizer/fuel immiscibility.

Collection System. The specific details of the collector are illustrated in Fig. D-4 through D-6. An overall view of the tubing arrangement and test tube rack is presented in Fig. D-4. As can be noted, the tubing slants outward from the collection plane to a 7 by 7 foot base. The base is 1/2-inch aluminum plate and separates the upper portion of the assembly from the Pyrex tube racks. Beneath the aluminum plate is a cart which houses the tube racks. The cart is mounted on wheels so that the entire tube matrix can be easily removed from under the collector and rolled to the measurement station.

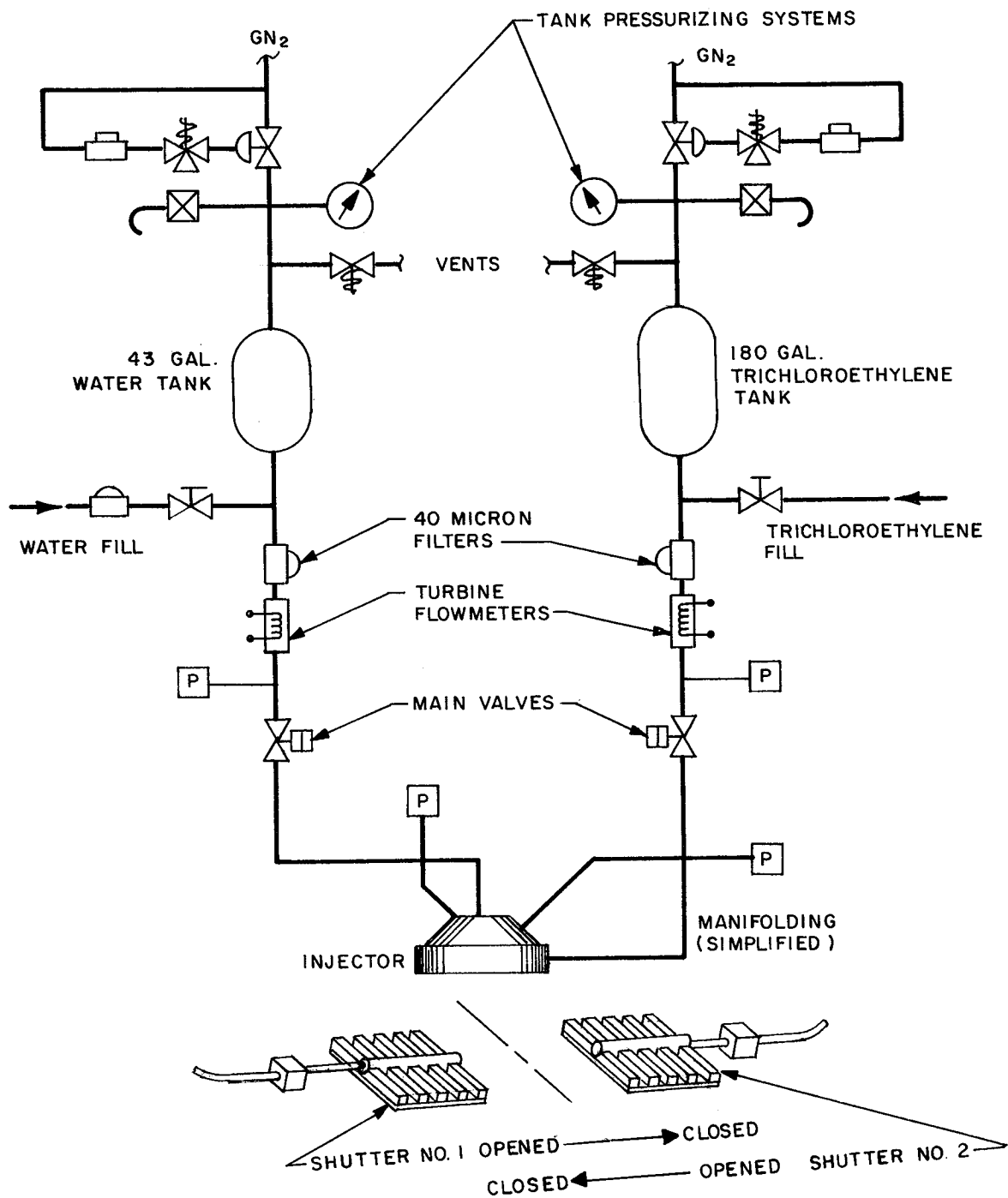


Figure D-3. Schematic Diagram of the Flow System Used in the Cold-Flow Mass and Mixture Ratio Distribution Study



5AA51-6/5/67-S1D

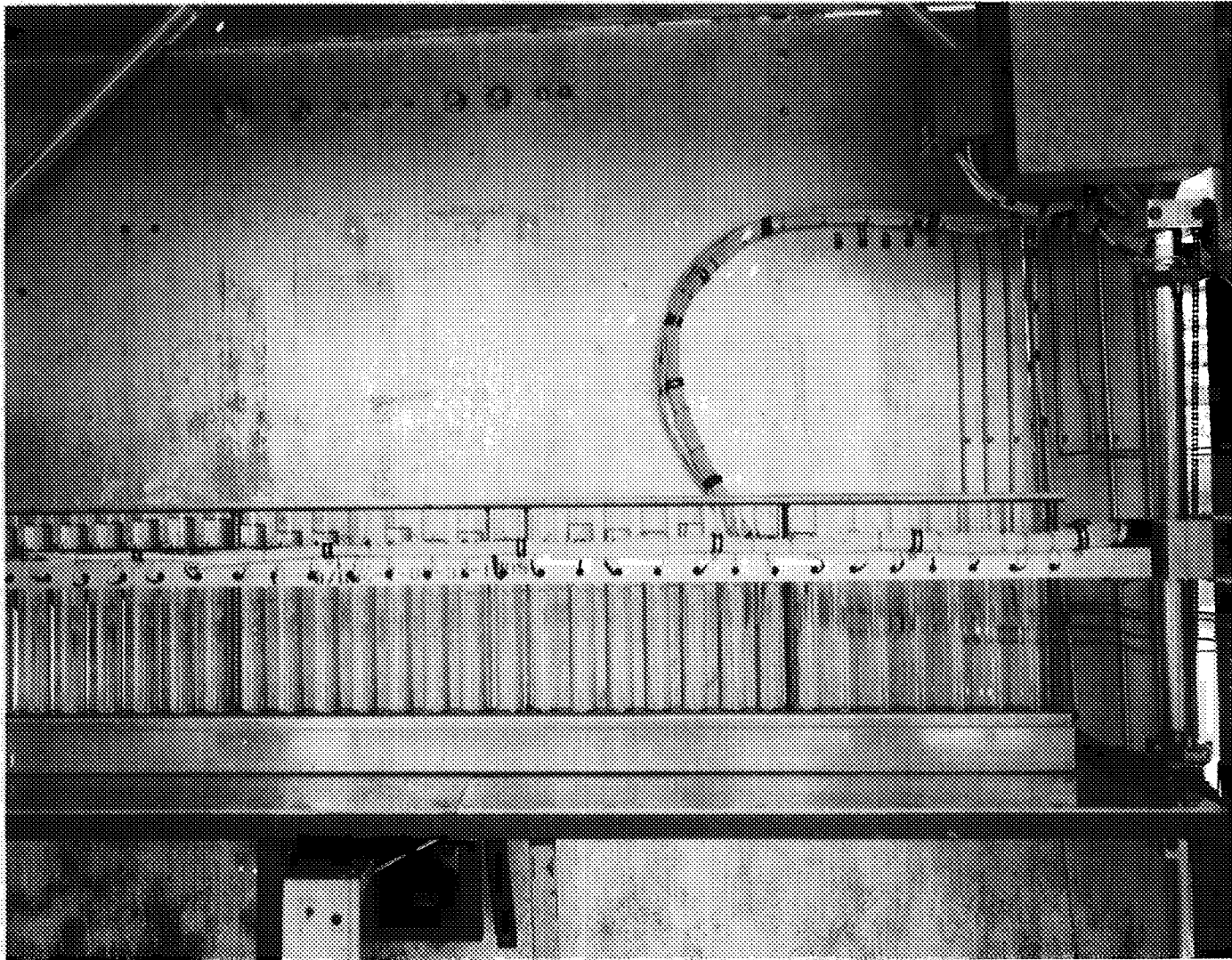
Figure D-4. Injector Spray Collection System Used in the Cold-Flow Mass and Mixture Ratio Distribution Study

The cart holds the 29 individual racks of tubes, each rack containing 29 tubes (one tube for each collection site). A rack of collector tubes is shown in Fig. D-5. The total number of tubes and collection sites is 841. The racks are fabricated from aluminum and the top and bottom holders are braced at five separate locations for rigidity with 1/8-inch rods. This construction results in a light-weight assembly which can be easily removed from the cart. Each tube can contain up to 650 milliliters of liquid, which is sufficient for extended-duration experiments. This is important since the longer the sampling time, the greater the experimental accuracy. This is principally due to reduction in the flow start-and-stop errors as well as liquid height reading accuracy.

The collector grid and shutter arrangement is illustrated in Fig. D-6. The collection grid is composed of 1/4-inch-diameter, 0.020-inch wall thickness, stainless-steel tubing arranged in a 29 by 29 tube matrix. The overall size of the tube matrix is 7-3/4 by 7-3/4 inches. Each of the collection tubes has been squared at the end to maximize the collection grid sampling area. This arrangement resulted in collection of more than 90 percent of the injected spray masses. This overall grid design results in extremely accurate distribution measurements.

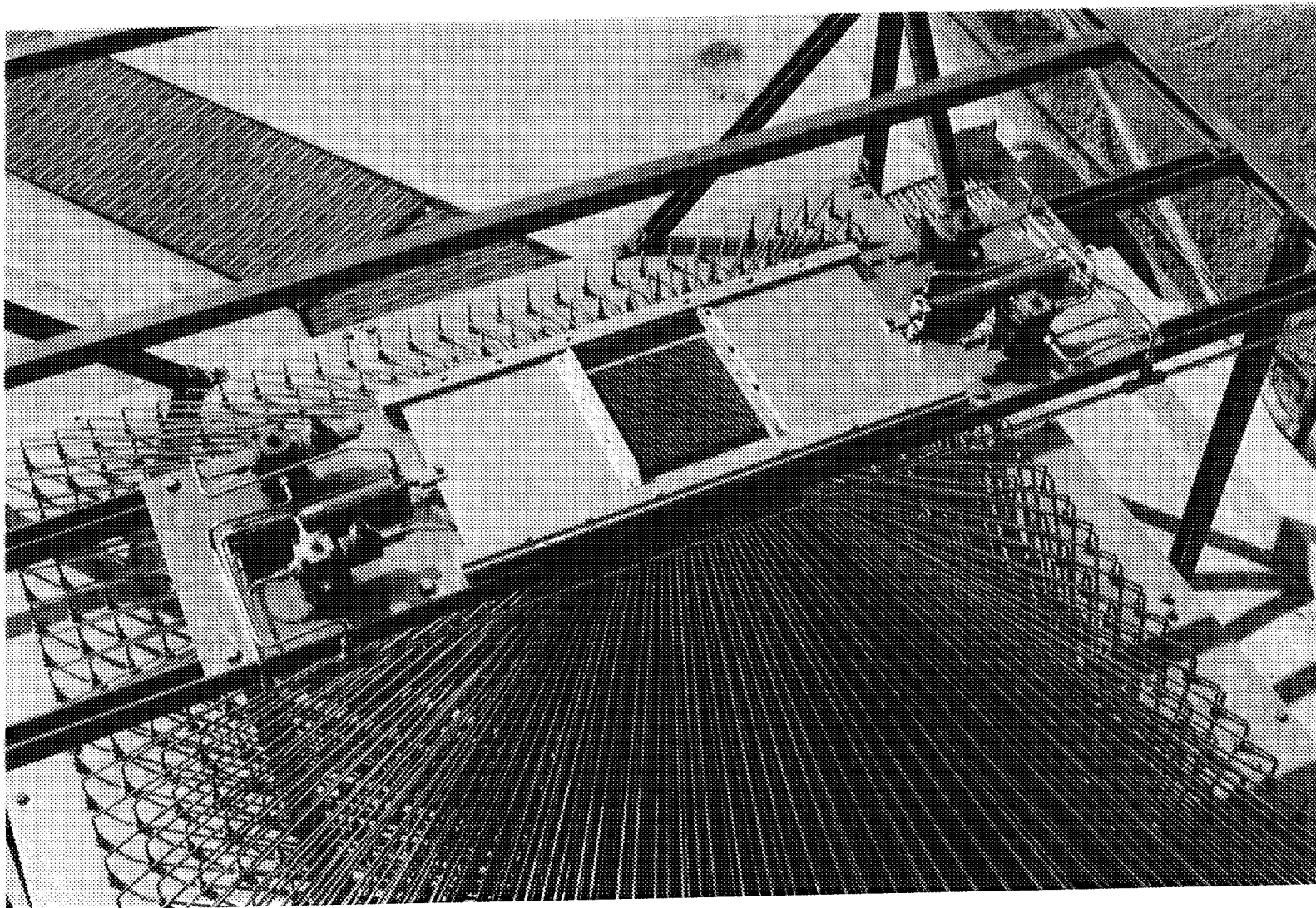
Close observation of the collection system during the cold flow tests indicated that there were no collection grid flooding problems, and blowing gaseous nitrogen through the collection system immediately after a test indicated that only negligible amounts of liquid are held up in the 1/4-inch-diameter stainless-steel tubes.

The shutters, which deflect the spray away from the collector until steady-flow conditions are obtained, are employed to reduce the start-and-stop transient errors. The shutters are pneumatically operated, and have an opening and closing travel time on the order of 200 milliseconds. Two shutters are employed to reduce the error bias introduced by the direction of the shutter opening and closing.



5AA51-6/5/67-S1C

Figure D-5. Rack of Collector Tubes Used in the Cold-Flow Mass and Mixture Ratio Distribution Study



5AA51-6/5/67-S1A

Figure D-6. Spray Collector Grid and Shutter Arrangement of Injector Spray Collection System Used in the Cold-Flow Mass and Mixture Ratio Distribution Study

Procedures

Experimental Procedures. The procedure for each of the cold-flow tests was as follows: The fuel and oxidizer simulant tanks were pressurized to give the desired flowrates. The main valves were opened and after injection pressures had become steady, the shutter was opened for a selected time interval and then closed. The main valves were then closed to conclude the test run. Time intervals were between 10 and 20 seconds for all injectors/ conditions tested. All tests were conducted with the injector centered above the collector at a distance of 3.25 inches. This distance of approximately 3 inches was chosen since prior analytical and experimental data indicated that this represented a good approximation of the primary propellant mixing region during combustion.

In each of the cold-flow tests the injector spray field was allowed to expand freely. Hence, small amounts of the spray were collected at the outer edges of the collector. The collector grid measures 7.7 inches square, which is approximately the diameter of the thrust chamber.

Although the basic approach to definition of the effect of mixing on performance for unlike-impinging stream injectors is similar to that of like-impinging stream injectors, the mechanical and hydraulic injector design variables which effect mixing differ. With unlike-impinging patterns, the distribution is altered by variations in the relative momentum and orifice diameter ratios between the fuel and oxidizer streams. Consequently, hot-fire conditions were simulated on the cold-flow basis by simulation of hot-fire momentum ratios. For the like-impinging stream patterns, mixture ratio distribution uniformity (E_m) is known to be primarily a function of element arrangement. For a particular element arrangement, velocity level and ratio (fuel-to-oxidizer) appear to be the parameters which effect propellant mixing the most (Ref. D-4). For this reason, hot-fire conditions for the like-doublet injector were simulated on the cold-flow basis by simulation of hot-fire injection velocities (i.e., simulation of volumetric flowrates).

Data Acquisition. The data recorded for each test included oxidizer and fuel simulant flowrates, injection pressures, flow duration, and the volume of oxidizer and fuel simulants in each of the 841 collection tubes.

The individual volumes were determined by a volumetrically calibrated metal strip or graduated cylinders. The metal strip resembled a thin metal scale with a scribe mark at 10-milliliter increments. This strip was inserted into the test tube and the volume of oxidizer simulant and the volume of fuel simulant were read directly. For tubes containing insufficient liquid quantities for accurate measurement, the volumetric measurements were obtained by use of graduated cylinders.

Data Analysis. The collector matrix data and the other recorded data were processed by computer to produce the following output: mass of oxidizer simulant, mass of fuel simulant, mixture ratio, and mass fraction for each tube. The mixing factor (E_m), predicted c^* efficiency (η_{c^*} ; dist.), center of collected mass (row and column), and percentage of the injected mass collected were also computed.

For all mass and mixture ratio distribution cold-flow experiments conducted during the program, Eq. 5 (page 17) and Eq. 6 (page 18), which are presented in the main text, were used to calculate c^* , dist. and E_m , respectively. Because the characteristic exhaust velocity is related to the actual hot-fire condition, the mixture ratio used in the calculation of c^* was not the injected cold-flow mixture ratio, but rather the mixture ratio corresponding to the simulated flow condition. Because for the like-doublet injectors an equal velocity simulation was used, the relationship between simulated and actual cold-flow mixture ratio is:

$$(MR)_{\text{simulated HF}} = \left(\frac{\rho_o}{\rho_f} \right) \left(\frac{\rho_{H_2O}}{\rho_{\text{tritic}}} \right) (MR)_{\text{cold flow}} \quad (D-1)$$

where

MR = mixture ratio (oxidizer/fuel)

ρ = density

Subscripts

o = oxidizer

f = fuel

For the pentad injector, where equal momentum ratio simulation was used, the following relationship exists between simulated and actual cold-flow mixture ratio:

$$(\text{MR})_{\text{simulated HF}} = \left[\left(\frac{\rho_o}{\rho_f} \right) \left(\frac{\rho_{\text{H}_2\text{O}}}{\rho_{\text{tric}}} \right) \right]^{1/2} (\text{MR})_{\text{cold flow}} \quad (\text{D-2})$$

REFERENCES

- D-1. Arbit, H. A. and S. D. Clapp: Fluorine-Hydrogen Performance Evaluation. Part I: Analysis, Design, and Demonstration of High-Performance Injectors for the Liquid Fluorine-Gaseous Hydrogen Propellant Combination, Research Report No. 66-10, Rocketdyne, a Division of North American Aviation, Inc., Canoga Park, California, April 1966.
- D-2. Fischer and Porter Co.: Instruction Bulletin 10C1510.
- D-3. AFRPL-TR-65-12: Design Handbook for Liquid Fluorine Ground Handling Equipment, Second Edition, Air Force Rocket Propulsion Laboratory, Edwards Air Force Base, California, August 1965.
- D-4. AFRPL-TR-68-147: Correlation of Spray Injector Parameters With Rocket Engine Performance, Rocketdyne, a Division of North American Rockwell Corporation, Canoga Park, Calif., June 1968.

APPENDIX E

THEORETICAL PERFORMANCE, COMBUSTION GAS PROPERTIES, AND PROPELLANT DENSITIES FOR FLOX MIXTURES/LPG BLEND

INTRODUCTION

Theoretical performance, selected combustion gas properties, and propellant densities for several FLOX mixtures/55 percent methane-45 percent ethane LPG blend are presented in this appendix. These topics are presented and discussed briefly below under separate headings. The FLOX mixtures considered (FLOX-70 percent F_2 ; FLOX-80 percent F_2 ; and F_2) are those which were used during the hot-fire experimental portion of the program.

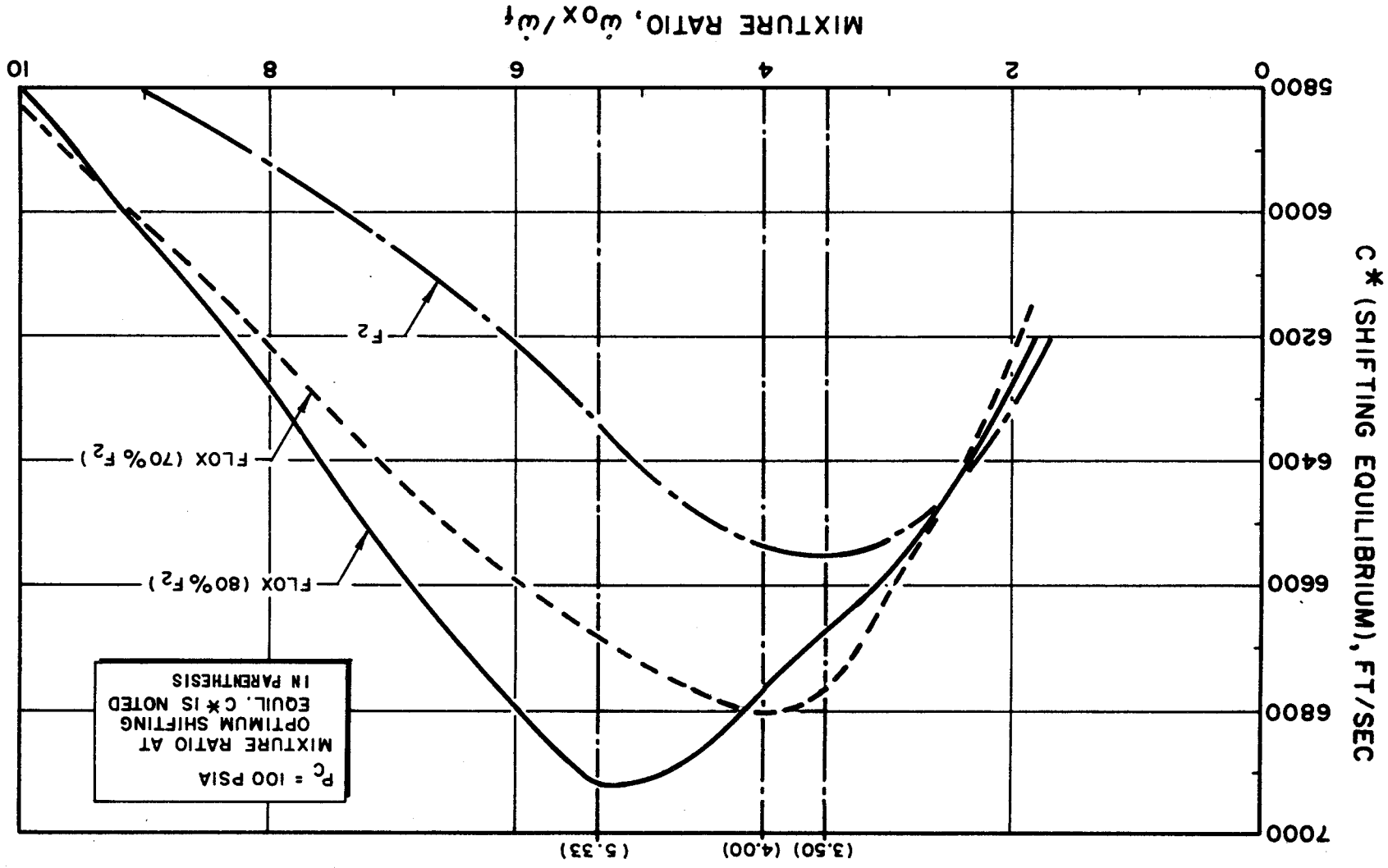
THEORETICAL PERFORMANCE

Theoretical performance (shifting equilibrium c^* ; $P_c = 100$ psia) is shown plotted as a function of mixture ratio for the three FLOX mixtures/55 percent CH_4 -45 percent C_2H_6 in Fig. E-1. The theoretical optimum performance and corresponding mixture ratio for the FLOX (80 percent F_2)/55 percent CH_4 -45 percent C_2H_6 are greater than those for the other two oxidizers with the subject fuel. The theoretical optimum c^* and corresponding mixture ratio, arranged in descending order, for the three propellant combinations are:

1. FLOX (80 percent F_2); 6921 ft/sec, 5.33
2. FLOX (70 percent F_2); 6802 ft/sec, 4.0
3. F_2 ; 6556 ft/sec, 3.5

Detailed examination of this figure reveals that:

1. Performance for the FLOX/LPG propellant combinations decreases more rapidly on each side of the optimum mixture ratio than



for the common earth storable propellants. Thus, performance for these propellant combinations is more sensitive to distribution than most propellant combinations (page 59).

2. The performance penalty paid for nonuniform distribution is most severe for the FLOX (80 percent F_2) mixture (page 57). This is caused primarily by the more rapid decrease in c^* with mixture ratio (for mixture ratios \geq optimum) for this propellant combination relative to the other two.

Theoretical vacuum specific impulse (at an expansion ratio of 40; $P_c = 100$ psia) is plotted as a function of mixture ratio for the FLOX (80 percent F_2)/LPG blend in Fig. E-2. This was the primary propellant combustion employed during the program. The optimum specific impulse of approximately 416 seconds occurs near theoretical optimum c^* mixture ratio (5.33).

THEORETICAL COMBUSTION GAS PROPERTIES

Theoretical combustion chamber gas temperature ($P_c = 100$ psia) is shown plotted as a function of mixture ratio for the three FLOX mixtures/LPG blend in Fig. E-3. As would be expected, the peak combustion gas temperature for the propellant combinations decrease in the order of decreasing optimum c^* . Peak values range from approximately 7600 R for the FLOX (80 percent F_2) to about 6900°R for the F_2 . In each case, the peak gas temperature occurs at a mixture ratio slightly above the (optimum) valve.

Combustion chamber gas molecular weight ($P_c = 100$ psia) is shown plotted as a function of mixture ratio for each propellant combination in Fig. E-4. In each case, the molecular weight increases with increasing mixture ratio. This is caused by the change in composition with mixture ratio. It is primarily due to the increase in HF/F concentration and corresponding decrease in H_2 /carbon-compound concentrations with increasing mixture ratio. Over the 1-to-10 mixture ratio range, the combustion gas molecular

7-11

VACUUM SPECIFIC IMPULSE, $\frac{\text{LB} \cdot \text{f} \cdot \text{SEC}}{\text{LB} \cdot \text{M}}$

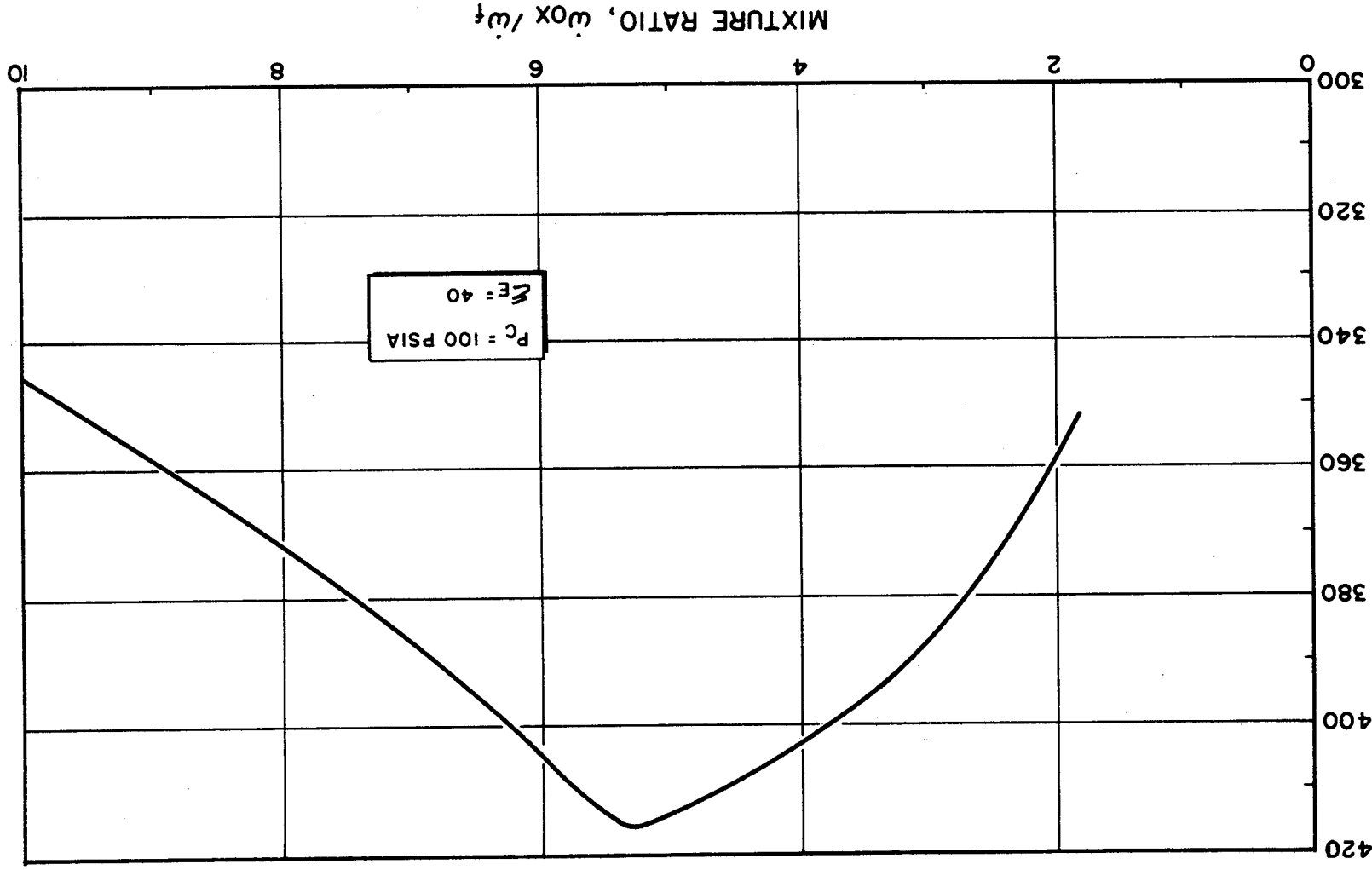


Figure E-2. Theoretical Vacuum Specific Impulse (to $\epsilon = 40$) as a Function of Mixture Ratio for FLOX (80 Percent F_2)/55 Percent CH_4 -45 Percent C_2H_6 Blend

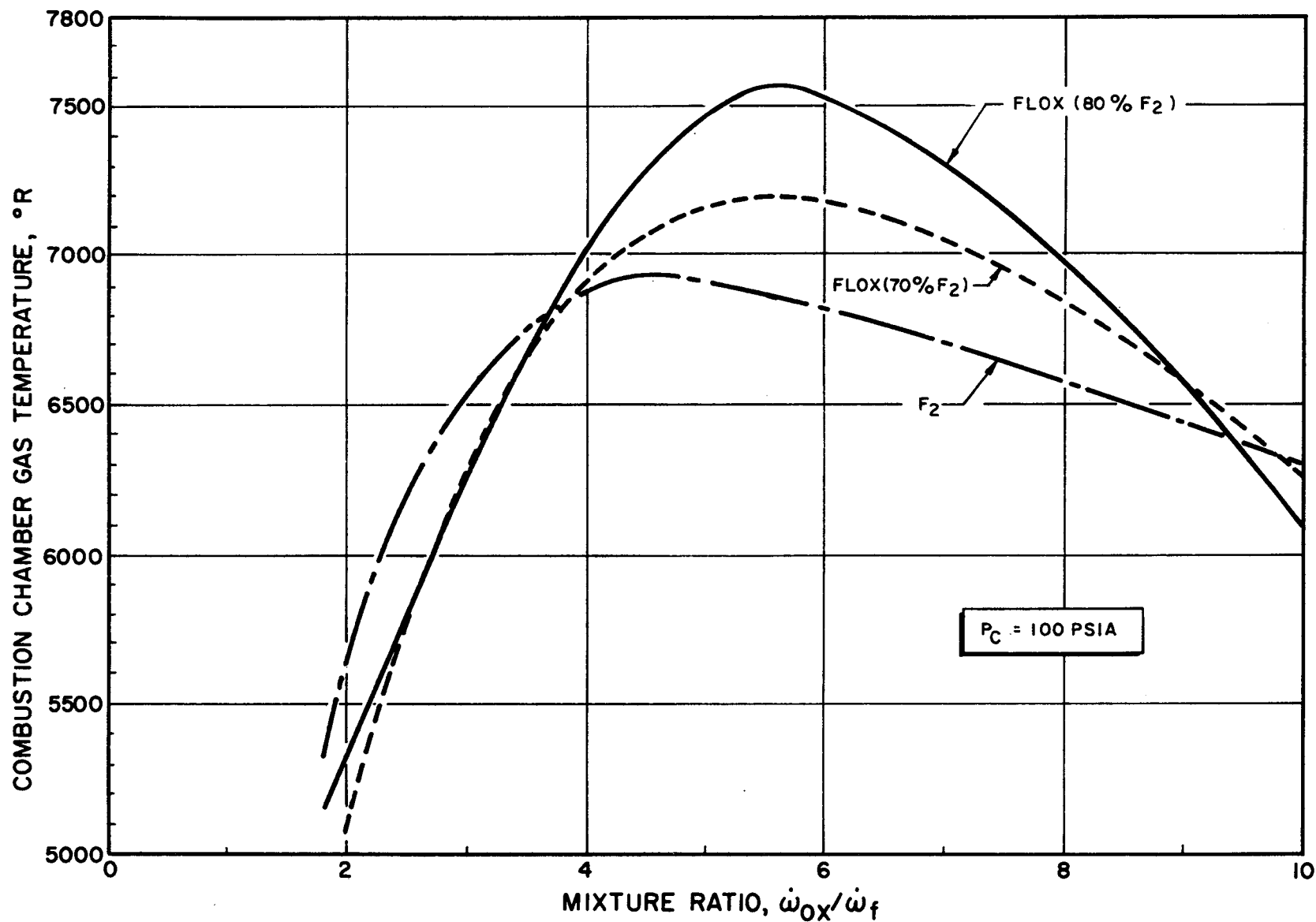


Figure E-3. Theoretical Combustion Chamber Gas Temperature as a Function of Mixture Ratio for Several FLOX Mixtures/55 Percent CH₄-45 Percent C₂H₆ LPG Blend

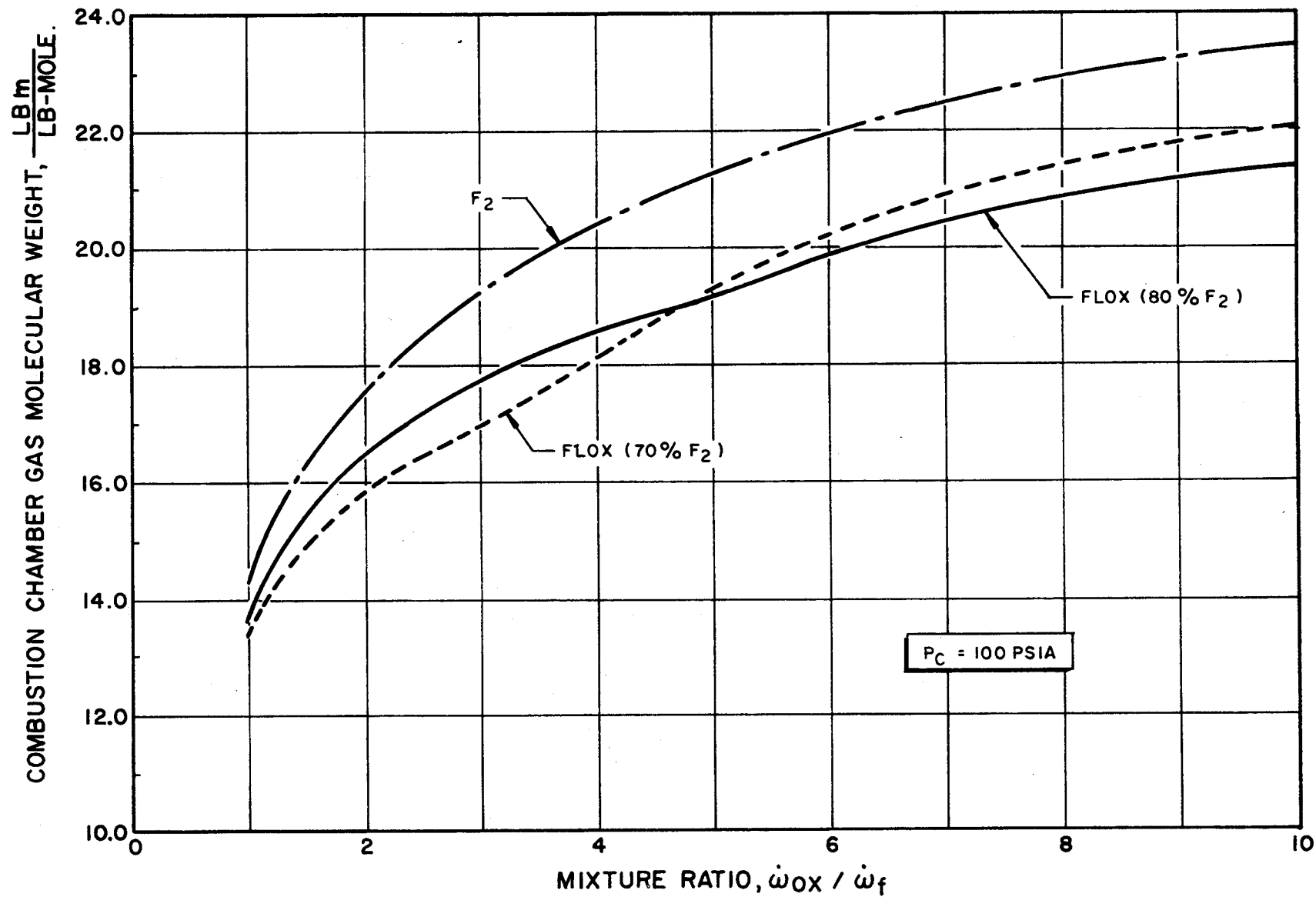


Figure E-4. Theoretical Combustion Chamber Gas Molecular Weight as a Function of Mixture Ratio for Several FLOX Mixtures/55 Percent CH_4 -45 Percent C_2H_6 LPG Blend

weight for the FLOX (70 percent F_2) and FLOX (80 percent F_2) are quite similar. It increases from approximately 14 at a mixture ratio of 1 to 22 at a mixture ratio of 10. The F_2 /LPG combustion gas molecular weight is slightly higher than that of the other propellant combinations over the entire mixture ratio range. In each case, the molecular weight at optimum mixture ratio is between 18 and 20.

Theoretical combustion gas composition, at optimum mixture ratio, for the three propellant combinations is shown in Table E-1. Examination of this table reveals that in each case the primary chemical species present is HF. Combustion gas composition for the FLOX (80 percent F_2) and FLOX (70 percent F_2) propellant combinations are quite similar. The F_2 /LPG propellant combination has a noticeable higher concentration of free carbon/carbon compounds.

PROPELLANT DENSITIES

FLOX Mixture

Densities for the FLOX mixtures (FLOX; 70 percent F_2 and FLOX; 80 percent F_2) were derived from experimental data for the pure components (LOX and LF_2). This was necessary because experimental data which defines density as a function of composition/temperature for the subject FLOX mixtures are not available. Densities were calculated based on the assumption that fluorine and oxygen behave as ideal liquids and that they follow Raoult's law (Ref. E-1). This is similar to the procedure that has been used on related programs (Ref. E-2). Thus, the density of the subject mixtures were calculated using the following equation:

$$\rho_{\text{mixture}} = \frac{1}{\frac{X_O}{\rho_O} + \frac{X_F}{\rho_F}} \quad (\text{E-1})$$

TABLE E-1

COMPARISON OF THEORETICAL COMBUSTION GAS COMPOSITION
AT OPTIMUM MIXTURE RATIO FOR SEVERAL FLOX
MIXTURES/55 PERCENT CH₄-45 PERCENT C₂H₆

Oxidizer	Composition, gram moles per 100 grams propellant			
	Chemical Species	Nominal Static Pressure, psia/Epsilon		
		100/Chamber Region	58/at Throat	14.7/1.85
FLOX (70 Percent F ₂) ↓	H	0.69831	0.58966	0.33644
	O	0.06033	0.04465	0.01292
	F	0.10721	0.06669	0.01574
	OH	0.06138	0.05560	0.03115
	HF	2.84035	2.88088	2.93183
	H ₂	0.40582	0.42608	0.49334
	H ₂ O	0.06327	0.08000	0.12614
	CO	1.26057	1.25515	1.24123
	CO ₂	0.02347	0.02897	0.04298
	O ₂	0.00370	0.00331	0.00133
FLOX (80 Percent F ₂) ↓	H	0.51952	0.43558	0.25193
	C	0.00208	0.00171	0.00083
	F	0.65781	0.55113	0.31984
	HF	2.92131	3.02795	3.25862
	H ₂	0.07185	0.06053	0.03704
	CO	1.01001	1.01031	1.01047
	CF	0.00129	0.00113	0.00069
	C ₂ F ₂	0.00020	0.00032	0.00089
F ₂ ↓	H	0.40641	0.41209	0.37996
	C	0.01250	0.00934	0.00282
	F	0.14217	0.12056	0.06101
	CH	0.00104	0.00070	0.00019
	C ₂ H	0.14860	0.11692	0.04826
	HF	3.86631	3.91272	4.01512
	H ₂	0.21774	0.22567	0.26054
	C ₂ H ₂	0.09222	0.07431	0.03900
	CF	0.07462	0.05368	0.01613
	CF ₂	0.00529	0.00342	0.00082
	C ₂	0.01595	0.01062	0.00222
	C ₃	0.05099	0.03611	0.00911
	C ₄	0.00125	0.00069	0.00008
	C ₅	0.00187	0.00103	0.00012
	C	0.65227	0.83970	1.19978

where

ρ = density

X = mass fraction

subscripts

O = oxygen

F = fluorine

The density of all three oxidizers (LF₂, FLOX; 80 percent F₂, and FLOX; 70 percent F₂) used during the program are shown plotted as a function of temperature in Fig. E-5. As is noted in the this figure, density is a strong function of both temperature and composition. Consequently samples of the FLOX mixtures were taken periodically throughout the experimental portion of the program to ensure that their compositions were correct and/or known. In addition, procedures were followed to ensure measurement of a valid temperature for use in determining oxidizer density and/or flowrates (Appendix D).

LPG Blend

The density of the LPG blend (55 weight percent CH₄-45 weight percent C₂H₆) is shown plotted as a function of temperature in Fig. E-6. The density of the fuel blend was determined in a manner similar to that for the FLOX mixtures. Experimental data which defines density as a function of temperature are not available for the subject LPG blend. Assumption of ideal mixing of the liquids should be quite good for adjacent members of a homologous series of organic compounds as was the case herein (Ref. E-1).

As was the case with the FLOX mixtures, density is quite dependent upon temperature and composition. Thus, procedures were followed to ensure that the composition was correct and that a valid temperature was measured for use in determining the fuel density/flowrate.

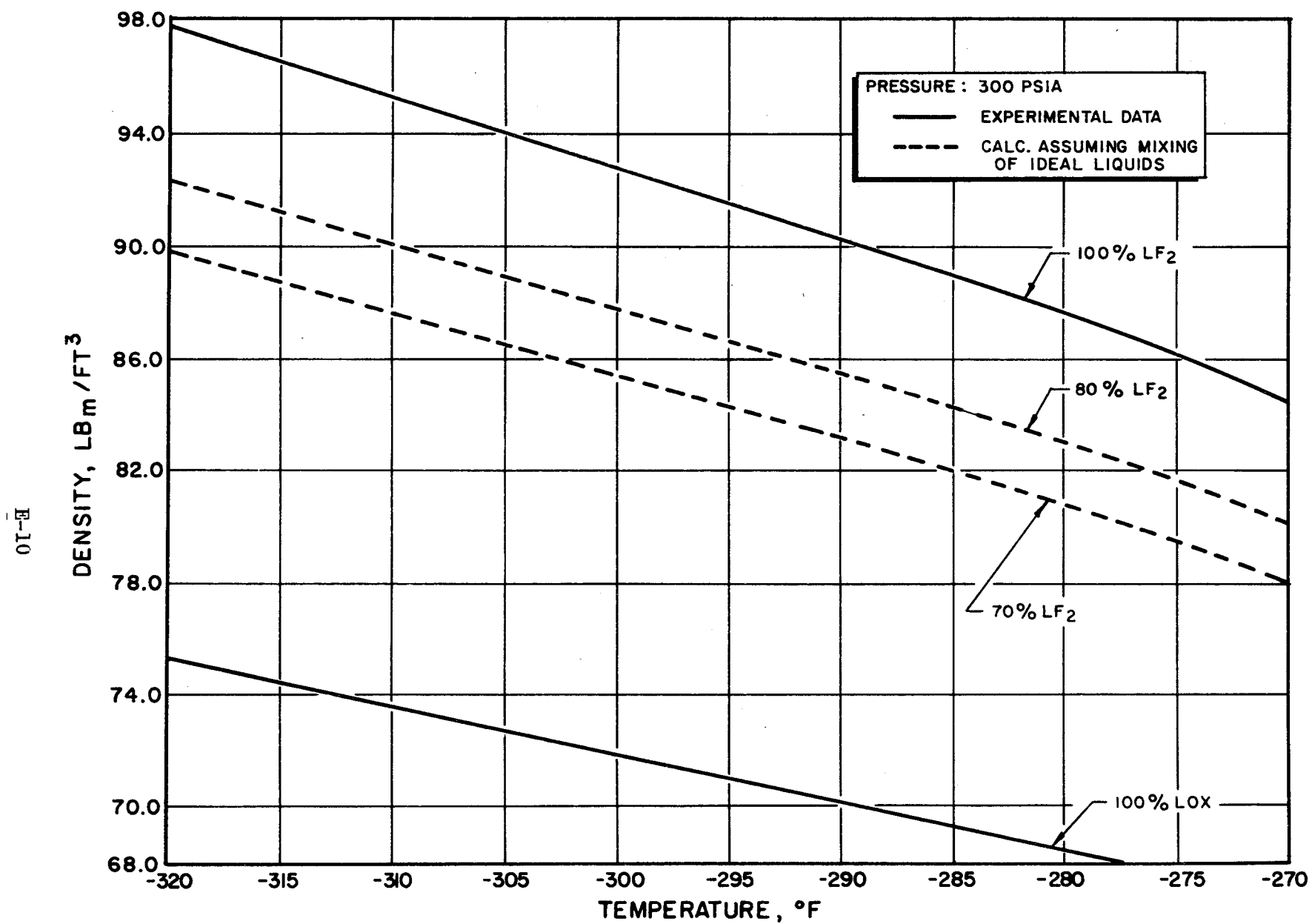


Figure E-5. Density of FLOX Mixtures as a Function of Temperatures

E-11

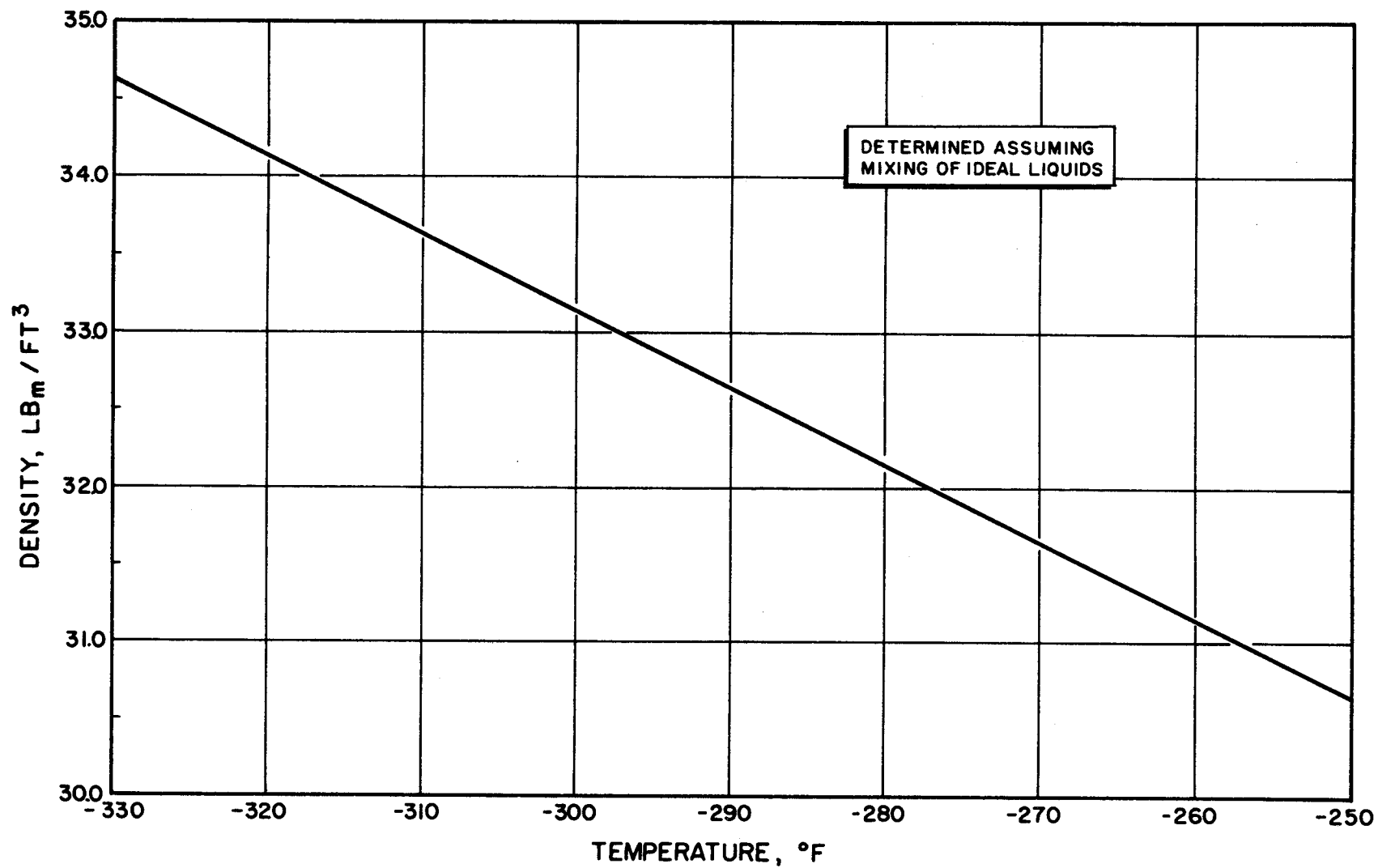


Figure E-6. Density of 55 Weight Percent Methane-45 Weight Percent Ethane LPG Blend as a Function of Temperature

REFERENCES

- E-1. Treybal, R. E., Mass-Transfer Operations, McGraw-Hill Book Company, Inc., New York, 1955.
- E-2. NASA SP-3037, Handling and Use of Fluorine and Fluorine-Oxygen Mixtures in Rocket Systems, NASA Lewis Research Center, Cleveland, Ohio, 1967.

APPENDIX F

HEAT TRANSFER DATA ANALYSIS TECHNIQUE

The technique selected for utilization in analyzing the heat transfer data is based on the "infinite conductivity method" using an uncooled copper calorimeter-type thrust chamber. This technique for mapping the heat flux distribution in rocket chambers, nozzles, etc. have been developed during previous Rocketdyne Research programs.

Thrust chamber heat flux, Q/A , was calculated by a heat balance on a heat transfer element over a small time interval:

$$Q/A = \frac{W \bar{C}_p}{A} \left(\frac{dt_c}{d\theta} \right) \quad \theta = \text{constant} \quad (\text{F-1})$$

where

- Q/A = heat flux, Btu/in.²-sec
- W = mass of isolated heat transfer segment, lbm
- \bar{C}_p = average specific heat of wall material, Btu/lbm
- A = area of isolated heat transfer segment, in.²
- t_c = cold-wall temperature, F
- θ = time, seconds

A typical plot of the hot-wall temperature, t_h , and the cold-wall temperature, t_c , as a function of time is presented in Fig.F-1. As shown in this figure, $dt_c/d\theta$ rises from zero initially, while $dt_h/d\theta$ decreases rapidly from some very high initial value. After a brief interval, θ_1 seconds, $dt_c/d\theta$ and $dt_h/d\theta$ are essentially constant and equal to each other and conditions are suitable for the application of the following heat transfer analysis method. During the interval from θ_i to θ_j , a nearly constant temperature differential exists across the heat transfer segment, indicating that a quasi-steady-state heat transfer condition exists and that the heat flux may be accurately determined from Eq. F-1.

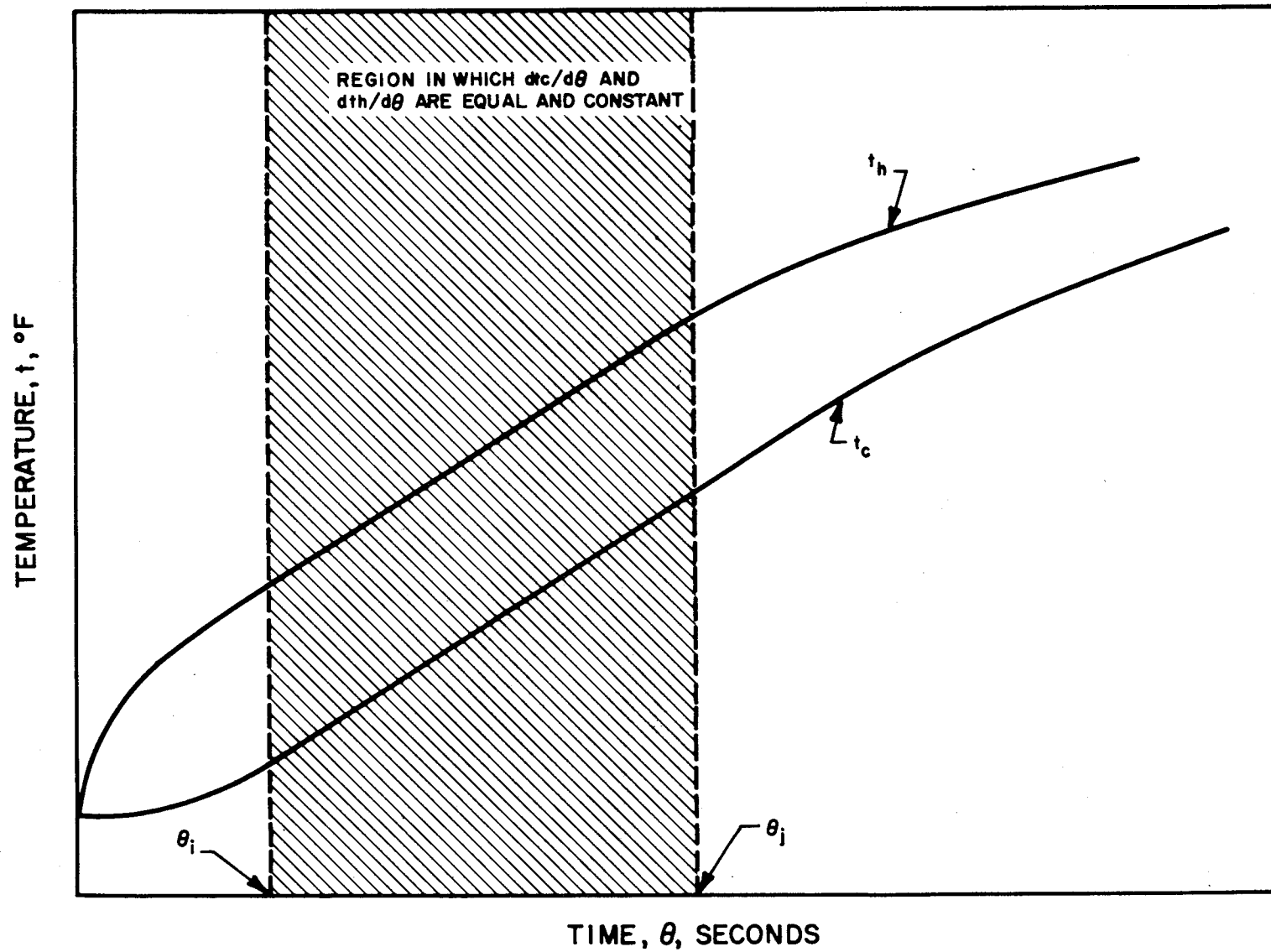


Figure F-1. Typical Time-Temperature History of Heat Transfer Segment in Chamber and/or Nozzle

For an accurate calculation of Q/A , a hand calculation of an average value of $dt_c/d\theta$ is made over the interval θ_i to θ_j and inputted into a computer for determination of local heat flux.

The local heat transfer coefficient, h_g , was calculated from heat flux as follows:

$$h_g = Q/A/(t_g - t_h) \quad (F-2)$$

where t_g is the theoretical combustion temperature corrected for combustion efficiency, i.e.:

$$t_g = t_{theo} \times \eta_{c*}^2 \quad (F-3)$$

and

$$\begin{aligned} h_g &= \text{gas-side heat transfer coefficient, Btu/in.}^2\text{-sec-F} \\ t_{theo} &= \text{theoretical combustion temperature, R} \\ \eta_{c*} &= \text{measured } c^* \text{ efficiency} \\ t_h &= \text{hot-wall temperature} \end{aligned}$$

Equation F-1 has been used throughout this program as the basic relations for defining heat flux based on the cold-wall temperature history. A determination of h_g can be made with reasonable accuracy by considering the following analysis.

A schematic cross section of a typical heat transfer segment and the assumed temperature distribution are shown in Fig.F-2. If the cold wall is assumed to be adiabatic (a good approximation), then

$$\frac{dt}{dx} \quad x = L = 0 \quad (F-4)$$

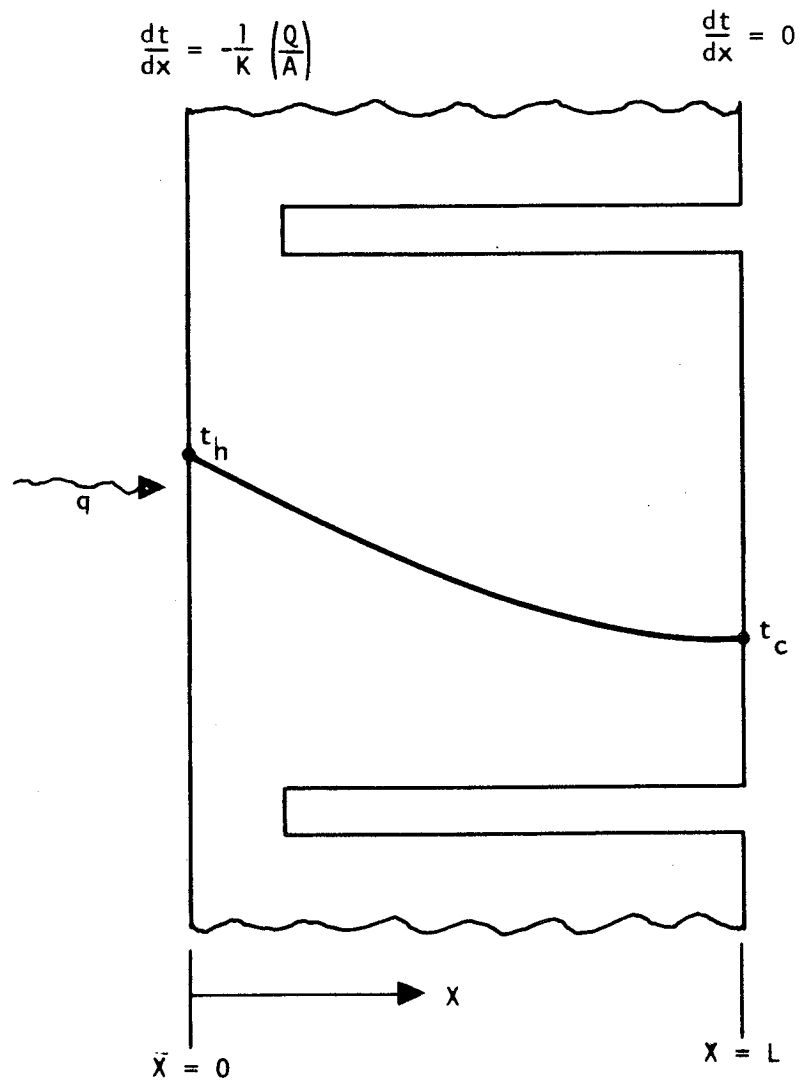


Figure F-2. Cross Section of Typical Heat Transfer Element

Furthermore, at $x = 0$

$$Q/A = -K_o \frac{dt}{dx} \quad x = 0 \quad (F-5)$$

where K_o should, in principle, be evaluated at t_h . With the additional specification that at $x = L$,

$$t_{x=L} = t_c \quad (F-6)$$

a parabolic temperature distribution is suggested as follows:

$$t = Ax^2 + Bx + C \quad (F-7)$$

Substitution of the boundary conditions into Eq. F-7 gives

$$t = t_c + \frac{(L-x)^2}{2K_o L} \frac{Q}{A} \quad (F-8)$$

and t_h may be evaluated from Eq. 8 as

$$t_{x=0} = t_h = t_c + \frac{L}{2K_o} \frac{Q}{A} \quad (F-9)$$

Equation F-8 may also be used to evaluate the average wall temperature, \bar{t} :

$$\bar{t} = t_c + \frac{L}{6K_o} \frac{Q}{A} \quad (F-10)$$

For the case of constant material properties (C_p and K) Eq. F-1, -2, -3, and -9 are sufficient to determine Q/A and h_g . In addition, the simplicity of the calculations would not warrant machine reduction.

The specific heat and thermal conductivity of oxygen-free copper (used in the calorimeter hardware) is shown in Fig. F-3. The variation of these properties with temperature is significant, particularly at temperatures below approximately 100 F.

The range of -300 to 0 F is of particular significance because wall temperatures in this band are frequently encountered at the start of a test, a result of pretest conditioning of the injector with liquid nitrogen (to ensure liquid flow of the cryogenic oxidizer). The extreme variation of C_p and K within this temperature range warrants the inclusion of variable properties into the above equations. This requirement, plus that of determining C_p and K at the average and hot-wall temperatures, respectively, considerably complicates the calculation procedure and warrants the use of computerized solution.

This calculation procedure has been programmed for the IBM 360 computer, which calculates Q/A and t_h from the measured $dt_c/d\theta$ and t_c values. In addition, a numerical integration of Q/A over the wall-surface area (from injector to chamber pressure tap location and to throat) is performed to determine the total heat loss, Q . The additional input of the measured performance parameters permits the calculation of local film coefficient and the heat loss correction factor which is applied to the measured c^* performance. The basic advantage of this procedure lies in the minimal amount of both hand and computer calculation time while maintaining a reasonable degree of accuracy. Although local values of h_g were also calculated, only specific heat flux values were used in the subsequent heat transfer analysis.

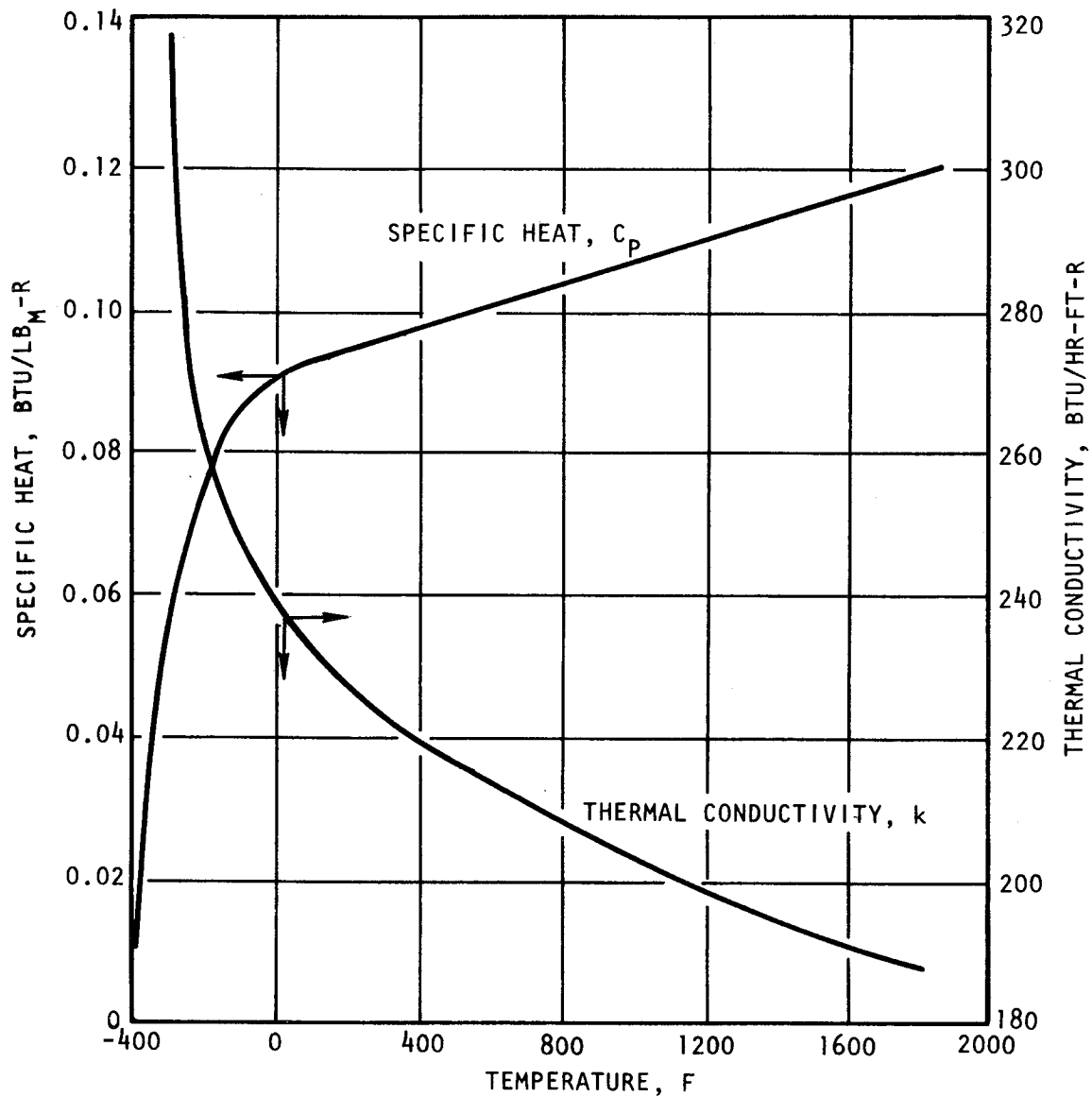


Figure F-3. Specific Heat and Thermal Conductivity vs Temperature for Oxygen-Free Copper.

APPENDIX G

Distribution List for Final Report NASA CR-72487
"Space Storable Propellant Performance Study"

NAS3-11199

Rocketdyne Division

North American Rockwell Corporation

COPIES

National Aeronautics and Space Administration	
Lewis Research Center	
21000 Brookpark Road	
Cleveland, Ohio 44135	
Attention: Contracting Officer, MS 500-313	1
Liquid Rocket Technology Branch, MS 500-209	8
Technical Report Control Office, MS5-5	1
Technology Utilization Office, MS 3-16	1
AFSC Liaison Office, MS 4-1	2
Library	2
C. Aukerman, MS 500-240	1
Office of Reliability & Quality Assurance, MS 500-203	1
J. Winters, MS 500-204	1
E. W. Conrad, MS 500-204	1
H. H. Valentine, MS 501-2	1
National Aeronautics and Space Administration	
Washington, D. C. 20546	
Attention: Code MT	1
RPX	2
RPL	2
SV	1
Scientific and Technical Information Facility	
P.O. Box 35	
College Park, Maryland 20740	
Attention: NASA Representative	6
Code CRT	

COPIES

National Aeronautics and Space Administration Ames Research Center Moffett Field, California 94035 Attention: Library	1
C.A. Syvertson	1
National Aeronautics and Space Administration Flight Research Center P.O. Box 273 Edwards, California 93523 Attention: Library	1
National Aeronautics and Space Administration Goddard Space Flight Center Greenbelt, Maryland 20771 Attention: Library	1
National Aeronautics and Space Administration John F. Kennedy Space Center Cocoa Beach, Florida 32931 Attention: Library	1
National Aeronautics and Space Administration Langley Research Center Langley Station Hampton, Virginia 23365 Attention: Library	1
National Aeronautics and Space Administration Manned Spacecraft Center Houston, Texas 77001 Attention: Library	1
National Aeronautics and Space Administration George C. Marshall Space Flight Center Huntsville, Alabama 35812 Attention: Library	1
Keith Chandler, R-P&VE-PA	1
Jet Propulsion Laboratory 4800 Oak Grove Drive Pasadena, California 91103 Attention: Library	1
W. Powell	1
Office of the Director of Defense Research & Engineering Washington, D. C. 20301 Attention: Office of Asst. Dir. (Chem. Technology)	1

COPIES

Defense Documentation Center Cameron Station Alexandria, Virginia 22314	1
RTD(RTNP) Bolling Air Force Base Washington, D. C. 20332	1
Arnold Engineering Development Center Air Force Systems Command Tullahoma, Tennessee 37389 Attention: AE01M	1
Advanced Research Projects Agency Washington, D.C. 20525 Attention: D.E. Mock	1
Aeronautical Systems Division Air Force Systems Command Wright-Patterson Air Force Base, Dayton, Ohio Attention: D.L. Schmidt, Code ASRCNC-2	1
Air Force Missile Test Center Patrick Air Force Base, Florida Attention: L.J. Ullian	1
Air Force Systems Command (SCLT/Capt. S.W. Bowen) Andrews Air Force Base Washington, D. C. 20332	1
Air Force Rocket Propulsion Laboratory (RPR) Edwards, California 93523	1
Air Force Rocket Propulsion Laboratory (RPM) Edwards, California 93523	1
Air Force FTC (FTAT-2) Edwards Air Force Base, California 93523 Attention: Mr. Donald Ross	1
Air Force Office of Scientific Research Washington, D.C. 20333 Attention: SREP, Dr. J. F. Masi	1
Office of Research Analyses (OAR) Holloman Air Force Base, New Mexico 88330 Attention: RRRD Maj. R. E. Brocken, Code MDGRT	1 1

COPIES

U.S. Air Force Washington 25, D.C. Attention: Col. C.K. Stambaugh, Code AFRST Commanding Officer	1
U.S. Army Research Office (Durham) Box CM, Duke Station Durham, North Carolina 27706	1
U.S. Army Missile Command Redstone Scientific Information Center Redstone Arsenal, Alabama 35808 Attention: Chief, Document Section Dr. W. Wharton	1 1
Bureau of Naval Weapons Department of the Navy Washington, D.C. Attention: J. Kay, Code RTMS-41	1
Commander U.S. Naval Missile Center Point Mugu, California 93041 Attention: Technical Library	1
Commander U.S. Naval Weapons Center China Lake, California 93557 Attention: Code 45 Code 753 W. F. Thorm, Code 4562	1 1 1
Commanding Officer Naval Research Branch 1030 E. Green Street Pasadena, California 91101	1
Director (Code 6180) U.S. Naval Research Laboratory Washington, D.C. 20390 Attention: H.W. Carhart	1
Picatinny Arsenal Dover, New Jersey Attention: I. Forsten, Chief Liquid Propulsion Laboratory	1
Union Carbide Corporation Nuclear Division ORGDP Records Department P.O. Box P Oak Ridge, Tennessee 37830 Attention: A. P. Huber, Superintendent Technical Division - ORGDP	1

COPIES

Air Force Aero Propulsion Laboratory Research & Technology Division Air Force Systems Command United States Air Force Wright-Patterson AFB, Ohio 45433 Attention: APRP (C.M. Donaldson)	1
Aerojet-General Corporation P.O. Box 296 Azusa, California 91703 Attention: Librarian	1
Aerojet-General Corporation 11711 South Woodruff Avenue Downey, California 90241 Attention: F.M. West, Chief Librarian	1
Aerojet-General Corporation P.O. Box 15847 Sacramento, California 95809 Attention: Technical Library 2484-2015A Dr. C.M. Beighley D.T. Bedsole	1 1 1
Aeronutronic Division of Philco Corporation Ford Road Newport Beach, California 92600 Attention: Dr. L. H. Linder, Manager Technical Information Department	1 1
Aeroprojects, Incorporated 310 East Rosedale Avenue West Chester, Pennsylvania 19380 Attention: C.D. McKinney	1
Aerospace Corporation P.O. Box 95085 Los Angeles, California 90045 Attention: J.G. Wilder, MS-2293 Library-Documents	1 1
Arthur D. Little, Inc. Acorn Park Cambridge 40, Massachusetts Attention: A.C. Tobey	1

COPIES

Astropower, Incorporated McDonnell-Douglas Astronautics Co. 2800 Campus Drive Newport Beach, California Attention: Dr. George Moe	1
Astrosystems, Incorporated 1275 Bloomfield Avenue Caldwell Township, New Jersey Attention: A. Mendenhall	1
ARO, Incorporated Arnold Engineering Development Center Arnold AF Station, Tennessee 37389 Attention: Dr. B. H. Goethert Chief Scientist	1
Susquehanna Corporation Atlantic Research Group Shirley Highway & Edsall Road Alexandria, Virginia 22314 Attention: A. Scurlock Security Office for Library	1 1
Battelle Memorial Institute 505 King Avenue Columbus, Ohio 43201 Attention: Report Library, Room 6A	1
Beech Aircraft Corporation Boulder Facility Box 631 Boulder, Colorado Attention: J.H. Rodgers	1
Bell Aerosystems, Inc. Box 1 Buffalo, New York 14205 Attention: T. Reinhardt W.M. Smith F. Herud	1 1 1
Bendix Systems Division Bendix Corporation Ann Arbor, Michigan Attention: John M. Bureger	1
The Boeing Company Aero Space Division P.O. Box 3707 Seattle, Washington, 98124 Attention: Ruth E. Peerenboom (1190) J. D. Alexander	1 1

	<u>COPIES</u>
Chemical Propulsion Information Agency Applied Physics Laboratory 8621 Georgia Avenue Silver Spring, Maryland 20910	1
Chrysler Corporation Missile Division Warren, Michigan Attention: John Gates	1
Chrysler Corporation Space Division New Orleans, Louisiana Attention: Librarian	1
Curtiss-Wright Corporation Wright Aeronautical Division Woodridge, New Jersey Attention: G. Kelley	1
University of Denver Denver Research Institute P.O. Box 10127 Denver, Colorado 80210 Attention: Security Office	1
McDonnell-Douglas Corporation Missiles & Space Systems Division 3000 Ocean Park Blvd. Santa Monica, California 90405 Attention: J.L. Waisman R.W. Hallet G.W. Burge P. Klevatt	1 1 1 1
Fairchild Strator Corporation Aircraft Missiles Division Hagerstown, Maryland Attention: Library	1
General Dynamics/Convair P.O. Box 12009 San Diego, California 92112 Attention: F. Dore Library & Information Services (128-00)	1 1
Convair Division General Dynamics Corporation P.O. Box 12009 San Diego, California 92112 Attention: Mr. R. Rovenger Centaur Resident Project Office	1

COPIES

General Electric Company Re-Entry Systems Department P.O. Box 8555 Philadelphia, Pennsylvania 19101 Attention: F.E. Schultz	1
General Electric Company Flight Propulsion Lab. Department Cincinnati 1t, Ohio Attention: D. Suichu	1
Grumman Aircraft Engineering Corporation Bethpage, Long Island, New York Attention: Joseph Gavin	1
Hercules Inc. Allegheny Ballistics Laboratory P.O. Box 210 Cumberland, Maryland 21501 Attention: Library	1
IIT Research Institute Technology Center Chicago, Illinois 60616 Attention: C.K. Hersh, Chemistry Division	1
Kidde Aero-space Division Walter Kidde & Company, Inc. 675 Main Street Belleville 9, New Jersey Attention: R.J. Hanville Director of Research Engineering	1
Lockheed Missiles & Space Company P.O. Box 504 Sunnyvale, California Attention: Y.C. Lee Power Systems R&D Technical Information Center	1 1
Lockheed-California Company 10445 Glen Oaks Blvd. Pacoima, California Attention: Library	1
Lockheed Propulsion Company P.O. Box 111 Redlands, California 92374 Attention: Miss Belle Berlاد, Librarian H. L. Thackwell	1 1

COPIES

Lockheed Missiles & Space Company
Propulsion Engineering Division (D.55-11)
1111 Lockheed Way
Sunnyvale, California 94087

1

Marquardt Corporation
16555 Saticoy Street
Box 2013 - South Annex
Van Nuys, California 91404
Attention: Librarian
 W.D. Boardman, Jr.
 C. Coulbert

1

1

1

Martin-Marietta Corporation
Martin Division
Baltimore 3, Maryland
Attention: John Calathes (1214)
 Library

1

1

McDonnell Aircraft Corporation
P.O. Box 6101
Lambert Field, Missouri
Attention: R.A. Herzmark

1

North American Rockwell
Space & Information Systems Division
12214 Lakewood Boulevard
Downey, California 90242
Attention: Technical Information Center D/096-722 (AJ01)
 H. Storms

1

1

Northrop Space Laboratories
1001 East Broadway
Hawthorne, California
Attention: Dr. William Howard

1

Purdue University
Lafayette, Indiana 47907
Attention: Technical Librarian

1

Radio Corporation of America
Astro-Electronics Division
Defense Electronic Products
Princeton, New Jersey
Attention: S. Airweather

1

Republic Aviation Corporation
Farmingdale, Long Island
New York
Attention: Dr. William O'Donnell

1

COPIES

Rocket Research Corporation Willow Road at 116th Street Redmond, Washington 98052	1
Rocketdyne Division of North American Rockwell 6633 Canoga Avenue Canoga Park, California 91304 Attention: Library, Department 086-306	1
Rohm and Haas Company Redstone Arsenal Research Division Huntsville, Alabama 35808 Attention: Librarian	1
Space-General Corporation 777 Flower Street Glendale, California Attention: C.E. Roth	1
Stanford Research Institute 333 Ravenswood Avenue Menlo Park, California 94025 Attention: Thor Smith	1
Texaco Experiment, Incorporated P.O. Box 3407 Richmond Virginia 23202 Attention: E.B. Monteath Librarian	1 1
Thiokol Chemical Corporation Alpha Division, Huntsville Plant Huntsville, Alabama 35800 Attention: Technical Director	1
Thiokol Chemical Corporation Reaction Motors Division Denville, New Jersey 07834 Attention: Librarian	1
Thiokol Chemical Corporation Redstone Division Huntsville, Alabama Attention: John Goodloe	1
TRW Systems, Incorporated 1 Space Park Redondo Beach, California 90200 Attention: G.W. Elverum STL Tech. Lib. Doc. Acquisitions H. Burge J. Mageean	1 1 1 1

COPIES

TRW, Incorporated TAPCO Division 23555 Euclid Avenue Cleveland, Ohio 44117 Attention: P.T. Angell	1
United Aircraft Corporation Corporation Library 400 Main Street East Hartford, Connecticut 06118 Attention: Dr. David Rix Erle Martin	1 1
United Aircraft Corporation Pratt & Whitney Division Florida Research & Development Center P.O. Box 2691 West Palm Beach, Florida 33402 Attention: R.J. Coar Library T.E. Bailey	1 1 1
United Aircraft Corporation United Technology Center P.O. Box 358 Sunnyvale, California 94088 Attention: Librarian	1
Vought Astronautics Box 5907 Dallas 22, Texas Attention: Warren C. Trent	1

UNCLASSIFIED

Security Classification

DOCUMENT CONTROL DATA - R & D

(Security classification of title, body of abstract and indexing annotation must be entered when the overall report is classified)

1. ORIGINATING ACTIVITY (Corporate author) Rocketdyne, a Division of North American Rockwell Corporation, 6633 Canoga Avenue, Canoga Park, California 91304		2a. REPORT SECURITY CLASSIFICATION Unclassified	
		2b. GROUP	
3. REPORT TITLE Space Storable Propellant Performance Study			
4. DESCRIPTIVE NOTES (Type of report and inclusive dates) Final Report			
5. AUTHOR(S) (First name, middle initial, last name) A. Y. Falk S. D. Clapp C. K. Nagai			
6. REPORT DATE 24 November 1968		7a. TOTAL NO. OF PAGES 257	7b. NO. OF REFS 25
8a. CONTRACT OR GRANT NO. NAS3-11199		9a. ORIGINATOR'S REPORT NUMBER(S) R-7677	
b. PROJECT NO.		9b. OTHER REPORT NO(S) (Any other numbers that may be assigned this report) NASA CR-72487	
c.			
d.			
10. DISTRIBUTION STATEMENT			
11. SUPPLEMENTARY NOTES		12. SPONSORING MILITARY ACTIVITY NASA Lewis Research Center Cleveland, Ohio	
13. ABSTRACT A 13-month applied research program encompassing an analytical, design, and experimental effort to develop high performance injectors for space storable propellants was conducted. The liquid-liquid propellant combination selected for study was FLOX (80% F ₂)/55% methane-45% ethane LPG blend. The program was apportioned into three basic technical tasks: Task I--Injector and Thrust Chamber Design, Task II--Injector and Thrust Chamber Fabrication, and Task III--Performance Evaluation Testing. The test matrix covered a range of chamber pressure (50 to 200 psia), mixture ratio (3 to 7), chamber geometry (15 inch $\leq L^* \leq$ 60-inch; at both 2 and 4:1 contraction ratios), and FLOX compositions (70 to 100% F ₂). Performance in the reference chamber ($L^* = 30$ -inch; $\epsilon_c = 2$) at nominal design conditions ($P_c = 100$ psia; MR = theoretical optimum c^* value = 5.33) was 97 percent of the shifting equilibrium c^* value. Results of the study provide a sound basis for positive design techniques for application to the general class of "space-storable" propellants.			

DD FORM 1473
1 NOV 65

UNCLASSIFIED

Security Classification

Unclassified

Security Classification

14. KEY WORDS	LINK A		LINK B		LINK C	
	ROLE	WT	ROLE	WT	ROLE	WT
FLOX LPG Injectors Spray Parmeters c* Performance						

UNCLASSIFIED

Security Classification